

**Investigation of Material Removal
Mechanism of SiC in Nano-scale Machining
Using Molecular Dynamics Simulation**

Zige Tian

A thesis Submitted in Partial Fulfilment of the Requirement of Liverpool John
Moores University Faculty of Engineering and Technology for the Degree of
Doctor of Philosophy

[This research programme was carried out in collaboration with Huaqiao
University]

December 2021

Abstract

Single crystal silicon carbide is widely used for microelectronics, optoelectronics and medicine sectors because of its specific properties. It is critical to completely eliminate the damaged layer and further reduce the surface roughness of the substrates to meet the requirements of epitaxy processes. Both mechanical removal and chemical removal play significant roles in the ultra-precision polishing. This research aims to investigate the nanomechanical performance, chemical reaction and removal mechanism of 4H-SiC and 6H-SiC polishing using molecular dynamics simulations and experimental validation.

Material deformation in the forms of amorphous transformation and dislocations are found to be the primary mechanisms of material removal, which are evidenced in both MD simulation and experiments. The dislocations in the scratched 4H-SiC and 6H-SiC are prone to crack growth when the fractured bonds do not recover. During scratching, dislocations and slips could occur on both the C face and the Si face, mainly on the (0001) basal plane and the (10-10) plane. It is found that the stress peak of scratching on C face is lower, which means the dislocations at C face on the (0001) plane occur more easily. Material removal efficiency of the C face is higher than that of the Si face, and there is less subsurface amorphous deformation on the C face. Moreover, in both experimental and simulation results, machining conditions, such as shape of abrasive particles, scratching speed and scratching direction, also have significant effects on nanometric material removal performance. Setting the scratching cutting depth as an integer multiple of the height of a half lattice crystal may be more beneficial for removing materials and better subsurface quality of substrates.

The occurrence of silicon dioxide when pure water is applied as the cooling liquid indicates that the 6H-SiC wafers can be oxidized by the water during polishing without any acid or alkali conditions. The occurrence and extent of the reactions between SiC and H₂O are influenced by the destruction of the 6H-SiC lattice structures. The material on the C face of 6H-SiC is oxidized faster than that on the Si face, directly resulting in a larger removal efficiency of the C face than the Si face in the same conditions. The research methods introduced in this research could also be applicable for the investigation of different SiC polytypes and other brittle materials. Understanding these problems could be beneficial to nanomachining of these hard and brittle materials.

Acknowledgments

My sincere gratitude goes to my supervisors Prof. Xun Chen and Prof. Xipeng Xu for their continuous support during my PhD. Many thanks for their efforts and patience.

I would like also to thank Prof. Feng Jiang, Prof. Jing Lu, Prof. James Ren, Dr Tahsin Opoz and Dr Qiufa Luo for their advice and suggestions.

I wish to thank the manufacturing technical teams in Liverpool John Moores University and Huaqiao University for their time, support and advice to accomplish my simulations and experiments in a good condition.

I would like to extend my gratitude to all members of the Faculty of Engineering and Technology, the staffs, the technicians, the secretaries and my fellow students.

I wish to thank my parents and my girlfriend for their patience, and endless support.

Contents

Abstract.....	III
Acknowledgments.....	IV
Contents	V
List of Figures.....	XI
List of Tables	XIX
Chapter 1. Introduction.....	1
1.1 Background	1
1.2 Project's aim and objectives.....	1
1.3 Structure of the thesis.....	2
Chapter 2. Literature review	4
2.1 Fundamentals of the silicon carbide.....	4
2.2 Literature of ultra-precision polishing technology.....	6
2.3 Literature of indentation and scratching tests	9
2.4 Literature of molecular dynamics simulation.....	15
2.4.1 Nanoindentation process	17
2.4.2 Nanoscratching process	18
2.4.3 Interfacial reaction	22
2.4.4 Chemical mechanical polishing process	24
2.5 Knowledge gaps and summary	25
Chapter 3. The methodology for the molecular dynamics simulation of nanomachining ..	28

3.1	Fundamentals of the molecular dynamics simulation	28
3.1.1	Integration algorithm for solving Newton's equation of motion	29
3.1.2	Empirical potential energy function.....	30
3.1.3	Thermodynamic ensembles	35
3.1.4	Other configurations	35
3.2	The simulation configuration	36
3.2.1	The workpiece.....	36
3.2.2	The abrasive tip.....	37
3.2.3	Model and setting-up for indentation simulations	37
3.2.4	Model and setting-up for scratching simulations.....	39
3.2.5	Model and setting-up for interfacial reaction simulations	42
3.2.6	Model and setting-up for scratching simulations on surface with oxide layer ..	44
3.3	Simulation procedure	46
3.3.1	Hardware consideration	46
3.3.2	Software consideration.....	47
3.3.3	Methodology flowchart.....	48
3.3.4	Dislocation extraction algorithm method.....	49
Chapter 4.	The methodology for the verification experiments.....	51
4.1	Nanoindentation tests	51
4.1.1	Indentation device	51
4.1.2	Specimens	52

4.1.3	Experiment setup and procedures	53
4.2	Nanoscratching tests.....	54
4.2.1	Scratching device	54
4.2.2	Specimens	55
4.2.3	Experiment set-up	55
4.3	Multiple grit scratching tests	55
4.3.1	Scratching machine	55
4.3.2	Scratching tool	56
4.3.3	Workpiece material	57
4.3.4	Experimental set-up and procedure	57
Chapter 5.	Nanoindentation tests and simulations.....	61
5.1	Indentation forces	61
5.2	Surface and subsurface morphology	63
5.3	Defect formation and evolution.....	66
5.4	Potential function comparison.....	70
Chapter 6.	Nanoscratching tests and simulations	73
6.1	Scratching forces	73
6.2	Material remove efficiency	75
6.3	Amorphisation.....	76
6.4	Dislocation analysis.....	80
6.5	Materials removal and surface deformation mechanism.....	83

Chapter 7.	Effects of machining conditions	87
7.1	Scratching performance in relation to SiC layer structure (1st-8th)	87
7.2	Effects of the shape of abrasive tip	90
7.2.1	Forces	90
7.2.2	Subsurface deformation	93
7.2.3	Stress distribution.....	95
7.2.4	Material removal efficiency	97
7.3	Effects of scratching speed.....	102
7.3.1	Forces.....	102
7.3.2	Subsurface deformation	103
7.3.3	Stress distribution.....	105
7.3.4	Material removal efficiency	107
7.4	Effects of scratching direction.....	109
7.4.1	Forces.....	110
7.4.2	Subsurface deformation	110
7.4.3	Stress distribution.....	113
7.4.4	Material removal efficiency	115
7.5	Experimental verification.....	117
7.5.1	Effects of the shape of abrasive tip	117
7.5.2	Effects of the scratching speed	119
7.5.3	Effects of the scratching direction	121

Chapter 8. Interfacial reaction	123
8.1 Reaction of SiC and H ₂ O during the heating process	123
8.2 Reaction of SiC and H ₂ O in the constant temperature	124
8.3 Reaction of SiC and H ₂ O during the loading process by diamond	125
8.4 Comparison of simulation and experimental results	126
8.5 Reaction mechanism during polishing	129
Chapter 9. Effect of oxide layer.....	132
9.1 Nanoscratching simulation at constant depths	132
9.1.1 Forces.....	132
9.1.2 Material removal characteristics	134
9.1.3 Subsurface deformation	135
9.2 Nanoscratching simulation in an inclined direction.....	138
9.3 Nanoscratching simulation under constant loads	140
Chapter 10. Conclusion, recommendations and future work.....	145
10.1 Conclusion.....	145
10.2 Contribution to knowledge.....	147
10.3 Recommendations and future work.....	148
References.....	149
Appendixes	164

List of Figures

Figure 2-1. Structures of 4H- and 6H- Silicon Carbide.....	5
Figure 2-2. Schematic diagram of the chemical mechanical polishing [14].....	7
Figure 2-3. Material removal mechanisms of SiC using the SG polishing tool (left) and fixed abrasive polishing tool (right) [29].	9
Figure 2-4. Surface morphology of 6H-SiC under different loading (a) 8 mN, (b) 10 mN, (c) 20 mN, (d) 40 mN, (e) 60 mN [35].....	11
Figure 2-5. Topography of scratched grooves under different normal loads [36].....	12
Figure 2-6. Topography of scratched grooves under different normal loads [37].....	13
Figure 2-7. Three-dimensional topography of the groove for a Δdy of 0.1 mm: (a) topography of the groove using a 3D-video microscope, (b) topography of the groove using a laser scanning confocal microscope, and (c) section profile having the maximum depth and width in the interference region.[38].....	14
Figure 2-8. Subsurface damage of brittle materials in micron-scale cutting.	15
Figure 2-9. The Coupling of FEM and SPH method used in the SiC scratching. (Material damage distribution of the workpiece after double scratching at different distances in the Y-direction: (a) $\Delta dy=0.05$ mm, (b) $\Delta dy=0.1$ mm, and (c) $\Delta dy=0.2$ mm) [38].	16
Figure 2-10. Coordination number distribution in cross section at (a) $h = 0.84$ nm, and (b) $h = 0.96$ nm; (c) Amorphization path from wurtzite structure to amorphous structure. [59]...	18
Figure 2-11. Deformation evolution in 6H-SiC due to the variation of the depth of cut d of the diamond cutting tool (total cutting length = 18 nm). (a) $d = 0.3$ nm, (b) $d = 0.5$ nm, (c) $d = 2$ nm, and (d) $d = 3$ nm. [63].....	19
Figure 2-12. Subsurface deformation of Silicon Carbide and Silicon. (a) 4H-SiC, (b) 3C-SiC, (c) 6H-SiC and (d) Si. [6]	20

Figure 2-13. Topography of machined surface under different crystal plane/orientation conditions, where a–f are the corresponding process modes (0001)/[2-1-10], (0001)/[10-10], (01-10)/[2-1-10], (01-10)/[0001], (11-20)/[1-100], and (11-20)/[0001], respectively. [65]....	21
Figure 2-14. Scratching model using a diamond tool with a V-shaped defect. [71]	22
Figure 2-15. Initial (left) and final snapshots of SiC oxidation by H ₂ O at 2000 K (centre) and 4000 K (right). The yellow arrows show the extent of SiO ₂ slab growth. Si = yellow, C = blue, O = red, and H = white. [78].....	23
Figure 2-16. Simulation snapshots of initial structures of the SiC/O ₂ interfaces for a- (11-20), C- (000-1), m- (1-100), and Si- (0001) oriented SiC at time = 0. [80].....	23
Figure 2-17. Schematic of the MD simulation model for nanoindentation on the Cu (001) surface with a water film [81].....	24
Figure 2-18. The model for ReaxFF reactive MD simulations of Si CMP in the aqueous H ₂ O ₂ . [84].....	25
Figure 2-19. The model of silica and diamond in aqueous H ₂ O ₂ . [87].....	25
Figure 3-1. The diagram of molecular dynamics simulation.	28
Figure 3-2. The schematic representation of the idea of PBC.	36
Figure 3-3. The Diamond Structure.	37
Figure 3-4. The MD model of indentation.	38
Figure 3-5. The MD model of scratching.	40
Figure 3-6. Different types of tips used as the scratching abrasive.	41
Figure 3-7. Diagram of two scratching directions from the top view.....	42
Figure 3-8. The RMD models. (a) The reaction between H ₂ O molecules and both faces of 6H-SiC. (b) The reaction between H ₂ O molecules and the Si face of 6H-SiC. (c) The reaction between H ₂ O molecules and the C face of 6H-SiC.	43

Figure 3-9. Workpiece model with oxide layers on Si face and C face.....	45
Figure 3-10. The flowchart of software methodology.	48
Figure 3-11. Schematic diagram of Burgers vectors.	50
Figure 4-1. The Fischer Scope HM 2000.....	52
Figure 4-2. 4H-SiC (left) and 6H-SiC (right) wafers.....	52
Figure 4-3. SIGMA 500.....	54
Figure 4-4. Nano Indenter G200.....	54
Figure 4-5. XR 610 CNC machine.	56
Figure 4-6. Scratching tool.	57
Figure 4-7. The 6H-SiC (0001) wafers used in multiple grit scratching tests.	57
Figure 4-8. The experimental tests set-up.....	58
Figure 4-9. The Bruker Nano Surfaces Division (left) and Scanning Electron Microscopy (right).	60
Figure 5-1. Load-displacement curves of indentation tests.	62
Figure 5-2. Load-displacement curves obtained from the MD simulations.	62
Figure 5-3. Surface morphology of Si face of 6H-SiC wafer after indentation at the load of 200 mN (left) and 300 mN (right).....	64
Figure 5-4. Upward views of subsurface deformation obtained using the DXA. (a) Si face of 4H-SiC (b) Si face of 6H-SiC (c) C face of 4H-SiC (d) C face of 6H-SiC.	65
Figure 5-5. Vertical cross-section morphology after indentation. (a) Si face of 4H-SiC (b) Si face of 6H-SiC (c) C face of 4H-SiC (d) C face of 6H-SiC.	65
Figure 5-6 Horizontal morphology after indentation. (a) Si face of 4H-SiC (b) Si face of 6H-SiC (c) C face of 4H-SiC (d) C face of 6H-SiC.....	66

Figure 5-7. Horizontal cross-sections using different slice depths for the Si face of 6H-SiC. (a) 7.6 nm, (b) 6.6 nm, (c) 6.2 nm, (d) 6.0 nm, (e) 5.7 nm, (f) 5.5 nm, (g) 5.0 nm, (h) 4.0 nm. ...	67
Figure 5-8. Horizontal cross-sections using different slice depths for the C face of 6H-SiC. (a) 7.6 nm, (b) 6.6 nm, (c) 6.2 nm, (d) 6.0 nm, (e) 5.7 nm, (f) 5.5 nm, (g) 5.0 nm, (h) 4.0 nm. ...	68
Figure 5-9. Horizontal cross-sections using different slice depths for the Si face of 4H-SiC. (a) 7.6 nm, (b) 6.6 nm, (c) 6.2 nm, (d) 6.0 nm, (e) 5.7 nm, (f) 5.5 nm, (g) 5.0 nm, (h) 4.0 nm.	68
Figure 5-10. Horizontal cross-sections using different slice depths for the C face of 4H-SiC. (a) 7.6 nm, (b) 6.6 nm, (c) 6.2 nm, (d) 6.0 nm, (e) 5.7 nm, (f) 5.5 nm, (g) 5.0 nm, (h) 4.0 nm.	69
Figure 5-11. Load-displacement curves obtained using the different potential parameters. ...	71
Figure 5-12. Horizontal morphology after indentation. (a) Group A, (b) Group B, (c) Group C, (d) Group D, (e) Group E.....	71
Figure 5-13. Horizontal cross-section view of subsurface morphology after indentation. (a) Group A, (b) Group B, (c) Group C, (d) Group D, (e) Group E.....	72
Figure 6-1. Comparison of specific scratching forces in MD simulations and experiments. (a) Tangential specific force of MD simulations. (b) Normal specific force of MD simulations. (c) Specific force of scratching experiments.	74
Figure 6-2. Scratching and ploughing actions in all scratching simulations. (a) Atom removal definition in a scratching. (b) Number of atoms above original surface. (c) Number of removed atoms.	76
Figure 6-3. Sectional views of scratching at 0.5 nm obtained by DXA.	77
Figure 6-4. Sectional views of scratching at 1 nm obtained by DXA.	77
Figure 6-5. Sectional views of scratching at 2 nm obtained by DXA.	78
Figure 6-6. Sectional views of scratching at 3 nm obtained by DXA.	78

Figure 6-7. Numbers of amorphous atoms in the subsurface of all scratching simulations. ...	79
Figure 6-8. Numbers of dislocations in the subsurface of all scratching simulations.	80
Figure 6-9. Deformation in the subsurface of a scratching and SiC basal plane view. (a) Subsurface morphology of deformation. (b) Schematic diagram of crystal.	81
Figure 6-10. Von Mises stress distribution of 6H-SiC during scratching.	82
Figure 6-11. Von Mises stresses of in the scratching of 6H-SiC at different time steps.	82
Figure 6-12. Forces of C face and Si face of 6H-SiC obtained by moving average at the scratching depth of 3 nm.	83
Figure 6-13. The cross-sectional subsurface image of 6H-SiC after scratching at the depth of 3 nm.	85
Figure 6-14. (a) Cross-sectional TEM image of 6H-SiC substrate after scratching test with 5 mN load by a tip with radius of 90 nm. (b) Magnified view of the regions indicated by circles 1 in a. (c) A bright-field TEM micrograph of the region at the bottom of the groove indicated by circles 2 in a. (d) A high-resolution TEM image of zone indicated by circle 3 in c. (after Meng, et al [36])	85
Figure 7-1. Atomic layout out 6H-SiC (left) and 4H-SiC (right).	87
Figure 7-2. The average forces obtained from the scratching stages.	88
Figure 7-3. The DXA results from 1 st to 8 th layer scratching on 6H-SiC.	89
Figure 7-4. The maximum thicknesses of the subsurface amorphous deformation at different scratching depths obtained using DXA on 6H-SiC (left) and 4H-SiC (right).	90
Figure 7-5. Forces of tips in different shapes obtained from the stable scratching stage.	92
Figure 7-6. Pressure of tips in different shapes obtained from the stable scratching stage.	93
Figure 7-7. DXA results of scratching cases using tips in different shapes. (Scratching depth of 3 nm and scratching speed of 100 m/s)	95

Figure 7-8. Numbers of (a) amorphous atoms and (b) dislocations in subsurface.	95
Figure 7-9. Stress distribution of workpiece using tips in different shapes. (All longitudinal-section views pass through the centre axis of the abrasive tip.)	97
Figure 7-10. Maximum stress using tips in different shapes.	97
Figure 7-11. Number of (a) atoms above surface and (b) removed atoms. Ratio of (c) atoms above surface and (d) removed atoms per nm ² in tangential direction.....	99
Figure 7-12. Distribution of Z positions of atoms above original surface using tips in different shapes. (Left: 2 nm; right: 3 nm)	100
Figure 7-13. The diagram of pile-up ratio.	101
Figure 7-14. Pile-up ratios of all scratching cases using tips in different shapes.	101
Figure 7-15. Tangential (left) and normal (right) forces in different scratching speeds.....	102
Figure 7-16. DXA results (left) and amorphous deformation (right) of scratching cases in different speeds.	104
Figure 7-17. Numbers of (a) amorphous atoms and (b) dislocations in subsurface.	105
Figure 7-18. Stress distribution of workpiece using different scratching speeds.	106
Figure 7-19. Maximum stress of machining area and machined area using different scratching speeds.....	107
Figure 7-20. Distribution of Z positions of atoms above original surface using different speeds.....	109
Figure 7-21. Numbers of atoms above original surface and removed atoms in subsurface. .	109
Figure 7-22. Tangential (left) and normal (right) forces in different scratching directions. .	110
Figure 7-23. DXA results (left) and amorphous deformation (right) of scratching cases in different directions.	112
Figure 7-24. Numbers of (a) amorphous atoms and (b) dislocations in subsurface.	112

Figure 7-25. Cross-section views of surface and subsurface atoms in different cases. (a) [1-210]_ 2 nm. (b) [1-100]_ 2 nm. (c) [1-210]_ 3 nm. (d) [1-100]_ 3 nm.	113
Figure 7-26. Stress distribution of workpiece using different scratching directions.	115
Figure 7-27. Maximum stress of machining area and machined area using different scratching directions.	115
Figure 7-28. Distribution of Z positions of atoms above original surface using different directions.	117
Figure 7-29. Numbers of atoms above original surface and removed atoms in subsurface. .	117
Figure 7-30. The SEM results of three scratches on Si face of 6H-SiC wafer. (Scratching direction: [1-210], scratching speed: 10 m/s)	119
Figure 7-31. The SEM results of scratches in different scratching speeds. (Left: 1 m/s, right: 10 m/s)	120
Figure 7-32. The average length of ductile deformations in different scratching speeds.	121
Figure 7-33. The SEM results of scratches on Si face of 6H-SiC wafer along different scratching directions. (Left: [1-210], right: [1-100]).	122
Figure 8-1. RMD simulation snapshots of the reactions between two faces of 6H-SiC and H ₂ O molecules with the temperature rose from 293 K to 3106 K.	124
Figure 8-2. RMD simulation snapshots of the reactions between two faces of 6H-SiC and H ₂ O molecules at the constant temperature of 2100 K.	124
Figure 8-3. RMD simulation snapshots of: (a) the reactions between the H ₂ O molecules and Si face of 6H-SiC and at 2100 K, with the diamond slab loading at an upward speed of 10 m/s; (b) the reactions between the H ₂ O molecules and C face of 6H-SiC and at 2100 K, with the diamond slab loading at a downward speed of 10 m/s.	126
Figure 8-4. (a) Silicon dioxide generated on the Si face. (b) Silicon dioxide generated on the C face. (c) Radial distribution functions of Si-O on Si face, C face and in SiO ₂ lattice.	128

Figure 8-5. Detection results of debris of 6H-SiC wafers [30]. (a) TEM image and SAED pattern of Si face. (b) High resolution diagram of Si face. (c) TEM image and SAED pattern of C face. (d) High resolution diagram of C face.	128
Figure 8-6. Schematic diagram of interface reaction between two faces of 6H-SiC and H ₂ O molecules.	130
Figure 9-1. Tangential (left) and normal (right) forces of Si face and C face with the oxide layer.....	133
Figure 9-2. Comparison of tangential forces on Si face (left) and C face (right) with and without the oxide layer.....	134
Figure 9-3. Comparison of material removal characteristics on Si face (left) and C face (right) with the oxide layers.	135
Figure 9-4. DXA results of Si face in different scratching depths.....	136
Figure 9-5. Intermediate structure in subsurface.	138
Figure 9-6. Tangential (left) and normal (right) forces of Si face with the oxide layer.	139
Figure 9-7. Tangential (left) and normal (right) forces of C face with the oxide layer.	139
Figure 9-8. DXA results of Si face (left) and C face (right) with the oxide layer in variable-depth scratching simulations.....	140
Figure 9-9. Normal forces of Si face with the oxide layer during constant-load scratching.	141
Figure 9-10. Normal forces of C face with the oxide layer during constant-load scratching.	141
Figure 9-11. Material removal of Si face with oxide layer under different normal loads. (a) 1600 nN, (b) 1680 nN, (c) 1760 nN, (d) 1840 nN, (e) 1920 nN, (f) 2000 nN.....	143
Figure 9-12. Material removal of C face with oxide layer under different normal loads. (a) 1360 nN, (b) 1440 nN, (c) 1520 nN, (d) 1600 nN, (e) 1680 nN, (f) 1760 nN.....	144

List of Tables

Table 2-1. SiC material properties [1].	5
Table 3-1. The usage of potentials.....	31
Table 3-2. Parameters in Tersoff potential for Si and C [107].	38
Table 4-1. SiC substrate specification.	53
Table 4-2. Machine specification of XR 610 CNC machine.	56
Table 4-3. Scratching tests parameters.	58
Table 5-1. Groups of parameter files.	70

Chapter 1. Introduction

1.1 Background

Silicon carbide (SiC), a third-generation semiconductor material, has wide applications in microelectronics, optoelectronics and medicine sectors because of its specific properties. Ultra-precision polishing, as the final step in the processing of SiC substrates, is a necessary means to obtain ultra-smooth, ultra-flat, damage-free substrate surfaces, which has a decisive influence on the subsequent epitaxy. Mechanical polishing (MP) and chemical mechanical polishing (CMP) are two main processes to achieve the ultra-precision polishing of substrates in commercial mass production. It is critical to completely eliminate the damaged layer and further reduce the surface roughness of the substrates to meet the requirements of epitaxy processes.

Ultra-precision polishing of the substrate is achieved during the alternative process of chemical and mechanical removal of the wafers. The mechanism of chemical reaction and mechanical action during this process has not yet been fully revealed. Although the current machining technology can obtain the surface with nanometre-level accuracy, it is necessary to further explain the microscopic material removal mechanism to achieve more efficient machining. It is difficult to observe and measure many instant details through experimental means, since the processing scale reaches the nanometre scale. Therefore, simulations can be adopted to investigate, analyse and predict the phenomena in the process, and then to guide the actual machining. Among them, the molecular dynamics (MD) simulation, an effective method to simulate the motion and interaction of molecules and atoms, is widely used in the ultra-precision machining.

1.2 Project's aim and objectives

Both mechanical removal and chemical removal play significant roles in the ultra-precision polishing. This research aims to investigate the nanomechanical properties, chemical reactions and removal mechanism of 4H-SiC and 6H-SiC during nanomachining using molecular dynamics simulations and experimental validation. The objectives of the project are to identify:

- Anisotropy of 4H-SiC and 6H-SiC in terms of forces, subsurface damage and material deformation during indenting and scratching.
- The influences of removal scale, abrasive shape, scratching speed and scratching direction on material removal mechanism.
- Interface chemical reactions between SiC and water in different levels of temperature and load.
- The effect of the oxide layer on material removal characteristics during scratching, especially under different constant loads.

1.3 Structure of the thesis

The thesis is sub-divided into 8 chapters.

Chapter 1 explains the background, aim and the objectives of the research work.

Chapter 2 introduces the fundamentals of the silicon carbide and various nanometric machining methods. It provides a review of the research on ultra-precision polishing technology and highlights some testing methods. It further reviews the MD method used in various atomic machining methods.

Chapter 3 introduces the fundamentals of the MD method with consideration to the various thermodynamic ensembles, the commonly used interatomic potentials, algorithms for the integration of the equations of motion. It also explains the configurations used for the MD simulation of nanometric machining; the MD software and the hardware platform used for the simulations in this project.

Chapter 4 introduces the methodology for the verification experiments performed in this project. It mainly provides the information of test device, specimens, experimental setup and procedures.

Chapter 5 provides the MD simulations and experimental results of nanoindentation. These results include the indentation forces, subsurface morphology and material deformation. Then the effect of different potential functions is compared and discussed. And the experimental verification in terms of surface morphology improves the reliability of the MD simulations.

Chapter 6 provides the MD simulations and experimental results of nanoscratching. These results include the scratching forces, material remove efficiency and subsurface deformation. The difference between Si face and C face of 4H-SiC and 6H-SiC are investigated. And the experimental verification in terms of scratching forces and material remove efficiency enhances the reliability the MD simulations.

Chapter 7 provides the MD simulations and experimental results in different scratching conditions. The effects of removal scale, tool morphology, scratching speed and scratching direction on material removal mechanism are investigated.

Chapter 8 provides the reactive molecular dynamics (RMD) simulation results of interfacial reactions between SiC atoms and water molecules in different levels of temperature and load. The difference in terms of reaction efficiency and reaction products between Si face and C face are investigated. And the reaction mechanism during polishing is discussed.

Chapter 9 provides the MD simulation results of nanoscratching on the SiC surface with the oxide layer. The effect of the oxide layer on material removal characteristics during scratching, especially under constant loads, is investigated.

Chapter 10 is a summary of the contribution of this research work and proposes directions for future work.

Chapter 2. Literature review

2.1 Fundamentals of the silicon carbide

Silicon carbide, a third-generation semiconductor material, has extensive applications in microelectronics, optoelectronics, aerospace, and medical sectors because of its specific properties, such as chemical inertness, high thermal conductivity and high-temperature stability [1]. The SiC substrate is considered as a typical hard-to-machine material because of its high hardness, high brittleness and stable chemical properties [2-4].

There are more than 250 polytypes of SiC which have been accepted, due to its one-dimensional polymorphism [5]. The hexagonal SiC (4H-SiC and 6H-SiC) and the cubic SiC (3C-SiC) are two major polymorphs, with hexagonal and zinc-blende lattice structures, respectively [6]. For these polytypes of SiC, the crystal structures differ in the stacking sequence of the close-packed layers. The stacking sequences of 4H-SiC and 6H-SiC are given by ABCB' and ABCA'C'B', respectively [1, 6]. Here, A, B, and C indicate the three possible lateral positions of the Si-C bilayers. A and A' (B and B', C and C') bilayers have equivalent spatial positions, but their bonds are rotated 180 degrees with respect to each other. The molecule crystal structures of 4H-SiC and 6H-SiC are illustrated in Figure 2-1, and the material properties are presented in Table 2-1.

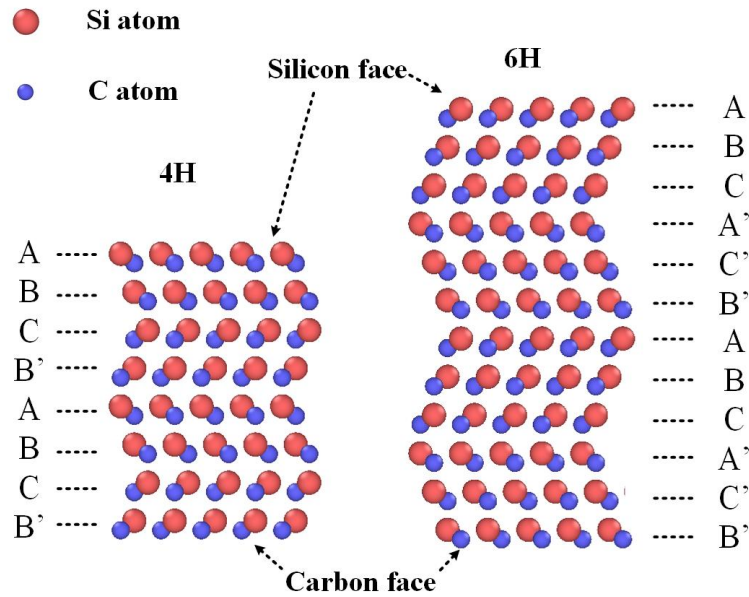


Figure 2-1. Structures of 4H- and 6H- Silicon Carbide.

Table 2-1. SiC material properties [1].

Property	4H-SiC	6H-SiC
Lattice Parameters	$a=3.076 \text{ \AA}$, $c=10.053 \text{ \AA}$	$a=3.073 \text{ \AA}$, $c=15.117 \text{ \AA}$
Stacking Sequence	ABCB'	ABCA'C'B'
Mohs Hardness	≈ 9.2	≈ 9.2
Density	3.21 g/cm^3	3.21 g/cm^3
Dielectric Constant	$\epsilon \sim 9.66$	$\epsilon \sim 9.66$
Thermal Conductivity	$a \sim 4.9 \text{ W/cm} \cdot \text{K@298K}$ $c \sim 3.9 \text{ W/cm} \cdot \text{K@298K}$	$a \sim 4.6 \text{ W/cm} \cdot \text{K@298K}$ $c \sim 3.2 \text{ W/cm} \cdot \text{K@298K}$
Band-gap	3.23 eV	3.02 eV

4H-SiC has wide applications for optoelectronic devices, high-temperature electronic devices, ultra-precision micro/nano dies, and high-performance mirrors; and 6H-SiC is primarily used in optoelectronic devices, such as laser diodes and blue light emitting diodes [7-9]. However, these ultra-precision micro/nano components require extremely high geometric accuracy, which adds difficulty to the machining process. Further the nanoscale

defects are harmful for SiC-based devices, which can originate from the growth of material or can be introduced during the machining process [10]. Thus, the study of the nanoscale characteristics of SiC has attracted much attention in recent years, both experimental and numerical.

2.2 Literature of ultra-precision polishing technology

Ultra-precision polishing, as the final step in the processing of SiC substrates, is a necessary means to obtain ultra-smooth, ultra-flat, damage-free substrate surfaces, which has a decisive influence on the subsequent epitaxy.

At present, the ultra-precision polishing of substrates in commercial mass production mainly includes two processes of mechanical polishing and chemical mechanical polishing. The purpose of polishing is to completely eliminate the damaged layer and further reduce the surface roughness of the substrates to meet the requirements of epitaxy processes. Traditional MP generally uses high-hardness materials, such as diamond or boron carbide, as abrasives to remove the surface materials of the substrate by scratching and ploughing [11]. The basic principle of CMP is to use the chemical substance in the polishing slurry to corrode the crystal surface and form a gel-like film layer, and then the soft film layer can be removed by micro-mechanical friction of the ultra-fine abrasives. In this way, ultra-precision polishing of the substrate is achieved during the alternative process of chemical deformation and mechanical removal of the wafers [12-14]. Figure 2-2 shows the schematic diagram of the chemical mechanical polishing on SiC substrates.

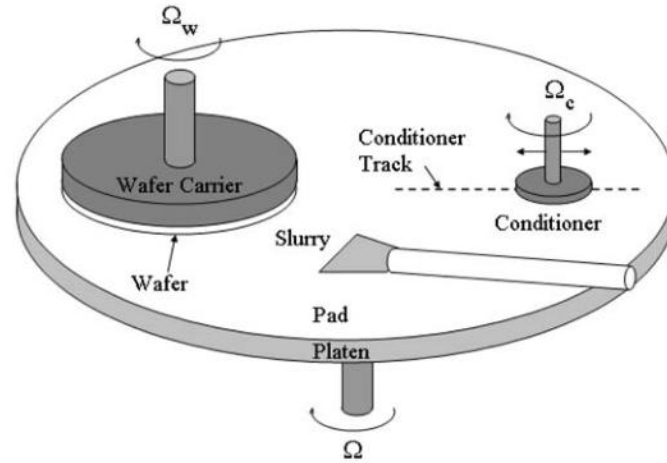


Figure 2-2. Schematic diagram of the chemical mechanical polishing [14].

In recent years, scholars have carried out a large number of theoretical explorations and experimental research to try to solve problems of low efficiency and difficulties in SiC ultra-precision polishing. Most of these researches focus on two aspects: the hardness of abrasives and the corrosiveness of polishing slurry. These two aspects focus on enhancing the mechanical removal and chemical reaction respectively. Lee [15] believed that the removal rate of SiC substrates, mainly depended on mechanical removal rather than chemical reaction, and it could be improved by adding the nano-diamond particles. However, the introduction of the nano-diamond particles not only increased the cost of CMP polishing slurry, but also had a great impact on the surface quality by self-agglomeration and re-agglomeration during processing, which might lead to new mechanical damage and lower the surface quality [16, 17]. Some scholars used nano-platinum particles, nano-iron particles, hydrogen peroxide or potassium nitrate as catalysts in acid or alkaline polishing slurry in order to promote the chemical reaction of SiC and then improve the removal rate [18-20].

In addition, researchers have also developed some new CMP-based methods for energy-assisted processing, such as electrochemistry, hydrogen etching, particle beam, laser, and ultrasound [21-26]. Among them, the plasma-assisted polishing method is based on the polishing principle of CMP, which uses the chemical corrosion effect of water vapour and the mechanical removal effect of soft abrasives to achieve ultra-smooth surfaces (rms about 0.2 nm) [21-23]. Electrochemical mechanical polishing is based on CMP combined with electrochemical means to control and enhance chemical reactions to achieve the purpose of improving the removal rate [24, 25]. Similarly, the photocatalytic-assisted CMP method can

promote the oxidation reaction by adding photocatalytic particles, thereby increasing the material removal rate by 30% [26].

Although these methods improve the polishing efficiency and precision to a certain extent, they also bring many problems, such as the consumption of expensive abrasives in the polishing liquid, the environmental pollution due to the corrosive liquid, and the unsuitability of industrial mass production.

Furthermore, the anisotropy, the chemical reactions and the removal scale of the material all had important influences on the processing properties at the nano scale. Some scholars had tried to study the effects of these aspects on the polishing process of SiC substrates. Chen et al. [8] found the Si face of 6H-SiC presented a higher material removal rate (MRR) than the C face during both mechanical polishing and chemical mechanical polishing in an alkaline solution. The Si face may have removed more easily because it was oxidized by the dissolved oxygen. However, other researches show opposite effects. Lu et al. [27] reported that the Si face is more difficult to remove than the C face during MP on both 4H- and 6H-SiC and considered that the variation in the MRRs was determined by the mechanical properties of different faces. Pan et al. [28] also reported that the C face of 6H-SiC showed higher MRR than the Si face in both acidic and alkaline solutions. Therefore, differences between the MRRs of the Si face and C face are controversial. A fundamental understanding of the removal mechanism of 4H-SiC and 6H-SiC is critical to provide a guide for improving polishing efficiency and quality.

Luo et al. [27, 29] put forward a semi-fixed abrasive polishing tool, based on the principle of sol-gel (SG), which would satisfy the processing demands of scratch-free and nanoscale roughness in substrate surfaces. This polishing pad is the flexible matrix made of sodium alginate, which enables the effects of abrasives yielding and then controls the material removal evenly. Figure 2-3 shows material removal mechanisms of SiC using the SG polishing tool (left) and fixed abrasive polishing tool (right). The polishing coolant used in this method is pure water, which is environment-friendly. By this means, Luo et al. [30] compared the effects of several abrasives (diamond, alumina, silicon carbide, and zirconia) on the processing properties of SiC substrate, and analysed the interface mechanism between abrasives and substrate surface. After chemical analysis of the chips and the processed surface, they found that the interfacial friction between the abrasives and the substrate surface

induced chemical reactions. The chemical products on the Si and C faces of SiC substrates were crystalline and amorphous silicon oxide, respectively [30].

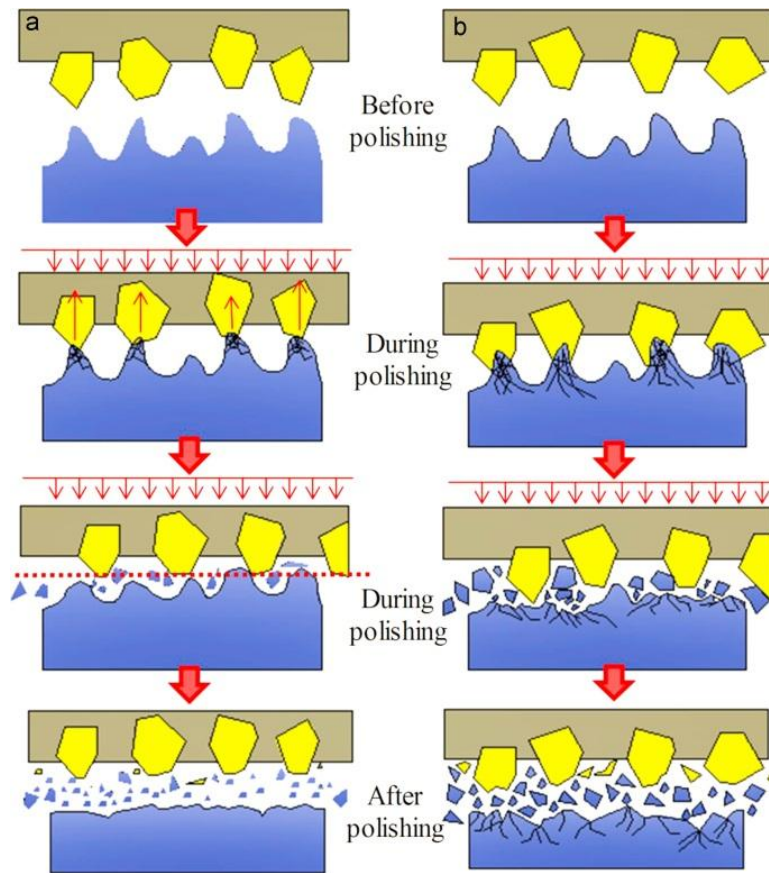


Figure 2-3. Material removal mechanisms of SiC using the SG polishing tool (left) and fixed abrasive polishing tool (right) [29].

2.3 Literature of indentation and scratching tests

In order to eliminate defects from SiC surfaces and improve polishing efficiency, a better understanding of material removal mechanisms at the nanoscale is critical. Considering the SiC crystal structure, it is inevitable and necessary to identify and evaluate different machining mechanisms and effectiveness for the crystal faces of SiC. Therefore, investigations of the nanoscale mechanical properties and machining mechanisms of SiC substrates have attracted significant attention in recent years [31-38]. Indentation and scratching experiments on SiC substrates are two common methods of studying the nanomechanical properties of materials. A review of the indentation and scratching tests on SiC substrates is presented in this section.

Demenet et al. [9] studied the nanoindentation of 3C-SiC at room temperature and analysed the microstructures by the transmission electron microscopy. It was found that 3C-SiC exhibited the same deformation mechanism as other semiconductor materials such as silicon under high stress, and this might be the general feature of all this family of materials. Schuh et al. [31] studied the indentation of 4H-SiC, and proposed the analysis of the incipient plasticity within a nucleation-based statistical framework, which was able to predict what were most likely mechanistic events during indentations. Goel et al. [32] explore the nanomechanical response of 4H-SiC through the quasistatic nanoindentation, and obtained the load-displacement curve from the indentation experiments. In Goel's study, the residual depths after the indentation were different when using different depths, which was deemed to arise from the compressive residual stresses and incipient plasticity. Li et al. [33] also assessed the evolution of the deformation behaviour of 6H-SiC and found its critical transition condition among elastic, plastic and fracture in the loads range of 3.99-7.13 mN. Indentation load-displacement curves also show that yielding or incipient plasticity in 4H-SiC and 6H-SiC happens at shear stresses of 21 GPa and 23.4 GPa with a pop-in event [33, 34]. Li et al. [35] also studied the indentation using a Berkovich indenter and the SEM results of the indentation surface morphology were shown in Figure 2-4. When the maximum load is 8 mN, there is only plastic deformation and no cracks on the surface of the workpiece after the unloading process, and when the maximum load is 10 mN, there is initiation of the crack occurring on the surface of the workpiece after the unloading process.

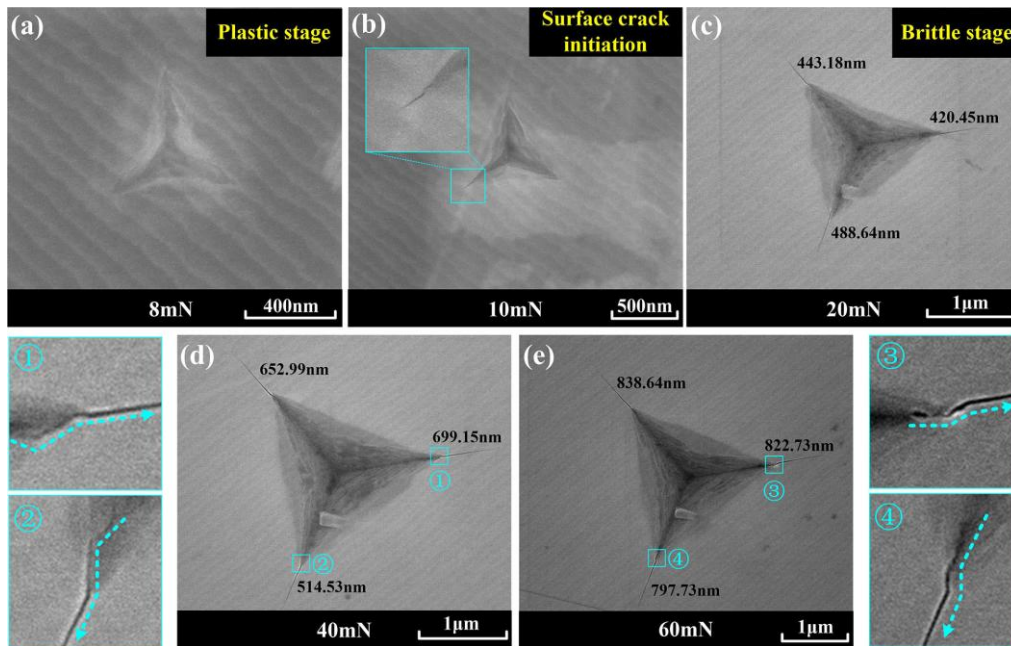


Figure 2-4. Surface morphology of 6H-SiC under different loading (a) 8 mN, (b) 10 mN, (c) 20 mN, (d) 40 mN, (e) 60 mN [35].

The mechanics involved in the scratching process include three main stages: rubbing, ploughing and chip formation. Rubbing has no effect on the grinding process because the abrasive grit only deforms elastically the material surface. Ploughing occurs when plastic deformation is induced on the material, and chip formation is when the fracture occurs. Grim et al. [34] experimentally confirmed that basal dislocation can also be activated in the subsurface of 6H-SiC during mechanical polishing. Meng et al. [36] undertook a series of nano-scratching tests on 6H-SiC substrates to investigate subsurface structures before and after scratching. Figure 2-5 shows the topography of scratched grooves under different normal loads. By observing the results from transmission electron microscopy (TEM), they found some micro-cracks on the subsurface with lengths (up to 1 μm) many times longer than the processed depth (90 nm). The subsurface damage may relate to lattice mismatch and bond rupture.

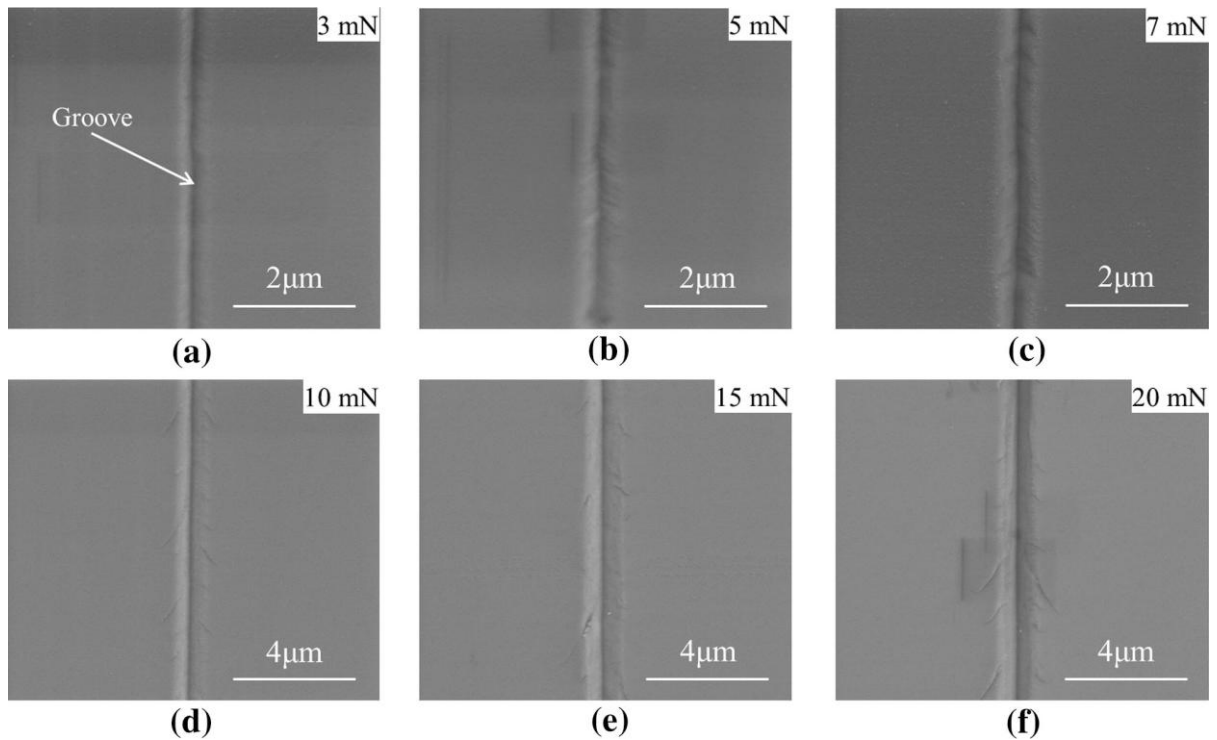


Figure 2-5. Topography of scratched grooves under different normal loads [36].

Wang et al. [37] carried out both single-grit scratch and double-grits scratch tests on the (0001) surface of 4H-SiC substrate by the abrasives on wire saw instead of using a standard indenter to obtain an in-depth understanding of the material removal mechanism and crack propagation during wire sawing. As shown in Figure 2-6, the radial cracks played an important role in the process of material removal by means of the interaction between radial cracks and the interaction between radial cracks and lateral cracks in double scratch tests. Duan et al. [38] also performed the scratching processes on SiC wafers, using two diamond grits at distances of 0.05, 0.1 and 0.15 mm in the Y-direction (Figure 2-7). In the scratching, as the distance of the two diamond grits in the Y-direction increases, the interference at the different distances of the Y-direction are primarily expressed as the interference of plastic damage, the interference of plastic damage and lateral cracks and the interference of lateral cracks.

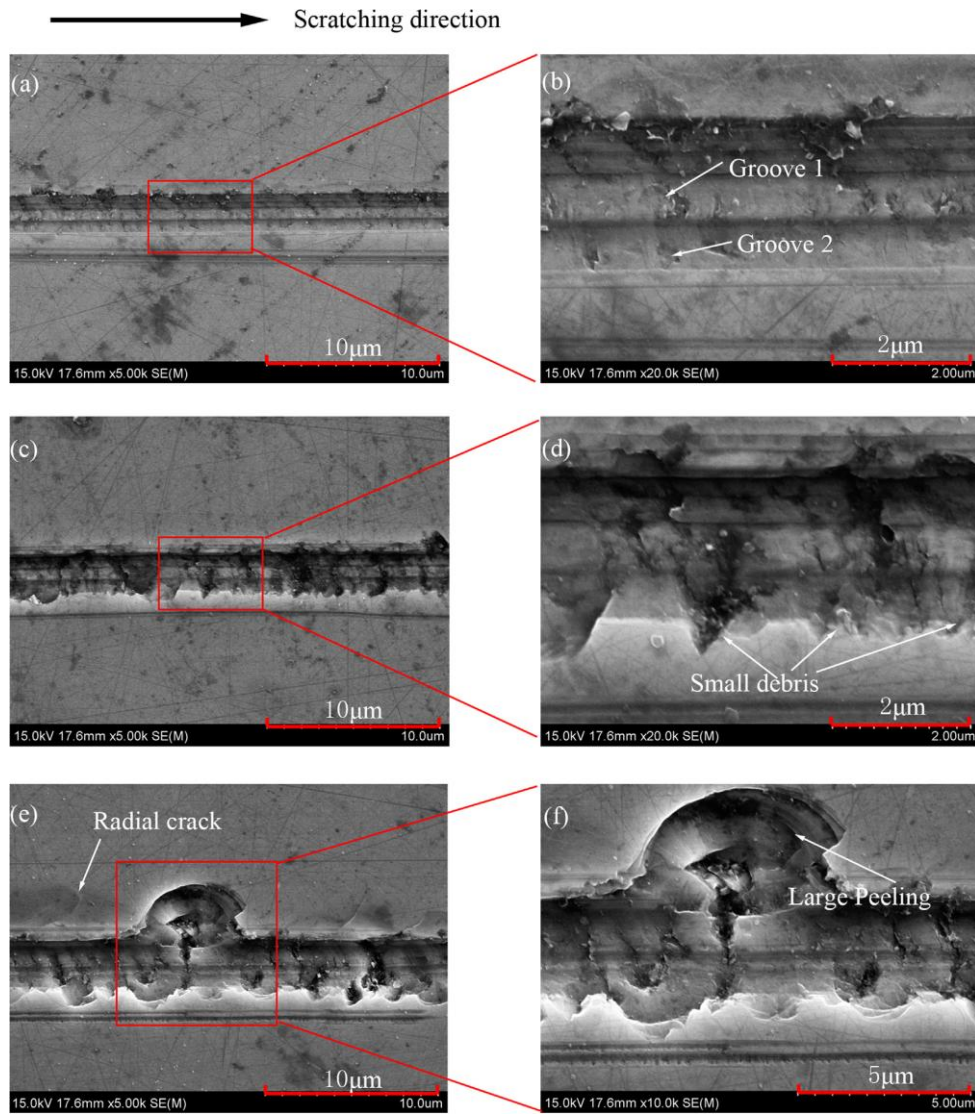


Figure 2-6. Topography of scratched grooves under different normal loads [37].

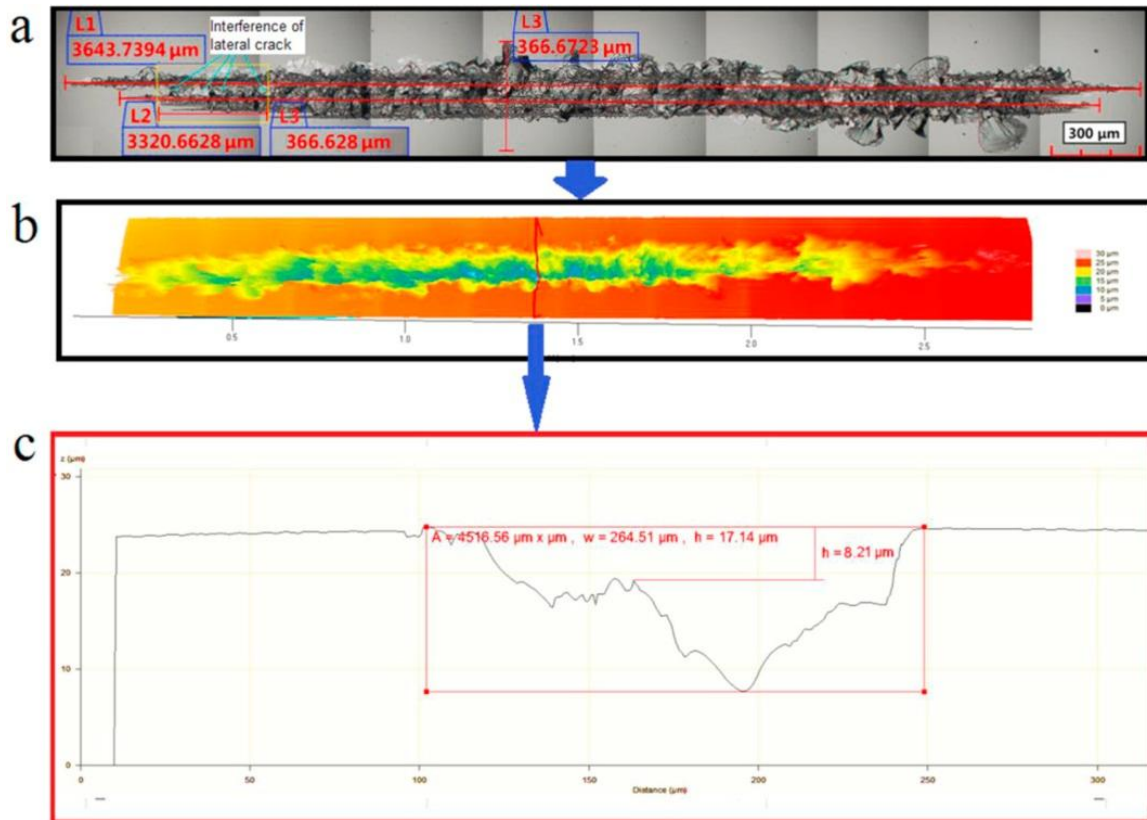


Figure 2-7. Three-dimensional topography of the groove for a Δd_y of 0.1 mm: (a) topography of the groove using a 3D-video microscope, (b) topography of the groove using a laser scanning confocal microscope, and (c) section profile having the maximum depth and width in the interference region.[38]

Dislocations can also lead to cracks. Zhang et al. [39, 40] observed diamond scratching on alumina samples and their results showed that for brittle materials, a pulverised material layer beneath the scratched grooves may appear as plastic deformation, forming ploughing ridges. After further investigating the materials in this pulverised region, Zhang concluded that the pulverised structures were actually micro crack clusters, which are easily removed by chemical etching. Visible cracks may appear beyond the pulverised region, as illustrated in Figure 2-8. When scratch depth is less 1 μm , pulverisation appears even when almost no material is removed [40].

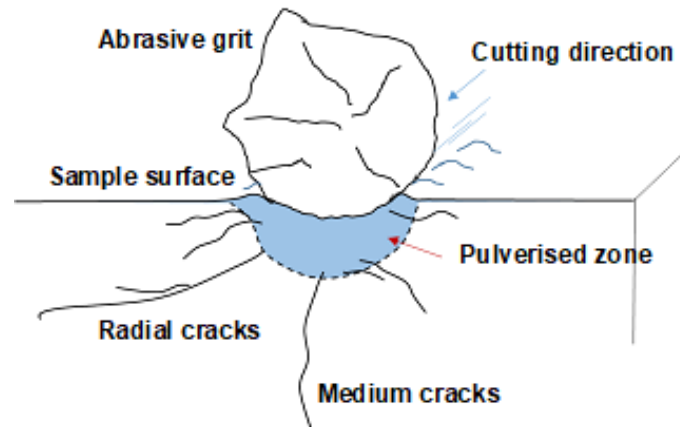


Figure 2-8. Subsurface damage of brittle materials in micron-scale cutting.

2.4 Literature of molecular dynamics simulation

In the ultra-precision polishing, it is difficult to observe and measure many instant details through experimental means, since the processing scale reaches the nanometre scale. Therefore, simulations can be adopted to analyse and predict the phenomena in the process, and then guide the actual machining. Many simulation methods, such as the finite element method (FEM), the smoothed particle hydrodynamics (SPH) and the molecular dynamics simulation, have been adopted to study the material removal process during machining in recent years [38, 41, 42].

For example, Duan et al. [42] combined two different simulation methods, FEM and SPH, to study influences of diamond shapes on the material removal process for the scratching of SiC. As shown in Figure 2-9, the results of the double-scratching simulation showed that the interference damages in the scratching process occurred in three circumstances: the interference of lateral cracks, the interference of lateral cracks and plastic damage, and the interference of plastic damage [38]. But the workpiece particles scattered apart during the scratching, which was different from the actual situation. The FEM is mainly used to investigate the material deformation process with continuous media assumption. FEM and SPH simulations are commonly used for the process performance down to sub-micron level with many linearized assumptions that may not fully represent the material molecule performance.

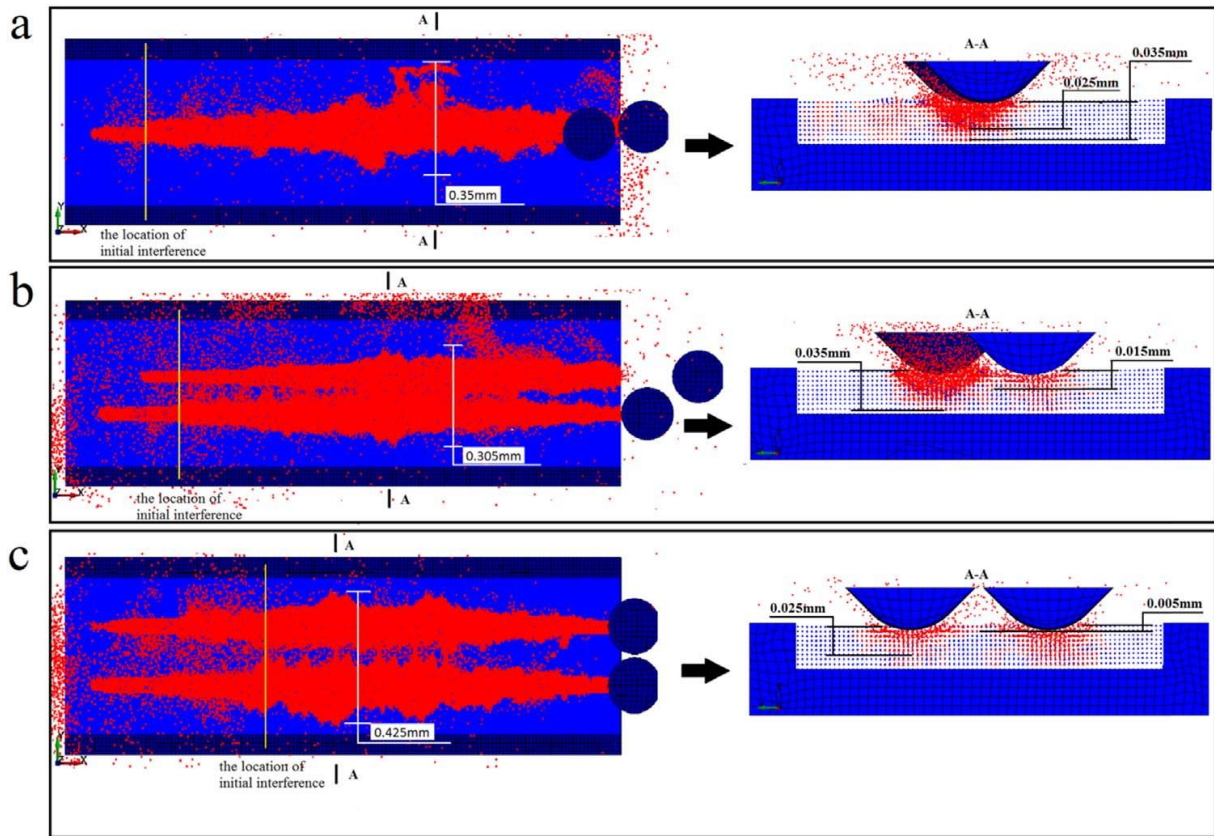


Figure 2-9. The Coupling of FEM and SPH method used in the SiC scratching. (Material damage distribution of the workpiece after double scratching at different distances in the Y-direction: (a) $\Delta dy=0.05$ mm, (b) $\Delta dy=0.1$ mm, and (c) $\Delta dy=0.2$ mm) [38].

The MD simulation, an effective method to simulate the motion and interaction of molecules and atoms, is a bridge that connects microscopic length scales and time scales with macroscopic properties. It can help us explore new phenomena and new results that cannot be discovered by other means at the nanoscale. MD simulation is an important tool for studying nano-machining. It can visualize the transient nano-machining process, allowing us to analyse and study various phenomena in the ongoing nano-machining process in detail.

The main advantage of MD is that it models material behaviours directly to molecular level or nanometre level, which is the material removal level of ultra-precision polishing processes. MD simulates and realizes the machining process by simulating the motion of the atoms, and then obtains the relevant physical quantities through the statistical mechanics analysis, so as to observe and analyse them. The base of MD simulation analysis is that each of these atoms follows the Newton's law, and the behaviours of these atoms are mainly derived from the

statistical potential functions. The fundamentals of the MD simulation method are presented in Section 3.1.

At present, the related research studies on the MD simulation of ultra-precision machining mainly focus on nano-cutting mechanism, tool wear, material defect evolution, material removal, interface reaction and so on [43-48].

2.4.1 Nanoindentation process

Nanoindentation simulation is a common method to study the nanomechanical properties of materials. Through nanoindentation simulation, load-displacement curve, subsurface deformation, dislocation and slip can be observed clearly. Thus, there are many MD studies focusing on nanoindentation, in which most of the MD research studies regarding nanoindentation focused on metallic material [49-52] and Si [53-56], while research on SiC remains relatively scarce.

Sun et al. [57] used the MD simulation to study the nanoindentation on 3C-SiC (111) thin films. They discussed the formation mechanism of prism ring during nanoindentation and suggested two kinds of mechanisms, the "lasso"-like mechanism and the extended "lasso"-like mechanism. Zhu et al. [58] studied the nanoindentation process of 4H-SiC by MD, with a cube corner diamond indenter adopted, and phase transformation from 4H-SiC to 3C-SiC is firstly observed. Wu et al. [59] simulated the nanoindentation on 6H-SiC using MD. The results showed that the amorphization process corresponds to the first "pop-in" event of the indentation load-displacement curve, while the dislocation nucleation and propagation are related to the consequent "pop-in" events. As shown in Figure 2-10, the amorphization is confirmed to achieve via an initial transformation from wurtzite structure to an intermediate structure, and then a further amorphization process.

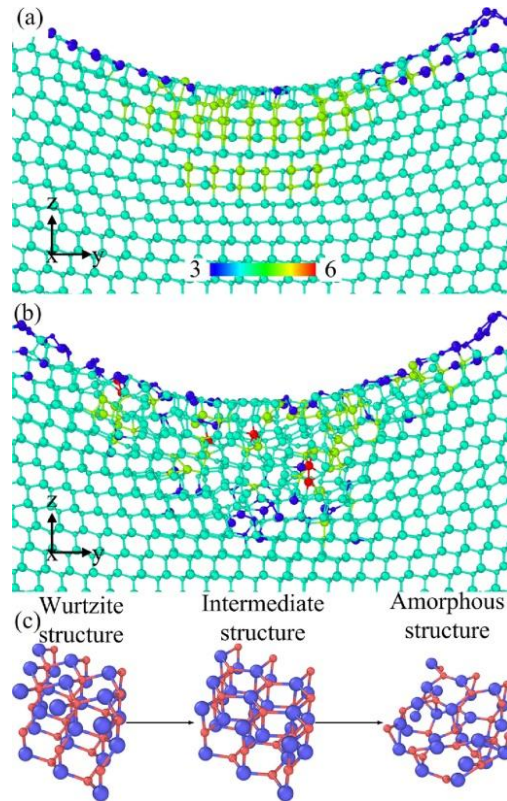


Figure 2-10. Coordination number distribution in cross section at (a) $h = 0.84$ nm, and (b) $h = 0.96$ nm; (c) Amorphization path from wurtzite structure to amorphous structure. [59]

2.4.2 Nanoscratching process

Nano scratching simulation is another common process to investigate nanomechanical properties, material deformation and material removal mechanism. And the single grit scratching can be regarded as a simplified polishing model. A review of the scratching tests on SiC substrates using MD simulation is presented in this section.

Among different polytypes of SiC, the scratching on 3C-SiC is well studied using MD simulation. For example, Goel et al. [60] studied the atomistic aspects of the ductile response of 3C-SiC in the nano-cutting process by the MD simulation. They believed that 3C-SiC underwent the sp^3 - sp^2 order-disorder transition, which led to the formation of the SiC-graphene-like substance, and the growth rate was related to the cutting conditions. In addition, Meng et al. [61] studied the coupling effect on the removal mechanism of 3C-SiC by the MD simulation, with the wear of abrasive considered. The results showed that multiple repeated processing under the same conditions contributed to higher removal efficiency and controllable surface damage. Liu et al. [62] simulated the scratching processes of 3C-SiC and

compared material removal behaviour between monocrystalline and polycrystalline silicon carbide.

The related research studies on 4H- and 6H-SiC are quite rare. Wu et al. [63] simulated the nano-cutting of 6H-SiC in different depths (Figure 2-11) and confirmed that 6H-SiC undergoes amorphous structural transformation. Meanwhile, dislocations occurred in the subsurface and their propagation leads to a basal plane stacking fault. Nano-indentation results of high-resolution transmission electron microscopy confirm two major material deformation mechanisms, including amorphous deformation generation near the indentation region and dislocation propagation along both the $\{0001\}$ basal and $\{1-100\}$ prismatic planes [59]. For these two methods of the plastic deformation of 6H-SiC, Xiao et al. [64] held that dislocation plasticity played a major role, through using shortest-path ring analysis and visualization of the dislocation core structures. Different polytypes of SiC show different machining properties. As shown in Figure 2-12, Luo et al. [6] compared the nano-cutting of 3C-SiC, 4H-SiC and 6H-SiC. They found 4H-SiC exhibited superior subsurface integrity after machining, while 6H-SiC showed poorer results under a cutting depth of 1.3 nm. In all four cases, no dislocations were found in the subsurface.

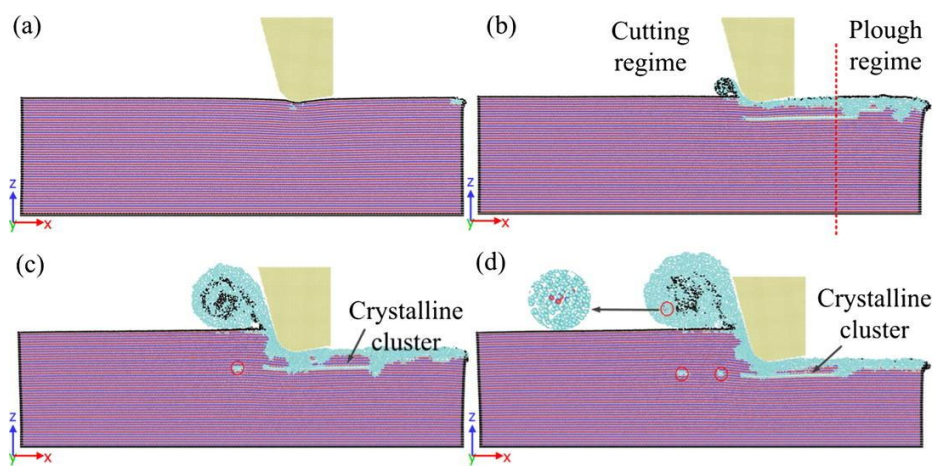


Figure 2-11. Deformation evolution in 6H-SiC due to the variation of the depth of cut d of the diamond cutting tool (total cutting length = 18 nm). (a) $d = 0.3$ nm, (b) $d = 0.5$ nm, (c) $d = 2$ nm, and (d) $d = 3$ nm. [63]

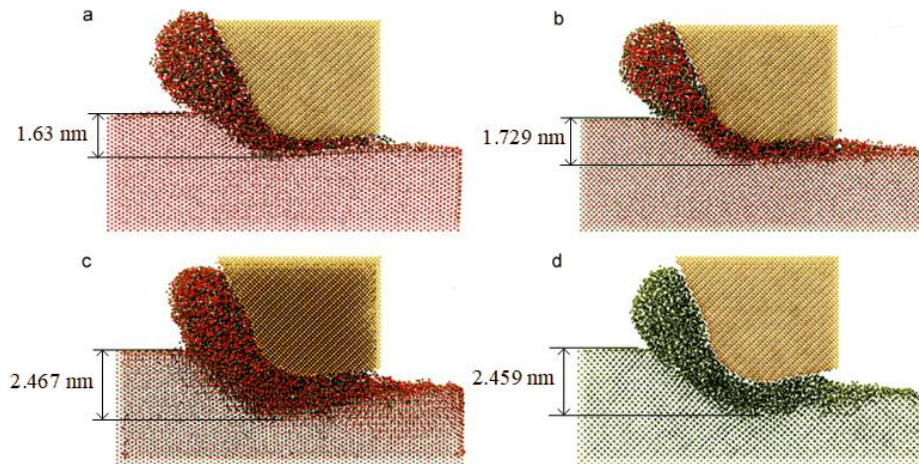


Figure 2-12. Subsurface deformation of Silicon Carbide and Silicon. (a) 4H-SiC, (b) 3C-SiC, (c) 6H-SiC and (d) Si. [6]

Considering the anisotropy of SiC, different crystal planes and orientations significantly influence the deformation mechanism and removal efficiency of the material. As shown in Figure 2-13, Meng et al. [65] compared the material removal rates in different combinations of crystal planes and orientations. It was found that machining on the surface of (01-10) with a cutting direction of [2-1-10] yielded a high removal rate and low abrasive wear. The differences in material removal rates caused by different scratch orientations were more obvious on the (01-10) plane and (11-20) plane, but not obvious on the (0001) plane. In addition to simulating traditional processing methods, MD has also been used to simulate femtosecond laser aided machining on 6H-SiC [66]. It was found that the modified 6H-SiC surface structure improved the removal efficiency and effectively reduced the depth of surface damage.

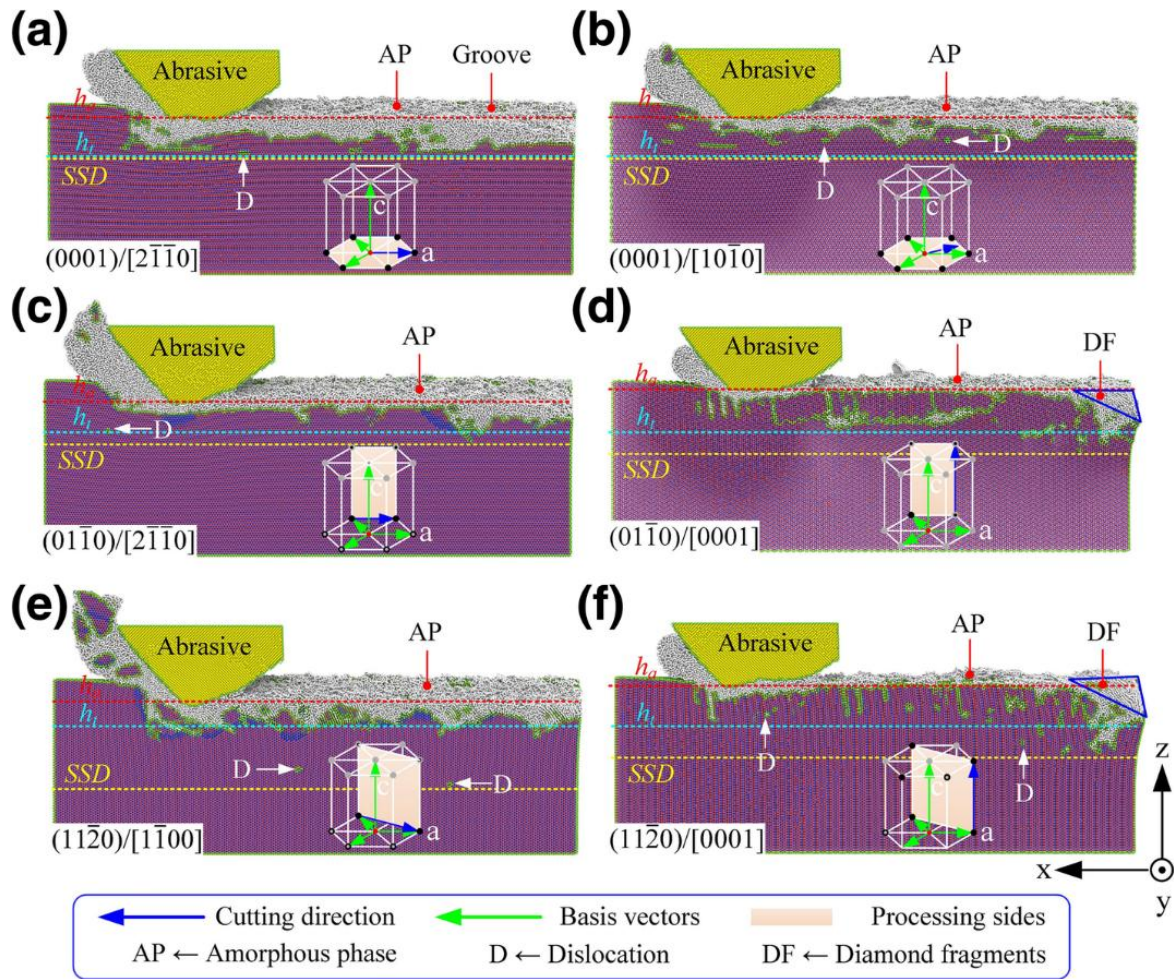


Figure 2-13. Topography of machined surface under different crystal plane/orientation conditions, where a-f are the corresponding process modes $(0001)/[2-1-10]$, $(0001)/[10-10]$, $(01-10)/[2-1-10]$, $(01-10)/[0001]$, $(11-20)/[1-100]$, and $(11-20)/[0001]$, respectively. [65]

At the nano or atomic scale level, the shape of diamond grits will influence the scratching process as well. In general, the spherical, conical and pyramid grits were widely used in these research studies. And there also are many tool models in complex geometry in specific applications. The effect of tool geometry [67-69] and size [70] in nanometric cutting has been an interesting topic in recent years, but the related studies on SiC are few. Fung et al. [71] used MD simulations to investigate the effect of the surface flaws of the diamond tool surfaces on the tool wear in nanometric cutting on 3C-SiC. In this research, a V-shaped notch (as shown in Figure 2-14) was created along the tool flank face to mimic a nano-sized flaw. It was found that the material loss from the flawed region was one order of magnitude larger than that from the flawless region, explaining the effect of the flaws on the microscopic wear resistance of diamond tools [71].

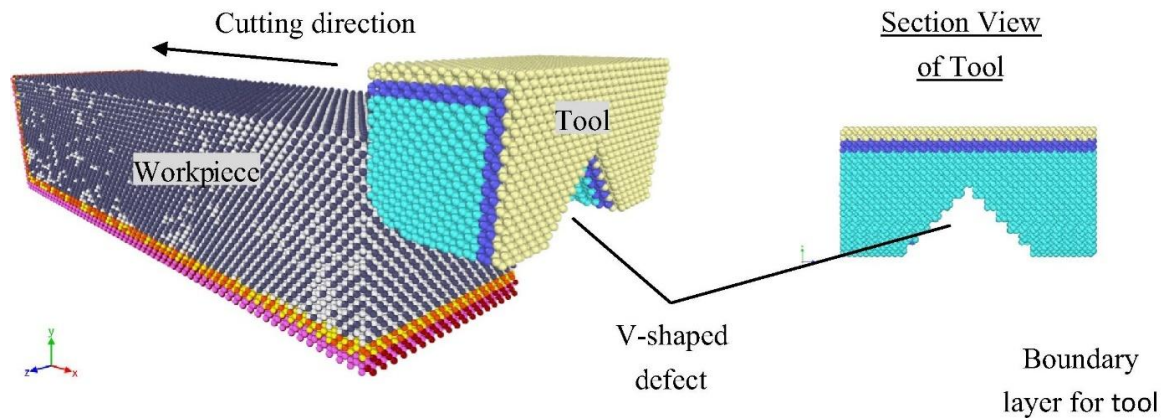


Figure 2-14. Scratching model using a diamond tool with a V-shaped defect. [71]

In addition, there also are some research studies on the effect of the workpiece with different defects, such as voids, polycrystalline and surfaces in grating or corrugated structures [66, 72-74], which provide in-depth understanding of the scratching process in some specific conditions.

2.4.3 Interfacial reaction

Both mechanical removal and chemical removal play significant roles in the ultra-precision polishing. The chemical reaction occurring on the surface of the wafers during polishing is the key factor to influence the removal rate and control the surface quality [75, 76].

Reactive molecular dynamics, based on the ReaxFF, is a program for modelling chemical reactions with atomistic potentials, which can simulate bond-breaking and bond-making [77]. Newsome et al. [78, 79] proposed the force field for the reaction of SiC and H₂O and studied its oxidation, which provided reliable support for the chemical reaction in the polishing on SiC substrates. The initial stages of oxidation of SiC by O₂, H₂O, and their mixture, respectively, were compared in the moderate to very high temperature range using the ReaxFF based reactive molecular dynamics simulations. The initial configurations of H₂O and SiC slab are shown in the left side of Figure 2-15, with the final configurations at 2000 K (centre) and 4000 K (right). Qualitatively, the SiO₂ slab from H₂O at 2000 K appeared similar to the SiO₂ slab at 1000 K from O₂, indicating the higher oxidation strength of O₂. Moreover, Simonka et al. [80] analysed the early stage of the highly anisotropic silicon carbide oxidation behaviour with reactive force field molecular dynamics simulations. The oxidation

of a-, C-, m-, and Si-crystallographic faces is studied at typical industry-focused temperatures in the range from 900 to 1200 °C based on the time evolution of the oxidation mechanism (Figure 2-16). The results indicated that the C-face has the highest oxidation rate, followed by the m-, a-, and Si-face, and the differences between the various faces have been observed to be decreasing with time.

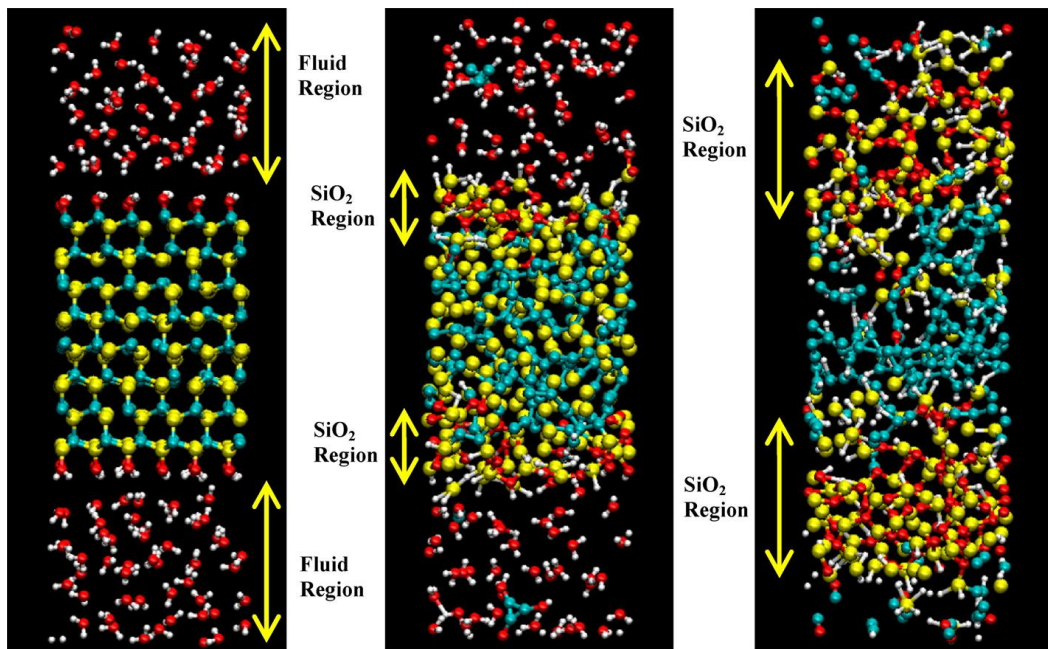


Figure 2-15. Initial (left) and final snapshots of SiC oxidation by H₂O at 2000 K (centre) and 4000 K (right). The yellow arrows show the extent of SiO₂ slab growth. Si = yellow, C = blue, O = red, and H = white. [78]

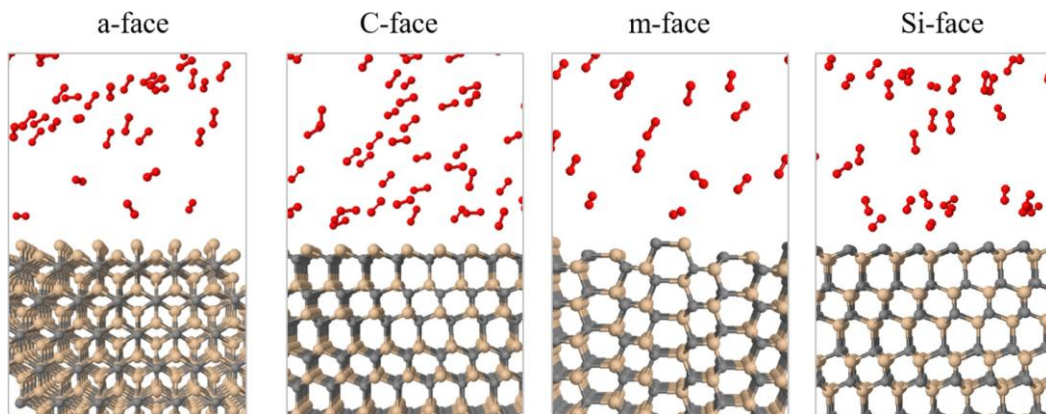


Figure 2-16. Simulation snapshots of initial structures of the SiC/O₂ interfaces for a- (11-20), C- (000-1), m- (1-100), and Si- (0001) oriented SiC at time = 0. [80]

2.4.4 Chemical mechanical polishing process

There are two common ways to simulate the CMP process using MD simulations. First is the classic MD method, in which the water layer is added on the workpiece surface in the normal scratching model. Some researchers have used this method to study the indentation and scratching on copper with a water film [81-83]. For example, Figure 2-17 shows the MD simulation model for nanoindentation on the Cu (001) surface with a water film. The results show that the presence and thickening of water film as a medium of force transmission from indenter to Cu thin film, leads to a wide range of plasticity within Cu, large load dissipation and surface damage [81].

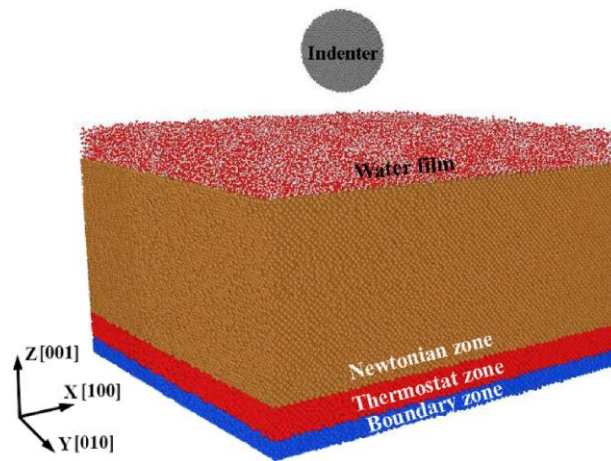


Figure 2-17. Schematic of the MD simulation model for nanoindentation on the Cu (001) surface with a water film [81].

Some scholars had also used RMD simulations, based on ReaxFF, to study the CMP process of brittle materials such as silicon and diamond. Wen et al. [84] adopted ReaxFF reactive force field to study the tribochemical wear mechanism of silicon and SiO₂ in aqueous environment during the CMP process, and the reactions and material removal processes were analysed. Figure 2-18 shows the schematic diagram of the model. They also compared the effects of different aqueous environments, and found that Si was more easily oxidized and removed in aqueous H₂O₂ than water [85]. Yeon et al. [86] also used ReaxFF reactive force field to study the effects of water on tribochemical wear of silicon oxide interface, and found the atomistic mechanisms of tribochemical reactions occurring at the sliding interface of fully hydroxylated amorphous silica and oxidized silicon. Guo et al. [87, 88] used the ReaxFF reactive molecular dynamics to elucidate the atomic removal mechanism of the CMP process

on diamond surfaces, polished with silica abrasives in pure water and H_2O_2 aqueous solution. The model is shown in Figure 2-19. Three removal pathways of C atoms were detected in the CMP process: removal in the form of CO , CO_2 and C chains, which occurred primarily in the first layer of C atoms.

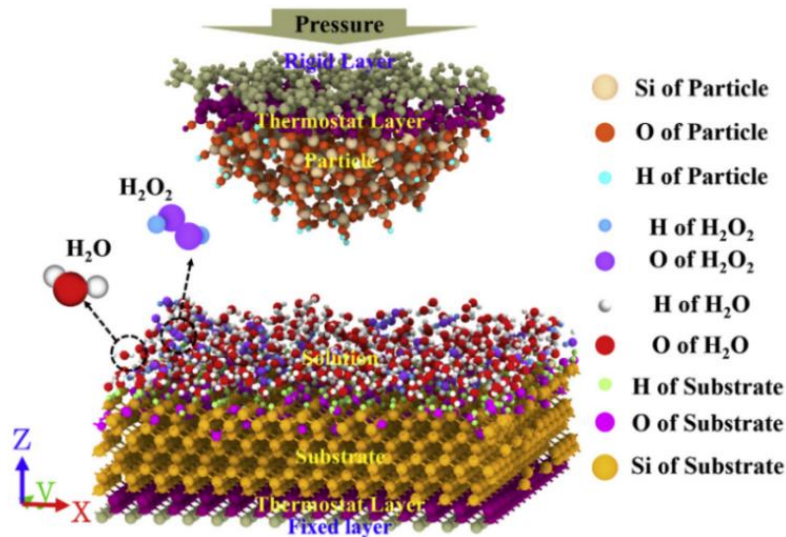


Figure 2-18. The model for ReaxFF reactive MD simulations of Si CMP in the aqueous H_2O_2 . [84]

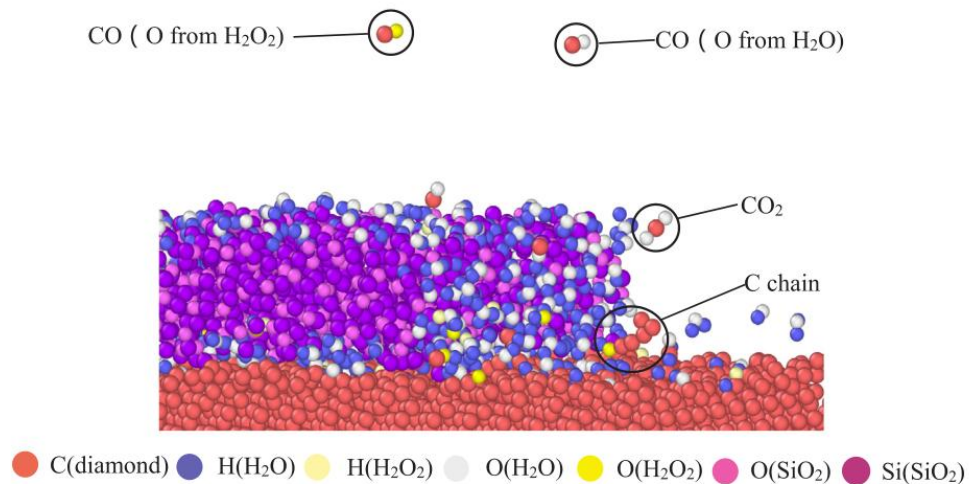


Figure 2-19. The model of silica and diamond in aqueous H_2O_2 . [87]

2.5 Knowledge gaps and summary

Under the high-performance requirements for semiconductor devices, the processing technology of substrate materials also faces critical challenges. Therefore, high-efficiency,

damage-free, and ultra-precision processing of SiC wafers is still a hot and difficult challenge in the mechanical manufacturing field. As reviewed in this chapter, the mechanism and conditions for chemical reactions between abrasives and SiC substrate surfaces has not been fully revealed, because of the discontinuous experimental conditions and results. In particular, although the Si face and C face have the same structures and atomic arrangements, they show obvious differences in polishing efficiency and chemical reaction rates, the reasons for which are not well clarified. A further investigation of the removal mechanism of 4H-SiC and 6H-SiC is a critical requirement to acquire relevant knowledge and provide a guide for improving polishing efficiency and quality. In addition, the knowledge of SiC removal mechanism under brittle and plastic formats at different material removal scales has not been defined clearly and is worth exploring. The influences of machining conditions on material removal and subsurface deformation are worth studying as well. And the effect of the reaction layer formed by the chemical reactions on the material removal is also unclear.

In order to fill the knowledge gaps in SiC nanomachining, MD and RMD simulations, together with validation experiments, will be used in this study to clarify the nanomechanical properties, chemical reaction mechanism and material removal mechanism.

Most of the MD research regarding SiC focuses on 3C-SiC, while research on 4H-SiC and 6H-SiC remains relatively scarce. In particular, the MD simulations, studying the difference between the C face and the Si face, were rare. The indentation or scratching depths, as well as the dimensions of indenters, selected in previous studies were so small, which could not simulate the material removal process in processing accurately. Moreover, some MD simulation studies set the system in two dimensions in order to reduce the amount of model calculation, thereby increasing the sizes of both workpiece and tool in the simulations. Unfortunately, the reliability of the simulations may suffer as a result.

The above-mentioned systems for the RMD simulations of CMP process are very small, containing only a few thousand atoms due to the limitation of calculation, while the actual machining scale is much larger than that. The correspondence between the conclusions obtained by the microscopic systems and the macroscopic experiments is not clear. Besides, mechanical removal and chemical reactions during polishing are usually carried out by classical MD and RMD respectively, but chemical reactions and mechanical interactions

occur synergistically in actual polishing, which may cause deviations between the simulation results and the experiments. Therefore, the results of the RMD simulations should be combined with the classical MD simulations, through adding the chemical reaction products in the small system (RMD) to the larger system (MD), which makes the simulation systems closer to actual polishing. The RMD simulations of the polishing on SiC substrates are still very rare. As mentioned before, the chemical reaction occurred during the polishing on SiC wafer using SG polishing tool [30]. The polishing coolant used in SG polishing method is pure water, which is environmental-friendly. Newsome et al. [78, 79] proposed the force field for the reaction of SiC and H₂O, which provided reliable support for the chemical reaction in the polishing on SiC substrates.

Chapter 3. The methodology for the molecular dynamics simulation of nanomachining

3.1 Fundamentals of the molecular dynamics simulation

Classical molecular dynamics simulation is a kind of molecular simulation method for solving many-body problems at the atomic and molecular levels. The basic idea is to establish an atomic system that conforms to the laws of classical Newtonian mechanics to simulate the microscopic phenomena [89, 90]. The numerical solution of the motion equations is used to obtain the definite trajectory of each atom, and then the corresponding macro-physical properties of the system are obtained. The flow diagram of molecular dynamics simulation is shown in Figure 3-1. Once the positions, velocities and accelerations of the atoms are known, the new positions, velocities and accelerations of the atoms at the next time step can be predicted. Then the state of the system, such as energy, temperature and pressure, can be obtained. The method is based on statistical mechanics, a way to obtain a set of configurations distributed according to some statistical distribution functions [91, 92]. MD simulation can predict the properties of materials at the nanometer scale by accurately describing the interaction between atoms, and reveal the dynamic atomic details of the material deformation process by simulating the basic processes related to the atomic motion path.

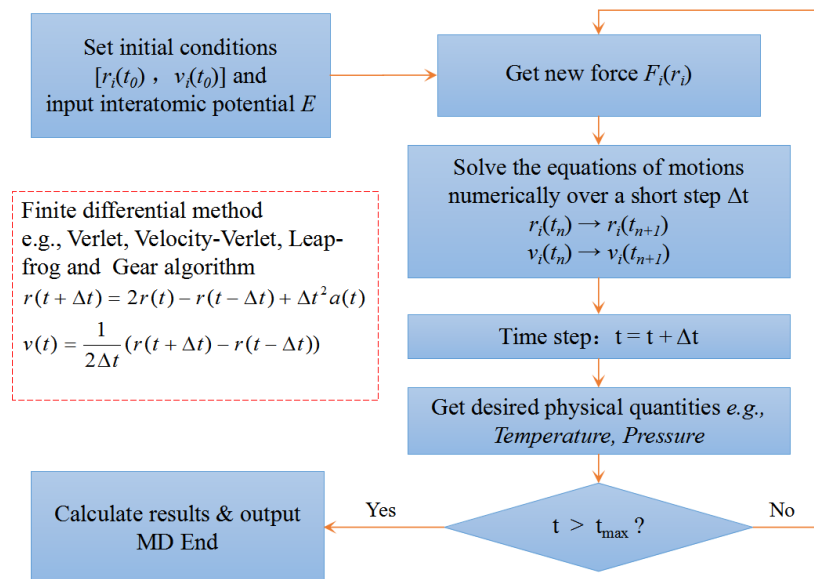


Figure 3-1. The diagram of molecular dynamics simulation.

Different from other simulation methods mentioned in Chapter 2, the particles in MD represent real atoms with nature properties instead of defined virtual particles. So MD is an important tool for studying the nanomachining processes because it models material behaviours directly to molecular level or nanometre level, which is the material removal level of ultra-precision polishing processes. It can visualize the transient nanomachining process, allowing us to analyse and study various phenomena in the ongoing nanomachining process in detail. MD simulation can be regarded as a bridge that connects microscopic length scales and time scales with macroscopic properties [93, 94]. It can help us explore new phenomena that cannot be discovered and analysed by other means at the nanoscale.

The methods of solving the classical Newton's equation of motion (integration algorithm), the empirical potential energy functions and the thermodynamic ensembles of the simulation system are the three most important aspects of MD simulations, which determine the accuracy of the simulation results. The following sections describe the settings of the above three aspects in the MD simulation.

3.1.1 Integration algorithm for solving Newton's equation of motion

The MD simulation is based on Newton's second law of motion. It consists of the numerical step-by-step solution of the classical equations of motion. For a set of N atoms,

$$F_i = m_i a_i \quad (3-1)$$

Where m_i is the mass of atom i , $a_i = \frac{d^2 r_i}{dt^2}$ is the acceleration of the atom i and F_i is the resultant force acting on atom i . These forces should be balanced by the potential energy between atoms, which is usually presented as the gradient of a potential energy function.

At present, the most commonly used method to solve the classical Newtonian equation of motion is the velocity-Verlet algorithm. Assuming that the position, velocity, and acceleration of atom i at time t are $r_i(t)$, $v_i(t)$, and $a_i(t)$, respectively, then the position, velocity, and acceleration of atom i at time $t + \Delta t$ can be determined by the velocity-Verlet algorithm obtained as formula [95].

$$\vec{r}_i(t + \Delta t) = \vec{r}_i(t) + \vec{v}_i(t)\Delta t + \frac{1}{2}\vec{a}_i(t)\Delta t^2 \quad (3-2)$$

$$\vec{v}_i\left(t + \frac{1}{2}\Delta t\right) = \vec{v}_i(t) + \frac{1}{2}\vec{a}_i(t)\Delta t \quad (3-3)$$

$$\vec{v}_i(t + \Delta t) = -\frac{1}{m_i}\vec{r}_i(t + \Delta t) \quad (3-4)$$

$$\vec{v}_i(t + \Delta t) = \vec{v}_i(t) + \frac{1}{2}[\vec{a}_i(t) + \vec{a}_i(t + \Delta t)]\Delta t \quad (3-5)$$

3.1.2 Empirical potential energy function

MD simulation requires the definition of a potential function to describe the particle interaction in the simulation. The potential energy function is usually called the force field in chemistry and biology, and in materials physics it is called the interatomic potential. The potential can be defined at many levels of physical accuracy, which determines the accuracy and reliability of the MD results. The crucial task in an MD simulation is the selection of the potential function, and if the potential doesn't present the behaviour of the atoms correctly, the results produced from the simulation would be useless. The lack of clear understanding about the scope and the limitations of a given model may lead to its innocent misuse and sometimes, to the dissemination of nonsensical results [96].

In the MD simulation of nanomachining, in order to reveal the mechanism of nanomachining more clearly and completely, the simulation system is required to contain as many atoms as possible. For a simulation system containing a large number of atoms, it is difficult to use a quantum force field to describe the relationship between the atomic structure, function and dynamics in the system. This is because although the calculation accuracy of the quantum force field is very high, the calculation efficiency is very low, and it takes an extremely long calculation time. Using empirical potential energy functions to describe atomic interactions can not only save a lot of calculation time, but also take the calculation accuracy into account. Therefore, empirical potential energy functions, such as Lennard-Jones, Morse, Embedded-Atom Method (EAM), Tersoff, Modified Embedded-Atom Method (MEAM), etc., are widely used in molecular dynamics simulation of nanomachining [97-100].

Consider the energy of N interacting particles, which can be written as [101, 102]

$$E = \sum_i V_1(r_i) + \sum_{i<j} V_2(r_i, r_j) + \sum_{i<j<k} V_3(r_i, r_j, r_k) + \dots + \sum_{i<j<k\dots<N} V_N(r_i, r_j, r_k, \dots, r_N) \quad (3-6)$$

Where r_i, r_j, r_k are the positions of the particles and the functions, and $V_1, V_2, V_3, \dots, V_N$ are the many-body potentials. For simplicity, pair potentials models are normally used for atomic interactions, and it follows from equation (3-6), that the second term, $\sum_{i<j} V_2(r_i, r_j)$ is the two-body or pair potential, (which also can be re-written as in equation 3-7), and the third term is the three-body potential and so on [101, 102].

$$V = \sum_i \sum_{j>i} V(r_{ij}) \quad (3-7)$$

Where r_{ij} is the distance between particles i and j . The pair potentials are the simplest interatomic potentials used for the interaction of a set of particles. For MD simulations, a potential energy function should have the following properties [103].

- **Flexibility.** It must be flexible enough to accommodate a wide range of fitting data.
- **Accuracy.** It should be able to accurately reproduce an appropriate database.
- **Transferability.** It must be able to describe structures not included in the fitting database.
- **Computational efficiency.** The evaluation of the potential should be relatively efficient.

In general, the EAM and the MEAM potentials should be used for metals; the Tersoff potentials are usually employed for covalent materials; and for the interface of materials where suitable potentials have not yet been developed, appropriate available LJ and Morse potentials can be used [104]. The Table 3-1 shows the usage of some common potentials.

Table 3-1. The usage of potentials.

Potential	Usage
Lennard-Jones potential	Al-C [47], O-C [47], Si-C [53], Cu-O[83], O-O[83], Cu [83],
Morse potential	Cu [45, 52], Cu-C [45, 51, 52, 68], Si-C [46, 48, 54, 55, 56, 58, 63], C-C [58, 63]
Tersoff potential	Diamond [43, 46, 48, 54, 55, 56, 58, 60, 61, 62, 63, 65, 66, 70, 71, 72], Si [44, 48, 54, 55, 56, 70], SiC [43, 46, 58, 60, 61, 62,

	63, 65, 66, 71, 72]
Embedded-Atom method potential	Al [50], Ni [50], Cu [51, 68, 69]
ReaxFF	Si [75, 76, 84, 85, 86], SiO ₂ [75, 84, 85, 86, 87], SiC [78, 79, 80], Diamond [81, 82, 87, 88], H ₂ O [78, 79, 81, 82, 84, 85, 86, 87, 88], H ₂ O ₂ [84, 87, 88], O ₂ [78, 79, 80], Cu [81, 82]

- **Lennard-Jones potential**

Lennard-Jones started with the general form equation [105-106].

$$V(r) = \frac{f}{r^m} - \frac{g}{r^n} \quad (3-8)$$

(The inverse n th power attractive force dominates at large distances and the inverse m th power repulsive force dominates at short distance.) He later arrived at $n = 6$, $m = 12$; $n = 7$ and $m = 13$, as the special cases of the equation. He didn't derive the equation as it were from first principles, but arrived at it by fitting experimental data. The values $n = 6$, $m = 12$ are widely used nowadays.

$$V_{ij} = 4\varepsilon \left[\left(\frac{\sigma}{r} \right)^{12} - \left(\frac{\sigma}{r} \right)^6 \right] \quad (3-9)$$

Where ε and σ are constants which are dependent on the interacting particles. The LJ potential is ideal for rare gases, where the interactions between the non-bonded and uncharged atoms are due to weak van der Waals forces.

- **Morse potential**

Morse potential has the characteristics of simple form and convenient calculation. Its expression is as formula (3-10).

$$V_{ij} = D\{\exp[-2\alpha(r_{ij} - r_e)] - 2\exp[-\alpha(r_{ij} - r_e)]\} \quad (3-10)$$

Where, r_{ij} and r_e are instantaneous and equilibrium distances between atoms i and j respectively; α and D are constants determined on the basis of the physical properties of the

material. The Morse potential is suitable for cubic metals and they can be used to model the interactions between an atom and a surface.

- **Tersoff potential**

Tersoff modelled the total energy of the system as a sum of pair-like interactions and as a function of the atomic coordinates, given as equation (3-11). The potential is based on the concept that the strength of a bond between two atoms is not a constant, but depends on the local environment [107].

$$E = \sum_i E_i = \frac{1}{2} \sum_{i \neq j} V_{ij} \quad (3-11)$$

$$V_{ij} = f_C(r_{ij})[f_R(r_{ij}) + b_{ij}f_A(r_{ij})] \quad (3-12)$$

$$f_C(r) = \begin{cases} 1 & , r_{ij} < R_{ij} \\ \frac{1}{2} + \frac{1}{2} \cos \left[\pi \frac{r_{ij} - R_{ij}}{S_{ij} - R_{ij}} \right] & , R_{ij} < r_{ij} < S_{ij} \\ 0 & , r_{ij} > S_{ij} \end{cases} \quad (3-13)$$

$$f_R(r_{ij}) = A_{ij} \exp(-\lambda_{ij}r_{ij}) \quad (3-14)$$

$$f_A(r_{ij}) = -B_{ij} \exp(-\mu_{ij}r_{ij}) \quad (3-15)$$

$$b_{ij} = \chi_{ij} (1 + \beta_i^n \zeta_{ij}^n)^{-\frac{1}{2n}} \quad (3-16)$$

$$\zeta_{ij} = \sum_{k \neq i, j} f_C(r_{ik}) \omega_{ij} g(\theta_{ijk}) \quad (3-17)$$

$$g(\theta) = 1 + \frac{c_i^2}{d_i^2} - \frac{c_i^2}{d_i^2 + (h_i - \cos \theta_{ijk})^2} \quad (3-18)$$

Where E is the total energy; the sub-function, V_{ij} , describes the energy between two atoms (i and j); (i, j and k) label the three atoms of the system; f_R represents a repulsive pair potential; f_A represents an attractive pair potential; f_C represents a smooth cut-off function to limit the range of the potential; r_{ij} is the length of the i - j bond; b_{ij} is the bond order term; ζ_{ij} counts the number of other bonds to the i atom, besides the i - j bond; ω_{ij} is a constant set as 1 in this case [107]; θ_{ijk} is the bond angle between the i - j bond and i - k bond; and χ_{ij} is the mixing parameter depends on the different atom pairs. The Tersoff potential is used for covalently bonded materials like silicon atoms.

- **Embedded-Atom method potential**

In deriving the embedded-atom method potential, it can be stated that the major contribution to the energetics is the energy to embed the atom into the electron density of the neighbouring atoms. The total energy of the system can be written as formula (3-19) [108, 109].

$$E_{tot} = \sum_i G_i(\rho_{h,i}) + \frac{1}{2} \sum_{i,j} V_{ij}(r_{ij}) \quad (3-19)$$

$$\rho_{h,i} = \sum_{j \neq i} \rho_j^a(r_{ij}) \quad (3-20)$$

Where $\rho_{h,i}$ is the total electron density at atom i due to the rest of the atoms in the system; G_i is the embedding energy for placing an atom into the electron density; $V_{i,j}$ is the short range pair interaction representing the core-core repulsion; r_{ij} is the separation of atoms i and j ; $\rho_j^a(r)$ is the atomic electron density of atom j at the distance r_{ij} from the nucleus.

- **Modified Embedded-Atom method potential**

The MEAM is theoretically an extension of the EAM potential [110] with modifications to include the directionality of the bonding. The bond-angle was explicitly handled so as to accommodate covalent systems. The total energy is given by Equation (3-19). The MEAM is suitable for modelling metals and alloys with fcc, bcc, hcp and cubic structures, and also for covalent materials such as silicon and carbon.

- **ReaxFF Reactive Force Field**

The ReaxFF reactive force field has been developed by van Duin and co-workers [77], to simulate large system with relatively cheaper computational cost, but with the comparable accuracy of quantum based simulation results. The way of calculation in the ReaxFF is based on the bond-order dependent concept, so that it allows us to predict highly accurate transition state modelling, when bonds are forming or breaking away [111]. ReaxFF aims to be as general as possible and the parameters used within this force field are developed by fitting against experimental and quantum mechanical calculations.

In the ReaxFF method, the forces are derived from a general energy expression (3-21) [77].

$$E_{system} = E_{bond} + E_{over} + E_{under} + E_{lp} + E_{val} + E_{vdWaals} + E_{coulomb} \quad (3-21)$$

The partial contributions in equation (3-21) include bond energies (E_{bond}), energy contributions to penalize over-coordination and (optionally) stabilize under-coordination of atoms (E_{over} and E_{under}), lone-pair energies (E_{lp}), valence angle energies (E_{val}) and terms to handle non-bonded Coulomb ($E_{coulomb}$) and van der Waals ($E_{vdWaals}$) interaction energies [77].

3.1.3 Thermodynamic ensembles

In MD simulation, it is necessary to constrain the simulation system through an ensemble, so that the MD simulation can be performed under certain macroscopically stable conditions. The ensemble refers to a collection of a large number of independent systems with the same properties and structures in various motion states under certain macroscopic conditions [112]. The ensemble is a large group of atoms or systems which are in different microscopic states, but have the same macroscopic or thermodynamic states. If a system of N atoms in a given macro-state is defined in terms of thermodynamic quantities, such as overall energy, pressure, temperature, volume etc, there are many configurations at the atomic scale, which will lead to the same macro-state. The microstate of a system, defined by the atomistic positions and momenta cannot be known in a deterministic manner, because of the uncertainty principle of quantum mechanics [104]. To avoid this problem, a statistical mechanics approach is used for the atomic description. According to the macro constraints, here are presented three commonly used ensembles in molecular dynamics [104].

- **Micro-canonical Ensemble (NVE).** This is an isolated system, with N atoms, which occupies a constant volume and the overall energy E of the system is constant.
- **Canonical Ensemble (NVT).** This is a system in a temperature bath, with N atoms and the volume V and the temperature T of the system are kept constant.
- **Isobaric Isothermal Ensemble (NPT).** This is a system in a temperature and pressure bath, with N atoms and the pressure P and the temperature T of the system are kept constant.

3.1.4 Other configurations

Boundary condition setting. Although MD simulation can provide the macroscopic properties of a particle system, the number of particles calculated is limited by the processing power of the computer. So, the boundary of the simulation system leads to a large impact on the simulation process. Periodic boundary condition (PBC) is used to eliminate the influence

of the boundary. Figure 3-2 shows the schematic illustration of PBC. N particles are regarded as the original unit of the infinite period lattice with the same unit. When a particle escapes the box from a certain boundary, the effect of PBC causes it to enter the box from the other side.

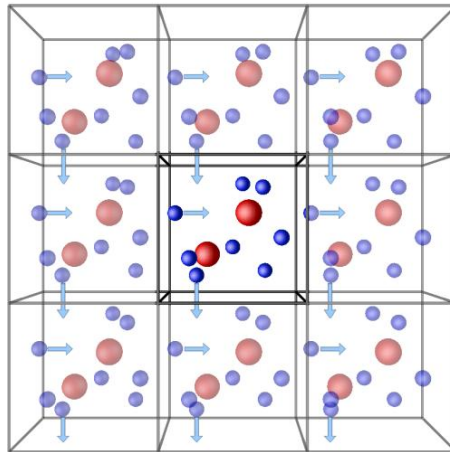


Figure 3-2. The schematic representation of the idea of PBC.

Integration timestep setting. In MD simulation, another key factor is how to choose an appropriate integration timestep to save calculation time without losing the accuracy. Generally, the moving distance of atoms in each integration step should be $1/20$ of the distance between atoms. In general, the atomic distance is 0.14 nm , and the atomic velocity is 0.0047 nm/fs , so the calculated timestep should be less than 1.5 fs [113].

3.2 The simulation configuration

There are several MD models used in this research. In this section, all models and settings used in different cases are presented.

3.2.1 The workpiece

In this research, the workpieces are the Si face and C face of single-crystal 4H-SiC and 6H-SiC. The molecule crystal structures and structural parameters of 4H-SiC and 6H-SiC are illustrated in Figures 2-1 and Table 2-1. For both 4H-SiC and 6H-SiC, if the top surface is the Si face, the bottom surface will be the C face. In MD simulations, the Si atoms and C atoms

are defined and distinguished by their different mass. Depending on the interest, the SiC workpiece can be positioned to align its C face or Si face to the cutting path plane.

3.2.2 The abrasive tip

The diamond is deemed to be the hardest material in the world so it is a common abrasive used in polishing. The crystal structure of diamond is illustrated in Figure 3-3. The indentation tip and scratching grit used in this research are the single-crystal diamond.

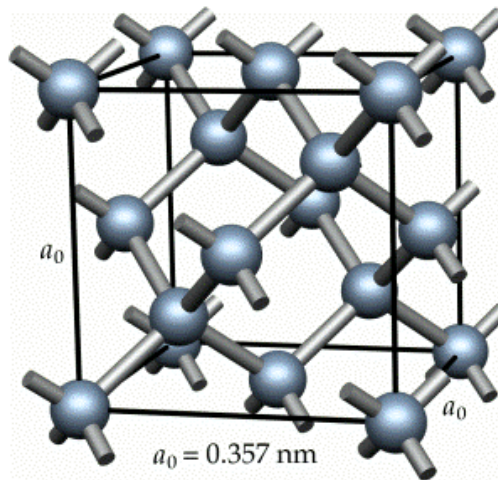


Figure 3-3. The Diamond Structure.

The tip of the abrasive grit is a hollow rigid hemisphere on a cylindrical column to reduce the computation time. The abrasive cutting tip is positioned below the workpiece surface at the required scratching depth. In addition, the tip atoms were set as rigid bodies because the diamond tip is much harder than both 4H-SiC and 6H-SiC.

3.2.3 Model and setting-up for indentation simulations

The MD simulation models used in the indentation simulations are shown in Figure 3-4. The workpiece size is 30 nm × 30 nm × 20 nm (x×y×z), containing about 1.75 million atoms in 4H-SiC and 1.83 million atoms in 6H-SiC. The indenter is designed to be hollow in order to reduce the amount of calculation, consisting of a hemisphere and a cylinder with the radius of 10 nm, which contains about 454,048 diamond atoms. The main content of this research is to study the deformation behaviour of 4H-SiC and 6H-SiC rather than the wear of the diamond indenter, so the indenter atoms can be set as rigid bodies.

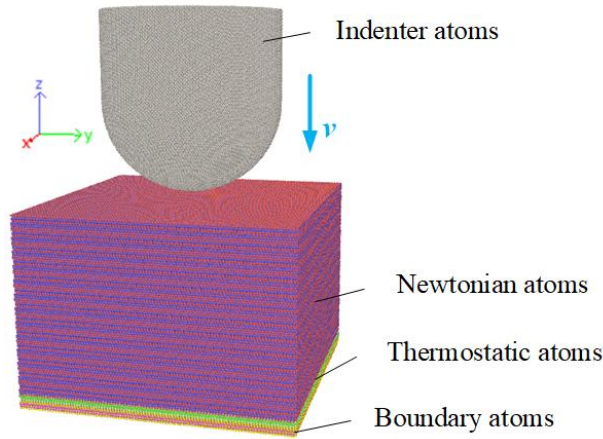


Figure 3-4. The MD model of indentation.

The selection of potential function for the MD analysis is critical to ensure the accuracy and reliability of the MD simulation. Appropriate potential functions can correctly simulate the behaviour of atoms to obtain accurate results [114, 115]. As mentioned in Section 3.1.2, the Tersoff potential function is a three-body potential function that provides a more realistic description of covalently bonded materials [107]. Therefore, in this research, the Tersoff potential function is used to describe the interaction between C-C, Si-Si, and Si-C atoms. The equations of Tersoff potential are shown in Section 3.1.2, and the parameters in Tersoff potential applied in this research are shown in Table 3-2.

Table 3-2. Parameters in Tersoff potential for Si and C [107].

Parameters	Si-Si	C-C
A (eV)	1830.8	1393.6
B (eV)	471.18	346.7
λ (nm ⁻¹)	24.799	34.879
μ (nm ⁻¹)	17.322	22.119
β	1.1000×10^{-6}	1.5724×10^{-7}
n	0.78734	0.72751
c	1.0039×10^5	3.8049×10^4
d	16.217	4.3484
h	-0.59825	-0.57078
R (nm)	0.27	0.18
S (nm)	0.3	0.21

$\chi_{\text{Si-Si}}=1.0$	$\chi_{\text{C-C}}=1.0$	$\chi_{\text{Si-C}}=0.9776$
---------------------------	-------------------------	-----------------------------

In addition, a reasonable selection of the ensemble is of great significance for obtaining accurate molecular dynamics simulation results. The workpiece is divided into three layers: the Newtonian atoms (NVE ensemble), the thermostatic atomic layer (NVT ensemble) and the boundary atomic layer. The Newtonian atoms are the main part of the workpiece, following Newton's laws of motion, which are used to investigate the phenomena that occur during the scratching simulation [60, 89, 93]. The boundary atomic layer can prevent rigid movements of the entire workpiece during scratching. The thermostatic atomic layer can control the temperature within a specified range by adjusting the atomic velocity using a Berendsen thermostat [116]. During scratching, the thermostatic atoms within the thermostatic layer absorbed the heat generated by the Newtonian atoms.

The fixed boundary conditions are applied in all directions in the simulation box during the indentation simulations, and the indentation processes are conducted along the negative direction of the Z axis (vertical to the (0001) basal plane). The depth of the indentation is 4 nm and the speeds of loading and unloading are both 100 m/s.

The temperature of the thermostatic layer is always controlled at 300 K during the simulation, and the relaxation process of the system is carried out for 150 ps before the simulations start. The time step is set as 1 fs. In addition, the MD results visualized and analysed using the OVITO and the dislocation extraction algorithm were used to analyse dislocations in the simulation process.

3.2.4 Model and setting-up for scratching simulations

The MD model used in nanoscratching simulations is shown in Figure 3-5. The size of 4H-SiC or 6H-SiC workpiece was 40 nm × 19.7 nm × 12 nm (x×y×z), containing about 0.923 million atoms. The cutting tip of the abrasive grit was a hollow hemisphere on a cylindrical column with a of radius 5 nm to reduce the computation time. Scratching direction was the main direction in this model, so periodic boundary condition was applied in the y-direction to induce the computation time. And the fixed boundary condition was applied in the x- and z-

directions. Other conditions in scratching simulations were the same as those in indentation simulations.

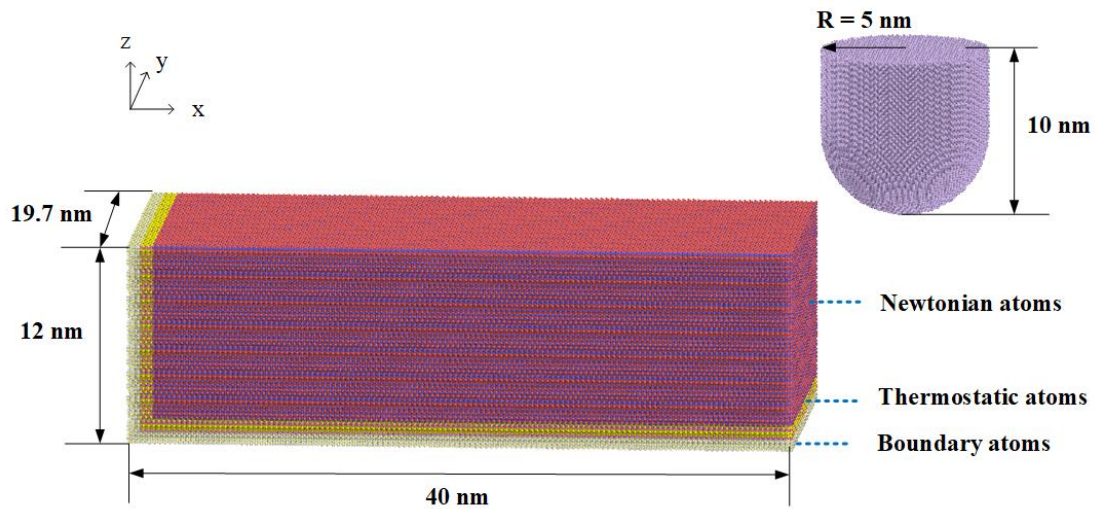


Figure 3-5. The MD model of scratching.

The scratching processes were conducted on the (0001) basal plane (perpendicular to z-axis) along direction [1-210] (along the x-axis). The depth of scratching ranged from 0.5 nm to 3 nm, and the scratching speed was held constant at 100 m/s. The temperature of the thermostatic layer was controlled at 300 K during the simulation, and the relaxation process of the system was taken for 150 ps before the simulated scratching began. The simulation time step was set at 1 fs, and the total scratching distance was set as 30 nm.

In addition, different machining conditions were taken into consideration in this project as well. Here, the different parameters in each condition are presented as follows.

- **Scratching performance in relation to SiC layer structure (1st-8th)**

The atomic structures of 4H-SiC and 6H-SiC are layered structures. In order to figure out the influence of different scratching depths according to the atomic layers, scratching simulations are investigated and the details will be discussed in Section 7.1. Si face of 6H-SiC is selected as the material of the workpiece. Table 3-3 shows the scratching depths according to the atomic layers.

Table 3-3. Scratching depths according to the atomic layers.

Number of atomic layers	Scratching depth (Å)	
	4H-SiC	6H-SiC
1	-0.623	-0.631
2	-3.137	-3.150
3	-5.650	-5.673
4	-8.163	-8.193
5	-10.676	-10.713
6	-13.190	-13.236
7	-15.703	-15.755
8	-18.216	-18.275

- **Different shape of abrasive tip**

In Section 7.2, the effects of abrasive shape during scratching are investigated and the details will be discussed in Chapter 7. Si face of 6H-SiC is selected as the material of the workpiece. As shown in Figure 3-6, five types of tips are taken into consideration in this research, sphere, cone, frustum cone, face of pyramid and edge of pyramid. The sphere tip is a hemisphere on a cylindrical column with a radius of 5 nm. The angle of the cone tip and frustum cone tip is 60°. The face angle of the pyramid tip is also 60°. All of them are designed to be hollow in order to reduce the computation time. The depths of the scratching are 2 nm and 3 nm and the scratching speeds are 50 m/s and 100 m/s.



Figure 3-6. Different types of tips used as the scratching abrasive.

- **Different scratching speed**

In Section 7.3, the effects of scratching speed during scratching are investigated and the details will be discussed in Chapter 7. Si face of 6H-SiC is selected as the material of the workpiece, and the scratching speeds are 10, 40, 60, 80 and 100 m/s.

- **Different scratching direction**

In Section 7.4, the effects of scratching direction during scratching are investigated and the details will be discussed in Chapter 7. Si face of 6H-SiC is selected as the material of the workpiece, and the scratching processes are conducted on the (0001) basal plane (vertical to z axis) along direction $[1-210]$ and $[1-100]$.

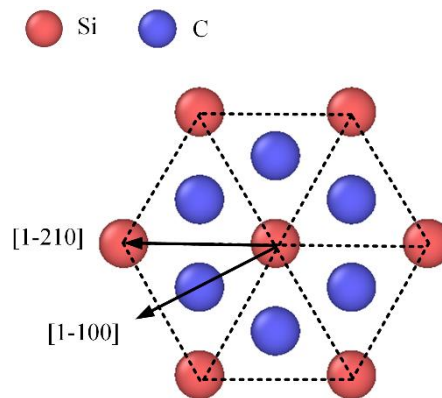


Figure 3-7. Diagram of two scratching directions from the top view.

3.2.5 Model and setting-up for interfacial reaction simulations

For the mechanical removal, it can be simulated by the classical molecular dynamics based on Newton's law, containing tens of millions of atoms in the system. Although there is still a huge gap with the actual polishing, it is sufficient to reflect the nano-machining conditions. The most commonly used ones are based on molecular mechanics and embody the classical mechanical treatment of particle-particle interactions. This interaction can replicate structural and conformational changes, but usually cannot replicate chemical reactions [96]. For the chemical removal, the reaction molecular dynamics based on ReaxFF is more practical for this type of interfacial chemical reaction, which can simulate the bond-breaking and bond-making. However, the simulation requires a huge amount of calculation, the number of atoms contained in the system cannot be too large. So, it is necessary to properly design the model

simulation parameters (temperature, load and speed, etc.) of the system, thereby reducing the calculation duration.

As shown in Figure 3-8, three RMD simulation models were used in this section: (a) The reaction between H₂O molecules and both faces of 6H-SiC; (b) The reaction between H₂O molecules and the Si face of 6H-SiC; (c) The reaction between H₂O molecules and the C face of 6H-SiC. For the left model, the size is 21.567 Å × 21.346 Å × 38.171 Å, containing 1,344 atoms in 6H-SiC and 300 H₂O molecules. And there are 1,344 atoms in 6H-SiC, 1,048 diamond atoms and 200 H₂O molecules in other two RMD models, with the size of 21.567 Å × 21.346 Å × 47.466 Å. There are some layers in the models, such as fixed layer and mobile layer. The role of the fixed layer is to prevent the whole rigid movement of the 6H-SiC during the process, and that of the mobile layer is to load. It is easy to find that the upper surface is the C face and the lower surface is the Si face in all models.

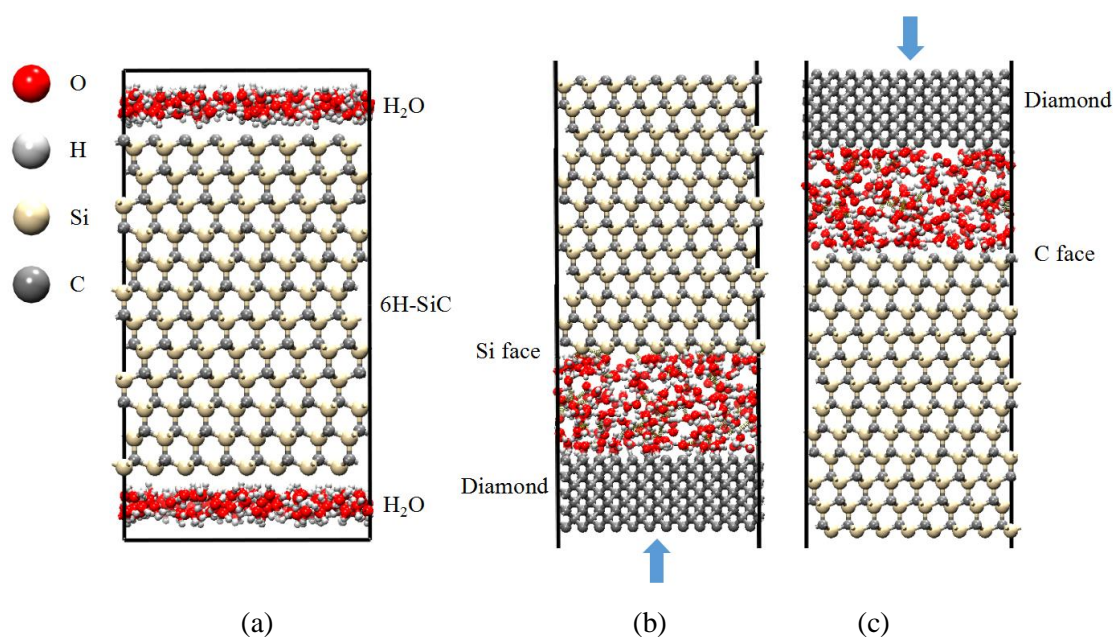


Figure 3-8. The RMD models. (a) The reaction between H₂O molecules and both faces of 6H-SiC. (b) The reaction between H₂O molecules and the Si face of 6H-SiC. (c) The reaction between H₂O molecules and the C face of 6H-SiC.

The accuracy and reliability of the RMD simulations fundamentally depends on an appropriate potential function. As introduced in Section 3.1.2, ReaxFF Reactive Force Field can be used to simulate the chemical reactions between atoms. Therefore, in this research, the ReaxFF proposed by Newsome et al. [78, 79] was adapted to describe chemical reactions

between SiC and H₂O molecules in this research. This potential was particularly developed for the atoms involved in the oxidation of SiC, i.e., the Si/C/H/O system, containing oxidation by O₂ molecules and by H₂O molecules.

For the model in Figure 3-8 (a), periodic boundary conditions are used in all directions. So the Si face and C face are in almost the same conditions, such as temperature and pressure, during the heating process. For the RMD models in Figures 3-8 (b) and (c), the Si face and C face are loaded separately, so the fixed boundary condition is adopted in the z-direction and periodic boundary conditions are used in x- and y- directions.

Four RMD simulations are presented in Chapter 8:

- The reactions between two faces of 6H-SiC and H₂O molecules with the temperature rising from 293 K to 3106 K.
- The reactions between two faces of 6H-SiC and H₂O molecules at the constant temperature of 2100 K.
- The reactions between the Si face of 6H-SiC and H₂O molecules at 2100 K, with the diamond slab loading at an upward speed of 10 m/s.
- The reactions between the C face of 6H-SiC and H₂O molecules at 2100 K, with the diamond slab loading at a downward speed of 10 m/s.

The first and second simulations aim to find the temperature of the chemical reaction between SiC and H₂O. The third and fourth simulations aim to compare the difference of Si face and C face. All simulations are performed in the canonical ensemble (NVT), with the time step of 0.25 fs. And the temperature was controlled by the Nose-Hoover thermostat with a damping constant of 10 fs. All RMD simulations are performed using the LAMMPS and the MAPS is used to build models, visualize the processes and analyse the results.

3.2.6 Model and setting-up for scratching simulations on surface with oxide layer

The above-mentioned systems for the RMD simulations are very small, containing only a few thousand atoms due to the limitation of calculation capacity, while the actual machining scale is much larger than that. The correspondence between the conclusions obtained by the microscopic systems and the macroscopic experiments is not clear. Besides, mechanical

removal and chemical reactions during polishing are usually carried out by classical MD and RMD respectively, but chemical reactions and mechanical interactions occur synergistically in actual polishing, which may cause deviations between the simulation results and the experiments. Therefore, the results of the RMD simulations should be combined with the classical MD simulations, through adding the chemical reaction products in the small system (RMD) to the larger system (MD), which makes the simulation systems closer to actual polishing.

The sample material block model for the MD simulation used in this chapter is shown in Figure 3-9. The size of 6H-SiC workpiece was $40 \text{ nm} \times 19.7 \text{ nm} \times 12 \text{ nm}$ ($x \times y \times z$). The heights of oxide layers on Si face and C face were 1.3 nm and 1.7 nm. The oxide layers were built from the RMD results in Section 8.4 and then underwent the relaxation process for 150 ps.

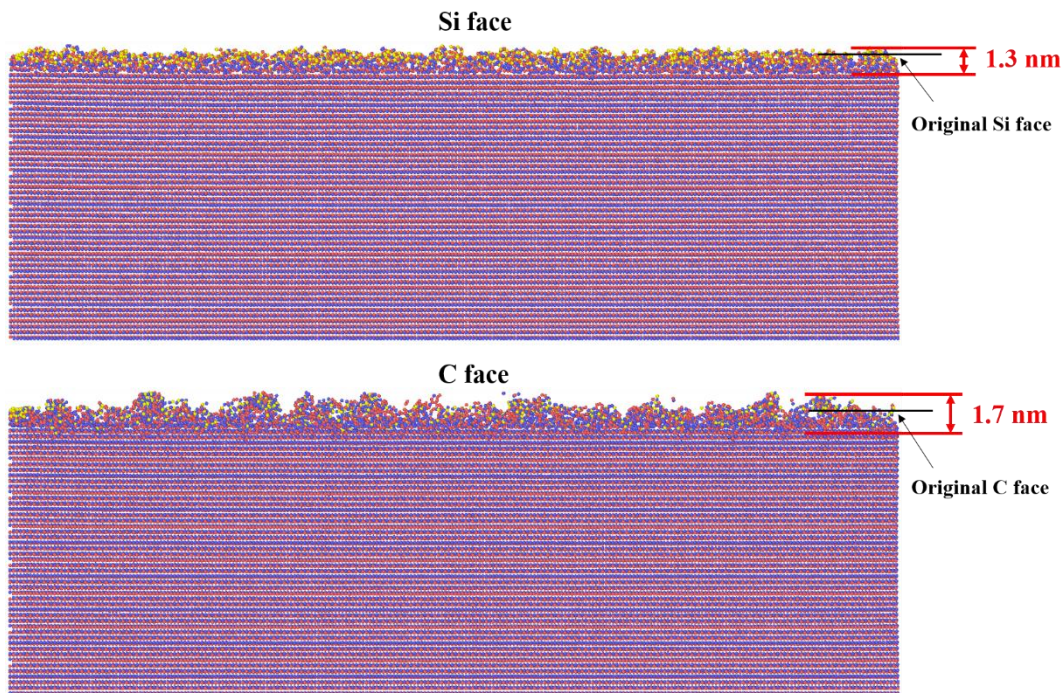


Figure 3-9. Workpiece model with oxide layers on Si face and C face.

Three types of MD simulations are presented in Chapter 9:

- Nanoscratching simulations at constant depths, ranging from 1 nm to 3 nm. As concluded in Chapter 8, the reaction depths on Si face and C face are different.

Taking this difference into consideration in this section, the scratching depth is defined as the depth from original surface before reaction.

- Nanoscratching simulations in an inclined direction (10 m/s along normal direction and 100 m/s along tangential direction).
- Nanoscratching simulations under constant loads, ranging from 1360 nN to 2000 nN.

The Tersoff potential function is used to describe the interaction between C-C, Si-Si and Si-C atoms in this research. In addition, the Tersoff potential is also adopted to describe the interaction of Si-O and O-O atoms [117]. The L-J potential is used to describe the interaction of Si-O atoms, and the ε and σ are 0.003442 eV and 3.001 Å [118, 119].

3.3 Simulation procedure

3.3.1 Hardware consideration

The MD simulations are very time-consuming, and the speed of calculation mainly depends on the number of cores used. The MD simulations in this research were carried out initially on a computer with 44 cores in Huaqiao University and later on the STOKES, the High Performance Computer (HPC) clusters in Liverpool John Moores University. All the simulations were run in the Linux system.

STOKES consists of a single head node and 8 compute nodes and has a total of 244 cores. The head node contains 2x Intel Xeon E5 2630v4 10 core CPUs operating at 2.20GHz. The compute nodes contain 2x Intel Xeon E5 2660v4 14 core CPUs operating at 2.00GHz. Each node, including the head node, contains 128GB of DDR4 RAM, so the total memory for the cluster is 1152GB. STOKES has 3 network switches. A 40Gb/s InfiniBand switch is used for MPI and storage traffic, a 1Gb/s Ethernet switch is used for provisioning and management traffic, and a 100Mb/s Ethernet switch is used for IPMI traffic. File storage for STOKES is provided by a 48TB hard disk drive array consisting of 10x 6TB HDDs configured in RAID 6, with 1x dedicated spare. 2x 1TB HDDs configured in RAID 1 are used for the root file-system and home directories. Each compute node contains a 1TB HDD which is used by the provisioned operating system. The operating system for STOKES is Red Hat Enterprise Linux, and Slurm Workload Manager is used for batch processing of jobs.

3.3.2 Software consideration

The MD simulations in this research are carried out by using the following software namely;

- **MATLAB.** It can be used for a range of applications, including deep learning and machine learning, signal processing and communications, image and video processing, control systems, test and measurement. Here, MATLAB is used to establish the basic atoms information in a unit cell, and then build the atoms in a much large region as required through writing a program.
- **LAMMPS (Large-Scale Atomic/Molecular Massively Parallel Simulator)** [120]. It is a classical molecular dynamics code with a focus on materials modelling. LAMMPS runs on single processors or in parallel using message-passing techniques and a spatial-decomposition of the simulation domain. Compared with other MD software, LAMMPS can simulate more atoms in a system. For example, in this thesis, there are more than 1,000,000 atoms in the scratching model, and the model is much larger than that in usual chemical or biologic simulations. So LAMMPS is selected in this research. Here, the LAMMPS is the core program for the research and it is used to build atoms, set parameters, set control commands and run simulations in this research.
- **OVITO (Open Visualization Tool)** [121, 122]. It is a scientific visualization and analysis software for atomistic and particle simulation data. Here, the OVITO is employed for the visual display of the LAMMPS MD simulation results.
- **Notepad++.** It is a text and source code editor for use with Microsoft Windows. It supports tabbed editing, which allows working with multiple open files in a single window. Here, Notepad++ is used to view and edit the input and output documents of LAMMPS.
- **Microsoft Visual C++.** It is a compiler from Microsoft for the C, C++, and C++/CLI programming languages. Here, the stress and temperature distribution information are calculated using C++ programs.
- **MAPS (Materials and Processes Simulations).** It is a modelling platform with state-of-the-art user-friendly graphical interface for model building of any types of materials, properties simulation and powerful analysis capability. Here, MAPS is used to build atomic structures with bonds and analyse the reaction products.

- **Origin.** It is a proprietary computer program for interactive scientific graphing and data analysis. Here, Origin is employed to graph the force-displacement curves.

3.3.3 Methodology flowchart

In this section, the MD procedure is introduced. Figure 3-10 shows the flowchart of the MD procedure together with software methodology.

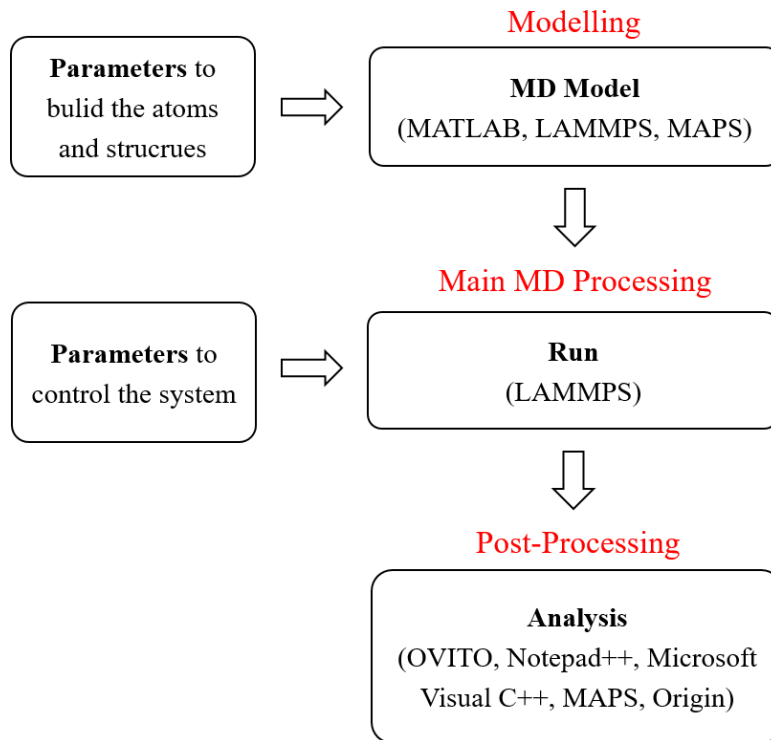


Figure 3-10. The flowchart of software methodology.

- **Modelling.** There are several models used in this research. The models can be largely divided to the classic MD models and RMD models. For the classic MD systems, the MD models can be built using MATLAB and LAMMPS together according to the atomic structures of diamond and SiC. For the RMD systems, the RMD model can be built using MAPS. Besides, for both 4H-SiC and 6H-SiC, if the top surface is the Si face, the bottom surface will be the C face. In MD simulations, the Si atoms and C atoms are defined and distinguished by their different mass.
- **Main MD processing.** The LAMMPS is the main processing software for the MD simulation. The input information, such as condition parameters, controlling and atomic information are setting or processed in LAMMPS. And all output information

is derived from LAMMPS. There is no visual display platform in LAMMPS, so all the procedures should be achieved by writing LAMMPS codes.

- **Post-processing.** The simulation results are visualised and analysed by OVITO and MPAS. The Common Neighbour Analysis (CNA) and Dislocation Extraction Algorithm (DXA) are used to investigate amorphous atoms and dislocations occurring in the subsurface, and the material deformation mechanism and slip systems can be analysed [122]. The temperature, forces and stresses of all directions can be calculated from the output documents of LAMMPS. The Load-displacement curves can be presented using Origin. The cloud pictures of the temperature and stress field can be calculated using C++ programs and then be visualised and analysed using OVITO.

3.3.4 Dislocation extraction algorithm method

In order to detect and analyse the deformation in subsurface, the CNA and DXA in OVITO are used to identify whether the lattice structure of a material is changed or damaged.

The CNA is an algorithm that computes a fingerprint of atom pairs to characterize the local structural environment [123]. The threshold distance criterion in CNA differentiates between bonded and unbonded pairs of atoms, which helps distinguish disordered atoms from perfectly structured atoms. For diamond structure, the algorithm analyses the local environment of each atom up to the second neighbour shell to determine the local structural type [124]. Here, the disordered atoms recognized by CNA are considered as atoms with amorphous structures.

The fundamental concept underlying the DXA is the Burgers circuit construction, which is the established method of discerning dislocations from other crystal defects and determining their Burgers vectors. In the formulation employed here, a Burgers circuit C is a path in the dislocated crystal consisting of a sequence of atom-to-atom steps (line elements Δx) [122]. There exists a mapping $\Delta x \rightarrow \Delta x'$ that translates each line element of the path to a corresponding image, $\Delta x'$, in a perfect crystal lattice. As shown in Figure 3-11, summing these transformed line elements algebraically along the associated path, C' , gives the true Burgers vector of the dislocation enclosed by C [122]:

$$\mathbf{b} = - \sum_{C'} \Delta \mathbf{x} \quad (3-21)$$

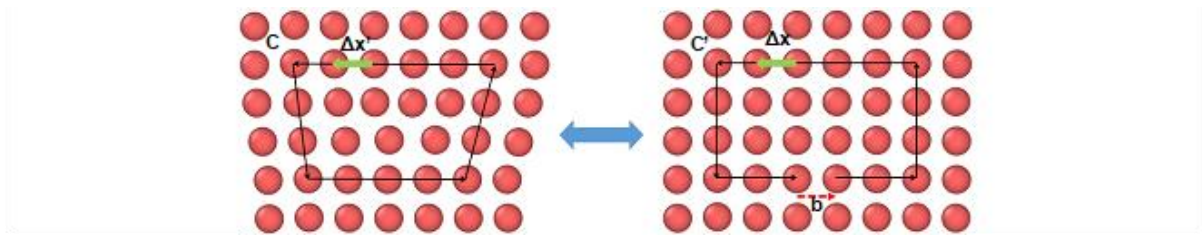


Figure 3-11. Schematic diagram of Burgers vectors.

Chapter 4. The methodology for the verification experiments

The verification of MD simulation has always been a key challenge regarding its accuracy and reliability. There is a general lack of experimental verification of MD simulation of nanomachining. The increase in the number of atoms in the MD model causes a tremendous amount of calculation, while the nanomachining in the experiment is very difficult to implement and measure. So it is difficult to compare the simulation and experiment. This study attempts to increase the model appropriately and adjust the parameters in order to approximate the experimental conditions. Although there remains a gap in scale between simulation and experiment, the validation can be considered by the trends and phenomena rather than exact values.

In this research, the nanoindentation tests and nanoscratching tests on the Si face and C face of 4H-SiC and 6H-SiC wafers were carried out in order to investigate the anisotropy of the material. And the effect of different scratching conditions was investigated through the multiple grit scratching tests on 6H-SiC wafers.

4.1 Nanoindentation tests

Nanoindentation is the most commonly applied means of testing the mechanical properties of materials. In this research, the nanoindentation tests aimed to clarify the nanomechanical properties on the Si face and C face of 4H-SiC and 6H-SiC wafers.

4.1.1 Indentation device

In the experiments, indentation tests were carried out on the Fischer Scope HM 2000 in Xiamen Golden Egret Special Alloy Co. Ltd., a professional nanoindentation measuring instrument, suitable for analysing mechanical and elastic properties of materials by nanoindentation. Figure 4-1 shows the overview of the Fischer Scope HM 2000. The three-sided pyramidal Berkovich probe was adopted in these tests, because the blunted geometry of the tip can often be approximately as spherical [125]. It was possible to predict the elastic response using the Hertzian law for mechanical contacts, with this approximation of the tip geometry, based on isotropic continuum elasticity [32].

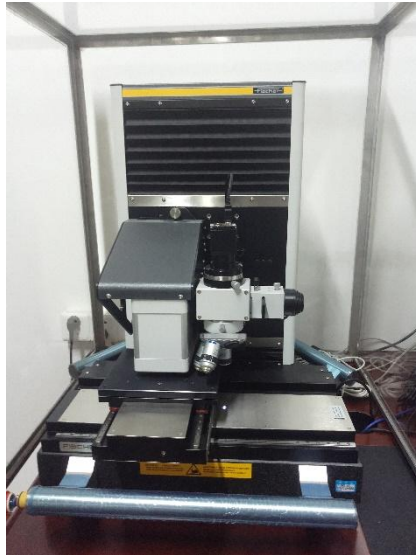


Figure 4-1. The Fischer Scope HM 2000.

4.1.2 Specimens

The specimens used were single crystal 4H-SiC and 6H-SiC wafers, with crystal orientation (0001) and (000-1), diameter 2 inch and thickness 0.33 mm, which were supplied by TankeBlue Semiconductor Co. Ltd., China. Figure 4-2 shows the 4H-SiC and 6H-SiC wafers, and Table 4-1 shows the properties of the wafers used in this research. The specimens were made in different shapes by a precision dicing saw (DS616) in order to identify them more easily, because the C face and Si face of the hexagonal silicon carbide were hard to distinguish by the naked eye.

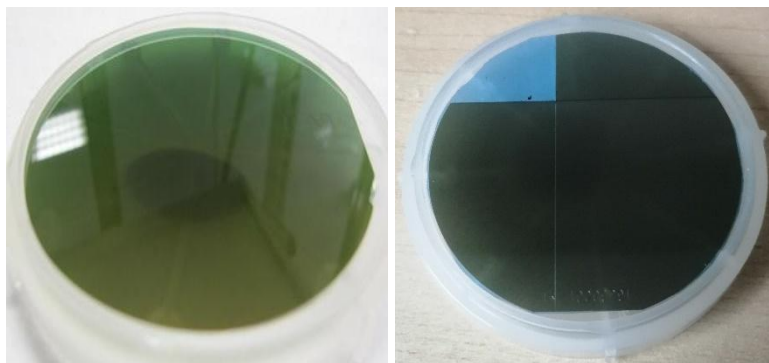


Figure 4-2. 4H-SiC (left) and 6H-SiC (right) wafers.

Table 4-1. SiC substrate specification.

Property	Value
Grade	Dummy Grade
Thickness	330 $\mu\text{m} \pm 25 \mu\text{m}$
Wafer Orientation	On axis: $\langle 0001 \rangle \pm 0.5^\circ$
Micro-pipe Density	$\leq 50 \text{ cm}^{-2}$
Resistivity	$> 1\text{E}5 \Omega \cdot \text{cm}$
Roughness	$\text{Ra} < 1 \text{ nm}$
Density	3.21 g/cm^3
Mohs Hardness	9.2
Band-gap	3.23 eV for 4H-SiC, 3.02 eV for 6H-SiC

4.1.3 Experiment setup and procedures

A series of nanoindentations were performed on the C face and Si face of 4H-SiC and 6H-SiC specimens. The experiments at normal temperature were carried out at a constant load rate, and the loads on each sample were 1 mN, 5 mN and 20 mN, respectively. The indenter was pressed down to contact the surface of the sample, then started loading up to the pre-set maximum load, held for 15 s (this step is to eliminate material creep), finally unloaded until completely withdrawn. After pre-setting the indentation load, the indenter automatically completed the process of indentation loading and unloading, and output the parameters required for the experiment in real time. In order to get more accurate data and observe easily, the array indentation experiments were carried out on each sample.

After nanoindentation tests, the samples were inspected through the scanning electron microscopy (SEM), SIGMA 500, Zeiss (Figure 4-3). Then, the surface morphology could be observed and compared with the corresponding MD results.



Figure 4-3. SIGMA 500.

4.2 Nanoscratching tests

Nanoscratching tests were also conducted on the C face and Si face of 4H-SiC and 6H-SiC specimens. Nanoscratching is another commonly applied means of testing the mechanical properties of materials. In this research, the force information during nanoscratching tests was compared with the MD simulation results.

4.2.1 Scratching device

In the experiments, scratching tests were carried out on a Nano Indenter G200 (Keysight, USA), an effective nanomechanical characterization tool for many applications. Figure 4-4 shows the overview of the Nano Indenter G200. The conical tip with the radius of 3 μm and the angle of 120 $^\circ$ was used in the scratching experiments.



Figure 4-4. Nano Indenter G200.

4.2.2 Specimens

The specimens used were single crystal 4H-SiC and 6H-SiC wafers (Figure 4-2), with crystal orientation (0001) and (000-1), diameter 2 inch and thickness 0.33 mm, which were supplied by TankeBlue Semiconductor Co. Ltd., China. The specimens were made in different shapes by a precision dicing saw (DS616) as well in order to identify them more easily, because the C face and Si face of the hexagonal silicon carbide were hard to distinguish by the naked eye.

4.2.3 Experiment set-up

A series of nanoscratching tests were performed on the C face and Si face of 4H-SiC and 6H-SiC specimens. The scratching processes were performed with the constant normal load of 4 mN, and the scratching speeds were constant as well, which were 0.1 m/s, 0.15 m/s and 0.2 m/s, respectively.

During the nanoscratching tests, the normal displacement and friction coefficient were obtained and then compared with the corresponding MD results.

4.3 Multiple grit scratching tests

In this study, multiple grit scratching tests on 6H-SiC wafers were conducted to investigate the effect of different scratching conditions. Two scratching directions ([1-210] and [1-100]) and two scratching speeds (1 m/s and 10 m/s) were compared in the tests.

4.3.1 Scratching machine

The experiment was carried out on the Bridgeport XR 610 VMC milling machine, which is a 5-axis Computer Numerically Control (CNC) machine. The Figure 4-5 and Table 4-2 show the overall view and the machine specification of the CNC machine that was used for the experiment. The CNC machine is equipped with a rotating disc attached to the electrical spindle that can be adjusted continuously from 50~12,000 revolutions per minute (RPM) and a multi-axial table moving along the rotational axis of the spindle.



Figure 4-5. XR 610 CNC machine.

Table 4-2. Machine specification of XR 610 CNC machine.

Parameters	Value
Spindle motor power (kW)	21
Torque (Nm)	134
Spindle speed (rpm)	50 ~ 12,000
Table (mm)	900 × 500
Travels XYZ axis (mm)	610 × 510 × 610

4.3.2 Scratching tool

The scratching tool used in the experiments consists of a steel wheel and a grit-holder on it. As shown in Figure 4-6, the diamond abrasives are bonded to the grit-holder and formed the scratching tool.

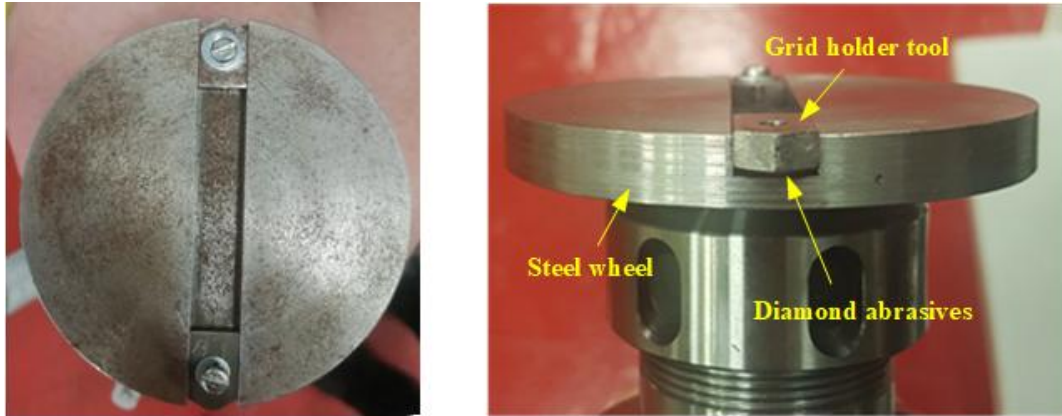


Figure 4-6. Scratching tool.

4.3.3 Workpiece material

Two pieces of 6H-SiC (0001) wafers are used in the experiments and are shown in Figure 4-7. The workpieces are two pieces of wafers derived from a circular wafer with a diameter of 2 inch and thickness of 0.33 mm.

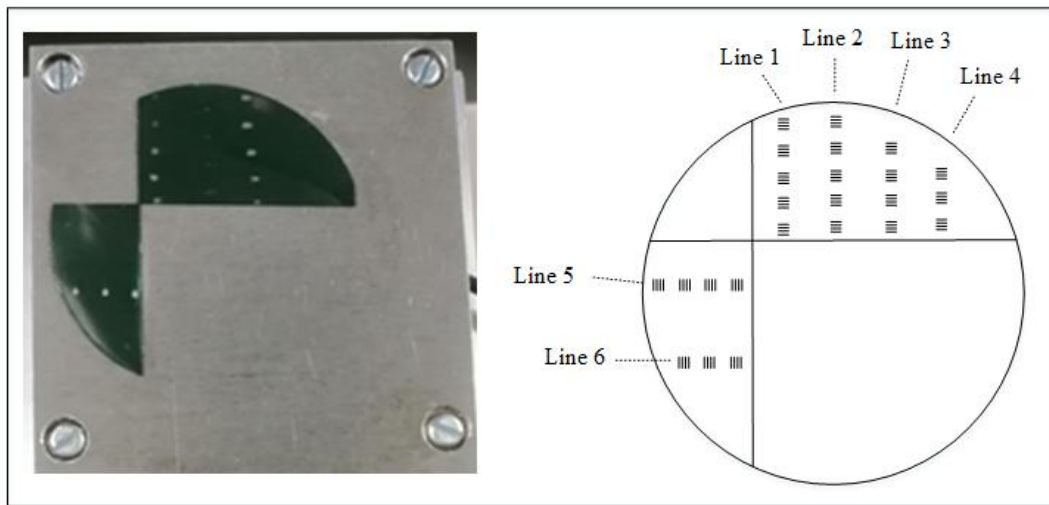


Figure 4-7. The 6H-SiC (0001) wafers used in multiple grit scratching tests.

4.3.4 Experimental set-up and procedure

The set of experimental tests were conducted on the XR 610 VMC Heidenhein CNC machine in dry condition using the developed test rig as shown in Figure 4-8. Each test was carried out with the cutting speeds of 1 m/s and 10 m/s, the downward feed rates of 1,000 mm/min and 10,000 mm/min. The scratching spindle rotational speeds were 238 rpm and 2,380 rpm.

Table 4-3 gives the overall parameters for the experimental work. The scratching tests were performed using abrasive cutting tools assembled to a rotating steel wheel. Diamond abrasives with the size of 20-30 μm were used for the cutting tools.

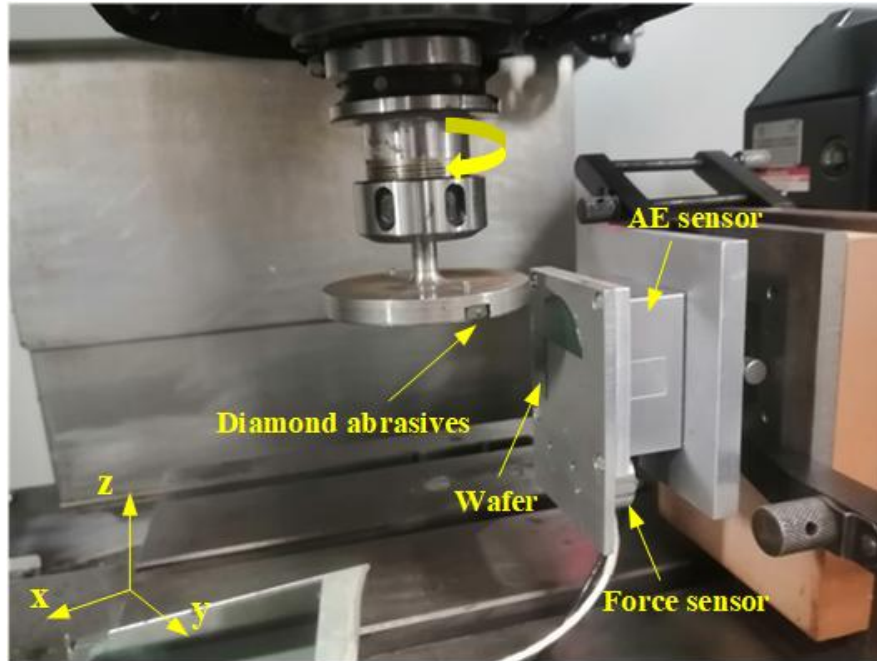


Figure 4-8. The experimental tests set-up.

Table 4-3. Scratching tests parameters.

Parameters	Value
Machine tool	XR 610 VMC CNC machine
Workpiece material	6H-SiC wafer
Abrasives	MDA M2030 normal size distribution
Wheel diameter	80 mm
Scratching condition	Dry
Scratching direction	[1-210] and [1-100]
Scratching speed	1 m/s and 10 m/s
Spindle speed n	238 rpm and 2380 rpm
Feed rate in Z direction v_z	1000 mm/min and 10000 mm/min

Line 1: [1-210], $n = 2380$ rpm, $v_z = 10000$ mm/min

Line 2: [1-210], $n = 238$ rpm, $v_z = 1000$ mm/min

Scratching lines	Line 3: [1-210], $n = 2380$ rpm, $v_z = 10000$ mm/min
	Line 4: [1-210], $n = 238$ rpm, $v_z = 1000$ mm/min
	Line 5: [1-100], $n = 238$ rpm, $v_z = 1000$ mm/min
	Line 6: [1-100], $n = 2380$ rpm, $v_z = 10000$ mm/min

The scratching proceeding was as follows: while the wheel is rotating, the worktable is moving through the X-axis towards the wheel's spindle. Once the abrasive grits touch the workpiece surface, the AE sensor detects an acoustic emission signal of contact between the abrasives and the workpiece. At this point, the wheel rotation was set to the desired speed before the scratch test commenced. The scratching marks are generated by moving the spindle from the top to the bottom along the Z-axis. The process was repeated by shifting the position of the worktable over the Y-axis to generate a new series of scratches. The scratching process was undertaken within six scratching lines on the two 6H-SiC wafers, where each scratching line was performed with a selected scratching speed, scratching depth and scratching direction.

In each machining trial, the acoustic emission (AE) was registered using a Physical Acoustics sensor with a sampling frequency of 2 MHz mounted as near as possible to the cutting zone in order to detect the contact between the abrasives and the workpiece and acquire the AE signal during scratching process. An Interface's 3-axis force sensor was used for the scratching force measurements with a sampling rate of 1,000 Hz. In order to assure the accuracy of the measurements and reduce the errors, the sensor was calibrated after installation. The recorded AE and force information will be analysed to indicate the grit performance.

After scratching tests, the scratching marks generated on the surface were inspected through the Bruker Nano Surfaces Division and the Scanning electron microscopy (Figure 4-9). Then, the material removal, crack generation and surface morphology can be observed and compared with the corresponding MD results.



Figure 4-9. The Bruker Nano Surfaces Division (left) and Scanning Electron Microscopy (right).

Chapter 5. Nanoindentation tests and simulations

In order to study the different nanomechanical properties of the C face and the Si face of 4H-SiC and 6H-SiC, the MD schemes were constructed by using the LAMMPS, in which the following factors were taken into account.

5.1 Indentation forces

There is a general lack of experimental verification of MD simulation of nanomachining due to the gaps in terms of time scale and length scale. This study attempts to increase the model appropriately and adjust the parameters in order to approximate the experimental conditions. A series of nanoindentation experiments were performed. Although the condition of experiments and simulations cannot match quantitatively, the material removal performance presents similar trends.

Load-displacement curve is an important method to analyse the material properties in nanoindentation experiments. A pop-in event in the load-displacement curve means the plastic deformation during indenting on the brittle materials [126]. Goel et al. [32] reported the pop-in events of 4H-SiC in the load-displacement curve, and each maximum implies the beginning of the plastic activity, while each corresponding minimum signifies the completion of the event. Figure 5-1 shows the load-displacement curves of the four different cases of indentation tests. It can be seen from the curves that the Si faces of both 4H-SiC and 6H-SiC show their pop-in events during loading to 5 mN, while there are no pop-in events happening on the C faces. And it is worth noting that the depths of indenter pressing into the samples are almost the same (about 72 nm) for these four cases.

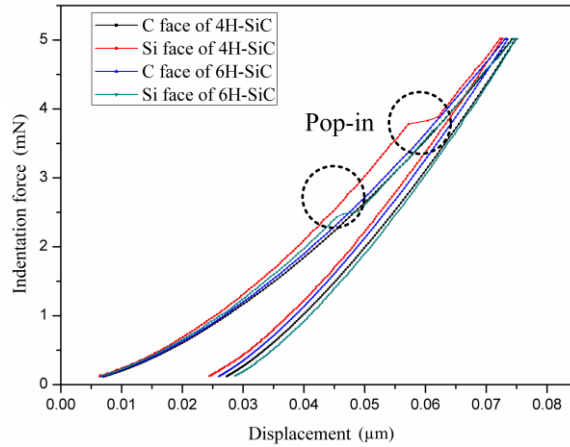


Figure 5-1. Load-displacement curves of indentation tests.

Different from experiments, although the pop-in events cannot be observed, the MD simulation provides a much better temporal and spatial resolution of each atomic scale event in the Load-displacement plots with extreme accuracy [127]. Figure 5-2 shows the P-h curves of the four different indentation cases in the MD simulations. It can be seen from the curves that the magnitudes and trends of the indentation forces are very similar in these four simulations in this scale, which is consistent with the former stage of the experimental results. The C face and the Si face have the same lattice structures for both 4H-SiC and 6H-SiC. Thus, it may be concluded that the lattice structure is the main factor affecting the nanomechanical properties of materials. It also should be noticed that the forces of the Si face are slightly greater than those of the C face in both experiments and MD simulations, even though there are only a few disparities.

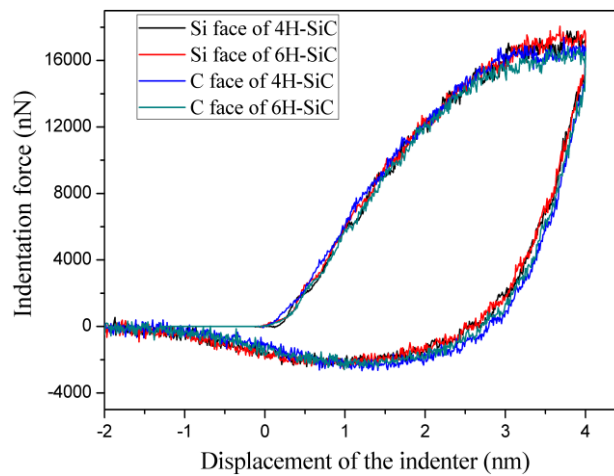


Figure 5-2. Load-displacement curves obtained from the MD simulations.

In addition, the extent of plastic response depends on the residual depth of material recovery during the unloading process. Comparing the four curves, it can be seen that the adhesion (negative indentation force) between the indenter and the sample is a little bit larger for the C face than for the Si face during unloading (from 4.0 to 0.8 nm). The interaction between atoms mainly depends on the covalent bonds, which is described by the Tersoff potential function in these MD simulations. And the covalent bond energy between C atoms (from diamond) and C atoms (from SiC) is larger than that between C atoms (from diamond) and Si atoms (from SiC) [9]. Hence, the C face shows slightly larger adhesion with the diamond indenter than the Si face when unloading.

5.2 Surface and subsurface morphology

After previous nanoindentation tests, all samples were inspected using the SEM. However, no indentation marks were found on the surfaces of all samples. This means the loads at 5 mN cannot cause detectable damage on both 4H-SiC and 6H-SiC wafers due to the extreme high hardness. Here, the damages of SiC wafer include the amorphous atoms on the surface and the dislocations, slippages and even microcracks in the subsurface. Therefore, some indentation tests on Si face of 6H-SiC with higher loads (200 mN and 300 mN) were carried out. A larger conical tip with the radius of 4.5 μm and the angle of 120° was adopted in the experiments.

The SEM results of surface morphology after indentation are shown in Figure 5-3. Although there are many scratching traces on the surfaces which might be caused by the previous polishing process, the cracks caused by indentation can be observed clearly. These cracks are generated and spread in six directions which belong to the same crystal direction system, $\langle 1-210 \rangle$. Interestingly, the shape of indentation marks seems like a regular hexagon though a conical tip is used. This phenomenon means that 6H-SiC shows distinct anisotropy.

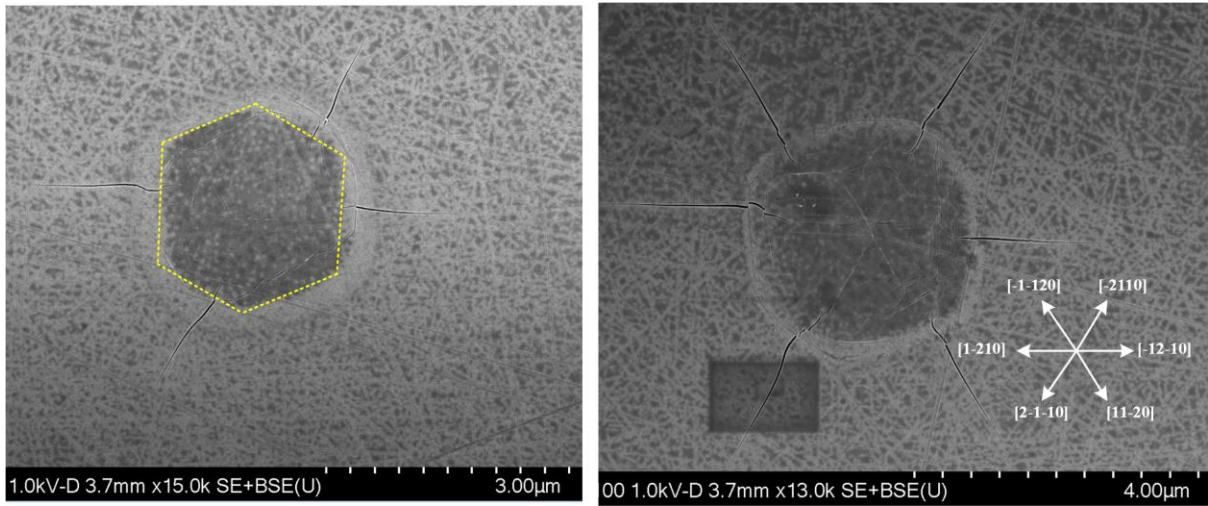
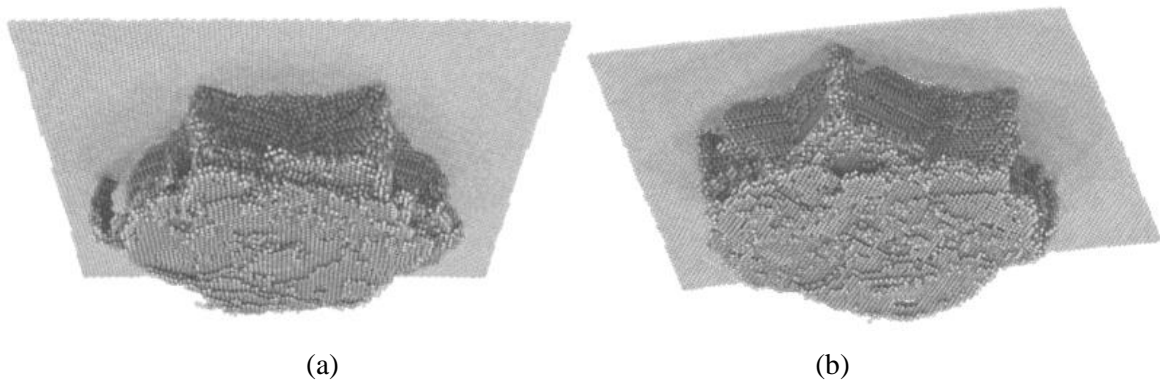


Figure 5-3. Surface morphology of Si face of 6H-SiC wafer after indentation at the load of 200 mN (left) and 300 mN (right).

Different from experiments, MD simulation can not only obtain the forces in the machining, but also analyse the subsurface morphology and crystal defects occurring during the process, which are comparatively difficult to study through experiments.

The DXA was used to investigate the evolution of materials in the indentations, which could identify the dislocations, determine their Burgers vectors, and output a line representation of the dislocation defects. Figure 5-4 shows the amorphous atoms of SiC after indentations, and it is clear that there are similar structures appearing in the subsurface for all cases. In addition, it is easy to find that there are more schistose structures along the (0001) plane at the bottom of the amorphous areas for the C face than for the Si face, which means the C face is more prone to slip.



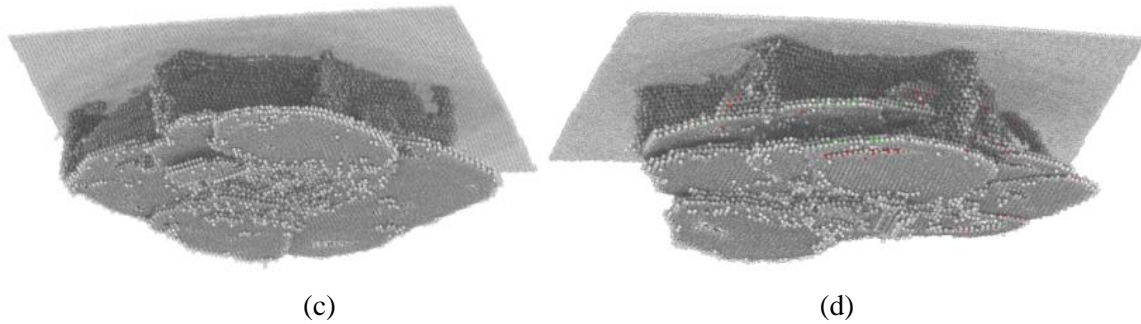


Figure 5-4. Upward views of subsurface deformation obtained using the DXA. (a) Si face of 4H-SiC (b) Si face of 6H-SiC (c) C face of 4H-SiC (d) C face of 6H-SiC.

Figure 5-5 shows the vertical cross-sectional views of the deformed specimens at the indentation depth of 4 nm by the DXA. The depths of the amorphous layers of the Si face and the C face of 4H-SiC were 7.3 nm and 7.7 nm (represented by white atoms in Figures 5-5 (a) and (c)), while those of the Si face and the C face of 6H-SiC were 7.2 nm and 8.0 nm (represented by white atoms in Figures 5-5 (b) and (d)). It is clear that compared with the Si face, there were 5% ~ 10 % thicker amorphous layers after indentations for the C face for both 4H-SiC and 6H-SiC. In other words, there is a deeper subsurface damage layer for the C face than for the Si face after indentations. However, there is no significant difference between 4H-SiC and 6H-SiC.

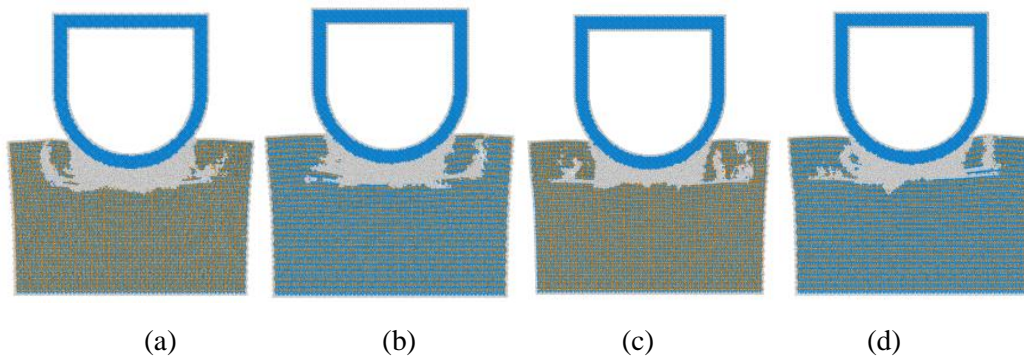


Figure 5-5. Vertical cross-section morphology after indentation. (a) Si face of 4H-SiC (b) Si face of 6H-SiC (c) C face of 4H-SiC (d) C face of 6H-SiC.

Figure 5-6 shows the horizontal views of the SiC surfaces after indentation. There are some clear patterns in all cases, which are very similar to the SEM figure obtained in the indentation experiment (Figure 5-3). Although there are no cracks found in this small area, the lines consisting by atoms in white colour are along the $\langle 1-210 \rangle$ direction as well, which

will be discussed in Section 5.3. The agreement between experimental and simulated results also verifies that the MD simulation models and methods used in this research are reliable.

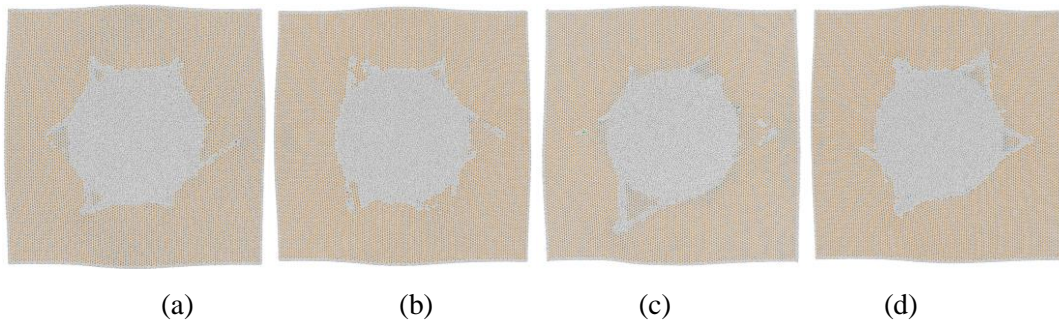


Figure 5-6 Horizontal morphology after indentation. (a) Si face of 4H-SiC (b) Si face of 6H-SiC (c) C face of 4H-SiC (d) C face of 6H-SiC.

5.3 Defect formation and evolution

The hexagonal patterns found in both experiments and MD simulations are further analysed in this section in order to clarify the defect mechanism.

The horizontal cross-sectional views using different slice depths using the DXA are shown in Figures 5-7 to 5-10. In other words, these pictures show the formation process of the amorphous atoms. It is easy to find that the amorphous regions of the Si face are more regular than those of the C face during the appearance of the hexagonal patterns for both 4H-SiC and 6H-SiC. And there are more dislocation loops, which results in the release of residual stress, formed on the (0001) basal plane of the C face than of the Si face. This explains that the indentation forces of the C face are less than those of the Si face in the load-displacement curves (Figure 5-2) when displacement of the indenter reaches 4 nm.

The formation process of the hexagonal pattern occurring in the Si face of 6H-SiC is almost the same as the patterns occurring in other three cases. Therefore, the Si face of 6H-SiC is selected as an example to explain the formation process of these patterns. There are hardly any amorphous atoms (represented by white atoms) at the depth of 7.6 nm (Figure 5-7 (a)), and the layered structures are destroyed along the horizontal direction. Amorphous atoms are beginning to increase at the depth of 6.6 nm (Figure 5-7 (b)) and show a triangle pattern when the depth reaches 6.2 nm (Figure 5-7 (c)). It is worth noting that a symmetrical triangle outline can be seen vaguely at the depth of 6.0 nm (Figure 5-7 (d)), in which region the

amorphous atoms was formed at the depth of 5.7 nm (Figure 5-7 (e)). Then, the region of the amorphous atoms has gradually formed a hexagonal pattern mentioned earlier, as shown in Figures 5-7 (g) and (h). Hence, it is clear that the hexagonal patterns are composed of two symmetrical triangles in these simulations, which may be related to slip systems of the crystal structures of 4H-SiC and 6H-SiC. In addition, the hexagonal patterns on the Si face and C face are similar. And the major difference is that there are more dislocation loops in the subsurface of C face, which confirms that the C face is more prone to slip along the (0001) plane as analysed in Section 5.2.

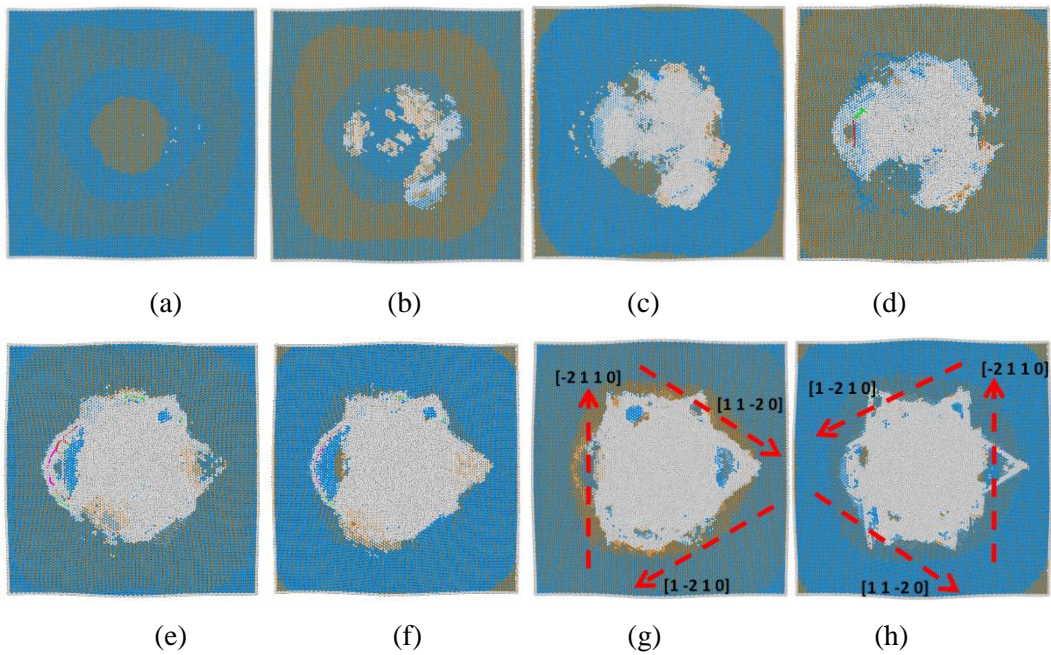
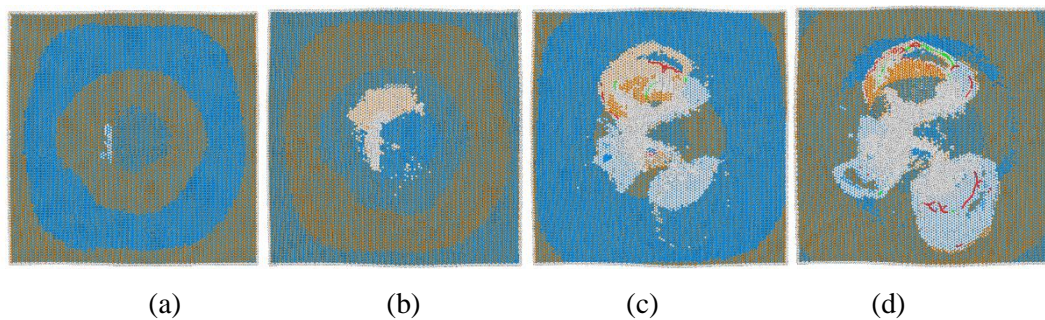


Figure 5-7. Horizontal cross-sections using different slice depths for the Si face of 6H-SiC. (a) 7.6 nm, (b) 6.6 nm, (c) 6.2 nm, (d) 6.0 nm, (e) 5.7 nm, (f) 5.5 nm, (g) 5.0 nm, (h) 4.0 nm.



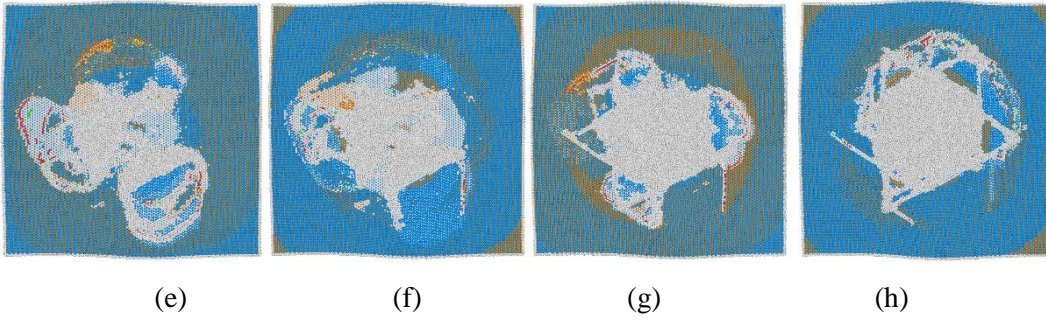


Figure 5-8. Horizontal cross-sections using different slice depths for the C face of 6H-SiC. (a) 7.6 nm, (b) 6.6 nm, (c) 6.2 nm, (d) 6.0 nm, (e) 5.7 nm, (f) 5.5 nm, (g) 5.0 nm, (h) 4.0 nm.

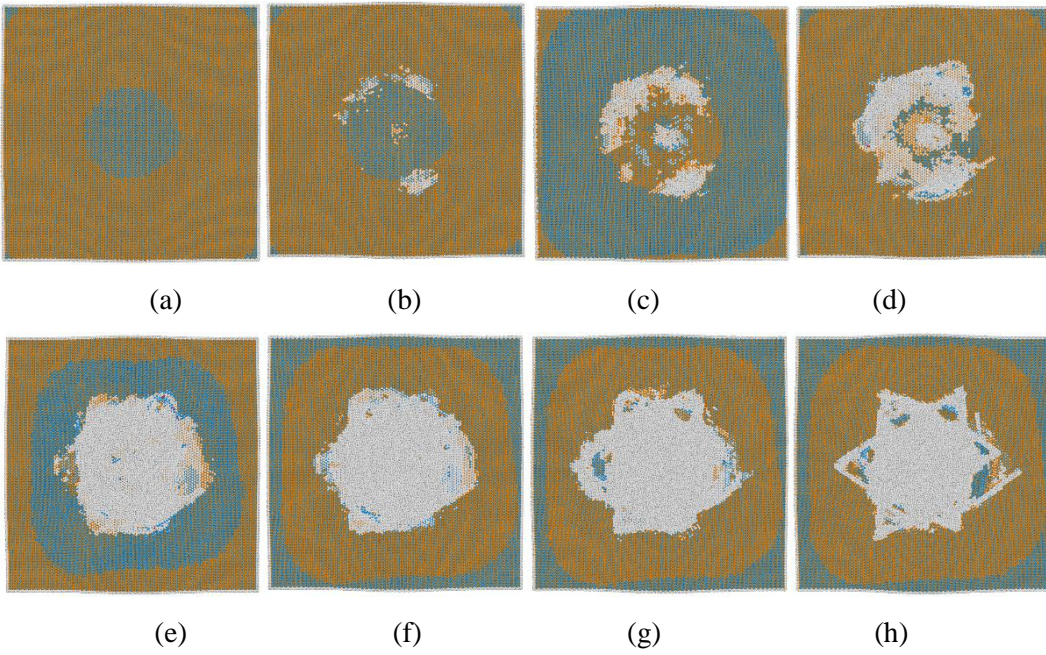
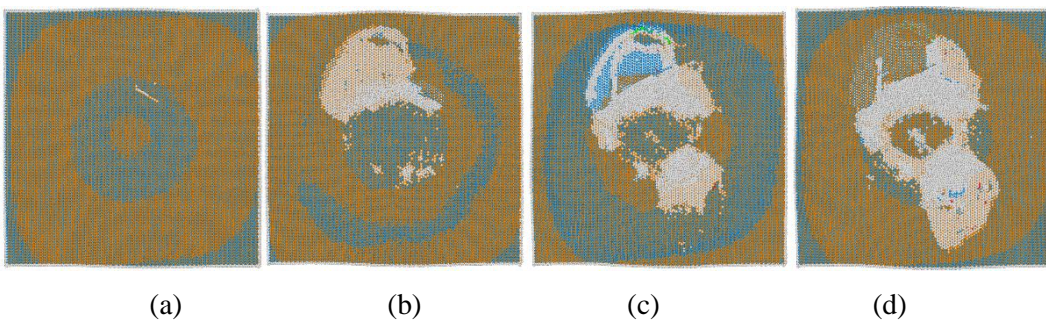


Figure 5-9. Horizontal cross-sections using different slice depths for the Si face of 4H-SiC. (a) 7.6 nm, (b) 6.6 nm, (c) 6.2 nm, (d) 6.0 nm, (e) 5.7 nm, (f) 5.5 nm, (g) 5.0 nm, (h) 4.0 nm.



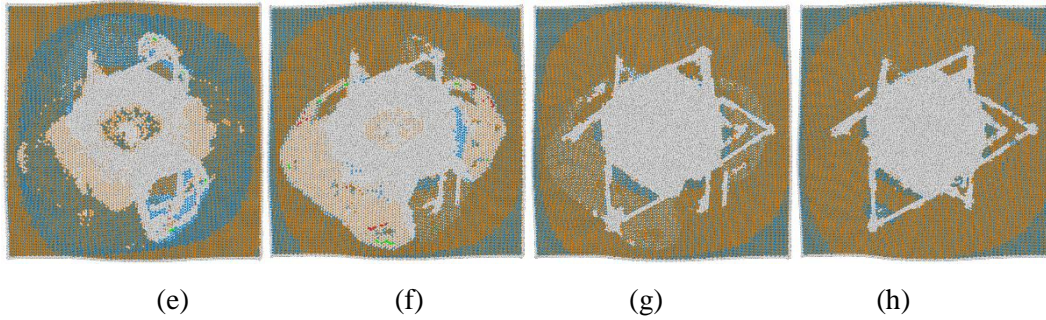


Figure 5-10. Horizontal cross-sections using different slice depths for the C face of 4H-SiC. (a) 7.6 nm, (b) 6.6 nm, (c) 6.2 nm, (d) 6.0 nm, (e) 5.7 nm, (f) 5.5 nm, (g) 5.0 nm, (h) 4.0 nm.

As reported by Kiely [128], triangular and quadrangular patterns appeared during indentation on different planes of Au, and they believed that this was related to the slip systems [31-35]. It is generally agreed that slip systems for HCP crystal structure mainly consists of the (0001) $\langle 11-20 \rangle$ basal slip, the (10-10) $\langle 11-20 \rangle$ prismatic slip, the (10-11) $\langle 11-20 \rangle$ and the (10-12) $\langle 11-23 \rangle$ pyramidal slip [33]. The ideal stacking value of the HCP structure is 1.633, and the atomic density of these pyramidal planes are close to the basal plane and may also slip when the c/a ratio (according to Table 2-1) is less than 1.633. On the contrary, the slip mainly takes place on the basal plane if c/a ratio is greater than 1.633 [33, 129]. Both Si face and C face of 4H-SiC and 6H-SiC have complicated Wurtzite diamond structures which belong to hexagonal crystal systems [63]. And the c/a ratio values of them are 3.3 and 4.9, which are much greater than the ideal stacking value. Therefore, the dislocation of 4H-SiC and 6H-SiC is more likely to take place on the basal plane slip.

The dislocation and slip occur simultaneously along these three directions when the indenter is pressed vertical to the basal plane, resulting in the triangular pattern as shown in Figure 5-7 (c). However, different from materials with general HCP structure, 4H-SiC and 6H-SiC both have central symmetry structure. This leads to the appearance of a triangle amorphous region (Fig. Figure 5-7 (f)) which is centrally symmetric with the one before, and these two triangle regions form the hexagonal pattern. Hence, such a conclusion is obtained that the hexagonal amorphous patterns appearing in the indentation simulation may be caused by the slip system of 4H-SiC and 6H-SiC.

5.4 Potential function comparison

As mentioned in Section 3.1.2, an appropriate potential function is a key factor affecting the accuracy and reliability of the MD simulations. In this research, the Tersoff potential is adopted to describe the interaction of SiC. However, there are several versions of Tersoff parameters for SiC. In this section, some versions of Tersoff parameters were compared. Table 5-1 shows the five groups of parameters adopted in the indentation simulations on the Si face of 6H-SiC.

Table 5-1. Groups of parameter files.

Group	Parameter file
<i>A</i>	SiC.tersoff [107]
<i>B</i>	SiC_1994.tersoff [130]
<i>C</i>	SiC_Erhart-Albe.tersoff [131]
<i>D</i>	SiC.tersoff.zbl [132]
<i>E</i>	Morse potential and SiC.tersoff [63, 107]

Figure 5-11 compares the force curves of five indentation cases using the different potential parameters. It can be seen that the forces curves in all five cases show the similar trends. There is no significant difference before the indentation depth reaches 2 nm and only a few disparities in later stages.

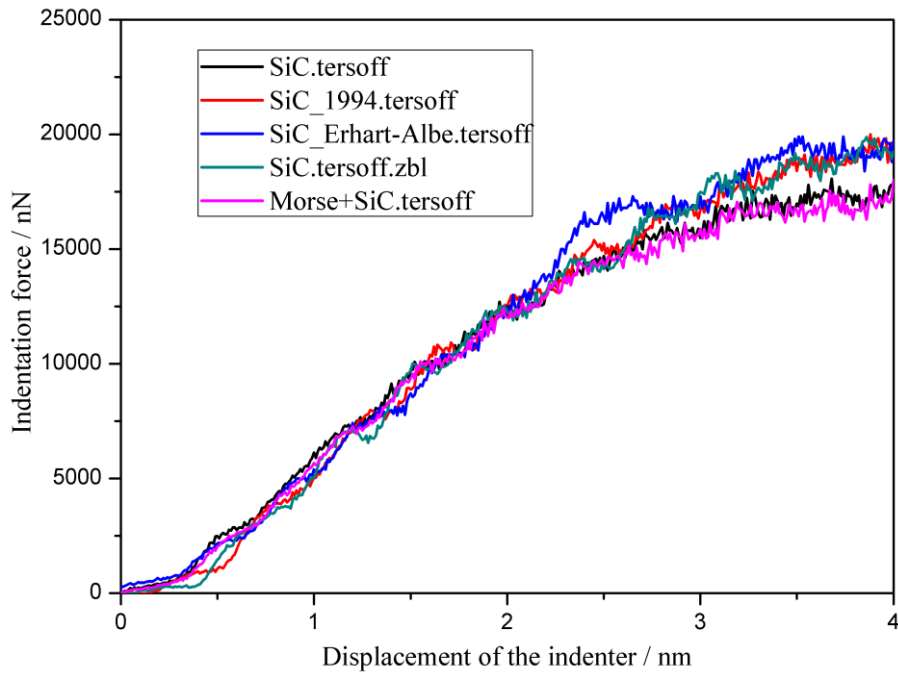


Figure 5-11. Load-displacement curves obtained using the different potential parameters.

In addition, as shown in Figures 5-12 and 5-13, the surface and subsurface morphology after indentation were compared using the DXA. The hexagonal indentation mark in group B is obvious, but the dislocation lines are not easy to observe. The results of group C show more lines but less amorphous atoms. By and large, all cases show the hexagon pattern and dislocation lines in subsurface though each group has its own characteristics. The agreement between experimental and simulated results also verifies that the MD simulation models and methods used in this research are reliable. The potential parameters of group A (SiC.tersoff [107]) are selected in this research.

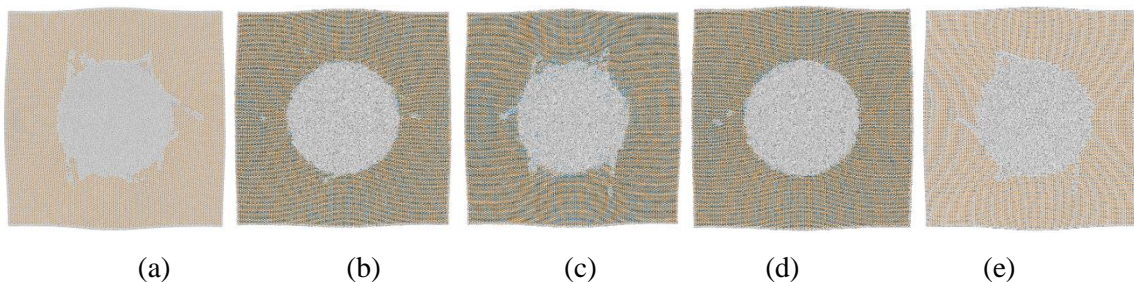


Figure 5-12. Horizontal morphology after indentation. (a) Group A, (b) Group B, (c) Group C, (d) Group D, (e) Group E.

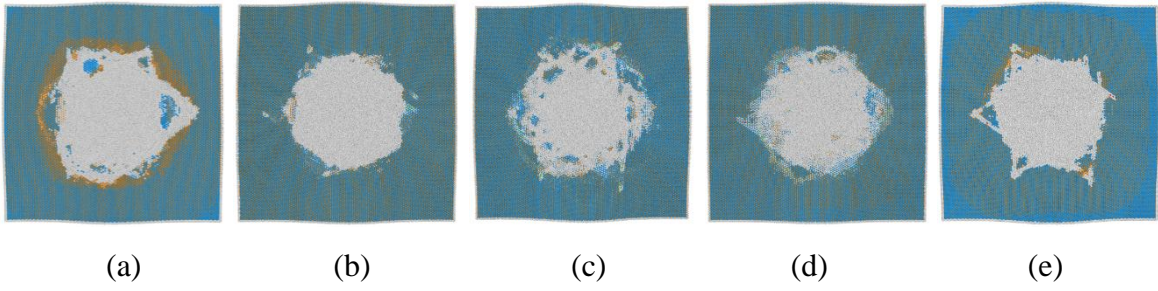


Figure 5-13. Horizontal cross-section view of subsurface morphology after indentation. (a) Group A, (b) Group B, (c) Group C, (d) Group D, (e) Group E.

Chapter 6. Nanoscratching tests and simulations

In order to study the different nanomechanical properties of the C face and the Si face of 4H-SiC and 6H-SiC, the MD schemes were constructed by using the LAMMPS, in which the following factors were taken into account.

6.1 Scratching forces

The verification of MD simulation has always been a key challenge regarding its accuracy and reliability. The MD model used in this paper was experimentally verified by indentation previously. Therefore, the MD model provided a reliable trend projection. Further in this chapter, the MD model is also verified in terms of forces and material removal rates.

Due to the limitation of scratching scales in experiments and MD simulations, it is difficult and unreliable to compare the results directly. Therefore, a specific force defined as force/depth is adopted to compare the results from the MD simulations and scratching experiments, as shown in Figure 6-1. For MD simulations in this research, the scratching depth is set as a constant of different values (e.g., 0.5 nm, 1 nm, 2 nm, and 3 nm), and the average tangential and normal forces on the scratching tip taken from the stable scratching stages are at the micron-Newton level.

For the scratching experiments, the scratching load is set as a constant (4 mN), and the average gouge depth obtained from the stable scratching stages is approximately 50 nm, which is much larger than the gouge depth presented in the MD simulation results in Figures 6-1 (a) and (b). The specific force provides a common platform for the comparison of the results from simulations and experiments.

Interestingly, in Figure 6-1 (a) and (b), the simulation revealed the following results for each scratching depth between 0.5 and 3 nm: 1) the highest specific force value was recorded on the Si face of 4H-SiC, followed by the C face of 4H-SiC and the Si face of 6H-SiC; 2) the C face of 6H-SiC had the lowest specific force value. The experimental results in Figure 6-1 (c) show the same trend. Thus, it can be concluded that the specific scratching force on the C faces are lower than those on the Si faces, and the specific forces on 4H-SiC are greater than

those on 6H-SiC. Even though the values of the ratios are significantly different due to the differences in tip sizes (5 nm in MD simulations and 3 μm in experiments) and scratching size scales, this trend is consistent with the experimental results. The specific forces decrease with the increase of scratching depth as shown in Figure 6-1 (a) and (b). This phenomenon, known as the size-effect, commonly occurs in abrasive machining processes [133, 134].

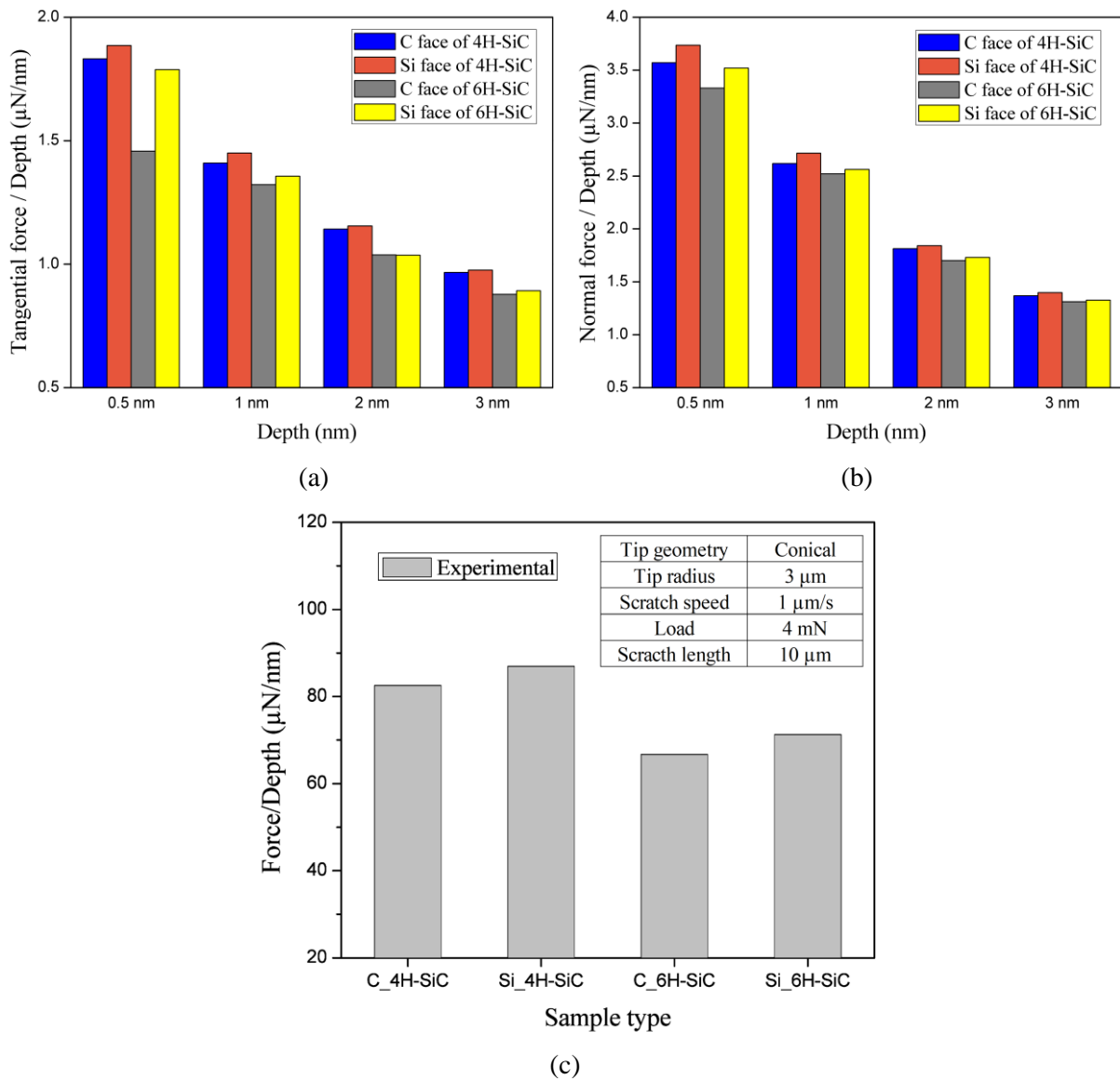


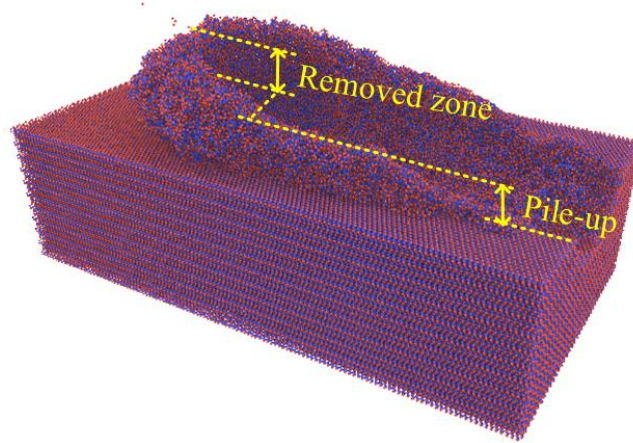
Figure 6-1. Comparison of specific scratching forces in MD simulations and experiments. (a) Tangential specific force of MD simulations. (b) Normal specific force of MD simulations. (c) Specific force of scratching experiments.

6.2 Material remove efficiency

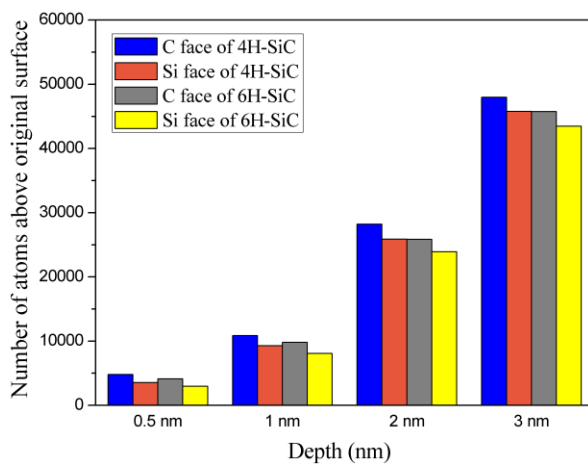
Owing to current computing capacity, most MD simulations only analyse nanoscale mechanisms and phenomena and rarely extend to the actual machining scale. Additionally, the potential functions used in MD analysis only partially represent material performance under particular space scale and environmental conditions. Even so, MD analysis could provide sufficient information of material behaviours that match the tendency illustrated in experiments.

MRR is an important measure for evaluating the efficiency of various machining processes. Material removal is an important measure to assess the scratching efficiency of MD simulation analysis. Atom displacement — which refers to the atoms that move above the workpiece surface after the scratching tip passes — is often used to represent scratching performance. However, the grit-workpiece interaction area in Figure 6-2 (a) shows ridges of bulged atoms that form on either side of the scratching path as a result of the “ploughing” action. These bulged atoms do not leave the workpiece, so they should not be included with the removed material. Only those atoms whose positions are higher than the ploughing ridge height can be defined as potentially removed atoms. Figures 6-2 (b) and (c) provide the number of removed and displaced atoms from various scratching tests. It can be seen that the number of atoms above the original workpiece surface is significantly greater than the number of potentially removed atoms.

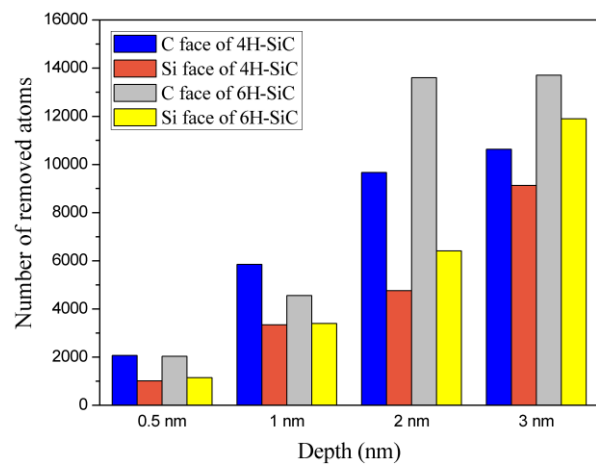
For the results of cut depths ranging from 0.5 to 3 nm, the C face shows more atom removal than the Si face. In the experimental results of reference [27], the MRR on the C face of 6H-SiC reached 13.94 nm/min, which was twice the MRR observed on the Si face (6.13 nm/min). Although the simulated and experimental material removal performances were not directly comparable due to differences in scale, both results suggest that the C face exhibits significantly higher material removal efficiency than the Si face.



(a)



(b)



(c)

Figure 6-2. Scratching and ploughing actions in all scratching simulations. (a) Atom removal definition in a scratching. (b) Number of atoms above original surface. (c) Number of removed atoms.

6.3 Amorphisation

Ductile-regime machining at the nanoscale can be achieved by the combination of dislocation activities and structural transformation [36]. This structural transformation can be considered as non-crystallization. Figures 6-3 to 6-6 show sectional views of the MD simulations. The white dots represent atoms with amorphous structures, while the blue and orange dots indicate atoms with a standard lattice structure, representing cubic diamond structures and hexagonal diamond structures, respectively. DXA also can identify dislocations, calculate the Burgers vectors and then display them as dislocation lines in OVITO.

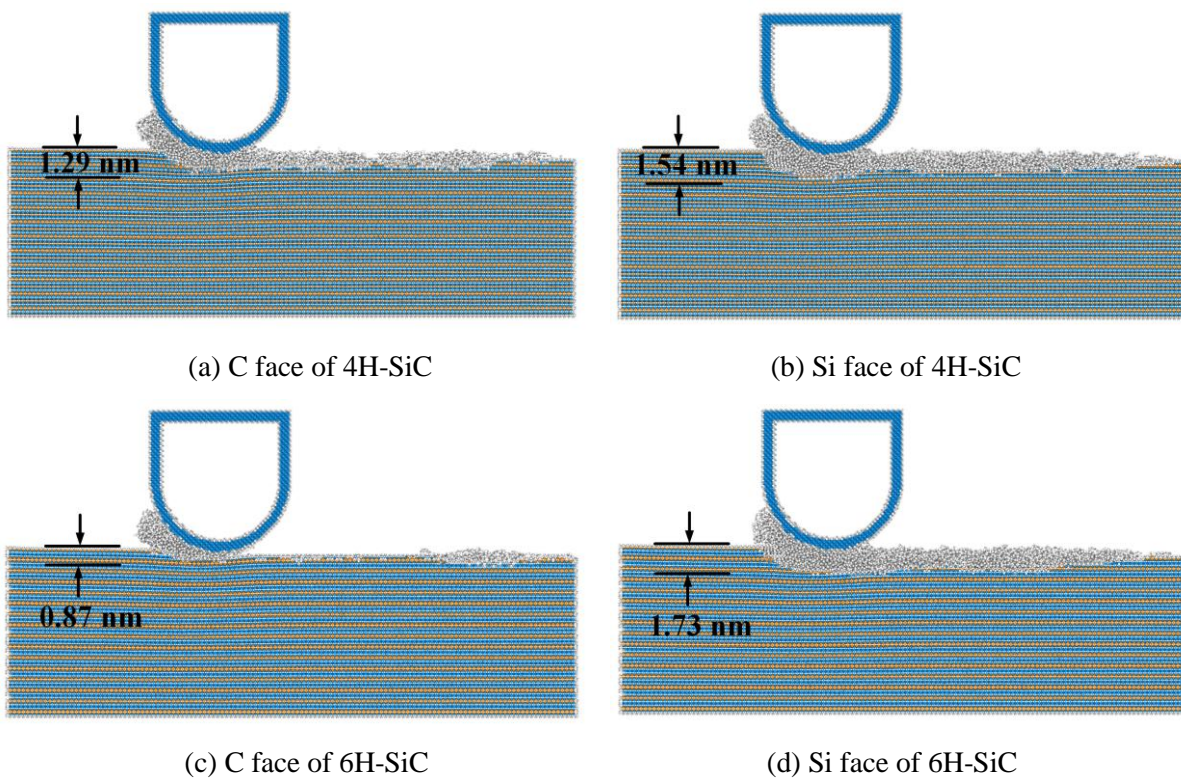


Figure 6-3. Sectional views of scratching at 0.5 nm obtained by DXA.

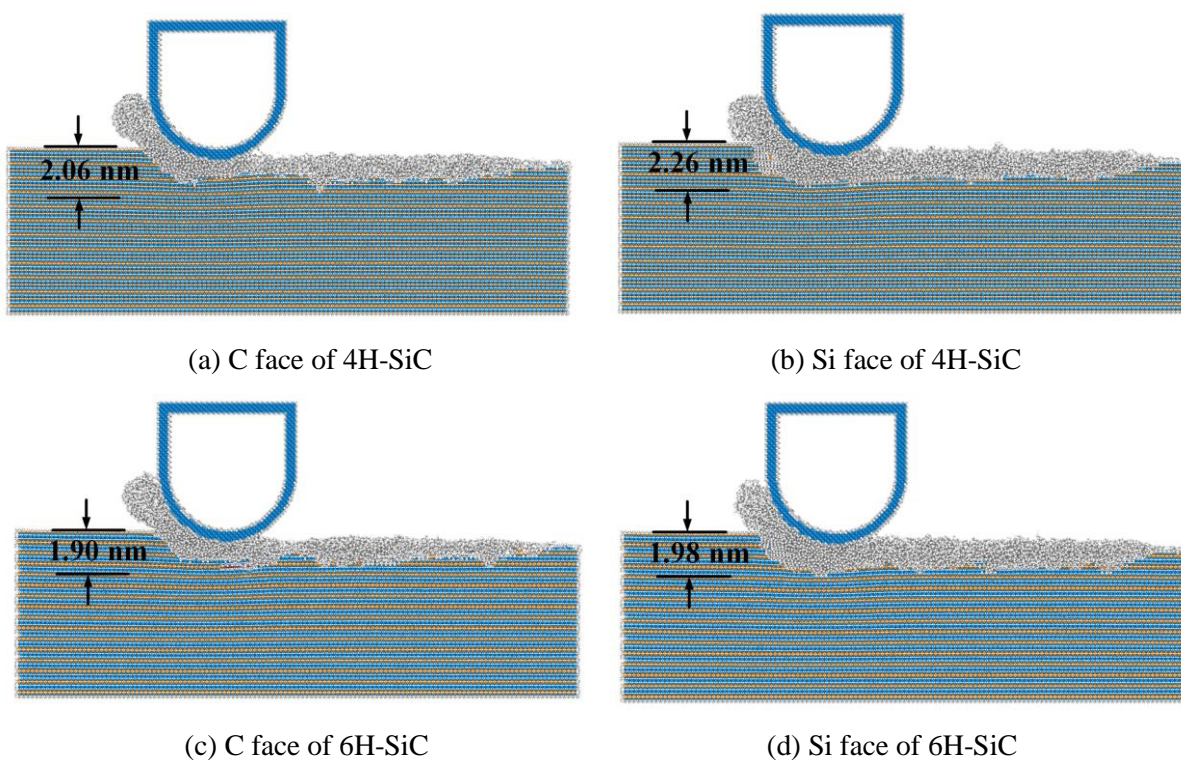


Figure 6-4. Sectional views of scratching at 1 nm obtained by DXA.

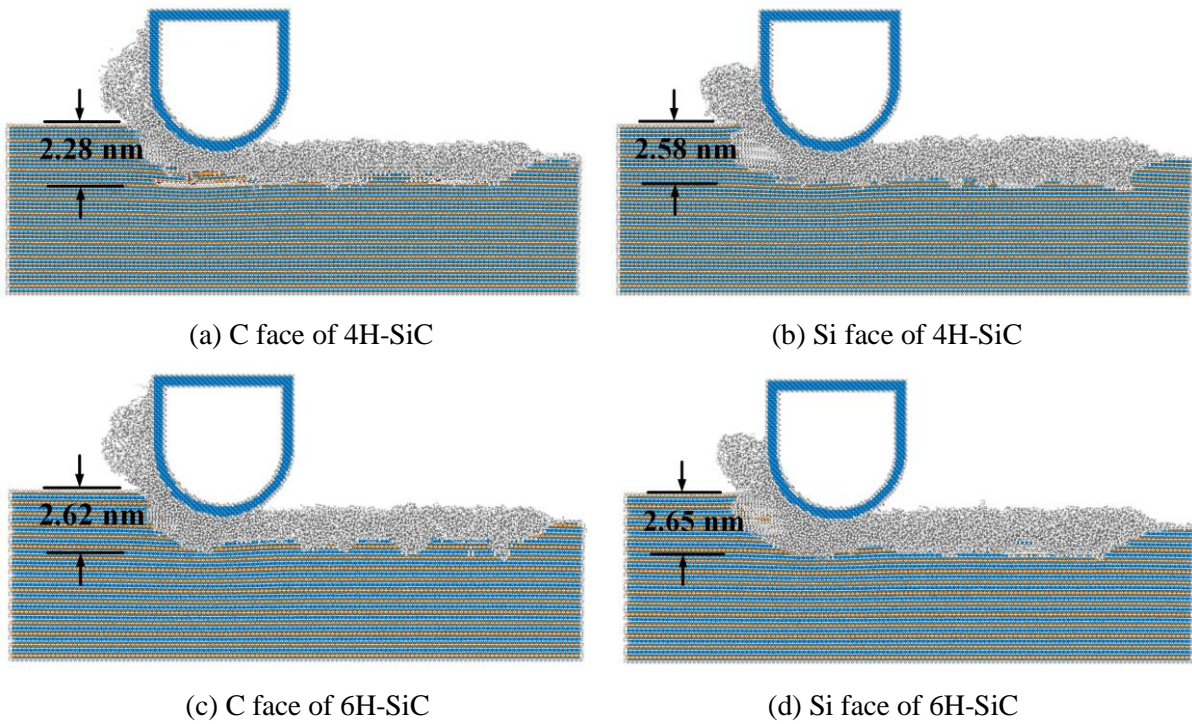


Figure 6-5. Sectional views of scratching at 2 nm obtained by DXA.

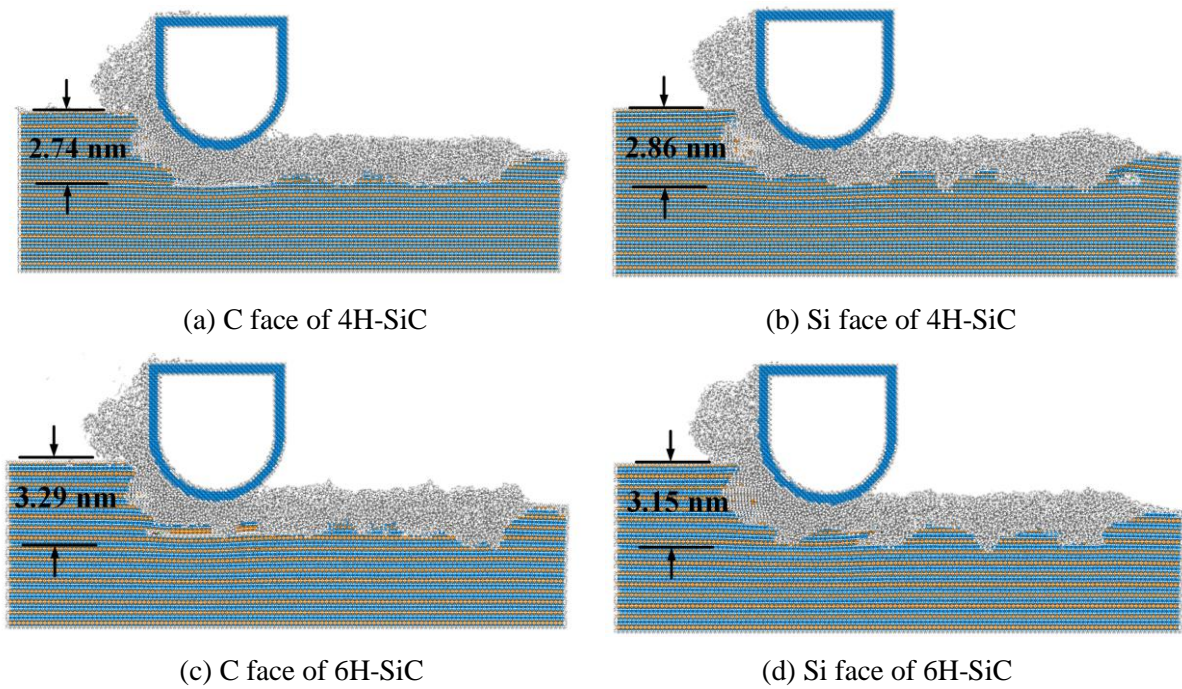


Figure 6-6. Sectional views of scratching at 3 nm obtained by DXA.

6H-SiC primarily underwent an amorphous transformation that could be considered plastic deformation [63]. Amorphous atoms are disordered atoms that have lost their regular lattice crystal structures as a result of scratching. Therefore, the amorphous atoms are considered as

subsurface defects, which affect the properties of the material. All four structure cases had similar maximum depths of subsurface amorphous deformation. For both the 4H-SiC and 6H-SiC samples, the subsurface amorphous layers of C faces were relatively flat, while the Si faces developed uneven layers.

Undoubtedly, the amount of chips that accumulate in front of the scratching tip and subsurface damage increase as the scratch depth increases. When the scratch depth is small, the subsurface damage layer is shallow and relatively flat. When the scratch depth increases, the subsurface damage layer becomes thicker and uneven. It is interesting to note that the thicknesses of the amorphous deformations on the C face are less than those on the Si face. For example, at a scratch depth of 0.5 nm (Figure 6-3), the maximum thickness of the amorphous deformation on the C face of 6H-SiC is only 0.87 nm, while that of the Si face reaches 1.73 nm. 6H-SiC shows thicker amorphous deformation than 4H-SiC at scratching depths over 2 nm.

The number of amorphous atoms in four cases was counted, as shown in Figure 6-7. Interestingly, the C face shows fewer amorphous atoms than the Si face for both 4H-SiC and 6H-SiC. This means that the C face has less subsurface amorphous deformation and superior subsurface quality than the Si face under the same machining conditions, which is consistent with Lu's experimental conclusion [27].

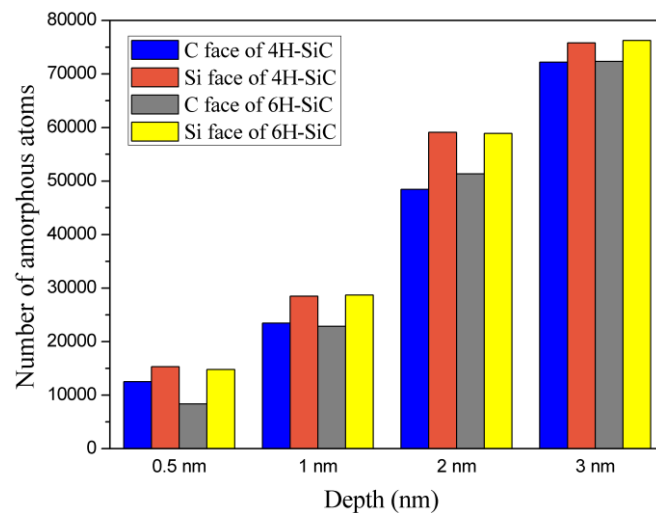


Figure 6-7. Numbers of amorphous atoms in the subsurface of all scratching simulations.

6.4 Dislocation analysis

In addition to amorphous atoms, the aforementioned DXA can also identify atom dislocations that are a type of material deformation. In the analysis of DXA, atom dislocations refer to those atom movements with regular lattice structures [122]. In the DXA results, there were two main types of dislocations found in the subsurface of both 4H-SiC and 6H-SiC, along $1/3\langle 1-210 \rangle$ and $1/3\langle 1-100 \rangle$. Figure 6-8 shows the number of dislocations that occurred in the subsurface of all the investigated cases. No dislocations developed at a scratch depth of 0.5 nm. The greater the scratch depth, the greater the number of dislocations. In particular, the C face can have up to twice as many dislocations as the Si face.

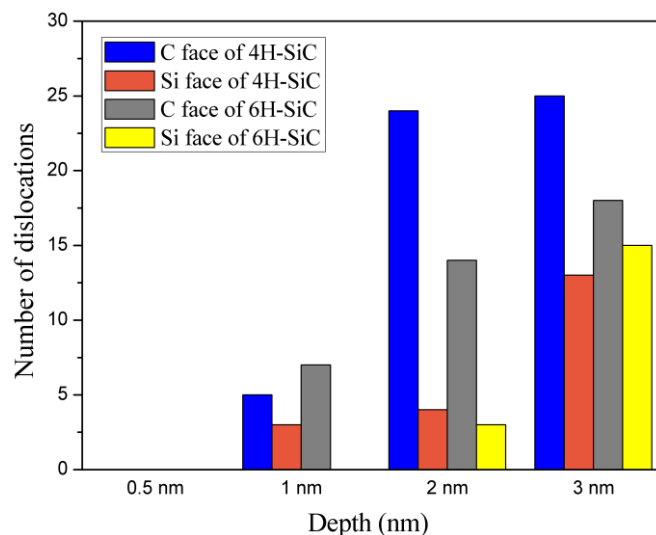


Figure 6-8. Numbers of dislocations in the subsurface of all scratching simulations.

Here, the scratching simulations on the C and Si faces of 6H-SiC were selected as the example to investigate dislocation formation. Figure 6-9 (a) shows the subsurface morphology of deformation using DXA. It can be seen that dislocations mainly occur on the (0001) basal plane and the (10-10) plane. The dislocations obtained in the MD simulation of Wu [63] principally occur on the (0001) and (11-22) planes. This difference may result from the MD model set-up. Wu [63] applied 2.58 nm scratches in the y-direction, which is too thin to detect dislocations on the planes perpendicular to the y-axis. The Von Mises stress distribution of 6H-SiC during scratching is shown in Figure 6-10. It can be seen that the stress concentration area is mainly located on the (0001) plane and (10-10) plane under the diamond tip. Dislocations are normally considered to be caused by the stress concentration

during the scratching process, so stress distributions of the C face and Si face were analysed. Figures 6-11 (a) and (b) show the changes of Von Mises stress in the local area before and after the dislocations occurred on the C face and Si face. The stress peaks shown in the figures may represent the occurrence of the dislocations. The stress peaks of dislocations on the C face (3148 MPa for the (0001) plane and 3972 MPa for the (10-10) plane) are lower than those on the Si face (3816 MPa for the (0001) plane and 4584 MPa for the (10-10) plane), which means that the C face is more prone to dislocations than the Si face under the same scratching conditions.

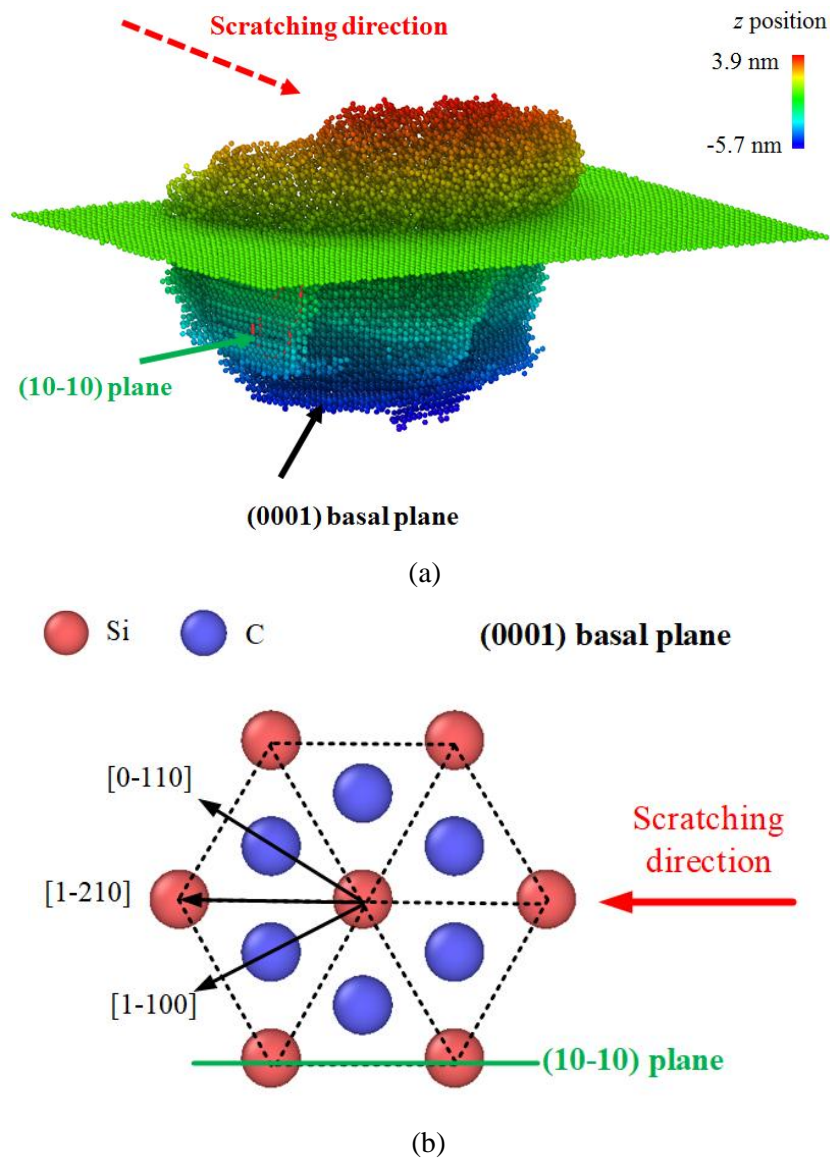


Figure 6-9. Deformation in the subsurface of a scratching and SiC basal plane view. (a) Subsurface morphology of deformation. (b) Schematic diagram of crystal.

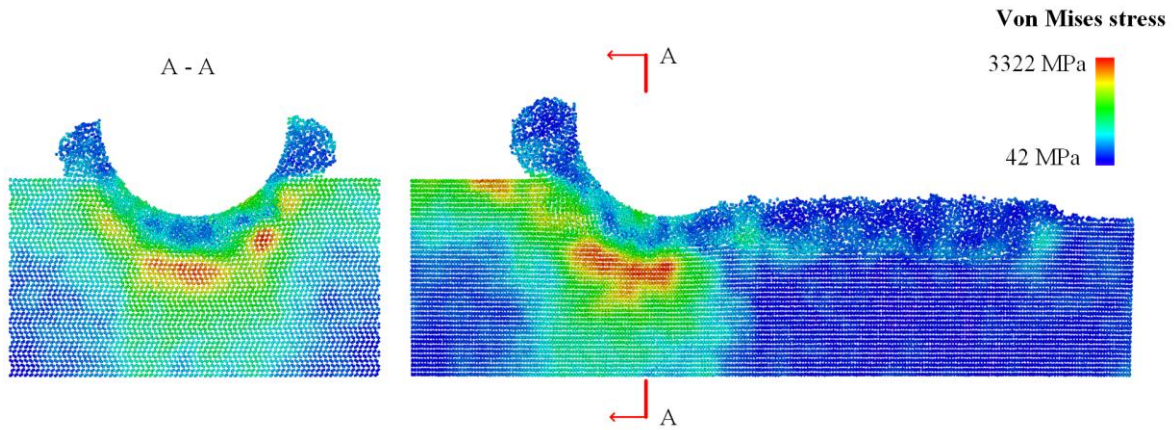


Figure 6-10. Von Mises stress distribution of 6H-SiC during scratching.

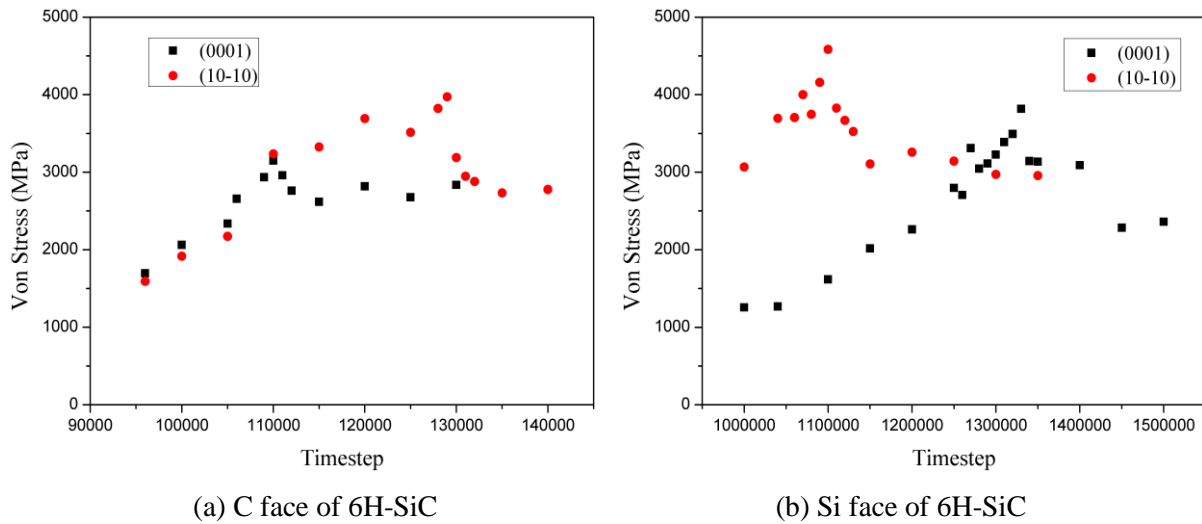


Figure 6-11. Von Mises stresses of in the scratching of 6H-SiC at different time steps.

Considering the occurrence of dislocations on the C and Si faces, the critical stress of dislocations on the (10-10) plane is higher than that on the basal plane. The dislocations on the (10-10) plane of the C face occurred later than those on the basal plane, while dislocations on the basal plane occurred later on the Si face. All of these dislocations eventually led to slips along the scratching direction. Dislocations and slips on the basal plane may contribute to material removal and improve subsurface quality, while those on the (10-10) plane could cause severe subsurface layer cracks. This explains why the amorphous structures of the Si face are uneven and the amorphous structures of the C face are smoother as mentioned previously.

As shown in Figure 6-12, a moving average with 30 data spans (equivalent to 0.3 nm) was applied to filter high-frequency noise from the force data of 6H-SiC at a scratching depth of 3 nm. The forces on the C face and Si face show similar fluctuation frequency ranging from 31.3 to 51.3 GHz (ΔL from 1.91 to 3.19 nm, and ΔT from 19.1 to 31.9 ps). In particular, the trends of both faces were almost identical before the stable scratching stage. The force of the Si face fluctuated while that of C face remained stable. Such a phenomenon may indicate that dislocations easily occur on the C face during scratching, which released stress fluctuation in the subsurface. In this way, the scratching force on the C face is lower and more stable than that on the Si face, and fewer amorphous atoms occurred in the subsurface, as shown in figure 10. A higher number of dislocations leads to a lower scratching force.

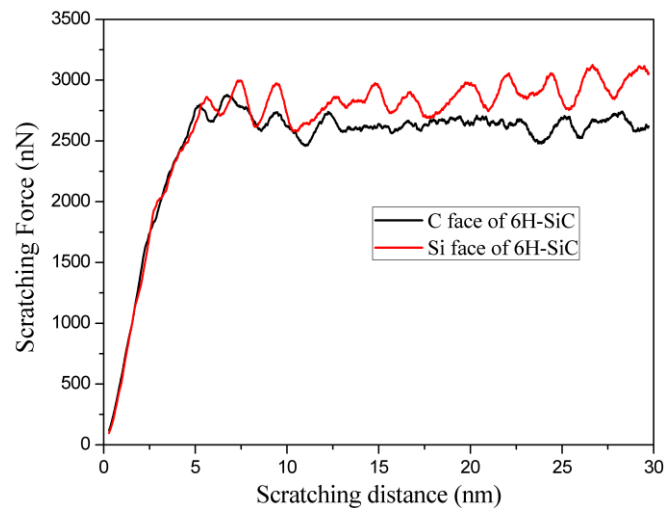


Figure 6-12. Forces of C face and Si face of 6H-SiC obtained by moving average at the scratching depth of 3 nm.

6.5 Materials removal and surface deformation mechanism

For brittle materials, the subsurface damage generated after micro-scale processing was considered to be amorphous layer, pulverization layer and cracked [36, 40]. Brittleness and plasticity behaviours of the subsurface layer are controversial in nanoscale processing. As previously mentioned, dislocations do not occur unless the scratching depth exceeds the critical level. The initial contact between the scratch tip and the SiC sample also plays a crucial role in material removal. As analysed in Section 5.3, Figures 5-7 to 5-10 show that amorphous atoms appeared in the subsurface layer, and dislocations and slippage occurred at a few nanometres level of engagement. The hexagonal patterns are composed of two triangles

facing opposite directions. The double triangular patterns on the Si face can reach depths of 6.0 and 6.2 nm below the original surface after indentation at a depth of 4 nm. However, this phenomenon was not obvious on the C face. The subsurface of the C face appears more like amorphous flake structures, which are related to the dislocations on the (0001) basal plane. Thus, the C face is more prone to dislocations and slippage on the (0001) basal plane.

Figure 6-13 is a cross-sectional view of the 6H-SiC-scratched groove obtained using the DXA. The amorphous atom region appears as an inverted triangle with distinct steps. These steps are six atom layers of atoms high, which is the height of the 6H-SiC unit cell. Dislocations on the (0001) basal plane were found under the right side of the groove. These results are highly consistent with the results from Meng's experiments [36], as shown in Figure 6-14. Figure 6-14 (b) also shows several dislocations on the basal plane in the subsurface of the scratch groove. As shown in Figure 6-14 (d), the amorphous layer region is also an inverted triangle, and a similar step shape can be seen on the right side of the amorphous region. Thus, the step shapes that appeared in both the experiments and the simulations indicate that subsurface deformation gradually propagated downward during the scratching process. Additionally, the shape of groove is not symmetric in Figure 6-13, because the SiC material shows anisotropy in its crystal structure. As shown in Figure 2-1, the atomic arrangement of 6H-SiC is not symmetric, so the stress distribution (Figure 6-10) and subsurface deformation are not symmetric under the same forces on both sides of the groove. This asymmetric feature can also be seen in experimental results as in Figure 6-14 (d). In particular, stacking faults and stress concentration are more likely to occur at the layer of those integer multiples of the 6H-SiC unit cell height.

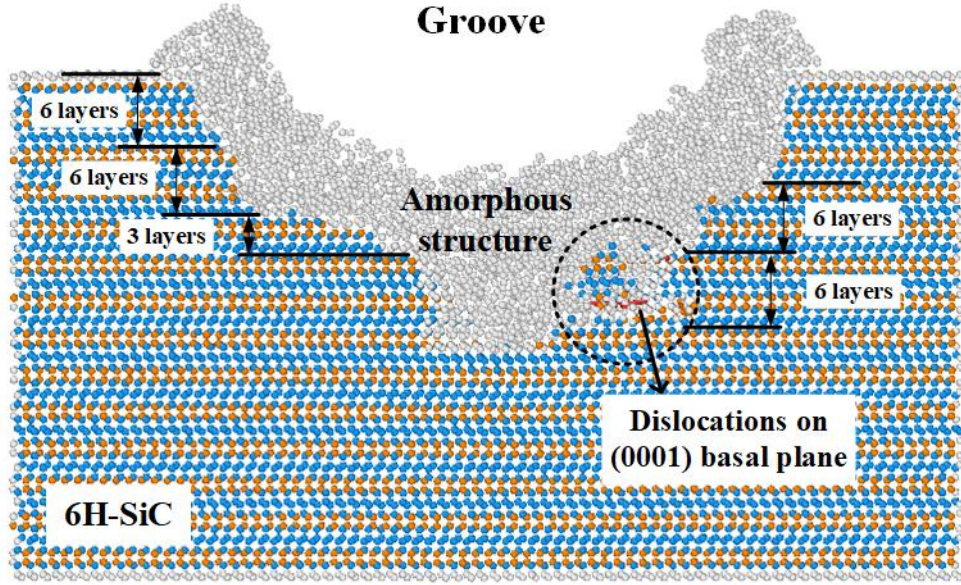


Figure 6-13. The cross-sectional subsurface image of 6H-SiC after scratching at the depth of 3 nm.

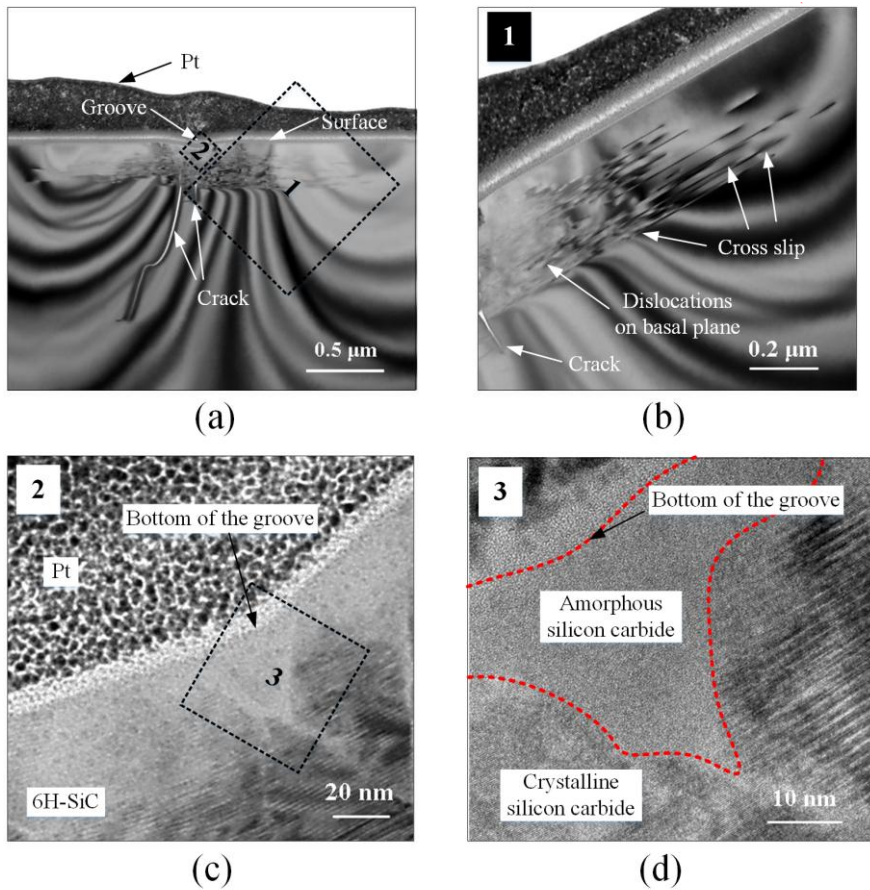


Figure 6-14. (a) Cross-sectional TEM image of 6H-SiC substrate after scratching test with 5 mN load by a tip with radius of 90 nm. (b) Magnified view of the regions indicated by circles 1 in a. (c) A bright-field TEM micrograph of the region at the bottom of the groove indicated by circles 2 in a. (d) A high-resolution TEM image of zone indicated by circle 3 in c. (after Meng, et al [36])

Although there were no obvious cracks, irreversible dislocations occurred in the nanoscale scratching. Due to local temperature and stress changes during processing, these dislocations potentially form micro-cracks. In nanoscale machining, amorphous deformation is a plastic deformation, and atom dislocation is an elastic deformation initiated regular slip or split. Such a slip or split could promote micro-cracks formation at the nanometre level or plastic deformation if the bonds do not break. Some of the dislocations that occurred during scratching can recover after the tip passes the deformation area. The slip and micro-cracks generated by the dislocations on the base plane are beneficial to the removal of the material, while the dislocations on the (10-10) plane generated along the scratch direction may cause deeper and more serious structural damage. The atoms that accumulated in front of the abrasive tip and at the ridges of the scratching path were of a disordered and amorphous structure, which appears to be plastic deformation.

Chapter 7. Effects of machining conditions

In order to study the different nanomechanical properties of the C face and the Si face of 4H-SiC and 6H-SiC, the MD schemes were constructed by using the LAMMPS, in which the following factors were taken into account.

7.1 Scratching performance in relation to SiC layer structure (1st-8th)

The arrangement of the atomic structure need be considered in the nanoscale machining, and setting machining parameters according to lattice structure is meaningful to control the material removal and improve surface quality. In this section, scratching simulations, setting scratching depth as an integral multiple of an atom layer, were carried out.

4H-SiC and 6H-SiC are hexagonal diamond structures [135], stacked cyclically in the manner of ABCB' and ABCA'C'B', respectively — these patterns are also referred to as layered structures. As analysed in Section 6.5, the dislocations on the (0001) basal plane have a positive contribution to material removal. Therefore, atom layer referenced scratching depths were selected in the simulations of 4H-SiC and 6H-SiC scratching processes to identify a potential beneficial strategy for improving material removal efficiency. The scratching depths were set as an integral multiple of an atom layer in order to explore the beneficial behaviour of atom dislocation. Figure 7-1 shows the atomic layout of 4H-SiC and 6H-SiC, and Table 3-3 shows the scratching depths according to the atomic layers used in this section.

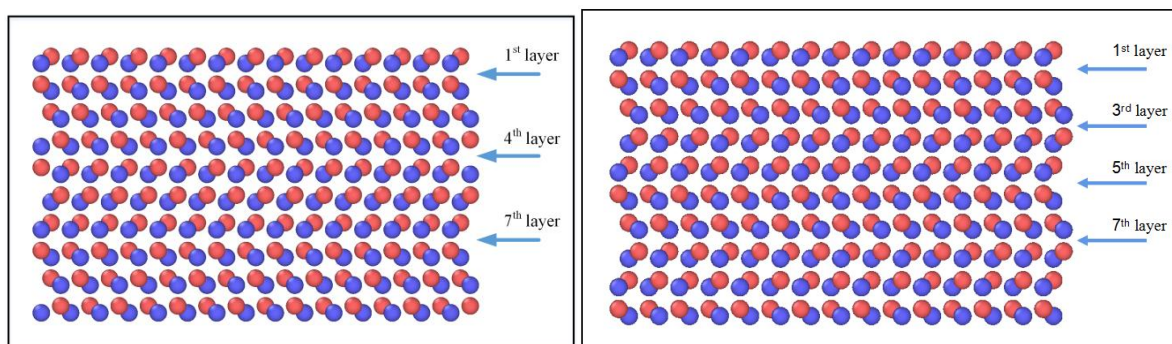


Figure 7-1. Atomic layout out 6H-SiC (left) and 4H-SiC (right).

Figure 7-2 shows the average forces obtained from the scratching stages in all cases. The forces become larger as more layers are removed.

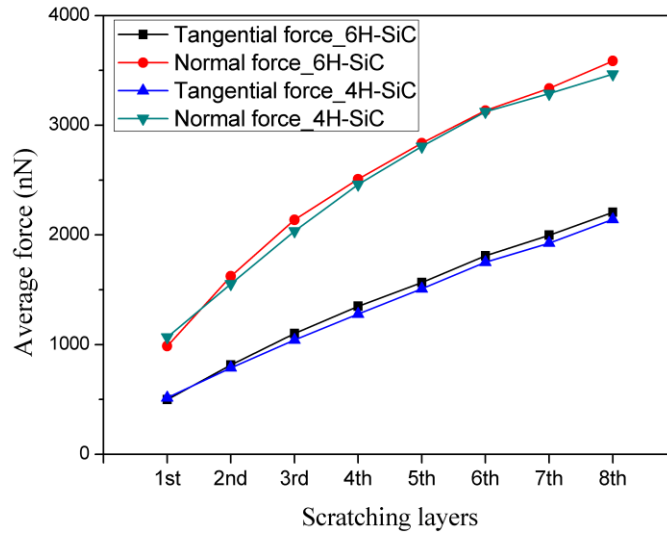


Figure 7-2. The average forces obtained from the scratching stages.

Figure 7-3 shows the DXA results of all cases and Figure 7-4 shows the maximum thicknesses of the subsurface amorphous deformation at different scratching depths. There is no doubt that the subsurface amorphous deformation becomes more severe as more layers are removed. However, it is interesting to note that for 6H-SiC, there was only a slight increase in the thickness of the subsurface amorphous deformation when the scratching depth changed from layer three to layer four. Furthermore, when the scratching depth reached 7 layers, the thickness of the subsurface amorphous deformation decreased. Figure 7-1 shows that the stacked structures of 6H-SiC between layers 6 and 7 flip their orientation from an arrow structure pointing left. Such a structural related plateau takes place every 3 layers. The fourth and seventh layers both correspond to the transition layer of 6H-SiC.

Similarly, for 4H-SiC, the crystal structure flips every 2 layers. When the scratching depths are three and five layers, the thickness of the amorphous deformation increases less than at layers four and six. When the scratching depth for 4H-SiC reached 7 layers, the thickness of the subsurface amorphous deformation decreased.

The above observed phenomena indicate that the subsurface amorphous deformation does not increase proportionally with SiC molecule layers. Therefore, taking a scratching depth at the SiC atom orientation transition layer could be a beneficial choice for removing materials and obtaining superior substrate subsurface quality. Such a strategy might also be used to investigate the machining of other materials with layered structures.

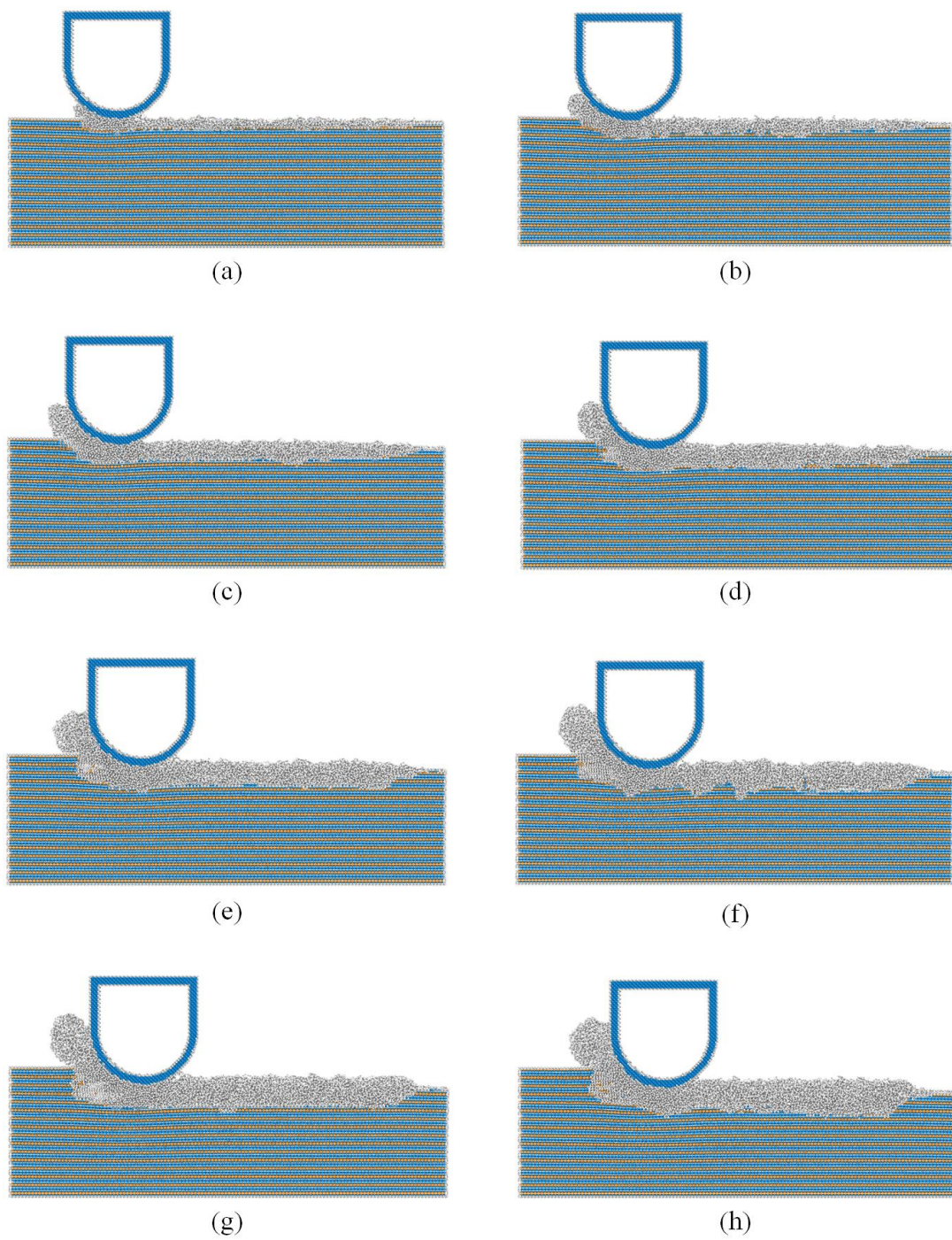


Figure 7-3. The DXA results from 1st to 8th layer scratching on 6H-SiC.

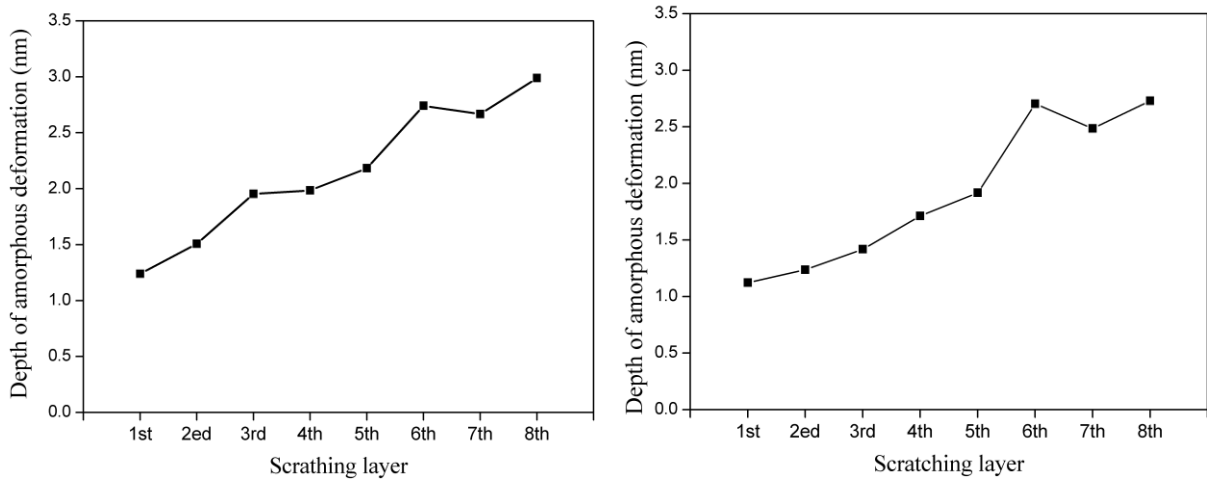


Figure 7-4. The maximum thicknesses of the subsurface amorphous deformation at different scratching depths obtained using DXA on 6H-SiC (left) and 4H-SiC (right).

In general, MD simulations can only be used to analyse atomic removal and deformation mechanisms qualitatively; it is difficult to provide quantitative guidance for actual machining because the potential function selected for the simulation may not accurately represent the molecular performance. Even so, the method proposed here is still a viable quantitative depiction of the actual process behaviour in relation to the material structure.

7.2 Effects of the shape of abrasive tip

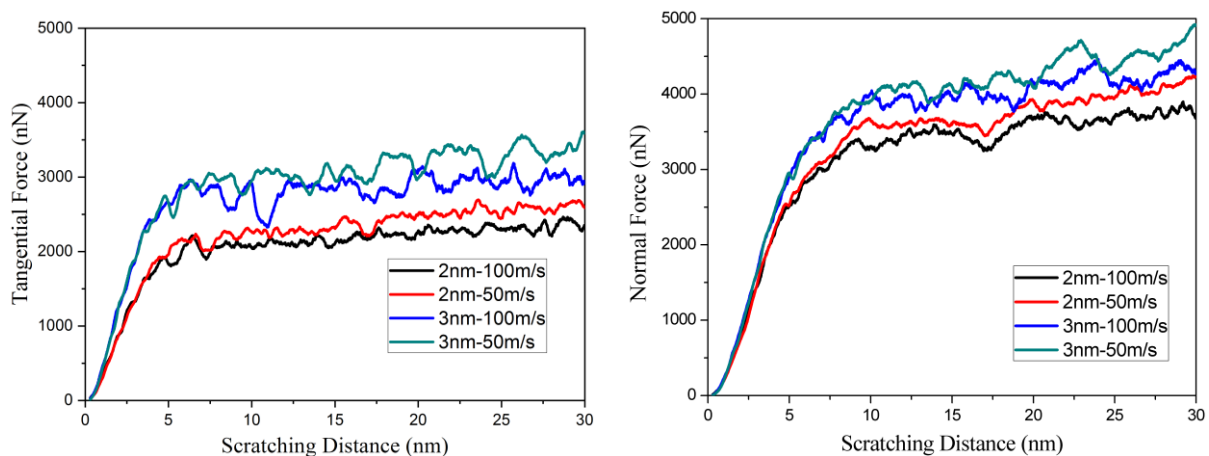
In the nanomachining process, the material removal scale highly depends on the shape of the abrasive tip and the shape of the contact area of the abrasive. Although the diamond abrasives used in ultra-precision polishing are in the size of 3 μm , the scratching depth of each grit is less than several nanometres during polishing. Thus, it is worth investigating the effect of tip shape on material removal efficiency and subsurface quality. In this section, Si face of 6H-SiC is selected as the material of the workpiece. Five types of tips are taken into consideration in this research, sphere, cone, frustum cone, face of pyramid and edge of pyramid.

7.2.1 Forces

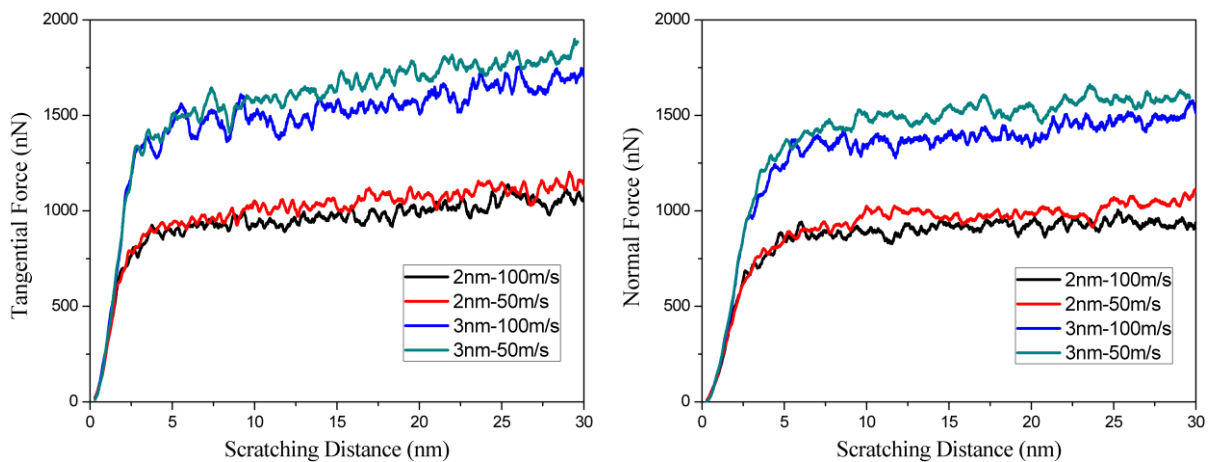
Figure 7-5 show the trends of forces in different cases. There is no doubt that the forces increase with the increase of scratching depth. In the initial scratching stage, there are no significant differences in forces at different scratching speeds. Interestingly, when it comes to

the stable scratching stage, the forces of the speed of 100 m/s are less than those of 50 m/s in all cases. In addition, the forces also show significant differences of the tip in different shapes. From large to small, they are sphere, frustum cone, face of pyramid, edge of pyramid and cone, respectively. The contact areas of tips of different shapes are different, which is one of the reasons for the difference in forces.

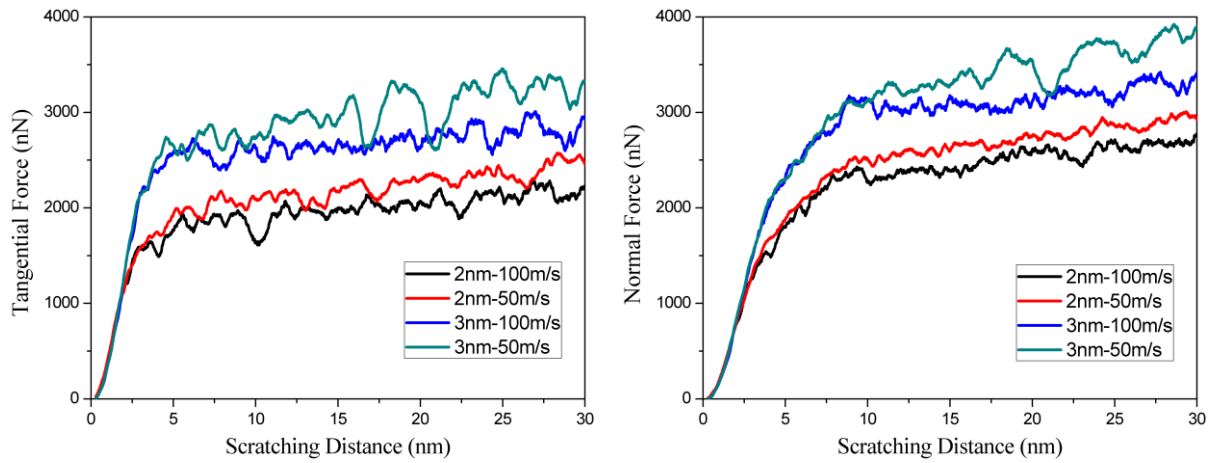
Here, the pressures shown in Figure 7-6 are defined as the ratio of force to contact area during the stable scratching stage. The tangential direction is the direction in which the material is removed. The pressures in the tangential direction of the sphere and the edge of pyramid are less, while the normal pressure of the sphere is significantly less than others. This is because the normal contact area of the sphere tip is much larger and more even than other shapes.



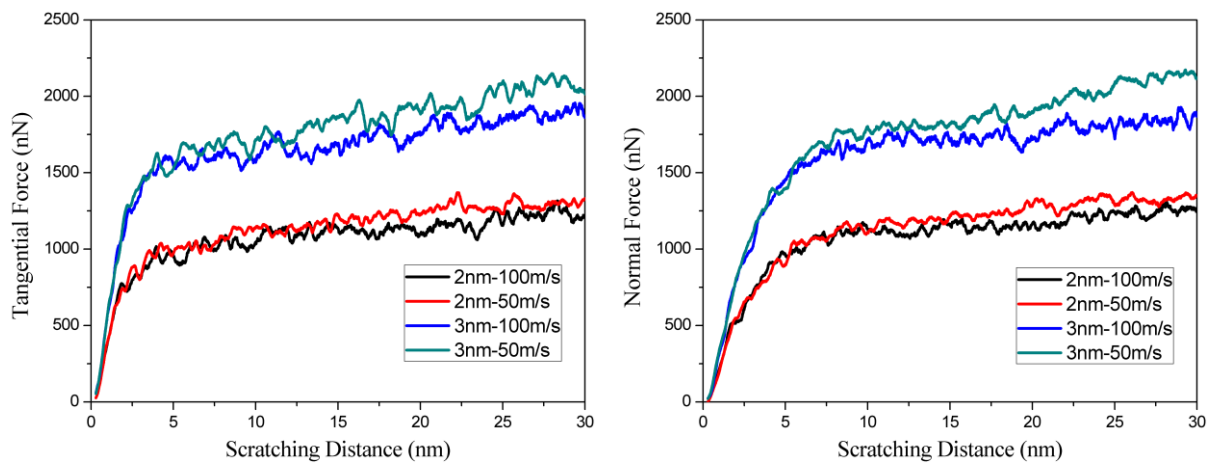
(a) Sphere



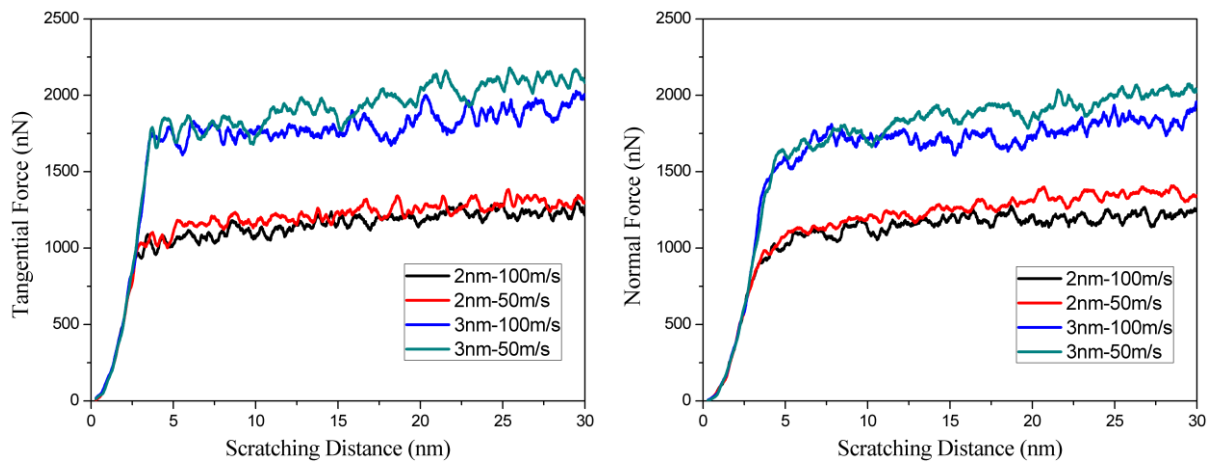
(b) Cone



(c) Frustum cone



(d) Face of pyramid



(e) Edge of pyramid

Figure 7-5. Forces of tips in different shapes obtained from the stable scratching stage.

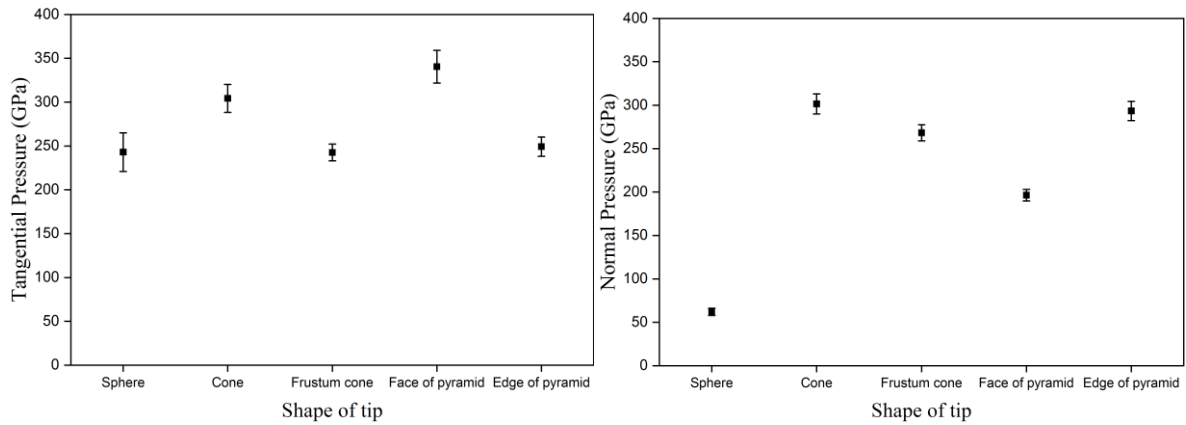


Figure 7-6. Pressure of tips in different shapes obtained from the stable scratching stage.

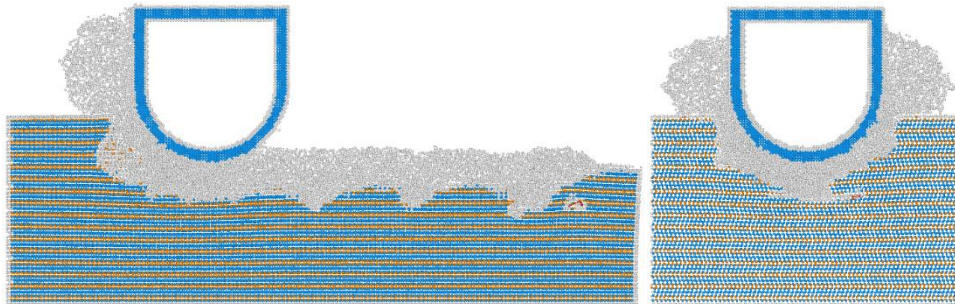
7.2.2 Subsurface deformation

In this section, scratching simulations with scratching depth of 3 nm and scratching speed of 100 m/s are selected to compare the subsurface deformation of the different tip shapes. Figure 7-7 shows the DXA results of the scratching cases, and the grey atoms represent the amorphous atoms. In addition, all longitudinal-section views in this chapter pass through the centre axis of the abrasive tip.

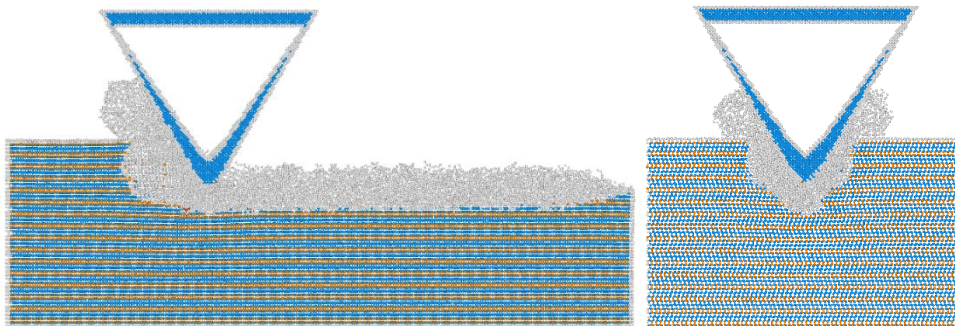
The numbers of amorphous atoms and dislocations caused during scratching are compared in Figure 7-8. Although the scratching depths are the same, the numbers of amorphous atoms are obviously different due to the difference in contact areas. The tips of sphere and frustum cone caused more amorphous atoms, while fewer amorphous atoms were caused by those in the other three shapes with fewer contact areas.

The dislocations generated in the subsurface are the key factor influencing the subsurface quality. From more to less, they are face of pyramid, frustum cone, sphere, cone and edge of pyramid, respectively. Dislocations are caused by local stress concentration, which means the face of pyramid leads to more stress concentrations during scratching. The workpiece material presents worse material fluidity and plasticity when the tip of pyramid face is used. On the contrary, no dislocations are found when the tip of pyramid edge is used, because there is less extrusion along the scratching direction.

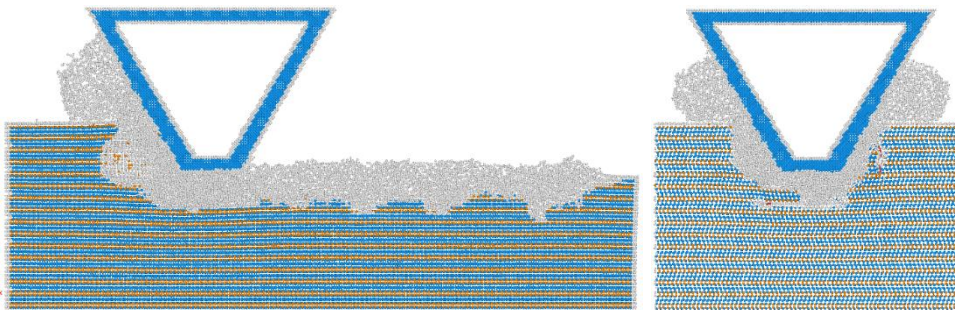
It can be concluded that the amorphous deformation largely depends on the contact area, while the number of dislocations mainly depends on local stress concentrations caused by the extrusion along the scratching direction.



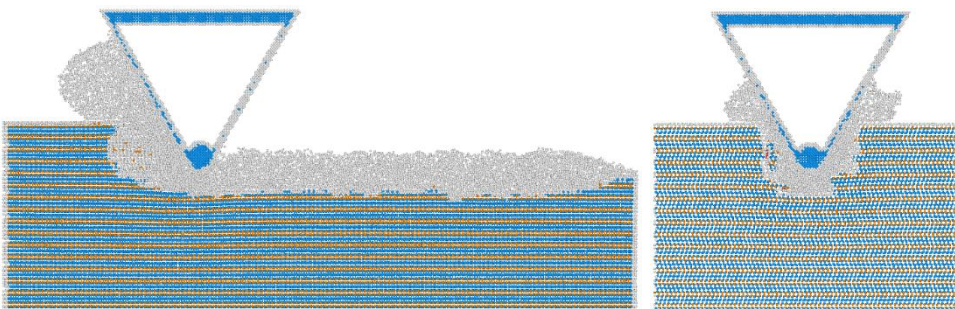
(a) Sphere



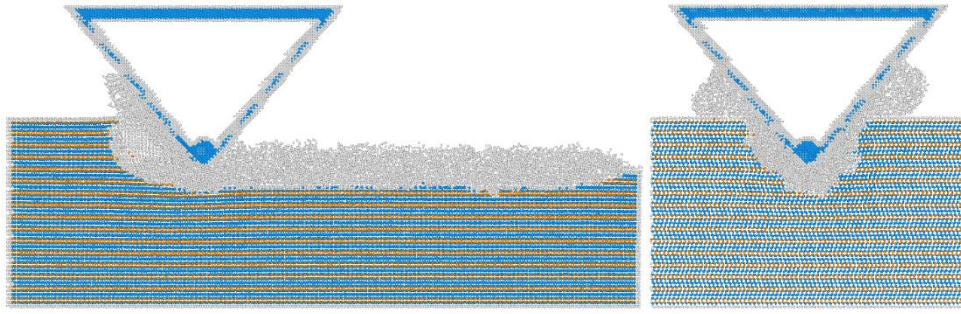
(b) Cone



(c) Frustum cone



(d) Face of pyramid



(e) Edge of pyramid

Figure 7-7. DXA results of scratching cases using tips in different shapes. (Scratching depth of 3 nm and scratching speed of 100 m/s)

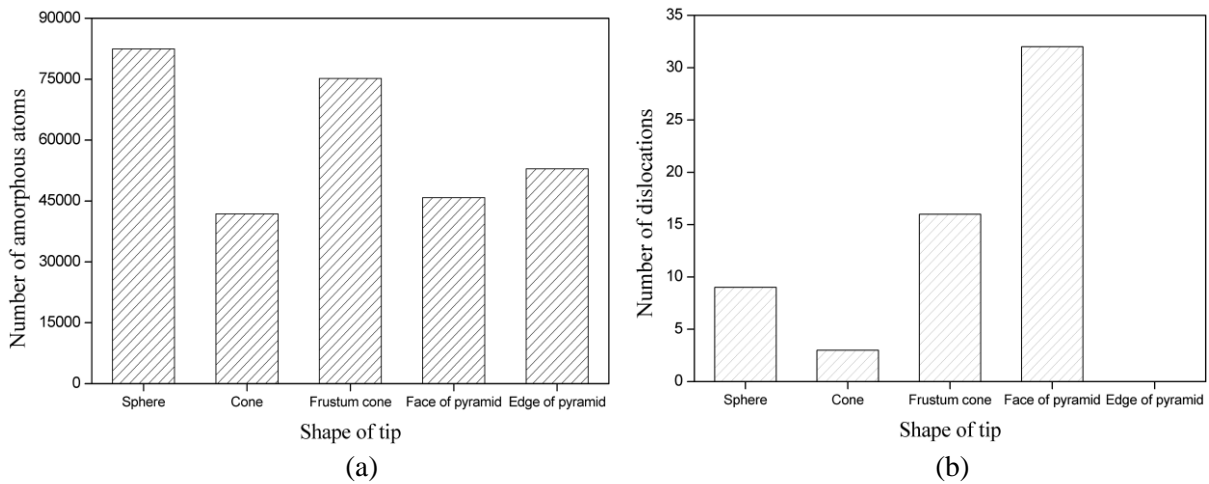


Figure 7-8. Numbers of (a) amorphous atoms and (b) dislocations in subsurface.

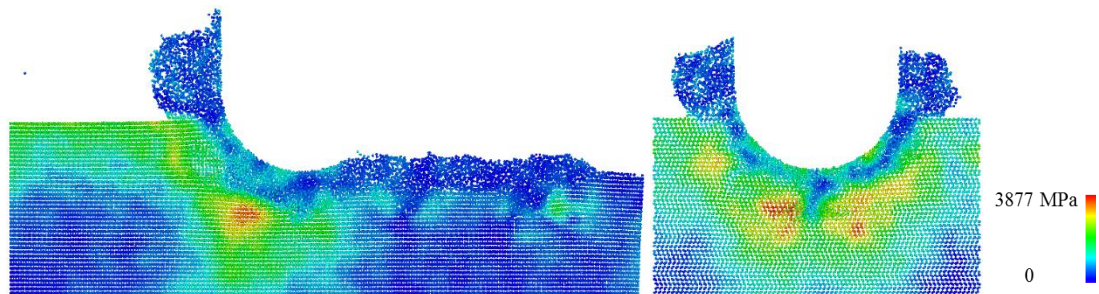
7.2.3 Stress distribution

As discussed before, the dislocations are caused by the local stress concentration, so the von Mises stress distributions in different cases are shown in Figure 7-9. These stress distributions are counted using C++ programmes and then visualized using OVITO.

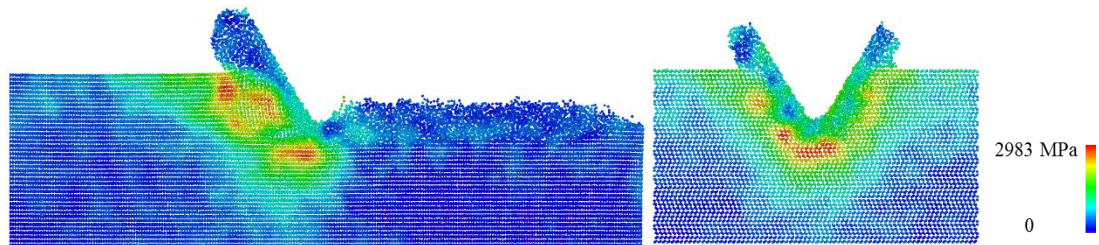
These regions in stress concentrations are mainly located in the subsurface both in front of and below the tip. Interestingly, in all cases, the stress concentrations are only located in the perfect lattice in the subsurface under the tip rather than the contact face between tip and workpiece surface. This means the atoms in the surface lattice were deformed into amorphous structure when the tip contacted, and the stress was released. From the aspect of energy, the perfect lattice in the surface was destroyed by the tip due to the high stress concentration, in which process the stress was offset by the bond energy of the perfect lattice. And the regions

in stress concentration are likely to be transformed into amorphous structures as the tip moves forward.

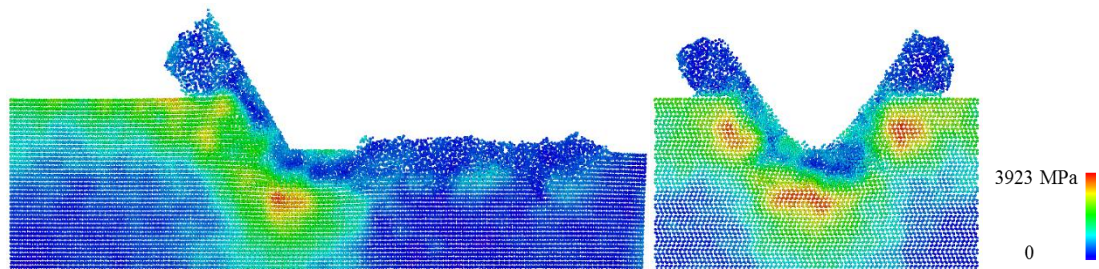
Figure 7-10 compares the maximum stresses of different tips, in the entire workpiece and in the machined zone, respectively. Here, the machined zone is defined as the workpiece region where the abrasive has passed. The maximum stress in each case is located around the contact area, while the stress in the machined zone means the residual stress after machining. It can be seen that sphere and face of pyramid show larger residual stress, while cone and edge of pyramid show less. And frustum cone shows the largest maximum stress in the entire workpiece but fewer residual stress in the machined zone.



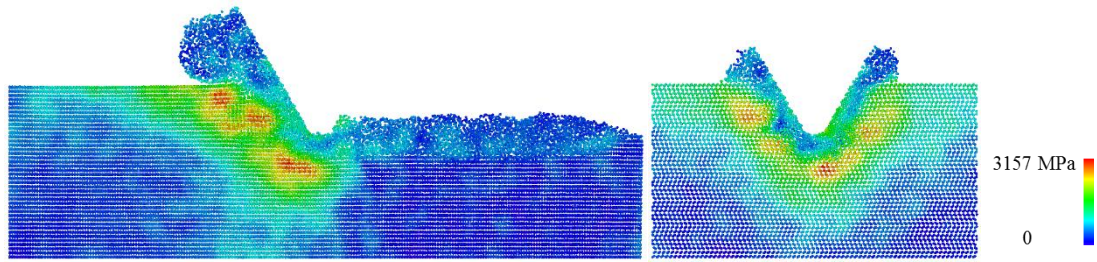
(a) Sphere



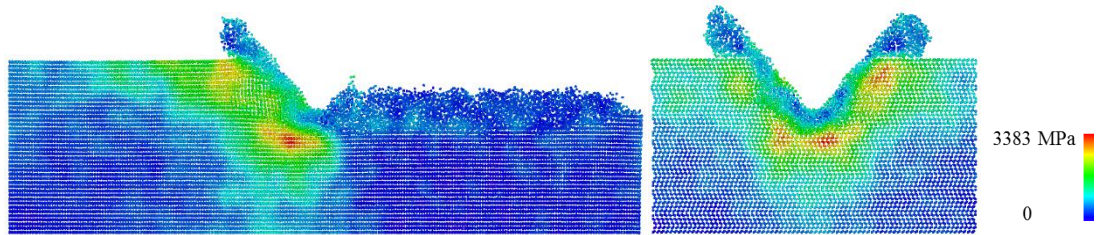
(b) Cone



(c) Frustum cone



(d) Face of pyramid



(e) Edge of pyramid

Figure 7-9. Stress distribution of workpiece using tips in different shapes. (All longitudinal-section views pass through the centre axis of the abrasive tip.)

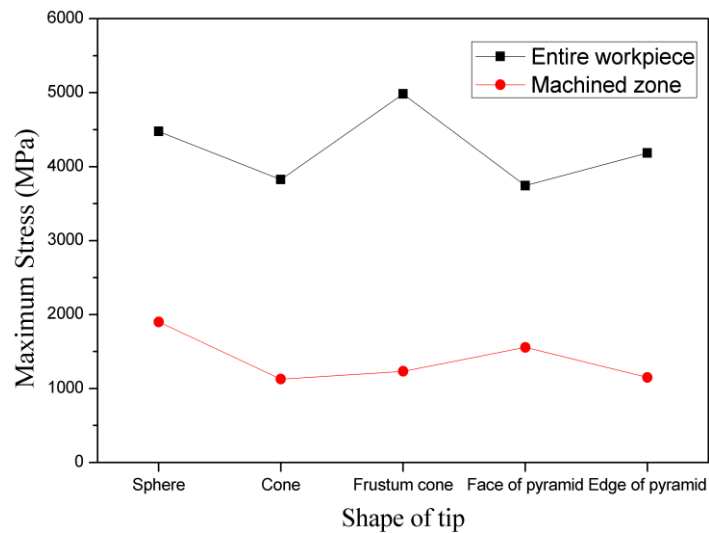


Figure 7-10. Maximum stress using tips in different shapes.

7.2.4 Material removal efficiency

Not only the surface quality and accuracy need to be taken into consideration, but also the material removal efficiency is an important factor in polishing, which determines whether it can be applied in industrial production. In this section, the cases with scratching depths of 2 nm and 3 nm using different tips are selected to discuss.

Figures 7-11 (a) and (b) compares the numbers of atoms above the surface and removed atoms. From more to less, they are sphere, frustum cone, face of pyramid, cone and edge of pyramid, respectively. It can be seen that the scratching speed can influence the material removal efficiency significantly, which is discussed in Section 7.3. Moreover, the ratio, defined according to atoms above the surface and removed atoms per nm^2 in tangential direction, is used to compare the energy efficiency using different abrasive shapes. As shown in Figure 7-11 (c), the ratios of atoms above the surface in sphere, frustum cone and face of pyramid are larger than others, which means the three shapes have higher energy efficiency during scratching. But in terms of removed atoms, from more to less, they are face of pyramid, sphere, cone, frustum cone and edge of pyramid, respectively.

Figure 7-12 shows the Z position distributions of atoms above the original surface in different cases. Obviously, there are more atoms accumulated both in front of the tip and on the two sides of the groove in the scratching depth of 3 nm. More atoms are accumulated both in front of the tip and on the two sides of the groove when the spherical and frustum-cone-shaped tips are used. The material accumulations caused by the three curved tips are significantly more even, while those caused by both pyramid-shaped tips show clear direction according to the direction of the tips.

In addition, using the tip of pyramid edge causes more accumulations on the two sides of the groove but fewer in front of the tip than using the tip of pyramid face. This is because the atoms can ‘flow’ along both sides of the tip rather than be extruded and stacked in front of the tip, which leads to less tangential force, less stress concentration and fewer dislocations as analysed in Sections 7.2.1 and 7.2.2. Therefore, the number of removed atoms using the tip of pyramid edge is the lowest.

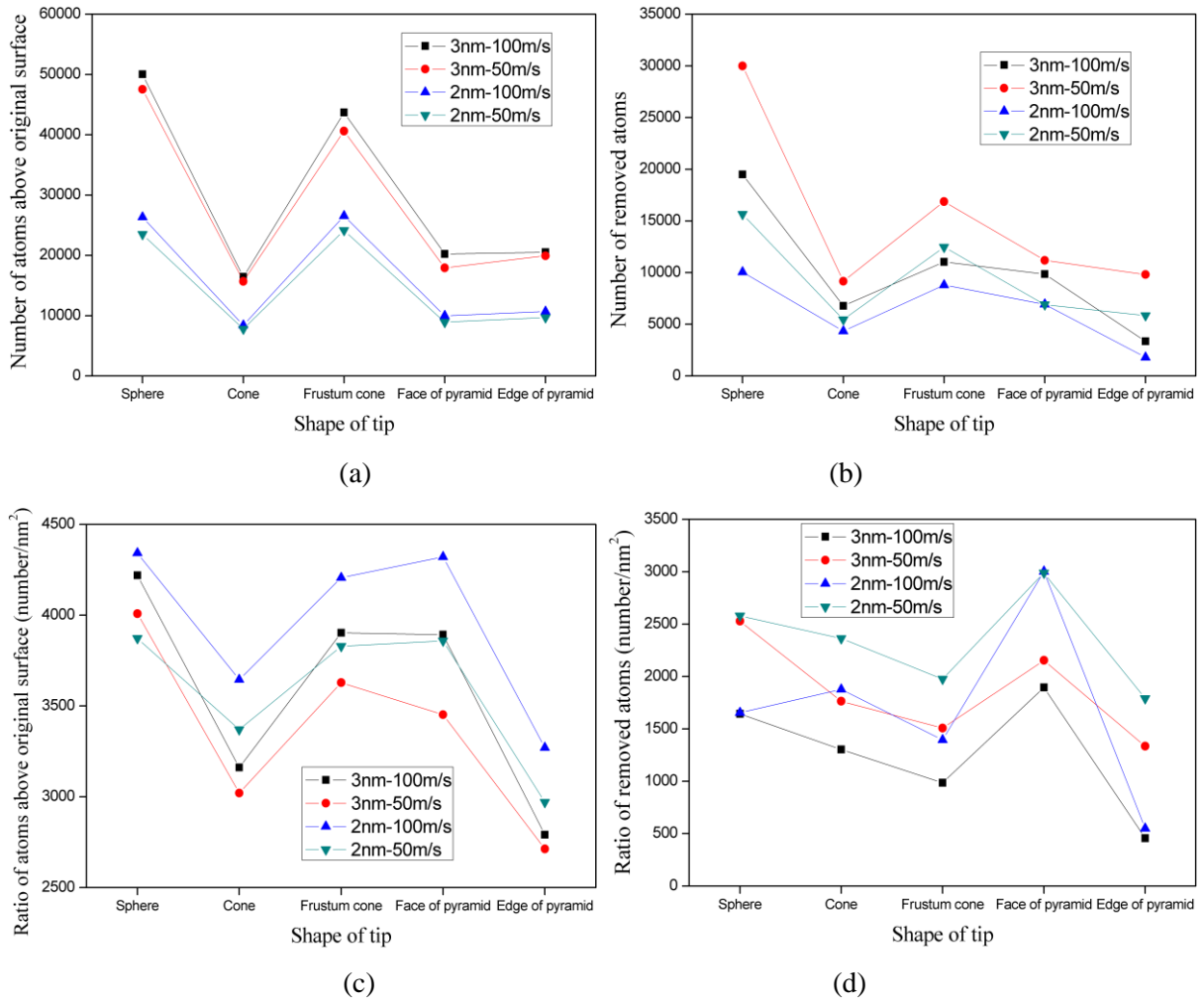
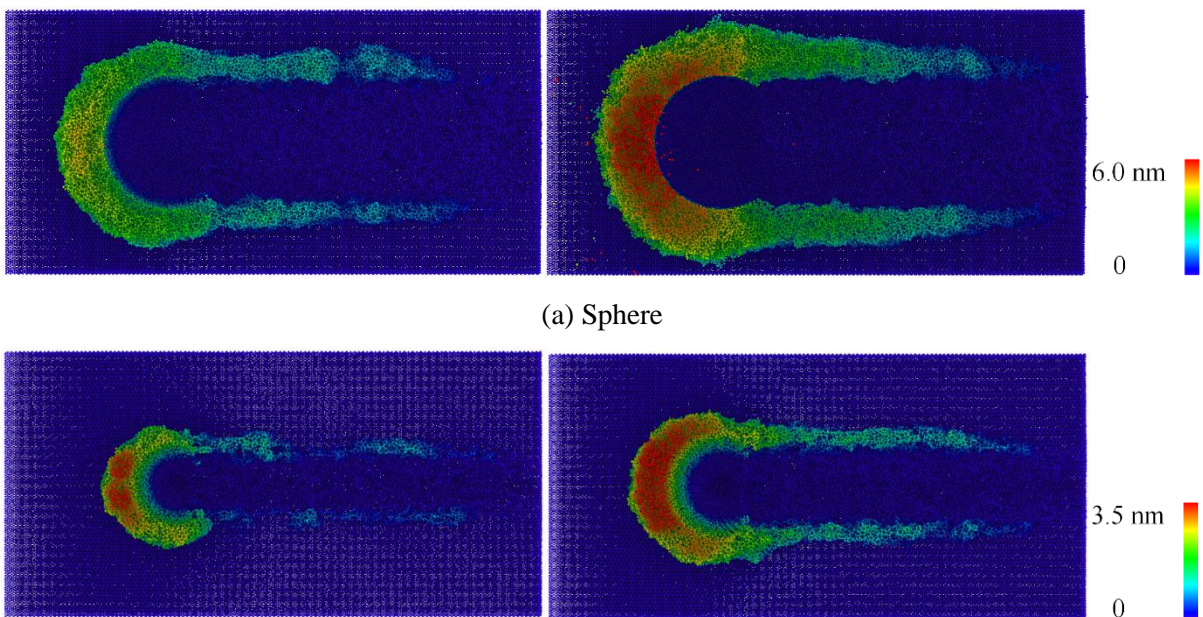


Figure 7-11. Number of (a) atoms above surface and (b) removed atoms. Ratio of (c) atoms above surface and (d) removed atoms per nm² in tangential direction.



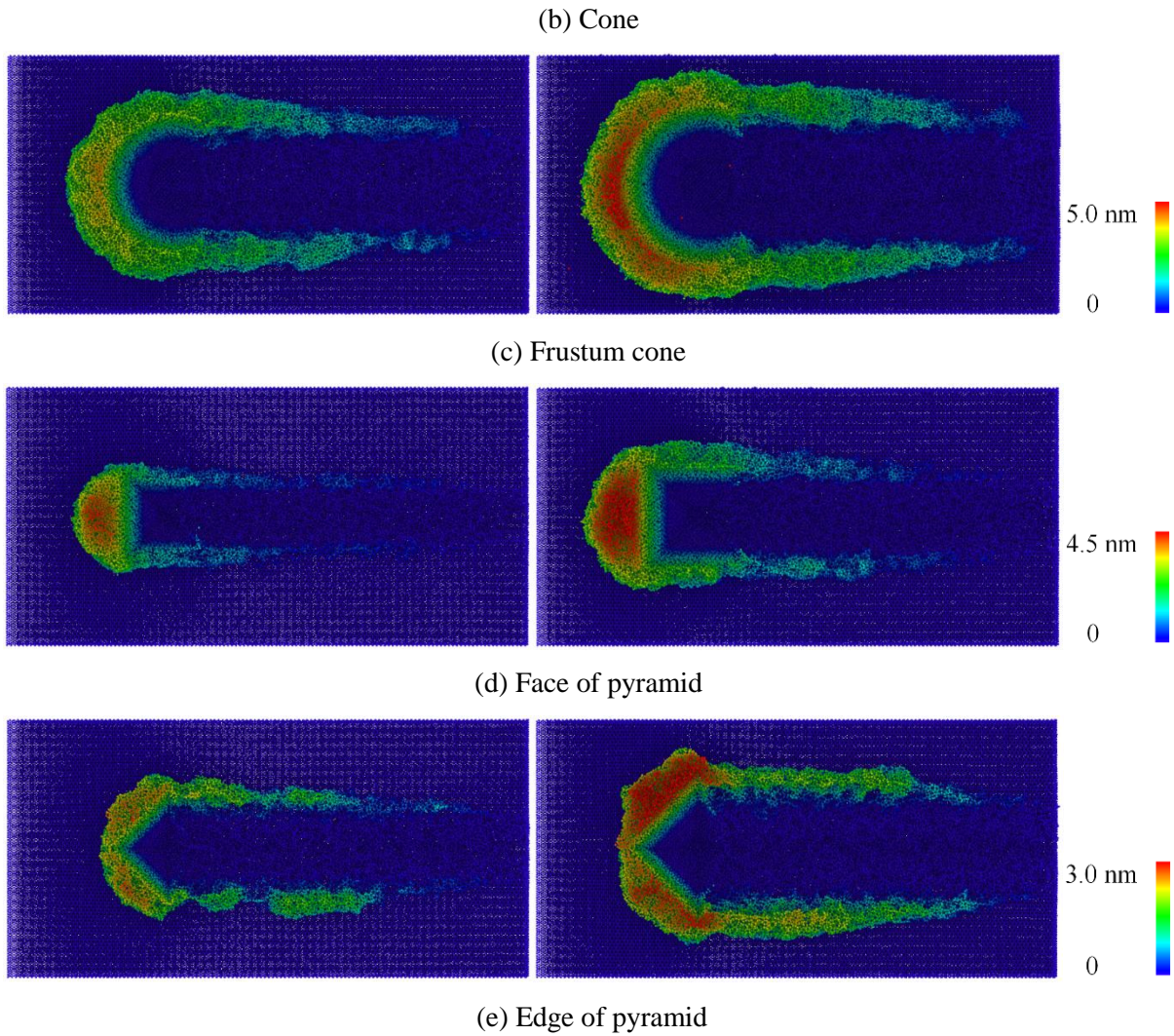


Figure 7-12. Distribution of Z positions of atoms above original surface using tips in different shapes. (Left: 2 nm; right: 3 nm)

Pile-up ratio is also a common parameter to assess the scratching process. The pile-up ratio is counted in terms of the size of area in normal scratching analysis, while in MD simulations, the numbers of atoms in the specific region are adopted. As shown in Figure 7-13, N is the number of workpiece atoms before scratching; N_1 , N_2 and N_3 represent the number of atoms in specific regions. So the pile-up ratio in MD simulation is counted as in the following equation.

$$\text{Pileup ratio} = \frac{N_1 + N_2}{N - N_3} \quad (7-1)$$

Figure 7-14 compares the pile-up ratios of all scratching cases using tips in different shapes. From more to less, they are edge of pyramid sphere, frustum cone, sphere, cone and face of

pyramid, respectively. It is noticeable that the ratio in the case of using the tip of pyramid edge with scratching depth of 3 nm and scratching speed of 100 m/s, is more than 1. This is consistent with the previous conclusion that atoms are likely to accumulate on the two sides of groove. Moreover, the scratching speed has a clear effect on the pile-up ratio.

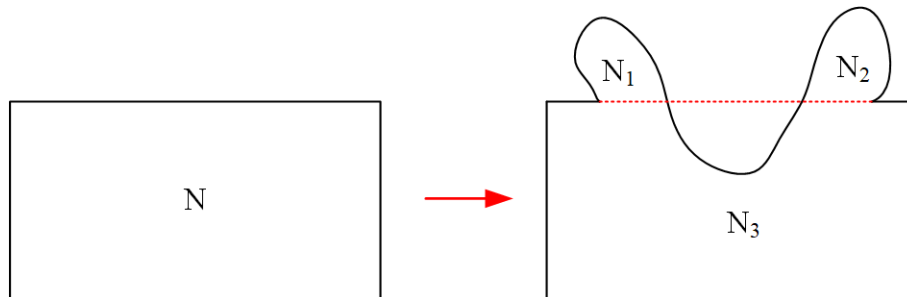


Figure 7-13. The diagram of pile-up ratio.

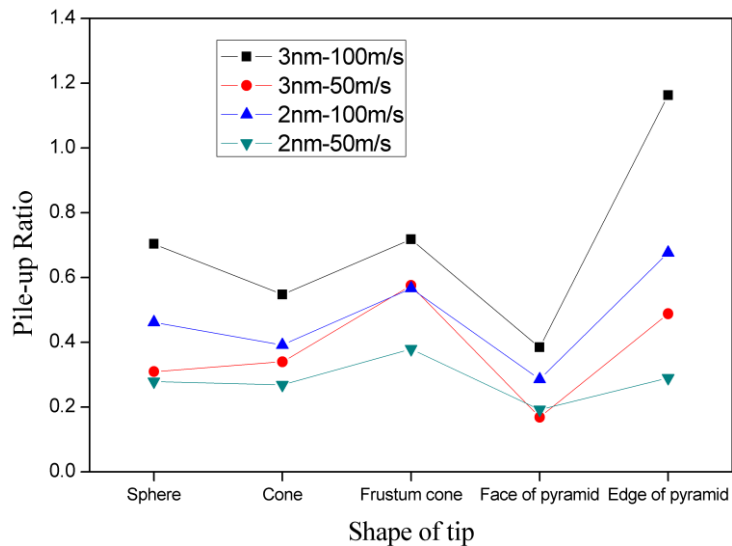


Figure 7-14. Pile-up ratios of all scratching cases using tips in different shapes.

In conclusion, from better to worse in terms of pile-up ratios, they are sphere, frustum cone, edge of pyramid, cone and face of pyramid; from better to worse in terms of subsurface quality, they are edge of pyramid, cone, face of pyramid, sphere and frustum cone; from large to small in terms of material removal efficiency, they are sphere, frustum cone, face of pyramid, cone and edge of pyramid.

7.3 Effects of scratching speed

Scratching speed is also a key parameter during the nanomachining process. Higher polishing speed can improve the material removal efficiency, but in the meantime, it may cause more wear and shedding of grits and damage on workpiece surfaces. In general, the speed in actual polishing was less than several m/s, but the scratching speeds were set ranging from 40 m/s to 500 m/s when MD simulation was used to simulate the nanomachining processes [136-141]. This is because the scratching model contains hundreds of atoms and the MD simulation is really time-consuming. Thus, in this section, different scratching speeds were adopted in both MD simulations and experiments to investigate the effect on scratching properties. In this section, Si face of 6H-SiC is selected as the material of the workpiece and the scratching speeds are 10, 40, 60, 80 and 100 m/s.

7.3.1 Forces

Figure 7-15 shows the trends of forces in different speeds. In the initial scratching stage, there are no significant differences in forces at different scratching speeds. Interestingly, when it comes to the stable scratching stage, the higher scratching speed leads to lower forces in both tangential and normal directions. The vibration amplitude and frequency of each force trend are almost the same in the stable scratching stage.

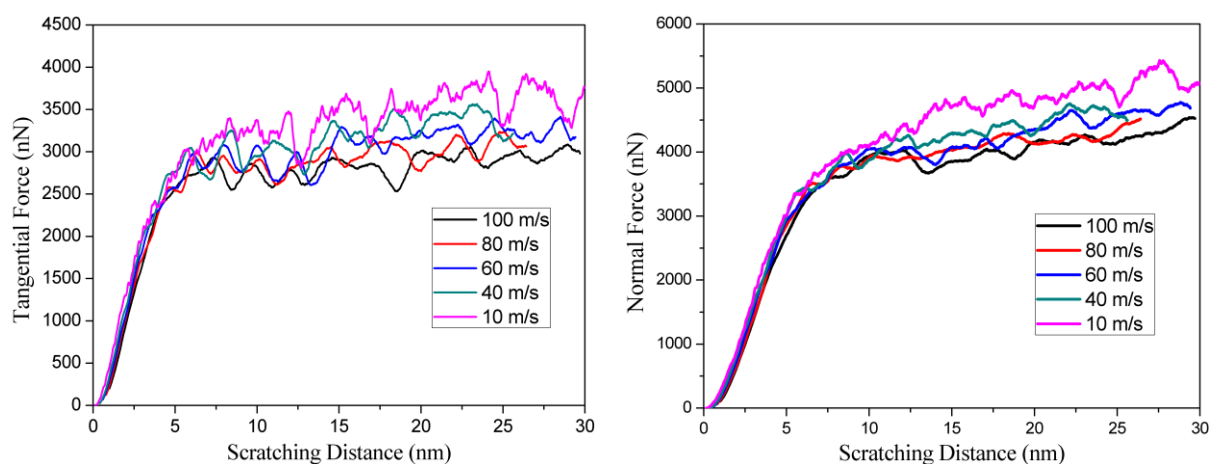
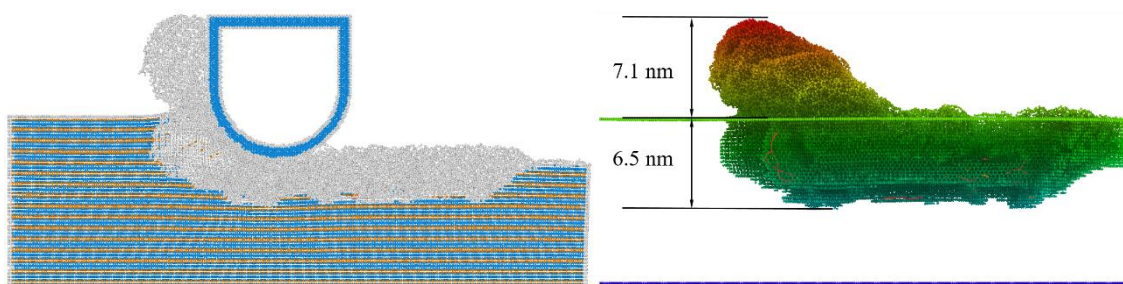


Figure 7-15. Tangential (left) and normal (right) forces in different scratching speeds.

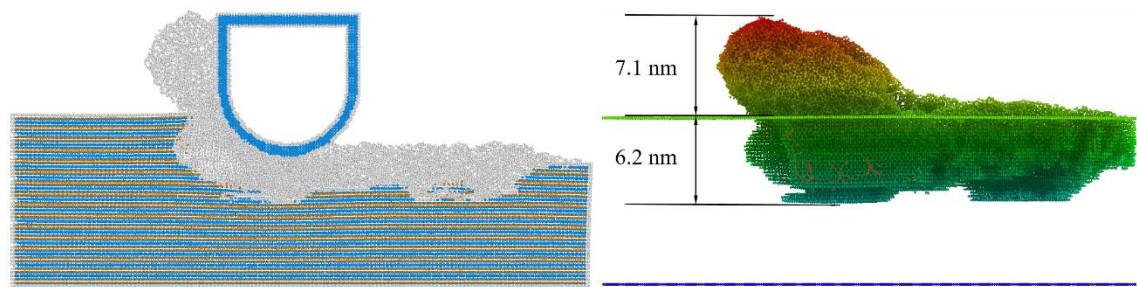
7.3.2 Subsurface deformation

Figure 7-16 shows the DXA results and amorphous deformation of the workpiece using different scratching speeds. It can be seen that the thickness of the subsurface deformation is almost the same at different scratching speeds. And there is no significant difference in the height of the workpiece material accumulated in front of the abrasive. As mentioned in Section 6.4, during the scratching process, there will be two types of dislocations in the subsurface, which are (0001) basal plane dislocations and (1-100) cylindrical plane dislocations. At different scratch speeds, both of these dislocations exist. But it is worth noting that the slower scratching speed leads to more obvious dislocations and slips in subsurface.

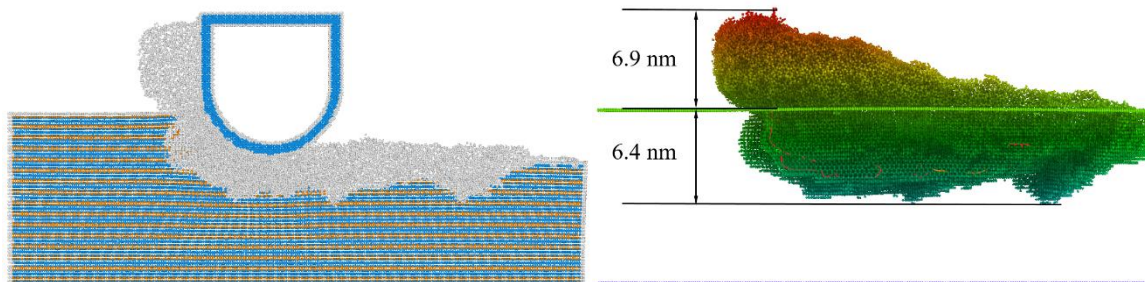
Figure 7-17 compares the number of amorphous atoms and dislocations in the subsurface of the workpiece material after scratching using different speeds. The number of amorphous atoms and dislocations decreases with the increase of the scratching speed. This means that the lower scratching speed will cause more dislocations and slips in subsurface. As previously analysed, the dislocations and slips discussed here are both irreversible deformations. Although they represent plastic deformation in the materials science field, they will gradually evolve and expand into microcracks in the subsurface during machining, which does harm to the quality of the wafer. Therefore, in this study, we believe that dislocations and slips are important factors that can cause brittle deformation.



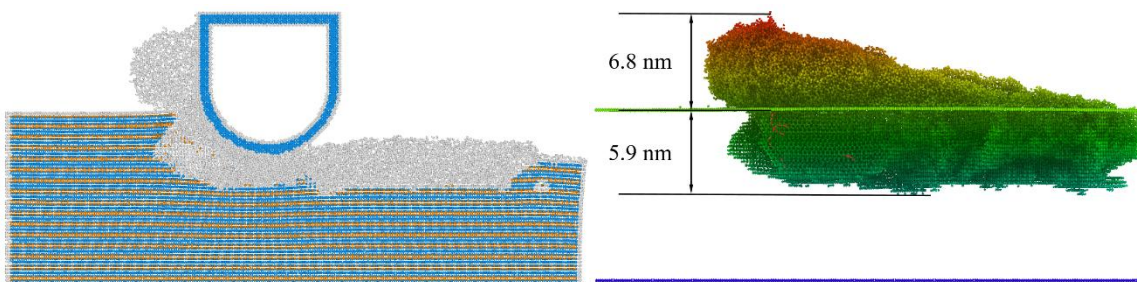
(a) 10 m/s



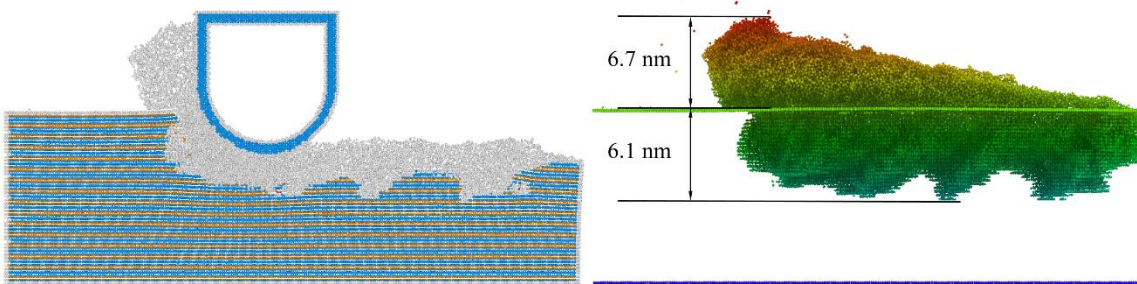
(b) 40 m/s



(c) 60 m/s



(d) 80 m/s



(e) 100 m/s

Figure 7-16. DXA results (left) and amorphous deformation (right) of scratching cases in different speeds.

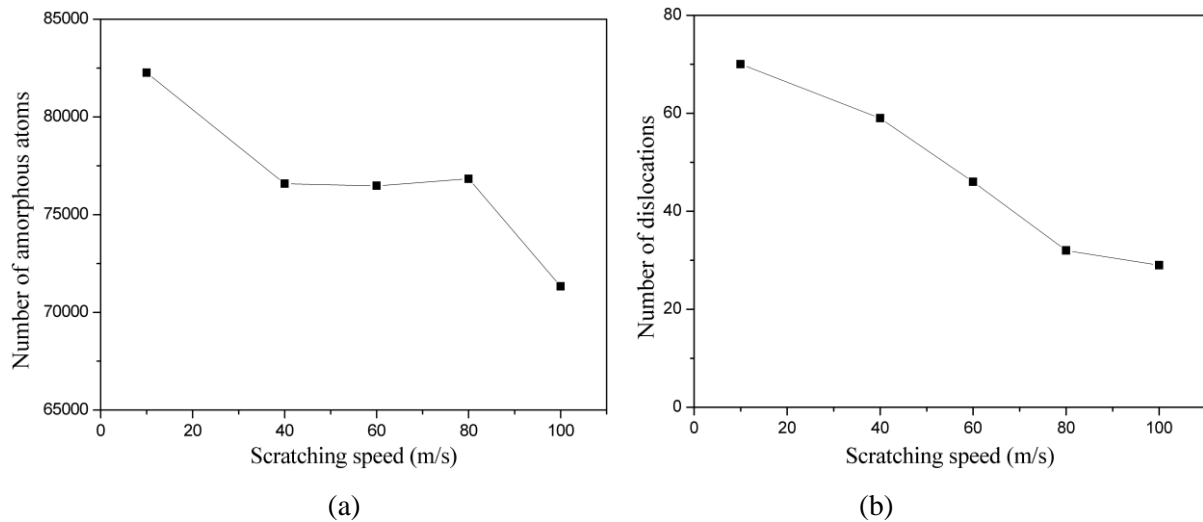
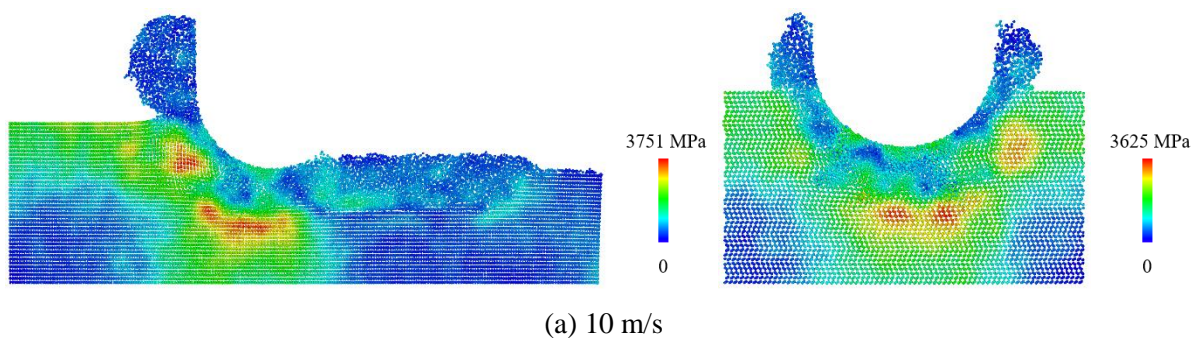


Figure 7-17. Numbers of (a) amorphous atoms and (b) dislocations in subsurface.

7.3.3 Stress distribution

Figure 7-18 shows the stress distribution of the workpiece using different scratching speeds. It can be seen that scratching speed has no obvious effect on the stress distribution. The stress concentration is mainly located in the vicinity of the abrasive and on both sides of the groove. Figure 7-19 compares the peak stress of the machining area and the machined area using different scratching speeds. The peak stresses are also around 4500 MPa as obtained in Section 6.4. When the stress value is higher than the critical stress for the occurrence of dislocations, dislocations will occur, allowing local stress concentration to be released. Thus, scratching speed has no significant effect on the stress in terms of the distribution and the peak value of stress.



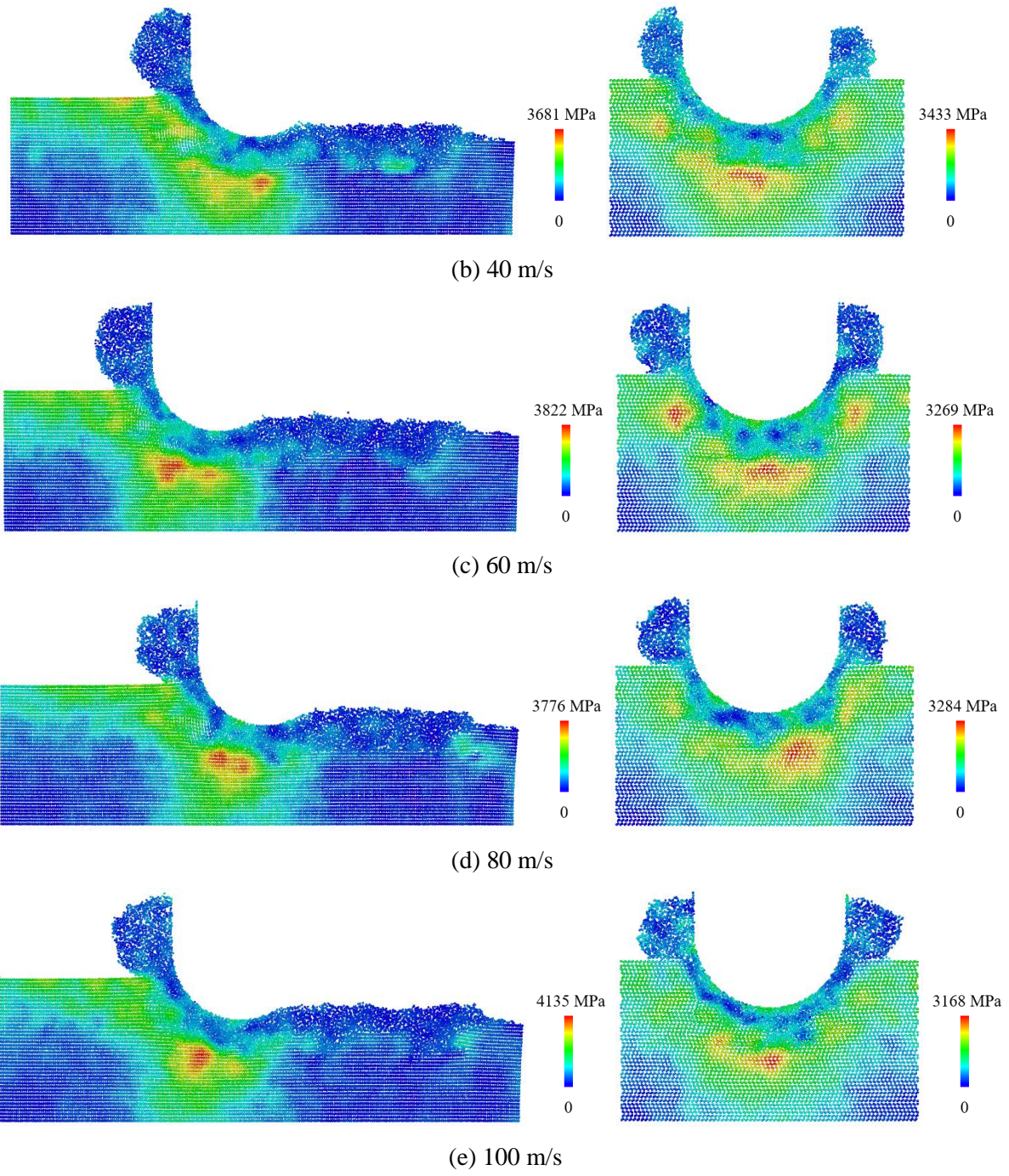


Figure 7-18. Stress distribution of workpiece using different scratching speeds.

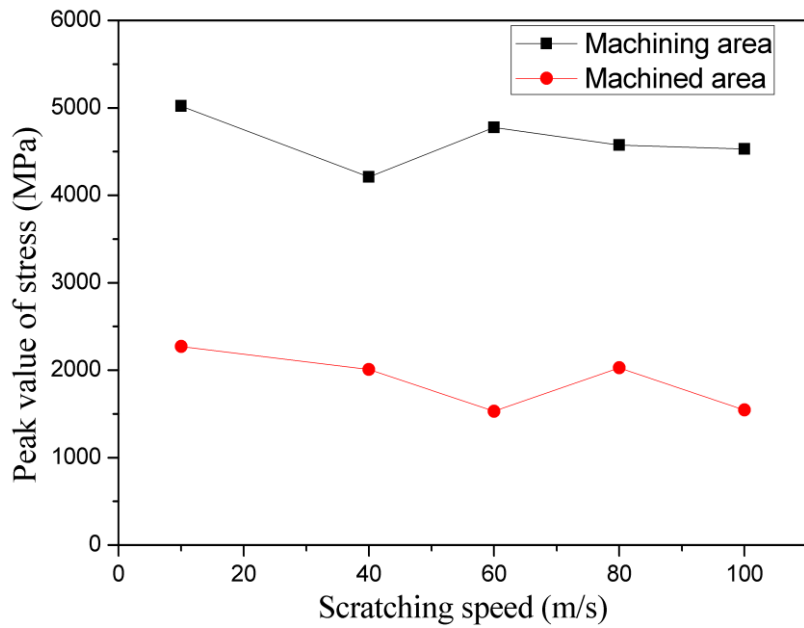
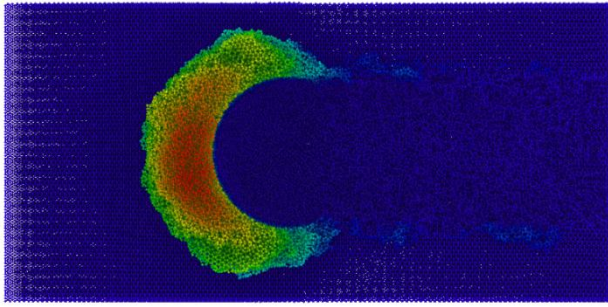


Figure 7-19. Maximum stress of machining area and machined area using different scratching speeds.

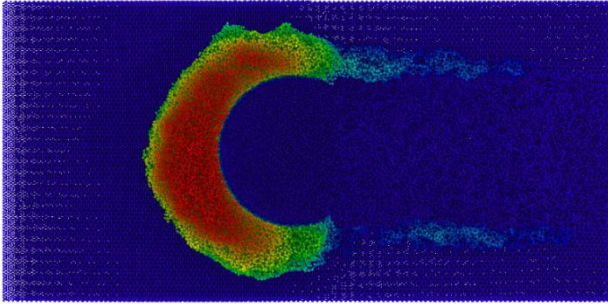
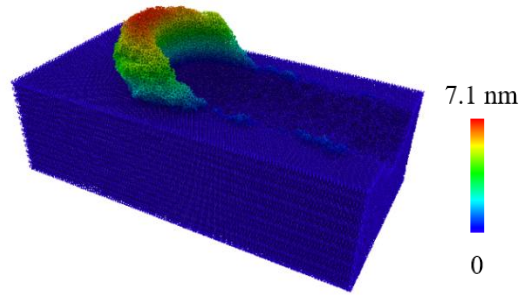
7.3.4 Material removal efficiency

Figure 7-20 shows the distribution of Z positions of atoms above original surface using different scratching speeds. It can be seen that there is no significant difference in the stacking height of the material at different scratching speeds. But there are obvious differences in the uplift of the material on both sides of the groove. At low speeds (10 m/s), there is almost no uplift of material on both sides of the groove. When the scratching speed increases, more and more workpiece materials are accumulated on both sides. When the speed reaches 100 m/s, the bulge on both sides is the highest. This means that the increase in the scratching speed will result in the more obvious plasticity of the material.

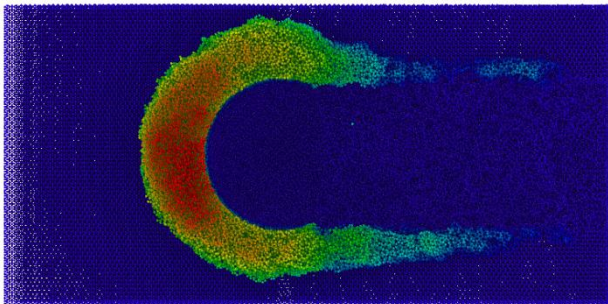
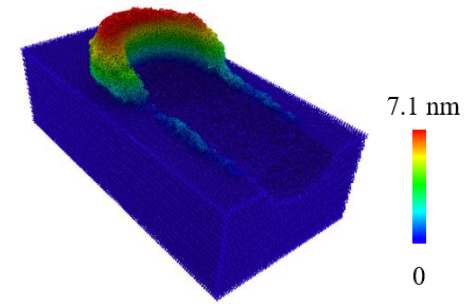
Figure 7-21 shows compares the number of atoms above the surface and removed atoms using different scratching speeds. It is clear that the higher the scratching speed, the more atoms are accumulated on the surface, but the fewer atoms are removed. This is because when the speed is higher, a large proportion of the material is accumulated on both sides of the groove rather than in front of the abrasive.



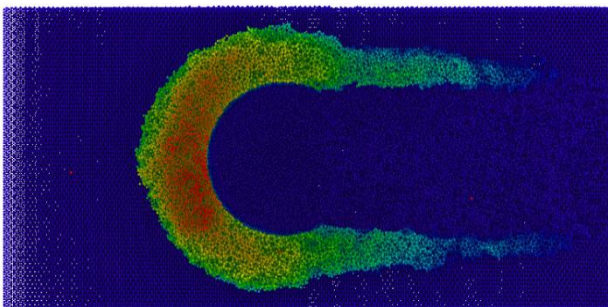
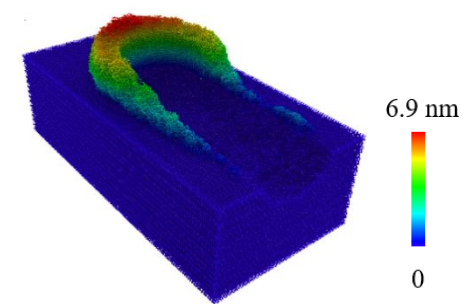
(a) 10 m/s



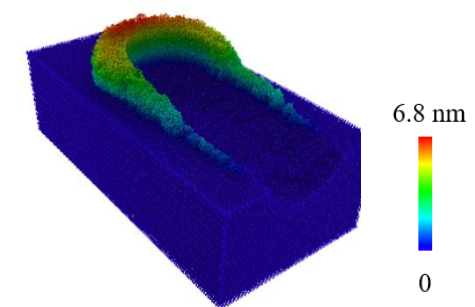
(b) 40 m/s



(c) 60 m/s



(d) 80 m/s



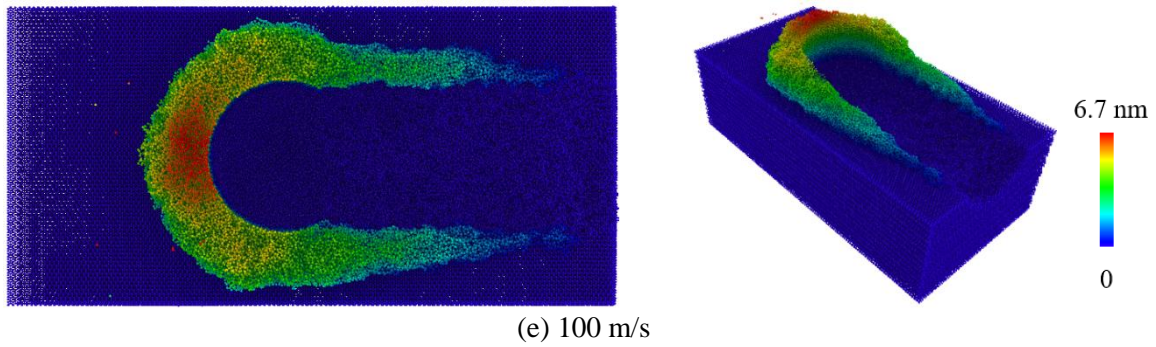


Figure 7-20. Distribution of Z positions of atoms above original surface using different speeds.

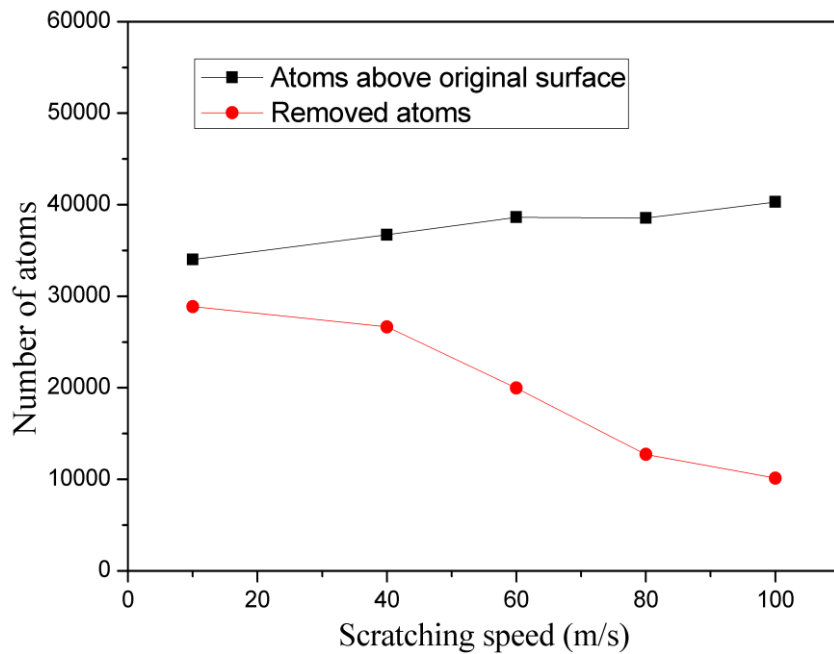


Figure 7-21. Numbers of atoms above original surface and removed atoms in subsurface.

7.4 Effects of scratching direction

Silicon carbide is a kind of crystalline material with obvious anisotropy. This anisotropy shows significant differences in material removal properties during machining. The differences between different crystal planes (Si face and C face) have been investigated and discussed in the previous chapters. This section will further discuss the difference in material removal characteristics and subsurface deformation when scratching along different crystal directions. As shown in Figure 3-26, the scratching processes are conducted on the (0001) basal plane (vertical to z axis) along direction [1-210] and [1-100].

7.4.1 Forces

Figure 7-22 shows the trends of normal and tangential forces in different scratching directions. It can be seen that when the scratching depth is 2 nm, the curves are smoother, and when the scratching depth gets larger, the normal and tangential forces fluctuate more intensely. At the small scratching depth, amorphization is the main deformation of the material, so the force fluctuation is less. When the scratching depth gets larger, a lot of dislocations and slips will occur in the subsurface, and the accumulation and release of stress will be more intense. In addition, there is no significant difference in the magnitude, trend, fluctuation amplitude, and fluctuation frequency of the force using these two scratching directions.

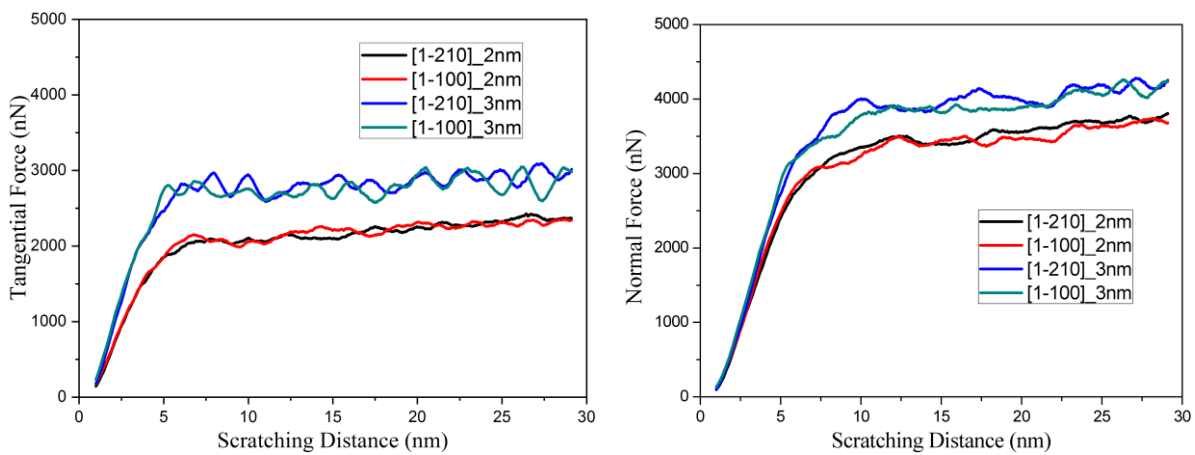


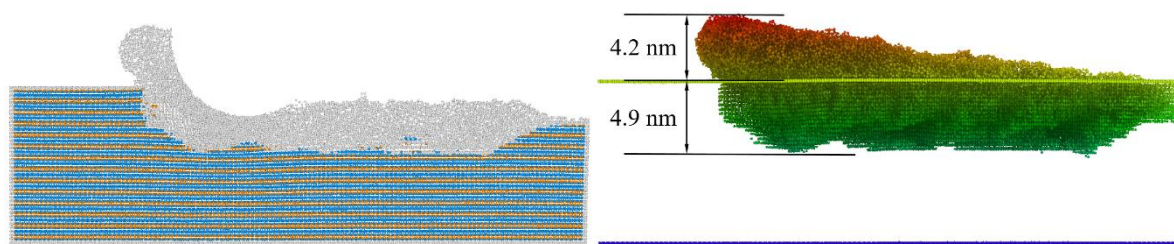
Figure 7-22. Tangential (left) and normal (right) forces in different scratching directions.

7.4.2 Subsurface deformation

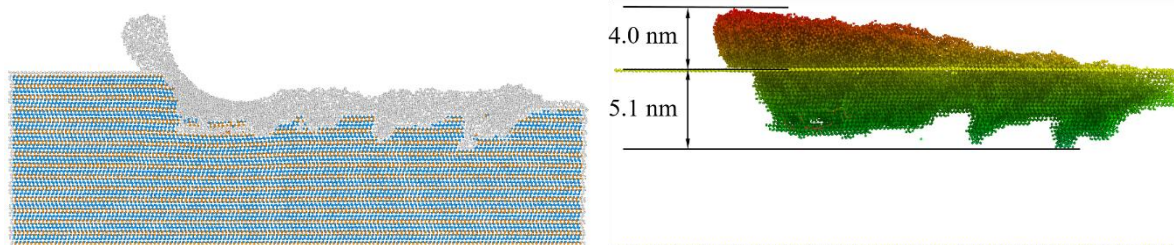
Figure 7-23 shows the trends of forces in different cases. The thicknesses of the subsurface damage in different scratching directions are almost the same. And the heights of the workpiece material accumulated in front of the abrasive are almost the same as well. It is worth noting that comparing the DXA results, the thickness of the amorphous layer caused by the [1-100] scratching direction is significantly less than that caused by the [1-210] scratching direction. As mentioned in Section 6.4, during the scratching process, there will be two types of dislocations in the subsurface, which are (0001) basal plane dislocations and (1-100) cylindrical plane dislocations. In different scratching directions, these two kinds of

dislocations also exist, but due to the difference in crystal orientation, the number of dislocations and the number of amorphous atoms are significantly different.

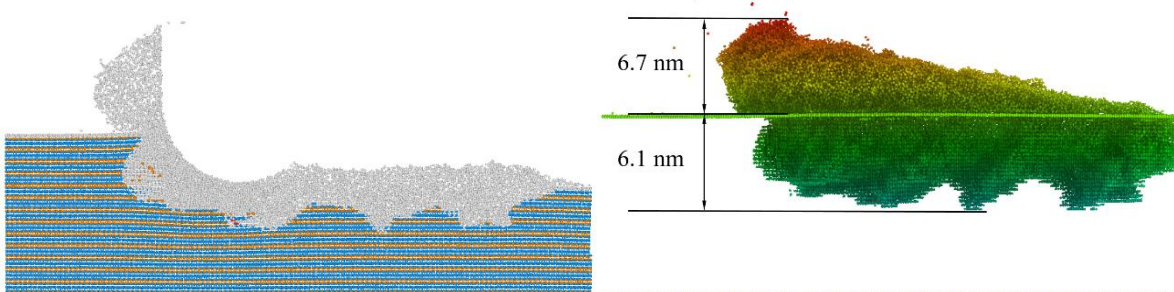
Figure 7-24 compares the number of amorphous atoms and dislocations in the subsurface layer of the workpiece material after being scratched along different directions. It can be seen that there is no difference in the number of amorphous atoms and dislocations in different scratching directions at scratching depth of 2 nm. But when the scratching is 3 nm, the difference is obvious. When the scratch direction is $[1-210]$, there are more amorphous atoms but fewer dislocations. This means that when the scratching depth is small, the deformation of the material is dominated by amorphization, and different scratching directions have little effect on it. When the scratching depth gets larger, many dislocations and slips will occur in the subsurface, resulting in obvious differences caused by the different scratching orientations.



(a) $[1-210]$ _2 nm



(b) $[1-100]$ _2 nm



(c) $[1-210]$ _3 nm

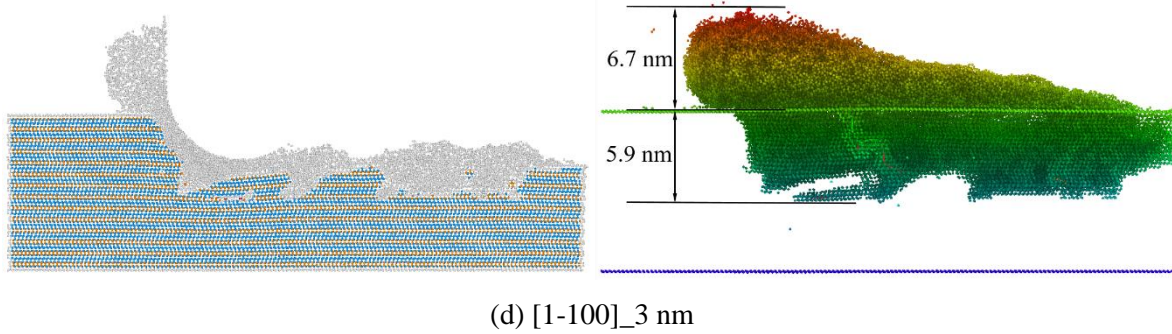


Figure 7-23. DXA results (left) and amorphous deformation (right) of scratching cases in different directions.

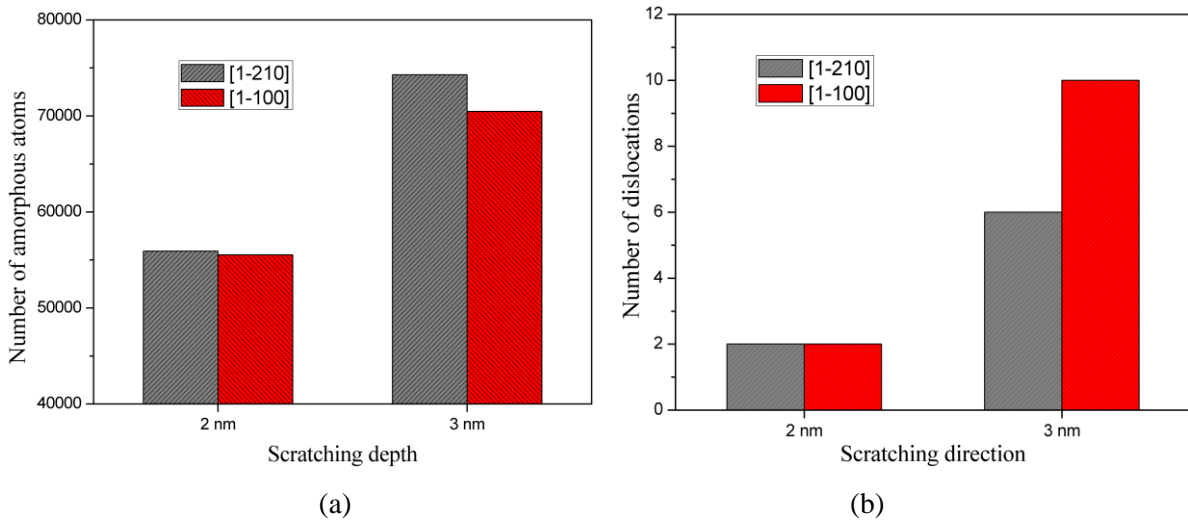


Figure 7-24. Numbers of (a) amorphous atoms and (b) dislocations in subsurface.

Furthermore, Figure 7-25 shows the cross-section views of surface and subsurface atoms in different cases. Interestingly, different scratching directions show different patterns of amorphous atoms and dislocations. As concluded in Chapter 5, the slip system of 6H-SiC is along $\langle 1-210 \rangle$ orientations. In particular, these dislocations along $\langle 1-210 \rangle$ orientations consist of the hex patterns in both nanoindentation simulations and experiments (Figure 5-8). Similarly, in scratching, these patterns also can be considered as the consequence of the dislocations along $\langle 1-210 \rangle$ orientations. For the scratches along [1-210], the angles of these lines and scratching direction are 60° , while the angles for the scratches along [1-100] are 30° . In addition, the material deformation in front of the abrasive is prone to occur at the front corner of the hexagon pattern for the scratches along [1-210]; and it is prone to occur at the two corners of the hexagon pattern for the scratches along [1-100].

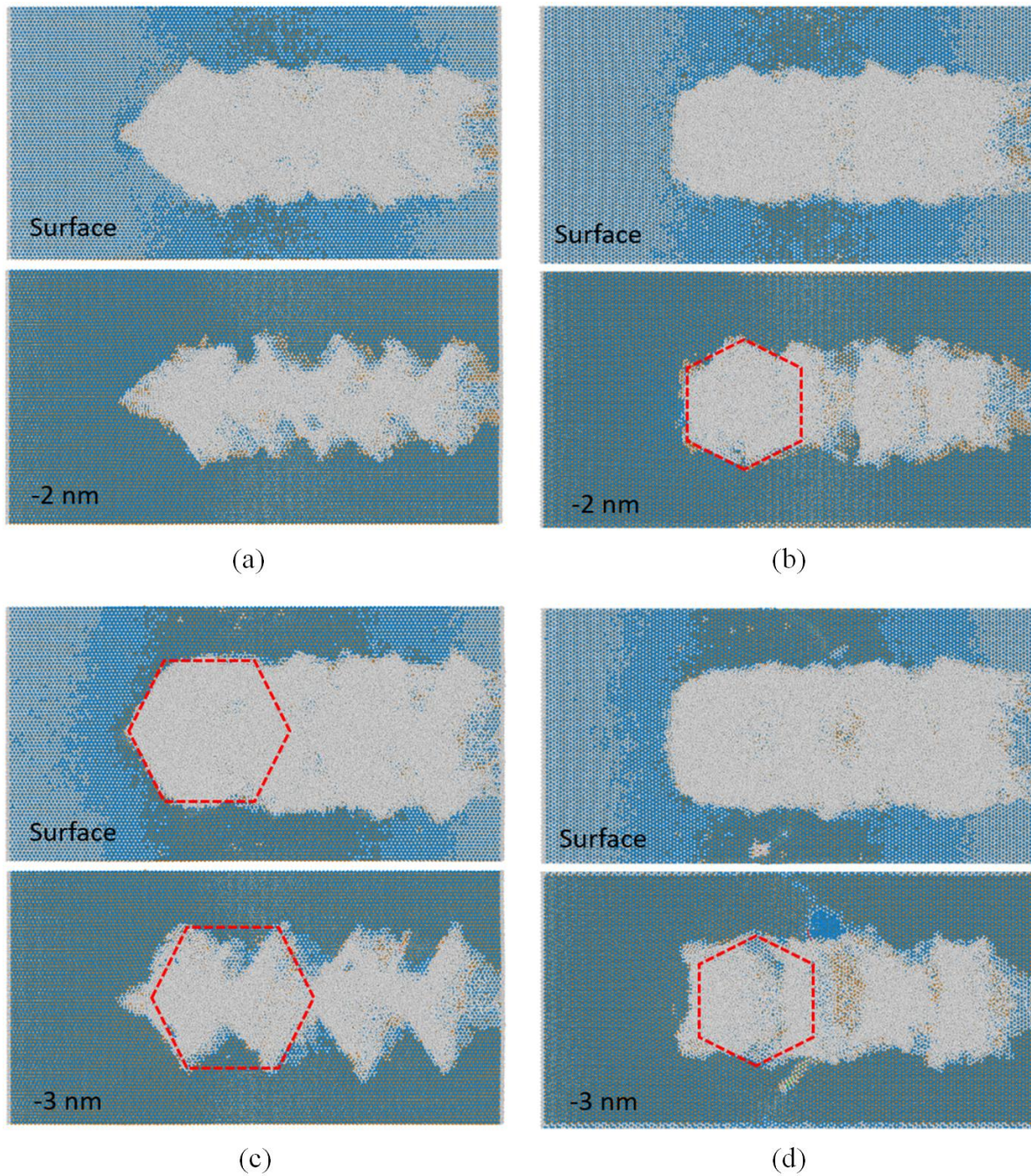


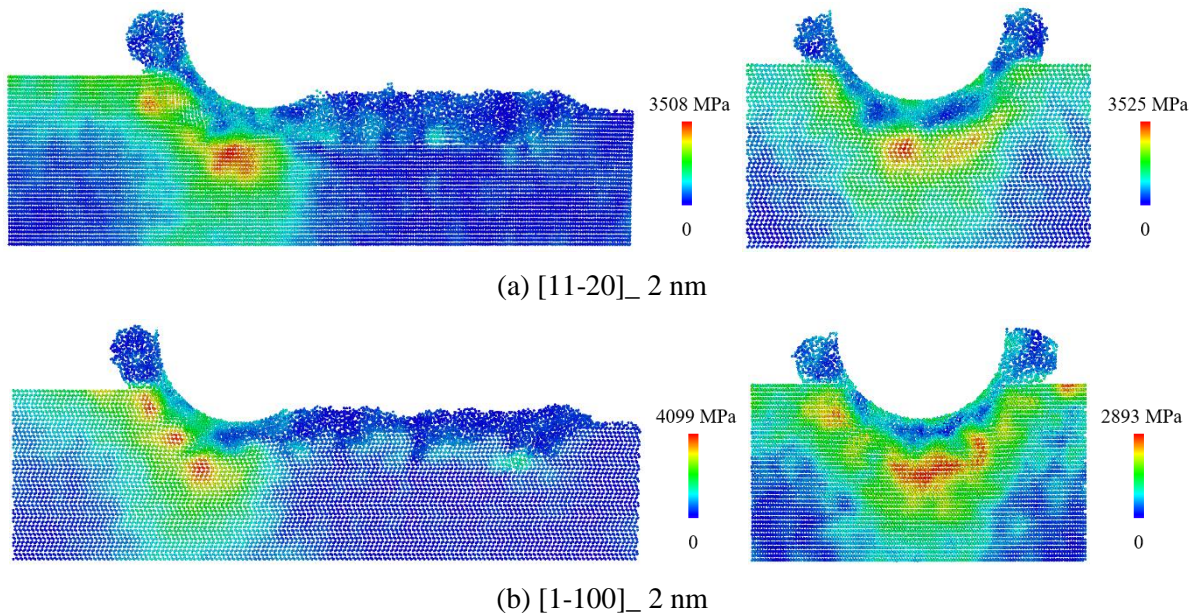
Figure 7-25. Cross-section views of surface and subsurface atoms in different cases. (a) [1-210]₂ nm. (b) [1-100]₂ nm. (c) [1-210]₃ nm. (d) [1-100]₃ nm.

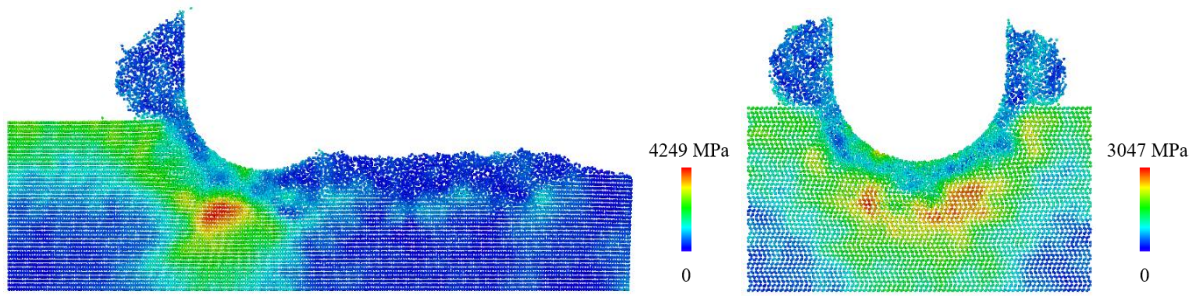
7.4.3 Stress distribution

Figure 7-26 shows the stress distribution of subsurface atoms under different scratching directions. It can be seen that when the scratching depth is 2 nm, the scratching directions have no significant effect on the stress distribution. When the scratching depth gets larger, the stress concentration obtained in the [1-210] direction is mainly located in the area directly

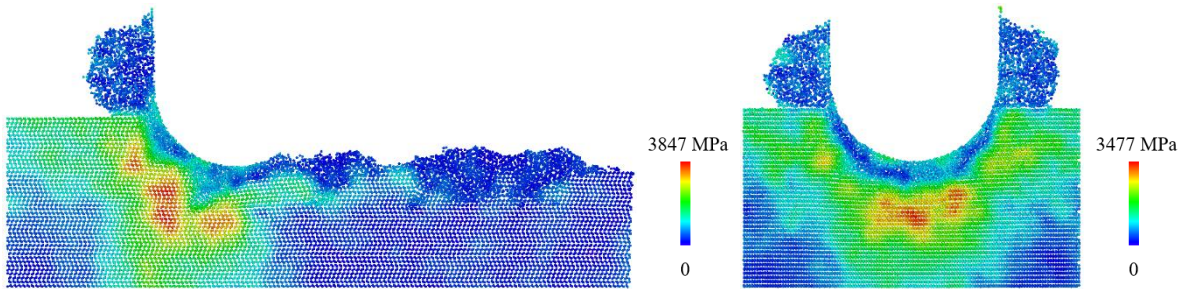
below the abrasive; while the stress concentration obtained in the $[1-100]$ direction is mainly located below and in front of the abrasive. In particular, the stress concentration in Figure 7-26 (d) (left) is located on the $(1-100)$ cylindrical plane in front of the abrasive. This difference is probably due to the propagation direction of dislocations discussed in Section 7.4.2. In the $[1-210]$ scratching direction, the stress is concentrated on one corner of the hexagon; while in the $[1-100]$ scratching direction, the stress will be concentrated on two corners and the left edge of the hexagon. The left edge of the hexagon pattern represents the $(1-100)$ plane in 3 dimensions.

Figure 7-27 compares the stress peak values in the machining area and the machined area using different scratching directions. The peak stress for $[1-210]$ and $[1-100]$ scratching directions are around 4500 MPa and 4000 MPa respectively. As discussed in Section 6.4, the stress peaks of dislocations on the Si face are 3816 MPa for the (0001) plane and 4584 MPa for the $(10-10)$ plane. When the stress value is higher than the critical stress for the occurrence of dislocations, dislocations will occur, allowing the local stress concentration to be released. Thus, it can be concluded that dislocations on (0001) plane are prone to occur in $[1-100]$ scratching direction, and dislocations on $\{1-100\}$ planes are prone to occur in $[1-210]$ scratching direction.





(c) [11-20]_ 3 nm



(d) [1-100]_ 3 nm

Figure 7-26. Stress distribution of workpiece using different scratching directions.

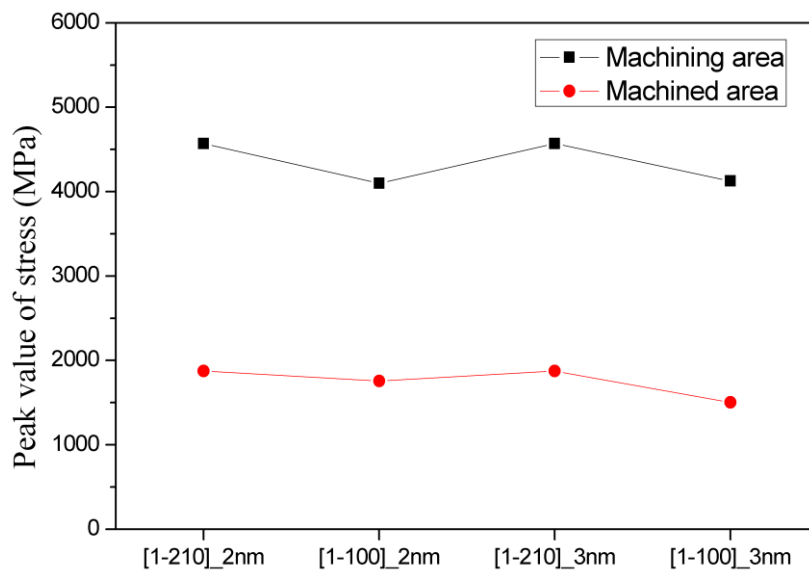
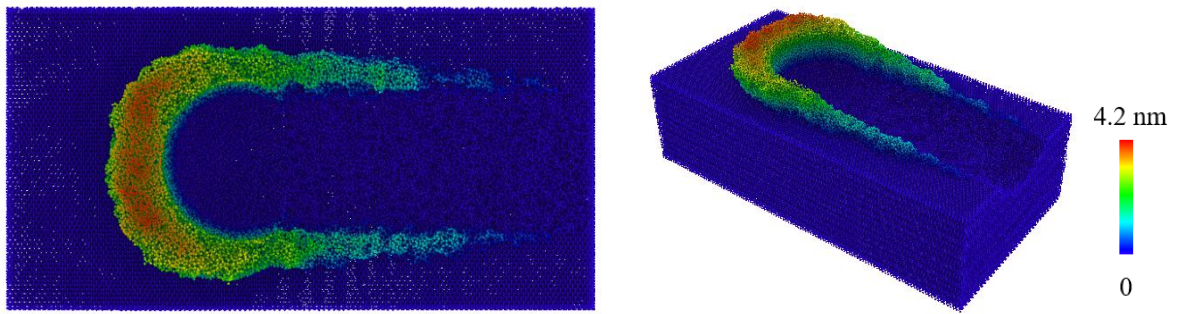


Figure 7-27. Maximum stress of machining area and machined area using different scratching directions.

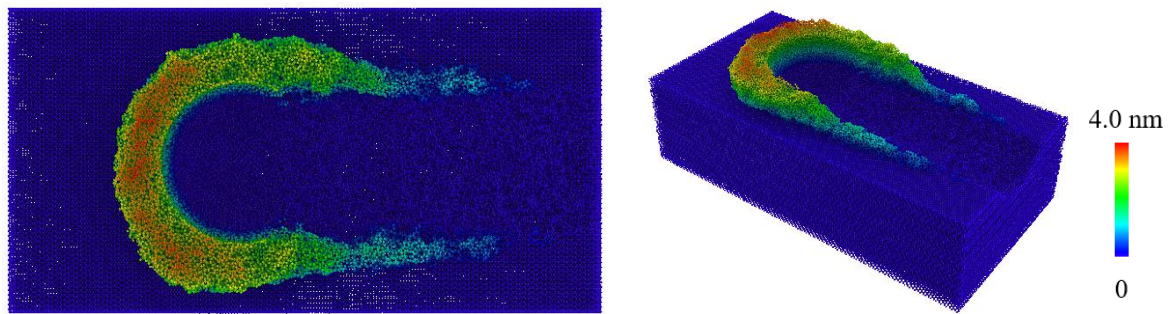
7.4.4 Material removal efficiency

Figure 7-28 shows the distribution of Z positions of atoms above the original surface in different scratching directions. It can be seen that there is no significant difference in the height of the material accumulation in different scratching directions. The uplifts of the

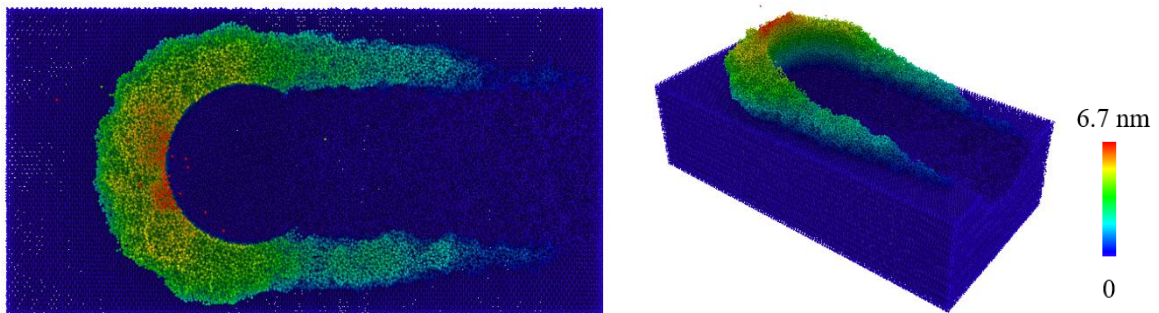
material on both sides of the groove show no obvious difference as well. This means that scratching has no effect on the plasticity and brittleness of the workpiece material. Figure 7-21 shows a comparison of the number of atoms above the surface and removed atoms using different scratching directions. There is no significant difference in the results in the two scratching directions.



(a) [11-20]_ 2 nm



(b) [1-100]_ 2 nm



(c) [11-20]_ 3 nm

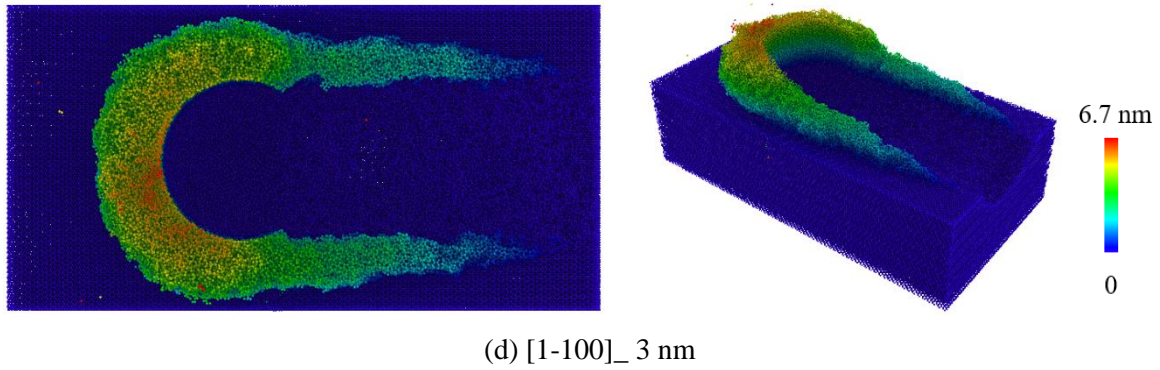


Figure 7-28. Distribution of Z positions of atoms above original surface using different directions.

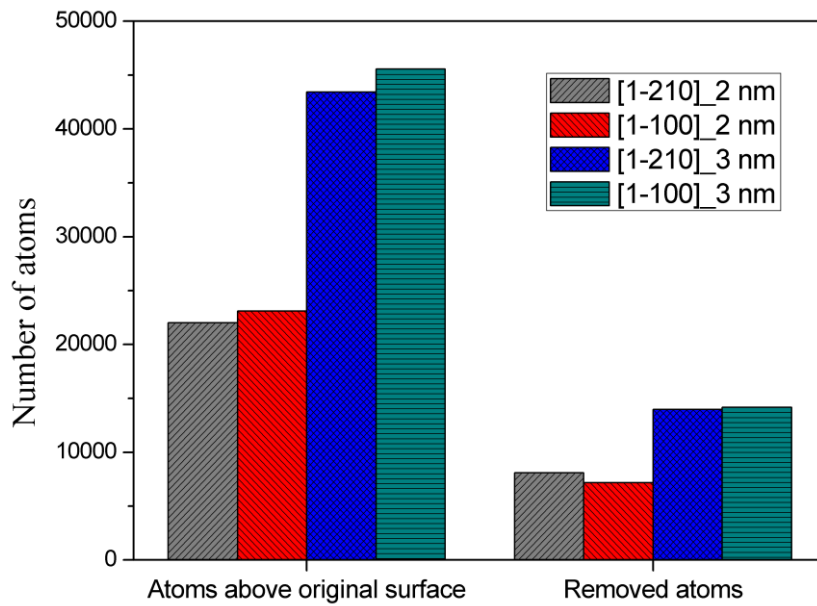


Figure 7-29. Numbers of atoms above original surface and removed atoms in subsurface.

7.5 Experimental verification

Some multiple grit scratching tests were carried out in order to verify the conclusions and phenomena found in MD simulations. The experimental set-up details have been presented in Section 4.3.

7.5.1 Effects of the shape of abrasive tip

Figure 7-30 shows the SEM results of three interesting scratches on the Si face of a 6H-SiC wafer. The scratching direction was [1-210] and the scratching speed was 10 m/s. These three scratches occurred at almost the same time and region, which means the three grits have the

same scratching depths. However, it is clear that the three scratches show different material deformations and cracks. For the scratch A, no distinct wrinkles or cracks occurred in the initial scratch stage, which means plastic removal is the main removal method in this case; for the scratch B, there were many wrinkles generated on both sides of the groove and then some cracks and brittle fractures occurred; for the scratch C, the wrinkles appeared at the same time as with the scratch B, but the cracks and brittle fractures occurred much earlier and more severely than scratch B.

These different phenomena in the three scratches mean the shapes of contact regions of the three grits are different. The slot width difference is the evidence of the grit shape difference. Compared with the simulation results in Figure 7-7, the widths, shapes and subsurface deformations of grooves formed by abrasives in different shapes were much different. Blunt grit shows higher stress or more dislocations than sharp grit, though using the same scratching depth. Therefore, it can be concluded that the shapes in nanoscale of grits have a significant influence on material deformations and removal mechanisms of the workpiece material. Due to the limitation of experimental and detective precision, it is difficult to verify the effect in nanoscale scratching of specific grit shapes in current experiments. This will be investigated in future works with the development of experimental and detective devices.

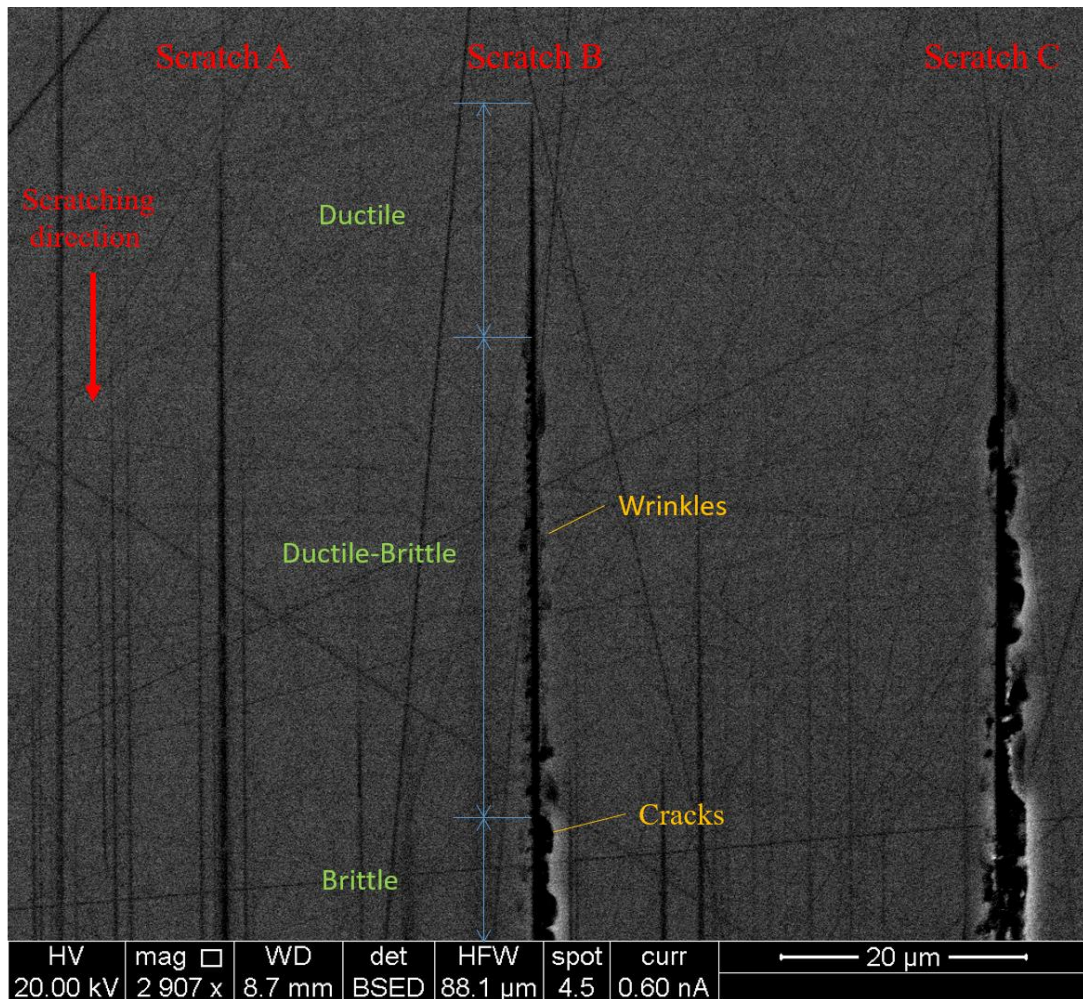


Figure 7-30. The SEM results of three scratches on Si face of 6H-SiC wafer. (Scratching direction: [1-210], scratching speed: 10 m/s)

7.5.2 Effects of the scratching speed

Figure 7-31 shows the SEM results of scratches obtained at scratch speeds of 1 m/s and 10 m/s. The scratches can be divided into three regimes, i.e., the ductile deformations, ductile–brittle transition, and brittle fractures, along the scratching direction according to the different surface morphologies of the residual grooves [135]. The scratch started with smooth surfaces and the sides of the grooves at a shallow scratching depth, implying the ductile regime. When the scratching depth increased, microcracks and minor fractures were found on the sides of the residual grooves. And then the fracture mode was dominant on the groove sides in the brittle deformation.

In this experiment, the abrasives cannot be accurately compared and the scratches in two scratching speeds cannot be compared directly, so the effect of speed on deformation is compared in terms of the average length of ductile deformations. Figure 7-32 illustrates the variation of the average lengths of ductile deformations of scratches which are shown in Figure 7-31. When the scratch speeds are 1 m/s and 10 m/s, the average length of ductile deformations are 37 μm and 58 μm respectively, in which the scratching depths are less than 1 μm . This means that at a lower scratching speed, the workpiece material is prone to the brittle deformation stage earlier. In other words, using a higher scratching speed, the 6H-SiC material shows better ductility, which is consistent with the conclusion obtained in MD simulations (Figure 7-20).

This phenomenon may be related to the scratching temperature. In the conventional machining of ductile materials, temperature has a significant effect on the generation of the surface metamorphic layer [39]. Temperature rise is a reflection of the heat generation in machining. The heat in machining is mainly generated from material shear and friction [39]. So higher scratching speed will cause the higher temperature of the material in the contact area, which makes the material exhibit better ductility [142, 143].

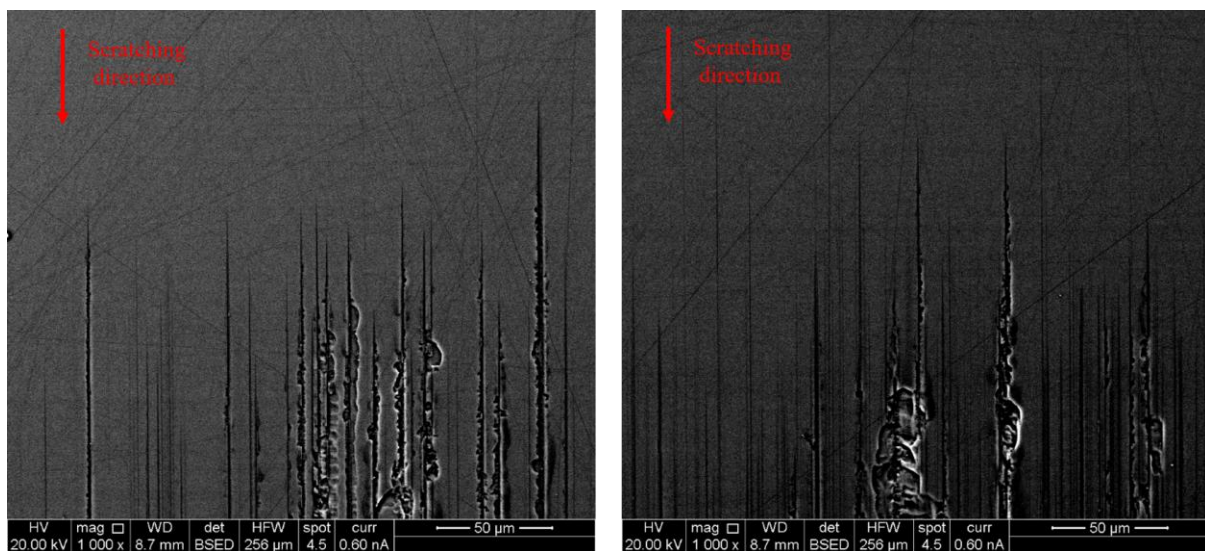


Figure 7-31. The SEM results of scratches in different scratching speeds. (Left: 1 m/s, right: 10 m/s)

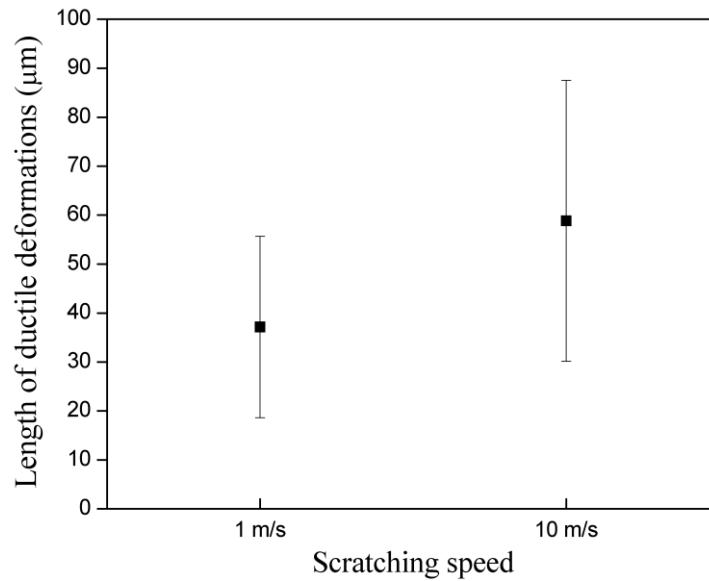


Figure 7-32. The average length of ductile deformations in different scratching speeds.

7.5.3 Effects of the scratching direction

Figure 7-33 shows the SEM results of scratches obtained in the scratch directions of [1-210] and [1-100]. It can be seen that in the two scratch directions, with the gradual increase in the scratching depth, the workpiece material has undergone plastic deformation, ploughing and brittle deformation. There are three forms of the brittle deformation, namely, wrinkles, microcracks and fractures. Figures 7-33 (c) and (d) compare the angles in the wrinkled area. It is clear that in the [1-210] scratching direction, the wrinkle angles are 60° , while in the [1-100] scratching direction, the wrinkle angles are 30° . This result is very consistent with the MD simulation results (Figure 7-25). This phenomenon can be considered as the consequence of the dislocations and slips along $\langle 1-210 \rangle$ orientations $\{1-100\}$ cylindrical planes, which are also found in nanoindentation tests (Figures 5-3 and 5-7).

In general, the effect of different scratching orientations has little effect on the removal efficiency, but has a significant effect on the deformation of the subsurface. And when the scratching depth is small (2 nm), the deformation is mainly amorphous and the difference is not obvious. The influence of scratching directions is more significant in larger scratching depth (greater than 3 nm) scratching due to the occurrence of dislocations.

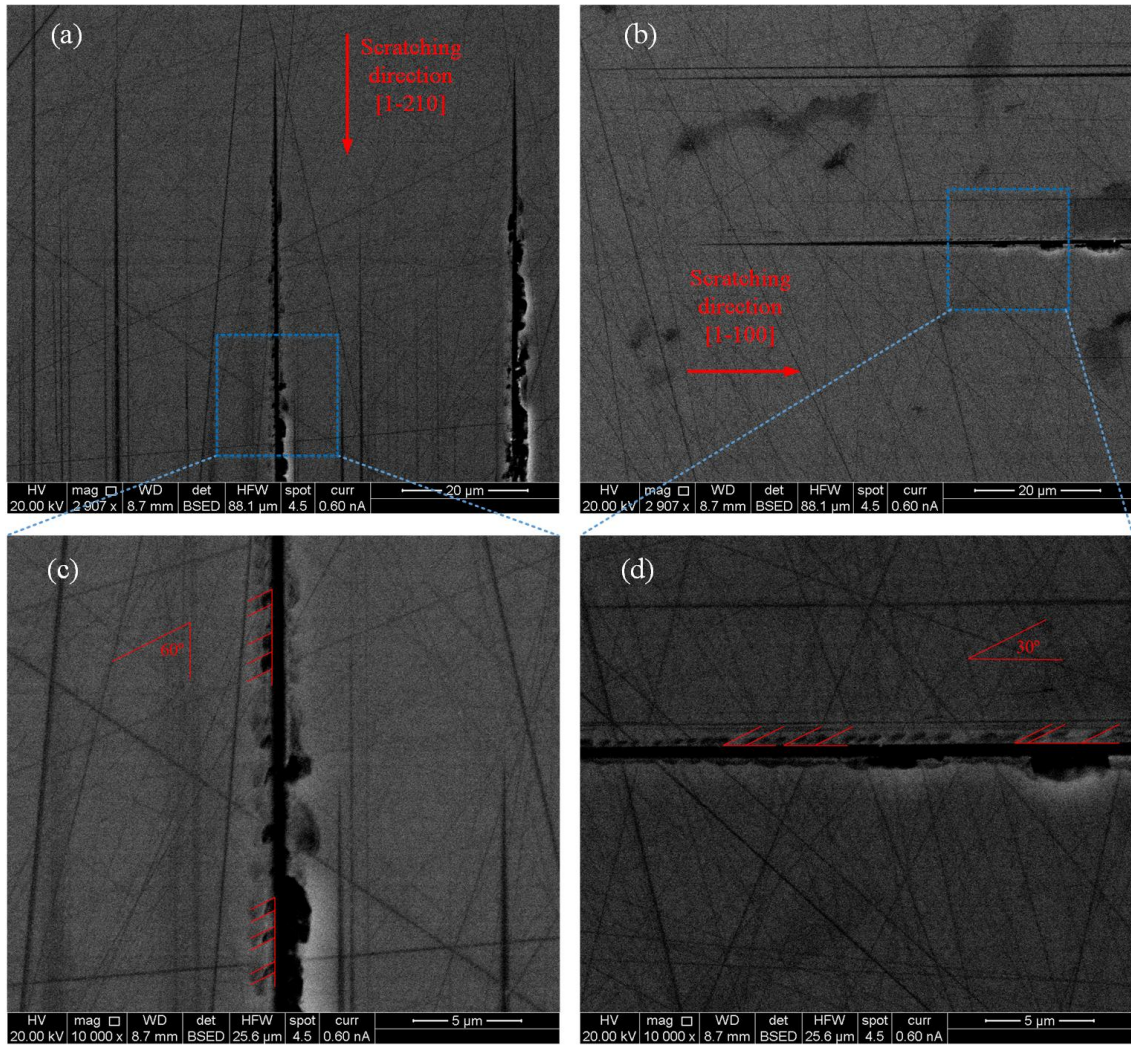


Figure 7-33. The SEM results of scratches on Si face of 6H-SiC wafer along different scratching directions. (Left: [1-210], right: [1-100]).

Chapter 8. Interfacial reaction

Both mechanical removal and chemical removal play significant roles in the ultra-precision polishing. The chemical products on the polished surface can be detected and analysed from experiments, while the mechanism of chemical reaction during polishing cannot be obtained directly from experiments. In order to shed light into the atomic chemical reactions occurring on the Si face and the C face of 6H-SiC during polishing, the RMD simulations were adopted.

Four RMD simulations were present in this chapter:

- The reactions between two faces of 6H-SiC and H₂O molecules with the temperature rising from 293 K to 3106 K.
- The reactions between two faces of 6H-SiC and H₂O molecules at the constant temperature of 2100 K.
- The reactions between the Si face of 6H-SiC and H₂O molecules at 2100 K, with the diamond slab loading at an upward speed of 10 m/s.
- The reactions between the C face of 6H-SiC and H₂O molecules at 2100 K, with the diamond slab loading at a downward speed of 10 m/s.

8.1 Reaction of SiC and H₂O during the heating process

SiC and H₂O are not reactive in normal conditions, while when temperature gets higher, the chemical reaction will occur. According to the simulations of SiC and H₂O molecules by Newsome [78, 79], the chemical reaction occurred after the temperature went to 2000 K and was much more intense at 4000 K. In addition, it was reported that the chemical reaction between 4H-SiC and H₂O molecules would occur from 1174 K to 1474 K [80]. Thus, the simulation to study the temperature of the chemical reaction between 6H-SiC and H₂O was carried out.

In this simulation, the water molecules of both sides were in the same condition due to the periodic boundary. The temperature rose from 293 K to 4000 K in 100 ps, and the process was shown in Figure 8-1. As time went by and the temperature rose, both Si face and C face of 6H-SiC were oxidized by H₂O molecules gradually. And silicon oxide, the production of

the reaction, also occurred on both sides. It is worth noting that the reaction occurred much more intensely and earlier on the C face than the Si face.

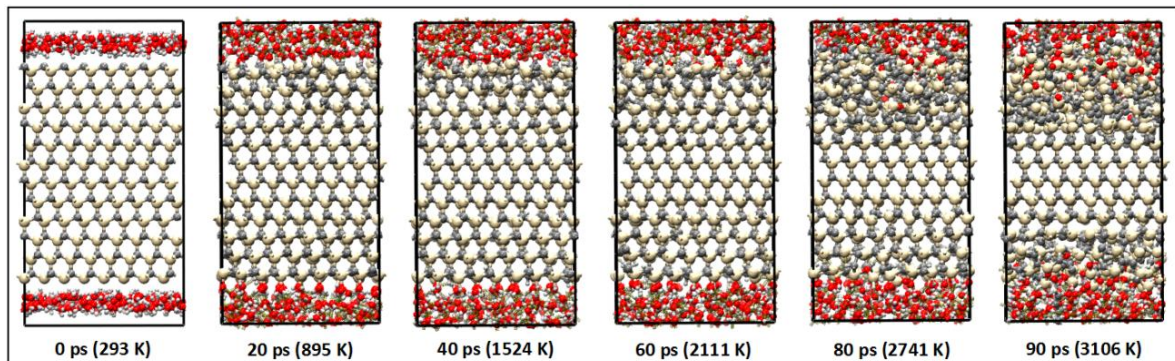


Figure 8-1. RMD simulation snapshots of the reactions between two faces of 6H-SiC and H₂O molecules with the temperature rose from 293 K to 3106 K.

8.2 Reaction of SiC and H₂O in the constant temperature

As the results shown in Section 8.1, the chemical reactions on the Si face occurred when the temperature reached 2100 K. So the simulation at the constant temperature of 2100 K was carried out to compare the differences between C face and Si face, and the process was shown in Figure 8-2. Both the Si face and C face reacted with the H₂O molecules, even though the reaction occurring on the C face was much more than on the Si face. It is also remarkable that only the first layer of Si atoms on the Si face had been oxidized before 90 ps. After that, there were only a few reaction occurring in the substrate on the Si face. In addition, with the reaction occurring, the lattice structure of the substrate of 6H-SiC was destroyed, and the substrate atoms of the C face were more disordered than those of the Si face.

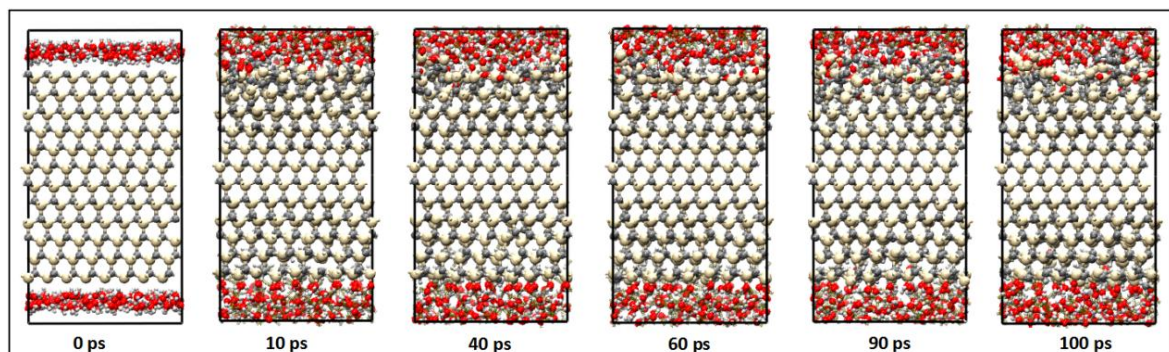
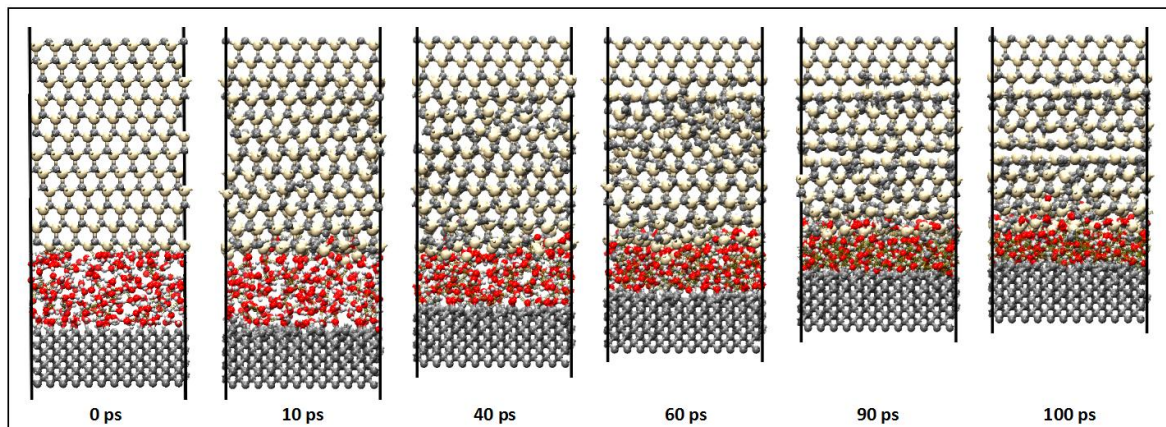


Figure 8-2. RMD simulation snapshots of the reactions between two faces of 6H-SiC and H₂O molecules at the constant temperature of 2100 K.

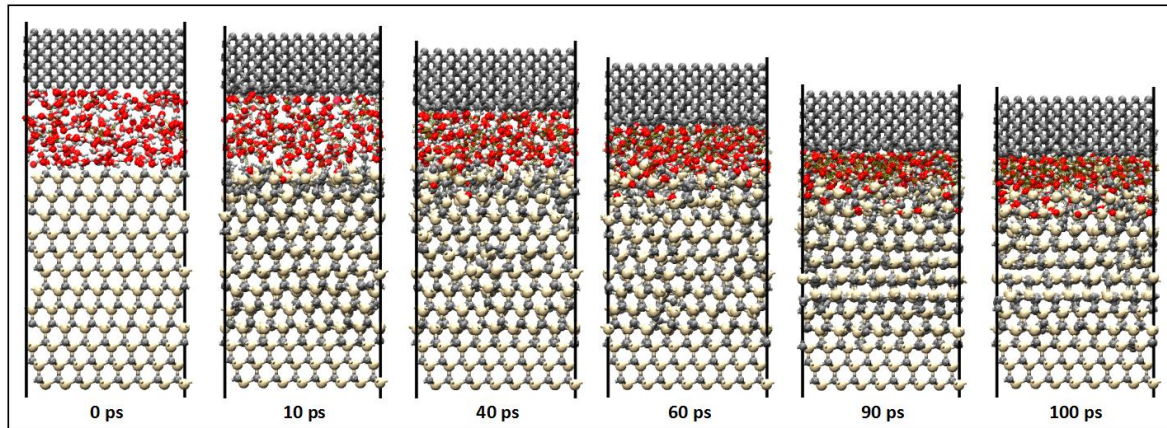
8.3 Reaction of SiC and H₂O during the loading process by diamond

Two RMD simulations had been conducted to imitate the different polishing processes of the Si face and C face of 6H-SiC. In the nano scale, the polishing process of workpiece materials can be simplified to be realized by temperature and stress. In order to be closer to the experimental conditions, the diamond slab was added. As shown in Figures 3-8 (b) and (c), the diamond slab moved upward to the Si face in one simulation and downward to the C face in another simulation, with the speed of 10 m/s. The temperature was set at 2100 K, because the reaction could occur on both faces at this condition.

Some snapshots during these two simulations are shown in Figure 8-3. It can be seen that both the Si face and C face of 6H-SiC had reacted with H₂O molecules under the load from the diamond slab. Compared with the Si face, the C face of 6H-SiC reacted more easily and more intensely in the same conditions, which was consistent with the results without load (Figure 8-2). In addition, it is worth noting that the reactions were easier and more intense under the load, and the difference in the reaction speed and extent between Si face and C face were smaller than that in the conditions without load. In other words, the load from the diamond slab promotes the reaction between 6H-SiC and H₂O molecules.



(a)



(b)

Figure 8-3. RMD simulation snapshots of: (a) the reactions between the H₂O molecules and Si face of 6H-SiC and at 2100 K, with the diamond slab loading at an upward speed of 10 m/s; (b) the reactions between the H₂O molecules and C face of 6H-SiC and at 2100 K, with the diamond slab loading at a downward speed of 10 m/s.

8.4 Comparison of simulation and experimental results

In this section, in order to improve the reliability of the RMD simulations, the RMD results are compared with the experimental polishing results in reference [30].

In Luo's polishing experiments [30], the MRR of the C face (6.13 nm/min) of 6H-SiC wafers was much higher than that of the Si face (2.55 nm/min). In all four RMD simulations, the chemical reactions on the C face were faster and more intense than those on the Si face. The reaction productions, such as silicon dioxide and hydrocarbons, are much softer than SiC lattice, and can be removed easily, which leads to a much larger MRR of the C face.

In addition, as shown in Figures 8-4 (a) and (b), the silicon dioxide generated on the Si face is more regular than that generated on the C face. In statistical mechanics, the radial distribution function describes how density varies as a function of distance from a reference particle [144]. Figure 8-5 (c) shows the radial distribution functions of Si-O on the Si face, C face and in SiO₂ lattice. The Si-O on the Si face and SiO₂ lattice show the same peak at 1.6 Å, which means the silicon dioxide generated on the Si face is in good crystalline structure. However, the Si-O on the C face has no peak at 1.6 Å and even no distinct peak on the entire curve. So the silicon dioxide generated on the C face is in amorphous structure.

This phenomenon is also consistent with the experimental results in reference [30]. Figure 8-5 shows the detection results of debris on Si and C faces of 6H-SiC wafers after polishing using the SG semi-fixed abrasive polishing tool. The wear debris of the Si face were curl strips, with a thickness of about 5-10 nm, while that of the C face were shards of several tens of nanometres [30]. The crystallization of the wear debris of the Si face was relatively regular, and the spacing of the lattice fringes in the high-resolution diagram was about 3.38 Å (Figure 8-5 (a)). The SAED pattern on the Si face showed a distinct polycrystalline concentric ring, with the inter-planar crystal spacing of 3.38 Å (Figure 8-5 (b)). However, the atomic arrangement of the wear debris of the C face had no periodic variation and no obvious crystalline state, but only a halo, indicating that the wear debris were in the amorphous phase, as shown in Figure 8-5 (c).

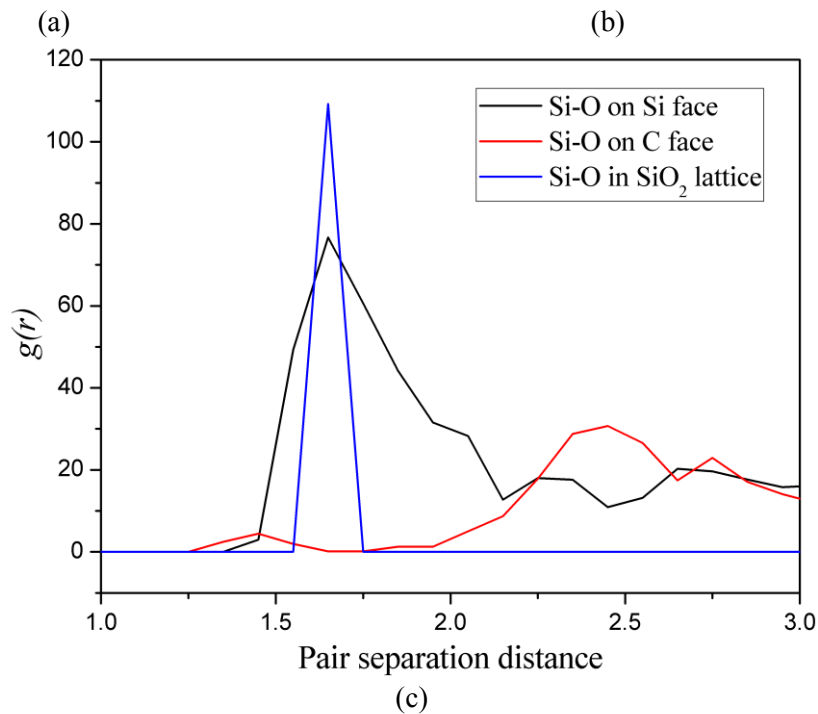
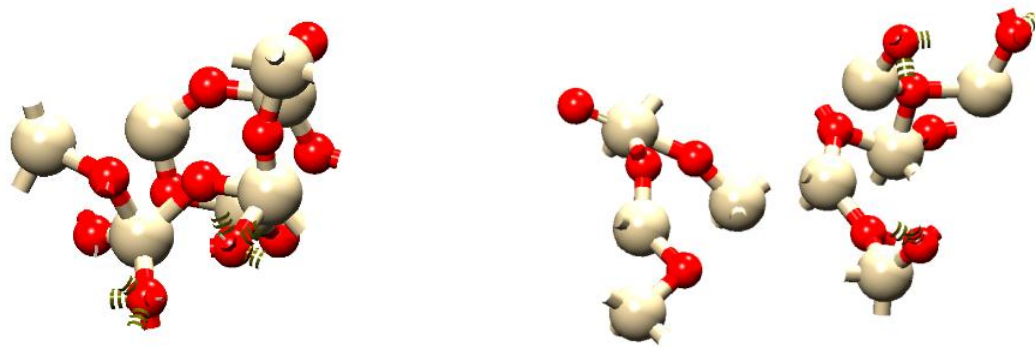


Figure 8-4. (a) Silicon dioxide generated on the Si face. (b) Silicon dioxide generated on the C face. (c) Radial distribution functions of Si-O on Si face, C face and in SiO₂ lattice.

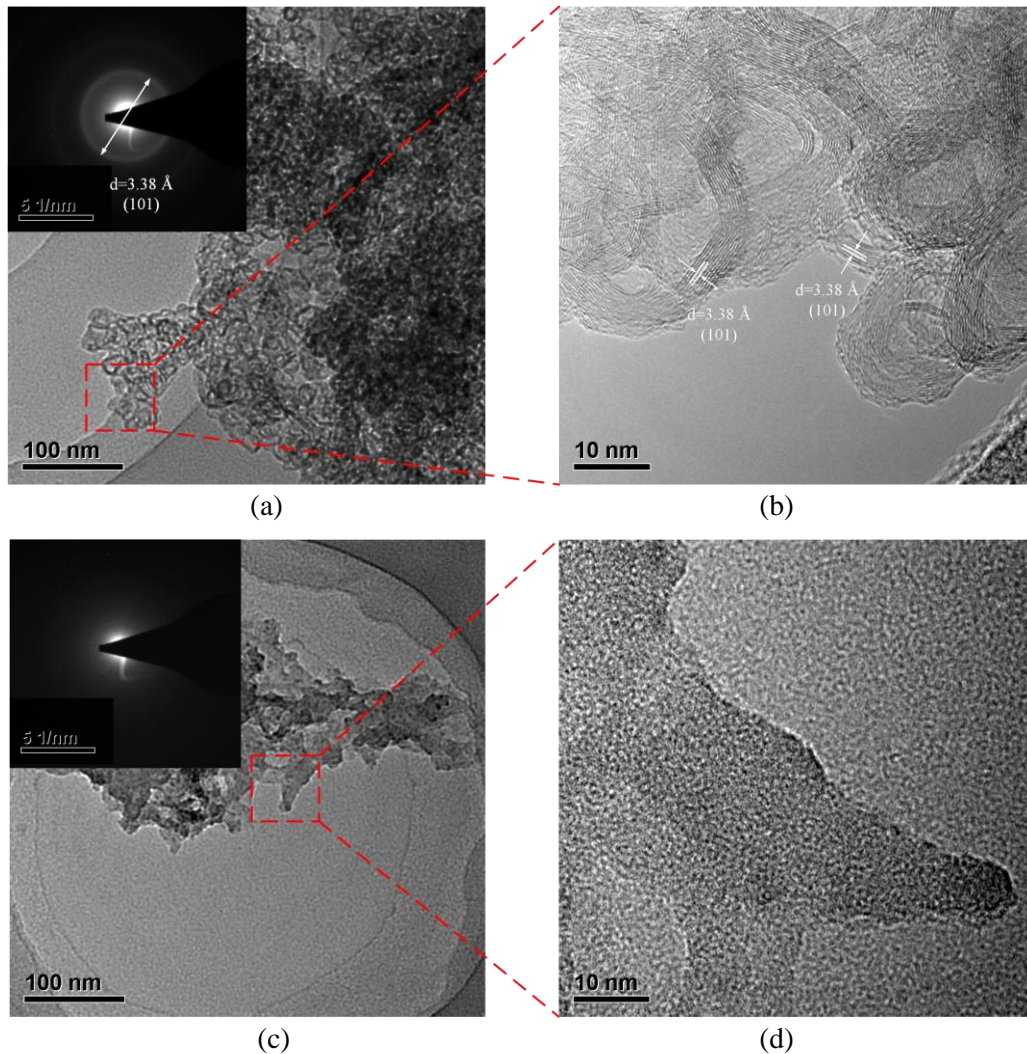


Figure 8-5. Detection results of debris of 6H-SiC wafers [30]. (a) TEM image and SAED pattern of Si face. (b) High resolution diagram of Si face. (c) TEM image and SAED pattern of C face. (d) High resolution diagram of C face.

The results of RMD simulations were highly consistent with the experimental results. Not only the presence of SiO₂ was found on both the Si face and C face of 6H-SiC, but also the reaction on the C face was faster than that on the Si face, which led to a much larger MRR of the C face. In addition, the silicon dioxide generated on the Si face was more regular than that generated on the C face. Accompanied with the experimental results, it can be concluded the main component of the wear debris of the Si face was crystallized silicon dioxide and that of the C face was amorphous silicon oxide.

8.5 Reaction mechanism during polishing

It is generally believed that Si atoms are more susceptible to be oxidized than C atoms [8], while in this simulation, the atoms in the C face were more likely to react with H₂O and form SiO₂. This is because the Si atoms on the surface of the Si face reacted with the H₂O molecules and formed the Si-O bonds which were relatively stable. On the contrary, the Si atoms under the C face could not directly react with the H₂O molecules and then were in a metastable state. As the temperature increased and the atomic motion became more intense, the Si-O bonds did not change significantly, while the lattice structure of the first C layer on the C face was destroyed, which led to the entry of H₂O molecules. Therefore, the Si atoms of the first Si layer on the C face could contact and react with the H₂O molecules gradually. After that, the second C layer was exposed to the H₂O molecules, and then the second Si layer was oxidized similarly (Figure 8-6). In this cycle, the Si atoms under the C face were quickly oxidized, and those under the Si face were not oxidized until the temperature went up to 2100K.

The occurrence and extent of the reactions were affected by whether the lattice structures of 6H-SiC were destroyed easily. The lattice structures of both faces of 6H-SiC were much easier to be destroyed under the load from the diamond slab (Figure 8-3), so the reactions occurred more easily than those without load (Figure 8-2). Moreover, the different extent of the lattice structure destruction caused the difference in reaction extent between the Si face and C face. So the difference between the Si face and C face gets smaller due to the load which causes similar destruction of the lattice structure.

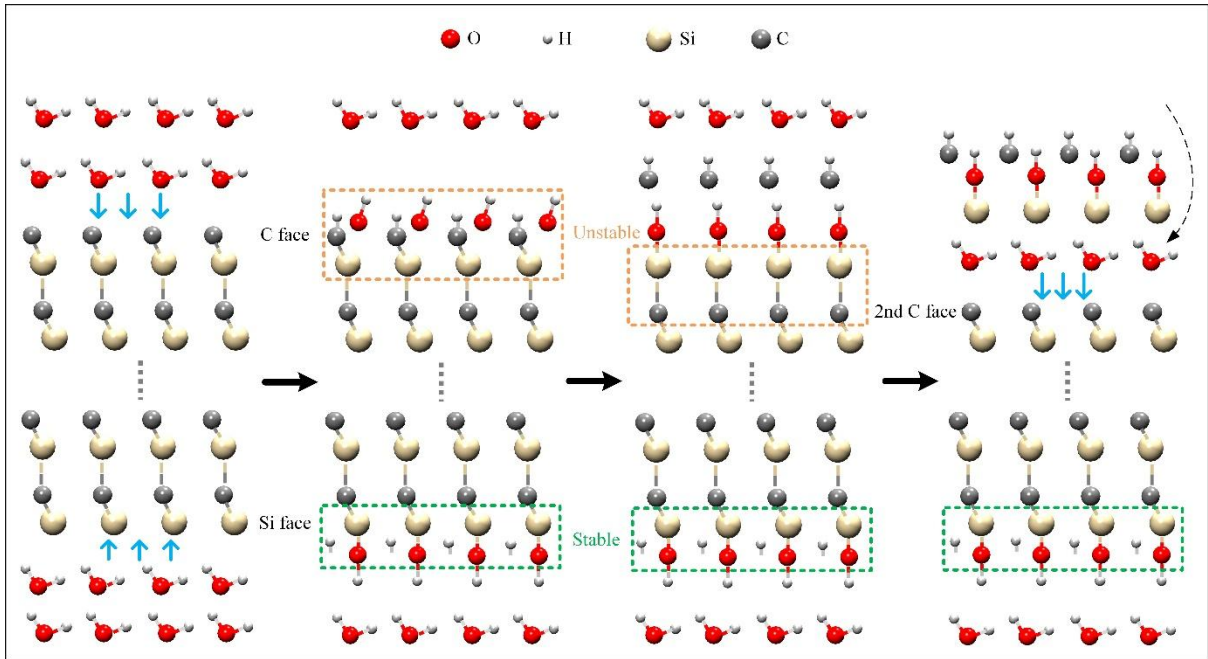


Figure 8-6. Schematic diagram of interface reaction between two faces of 6H-SiC and H₂O molecules.

Since the diamond abrasives and the 6H-SiC wafers had excellent chemical stability, chemical reactions are unlikely to occur on the surface just using deionized water as the coolant without any acid-based etching solution. However, fine abrasive particles would generate a large amount of mechanical energy due to loading and friction with the surface of the 6H-SiC wafers [30]. Some of the mechanical energy was directly converted into chemical energy, which effectively reduced the reaction activation energy, then increasing the chemical reaction rate [30].

Compared with the polishing results in literature [30], some new explanations for the chemical reaction between SiC and water could be provided. These procedures also can be considered as the consequence of the destruction of the lattice structure. Loading from diamond abrasive destroys the lattice structure of SiC, so the H₂O molecules can pass through the first layer of SiC and react with the Si atoms in the subsurface. Therefore, chemical reactions which are difficult or very slow to carry out at room temperature could be achieved by increasing mechanical load and friction. It should be clarified that although the experiments were performed at room temperature, the real temperature of the contacting area at nanoscale were much higher. It is hard to detect the real temperature of a nanoscale region during polishing, while the critical temperature allowing chemical reactions to occur on the Si face is 2100K in RMD simulations.

In conclusion, both the polishing experiments in previous literature [30] and the RMD results show that the occurrence of silicon dioxide in the conditions of pure water as the cooling liquid, indicates that the 6H-SiC wafers can be oxidized by the water during polishing without any acid or alkali conditions. The material on the C face of 6H-SiC is oxidized faster than that on the Si face, directly resulting in the larger material removal efficiency of the C face than the Si face in the same conditions. The discovery of this phenomenon in this research leads to a further understanding of the nanoscale chemical mechanism during polishing silicon carbide substrates. This reaction also can be controlled by adjusting the parameters of the polishing experiment to obtain the silicon carbide substrates with good surface quality more efficiently.

Chapter 9. Effect of oxide layer

Both mechanical removal and chemical removal play significant roles in the ultra-precision polishing. The chemical reaction products on the wafer surface will affect the polishing performance as well. Therefore, in this chapter, the effect of the oxide layer generated on 6H-SiC surface during polishing process will be investigated.

9.1 Nanoscratching simulation at constant depths

The polishing process is accompanied by the occurrence of chemical reactions and the production of chemical products, which will have an impact on the removal of materials. In this section, the scratch simulations of different scratch depths are performed on the 6H-SiC surface with the oxide layer. The differences in the removal effect between the presence and absence of the oxide layer and between the oxide layer on the C face and Si face will be compared.

9.1.1 Forces

Figure 9-1 shows the tangential and normal forces of the Si face and C face with the oxide layer during scratching. At different scratch depths, the normal and tangential forces of the Si face are greater than those of the C face, which is consistent with the scratching simulation and experimental results when there is no oxide layer on the SiC surface.

It is worth noting that when the scratch depth is small, only the atoms of the oxide layer are removed, and the difference between the Si face and the C face is small. As analysed in Chapter 8, the Si face undergoes a chemical reaction to produce crystalline silicon dioxide, while the C face produces amorphous silicon oxide. So, the oxide layer on the Si face is harder to remove than the oxide layer on the C face, which leads to the greater scratching force on the Si face. Because there are a lot of amorphous structures in both faces, the forces are still much less compared to scratching the SiC with the perfect crystal lattice. As the scratch depth increases, the removed atoms are not only oxide atoms, but also silicon carbide atoms of perfect lattice. According to the results of Section 6.4, the Si surface is harder than the C surface, so the forces of the Si face are greater than those of the C face as well.

Therefore, it can be concluded that regardless of the presence or absence of an oxide layer, the force of the Si face is greater than that of the C face, which means that the material on the C face is easier to remove than that on the Si face. As concluded in Luo's polishing experiments [27], the material removal rate on the C face is higher than that on the Si face.

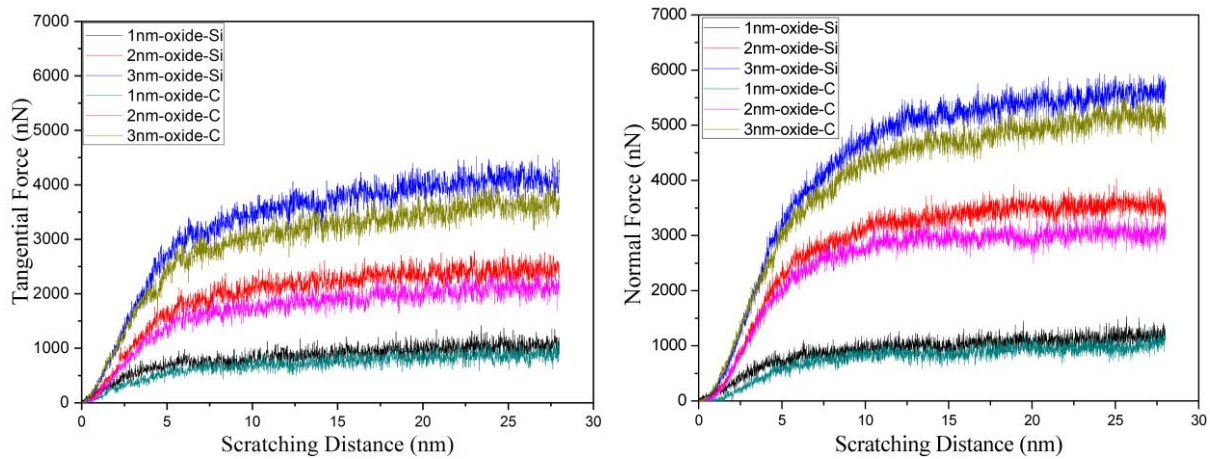


Figure 9-1. Tangential (left) and normal (right) forces of Si face and C face with the oxide layer.

In addition, Figure 9-2 also compares tangential forces on Si face (left) and C face (right) with and without the oxide layer. When the scratch depth is 1 nm, the tangential force of the surface with the oxide layer is less than that of the surface without the oxide layer. This is because the oxide layer is softer and easier to remove than the silicon carbide atoms with the perfect lattice. As the scratch depth increases, the removed atoms are not only oxide atoms, but also silicon carbide atoms of perfect lattice. Especially when the scratch depth is 3 nm, the force of the surface with the oxide layer is greater than that of the surface without oxide layer. More atoms are removed in the surface with the oxide layer due to the presence of oxygen atoms. So, the oxide layer is no longer the main factor when the scratch depth is large, and the main factor becomes the number of atoms removed.

Therefore, it can be inferred that the oxide layer can significantly reduce the force and improve the material removal efficiency in the case using a small scratching depth, but when the scratch depth gets larger, the oxide layer may not have a beneficial effect.

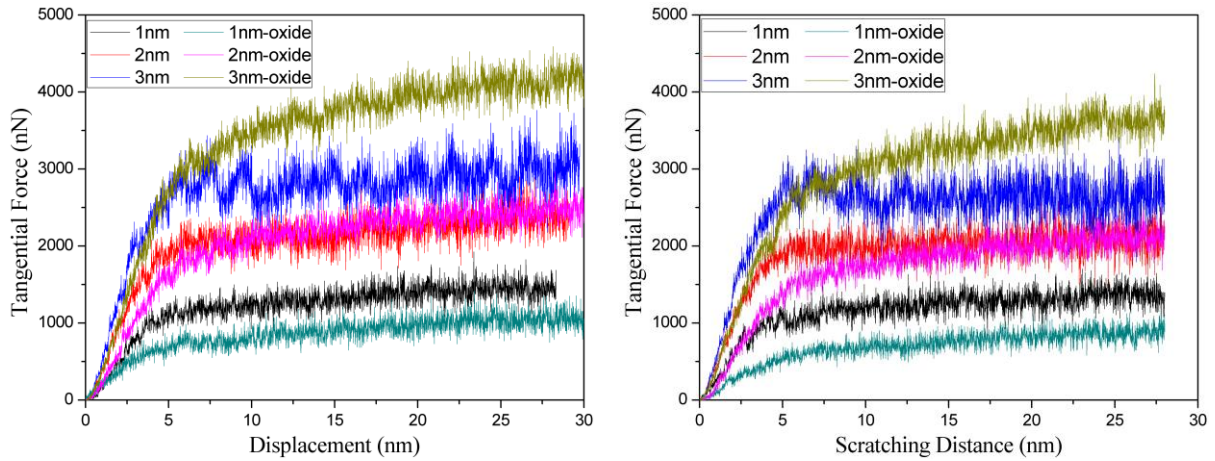
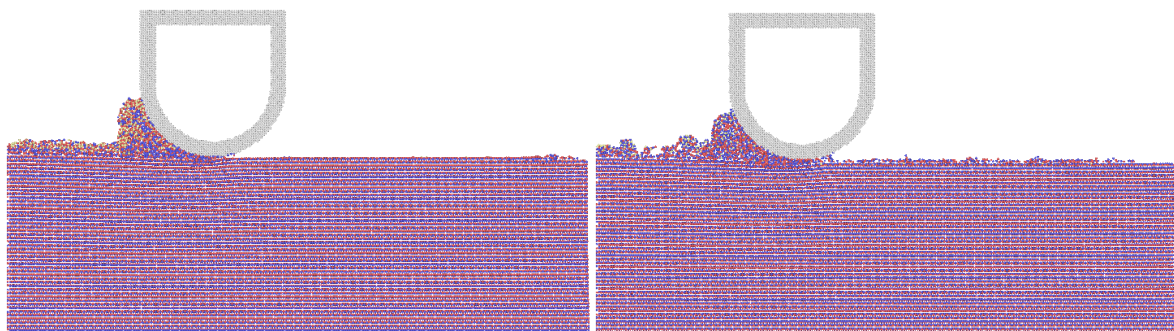


Figure 9-2. Comparison of tangential forces on Si face (left) and C face (right) with and without the oxide layer.

9.1.2 Material removal characteristics

Figure 9-3 compares the material removal characteristics on the Si face (left) and C face (right) with the oxide layers. When the scratch depth is 1 nm, the atoms of the oxide layer on the Si face are almost completely removed, while the atoms of the oxide layer on the C face are not totally removed and some of them still remain on the surface. In addition, all wear debris are atoms from the oxide layer, and the SiC atoms with perfect lattice are not destroyed. So it can be inferred that the strip-shaped silicon oxide in wear debris shown in Figure 8-6 (b) is generated at a small scratch depth. When the scratch depth is 2 nm, the atoms of the oxide layer and the SiC atoms with perfect lattice are both removed. So, the scratching debris are the mixtures of amorphous silicon oxide and SiC atoms. When the scratch depth is 3 nm or greater, the wear debris are mainly SiC atoms and a small number of silicon oxide atoms.



(a) 1 nm

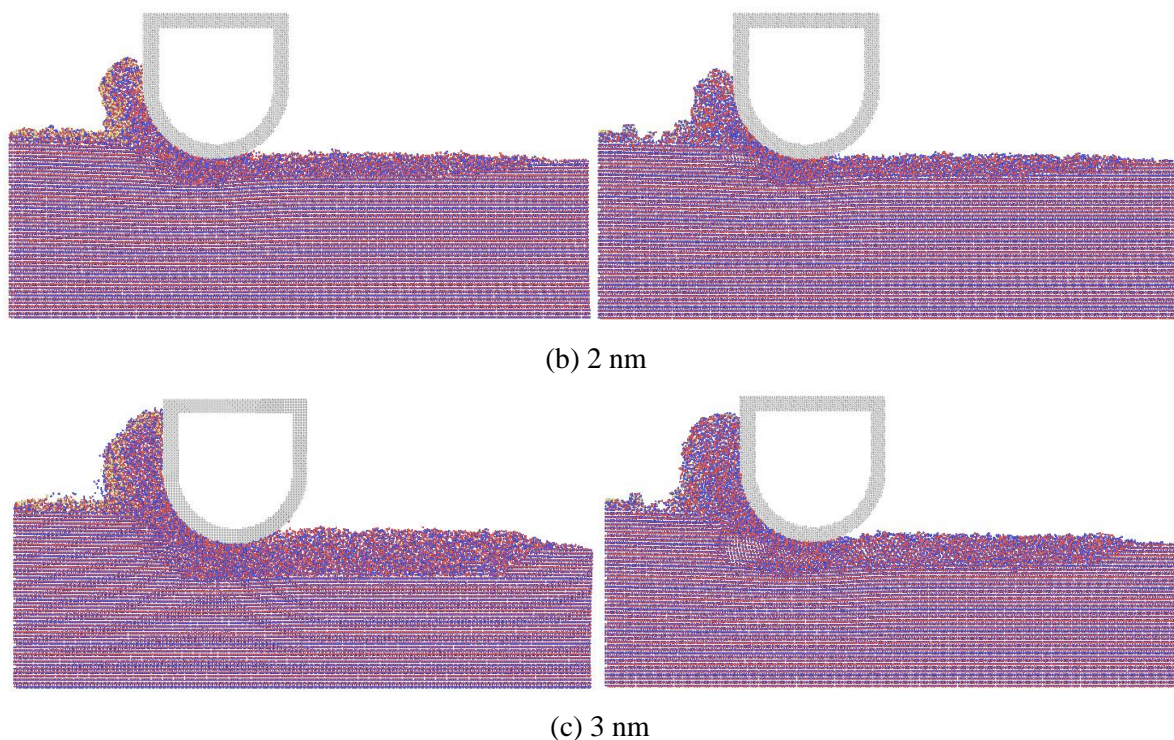


Figure 9-3. Comparison of material removal characteristics on Si face (left) and C face (right) with the oxide layers.

9.1.3 Subsurface deformation

In this section, the Si face is selected to investigate the subsurface deformation in the material removal of the oxide layer. Figure 9-4 shows the DXA results of the Si face in different scratching depths. When the scratch depth is 1 nm, no amorphous SiC atoms are produced on the surface. When the scratch depth is 2 nm, an obvious amorphous layer of SiC is formed on the subsurface, and dislocations occur concomitantly. When the scratch depth is 3 nm, there are more amorphous atoms and dislocations in the subsurface. In particular, these dislocations are mainly on the basal plane, and cylindrical dislocations have not been found. Compared with the scratch results on the SiC surface without the oxide layer, we can see that the presence of the oxide layer makes dislocations more likely to occur on basal planes. As discussed in Chapter 6, dislocations on basal planes facilitate material removal. Therefore, it can be concluded that the material removal process involving chemical reactions is better than pure mechanical removal.

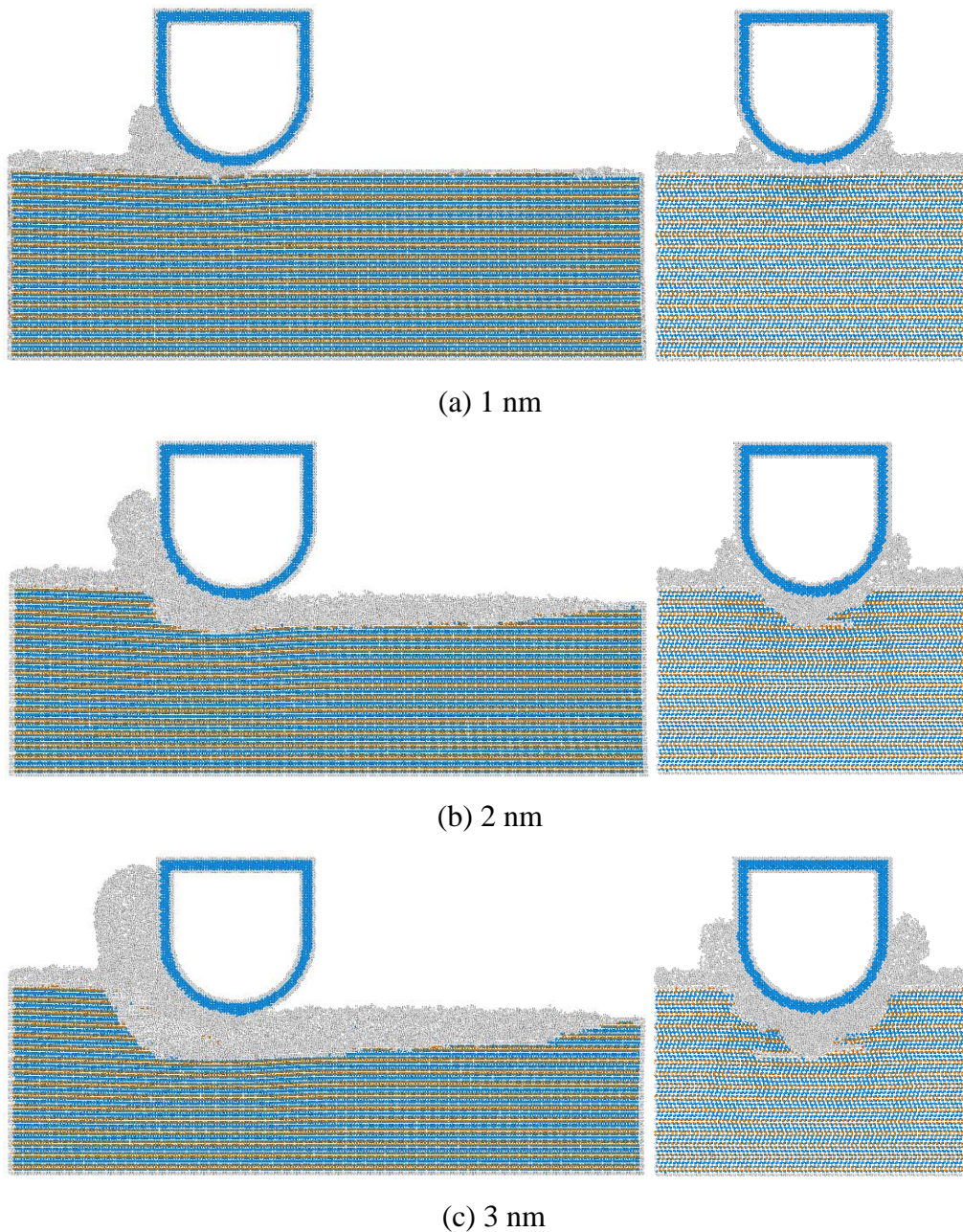


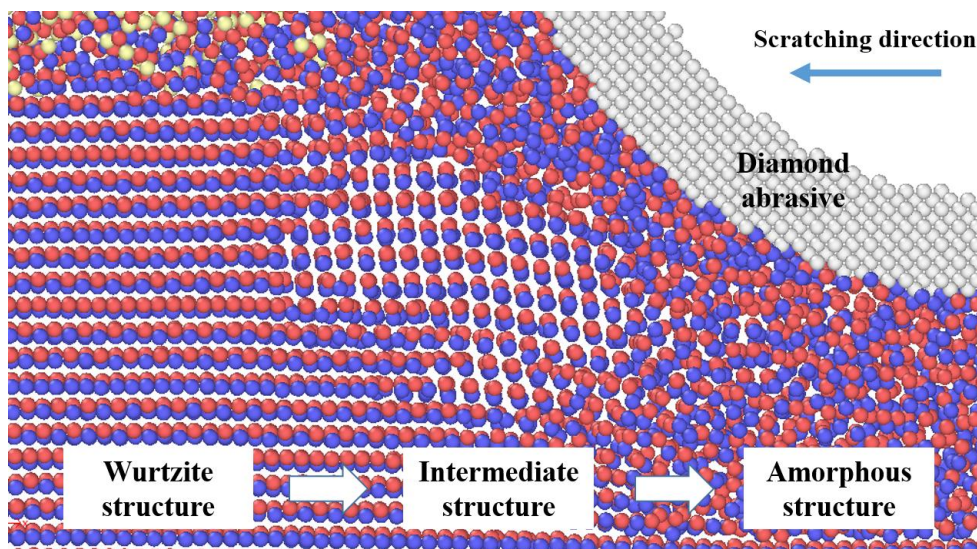
Figure 9-4. DXA results of Si face in different scratching depths.

In addition, in Figure 9-3 (c), it is worth noting that the arrangement of SiC atoms in a region below and in front of the abrasive is clearly different from that of perfect lattice atoms and amorphous atoms. The distance between atoms in this region is significantly different from that between atoms in the perfect lattice, which are 0.218 nm and 0.149 nm respectively. This structure in the region is regarded as the intermediate structure in the previous literature. In Wu's indentation experiments and simulations, the author believes that the amorphization is

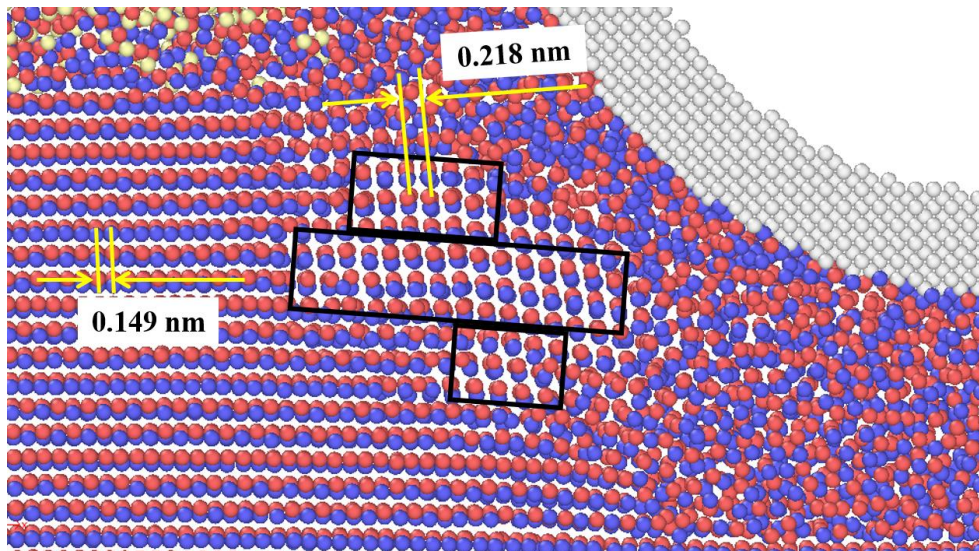
confirmed to be achieved via an initial transformation from wurtzite structure to an intermediate structure, and then a further amorphization process [59].

This phenomenon also occurs during scratching. When the scratching depth is less than 2 nm, the intermediate structure is not found; only when the scratching depth comes to 3 nm, does it occur. It might be inferred that the intermediate structure indicates the initial sign of brittle deformation during scratching. If the scratching depth gets much larger (larger than 10 nm), this intermediate structure may transform into small broken pieces retaining regular crystal structure.

Furthermore, in the scratching, this intermediate structure can be divided into three small areas. Obviously, each small area contains three layers of SiC atoms, which is related with the conclusion drawn in Section 7.1. The deformation of 6H-SiC is more likely to occur in the conversion layer with every three layers as a unit.



(a)



(b)

Figure 9-5. Intermediate structure in subsurface.

9.2 Nanoscratching simulation in an inclined direction

In actual processing, a wafer surface without subsurface damage is demanded. In order to figure out the critical condition in which subsurface damage (including amorphous structure) does not occur, this section performs the variable-depth scratching simulations with the oxide layer on the Si face and the C face of 6H-SiC.

Figures 9-6 and 9-7 show the trends of normal and tangential forces on two faces. From the trends of the normal forces, it can be seen that both the Si face and the C face undergo a rapid increase in the range from 1300 to 2200 nN. This means only the atoms of the oxide layer are removed under the load less than 1300 nN, because the corresponding scratch depth is exactly the thickness range of the oxide layer. The "small plateau" at 2200 nN means the pop-in stage when the abrasive scratches down into the SiC atoms. Therefore, when the load is 2200 nN, the perfect crystal lattice of the SiC is destroyed and then transforms into the amorphous structures. Therefore, the critical point should be within this load range.

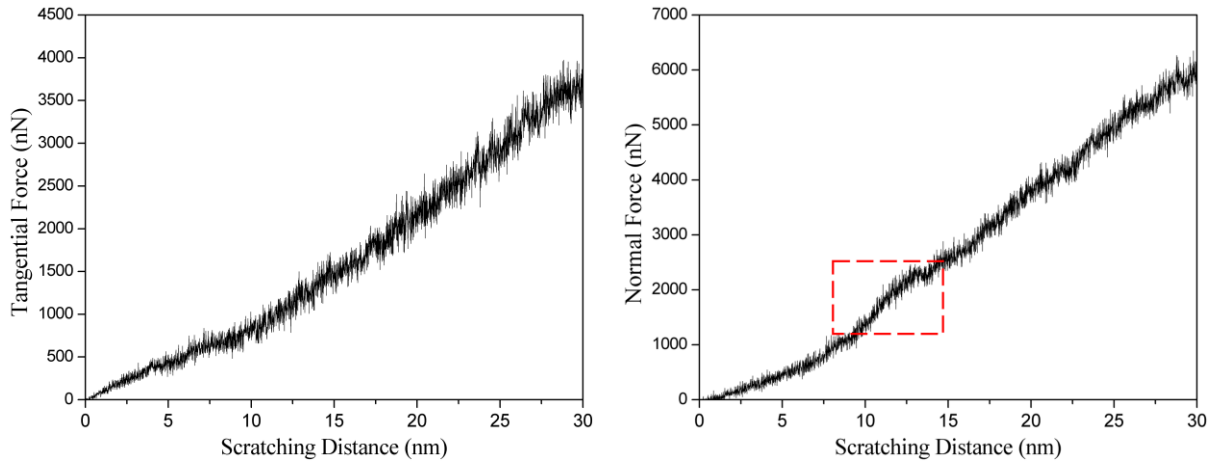


Figure 9-6. Tangential (left) and normal (right) forces of Si face with the oxide layer.

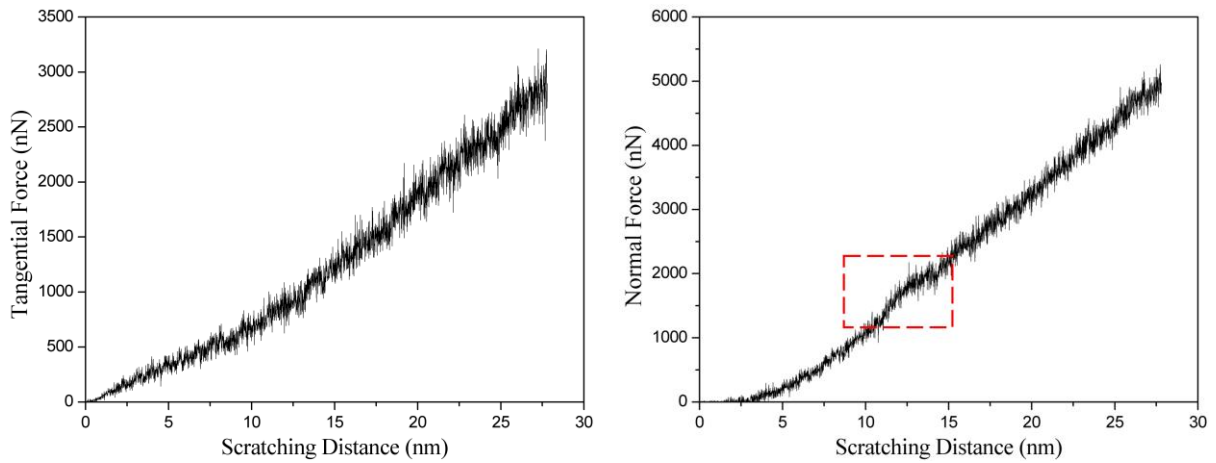


Figure 9-7. Tangential (left) and normal (right) forces of C face with the oxide layer.

Figure 9-8 shows the DXA results of both faces with the oxide layer in variable-depth scratching simulations. In the initial stage, only the atoms of the oxide layer are removed, so no subsurface deformation occurs. As the scratching depth gradually increases, the abrasive begins to scratch into the SiC layer. From then on, SiC atoms with an amorphous structure appear in the subsurface.

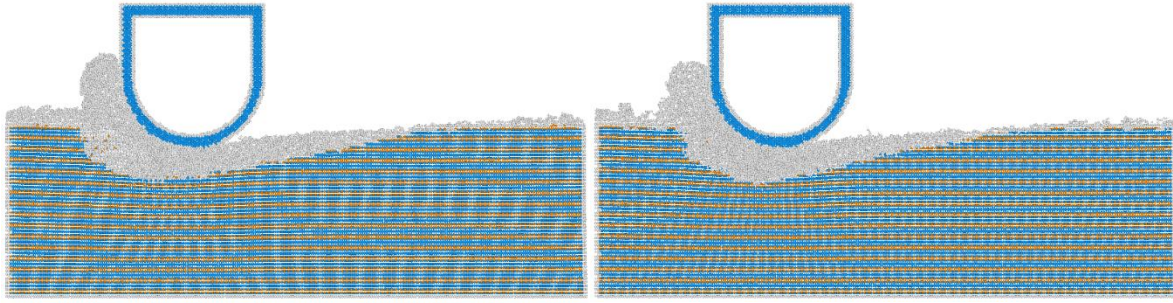


Figure 9-8. DXA results of Si face (left) and C face (right) with the oxide layer in variable-depth scratching simulations.

9.3 Nanoscratching simulation under constant loads

The best way is to remove only the atoms in the oxide layer without scratching the atoms in the perfect lattice. However, this is difficult to achieve by adjusting the scratching depth in actual polishing, because the removal depth is generally adjusted by controlling the load. Therefore, this section will perform a constant load scratching on the 6H-SiC surface with the oxide layer in order to figure out the critical load that can achieve accurate removal.

Figures 9-9 and 9-10 show the trends of normal forces of both faces with the oxide layer during constant-load scratching. The first 5 nm scratch part represents the initialization stage with a load of 1100 nN, which makes the load stabilize quickly. In the next 5 nm scratch part, the load gradually increases to a certain load. After 10 nm, the abrasive begins to scratch stably with a constant load. According to the results of the previous section, the load ranges of the Si face and C face are set between 1360 nN and 2000 nN. It can be seen that even in the stable scratch stage, the normal load still fluctuates.

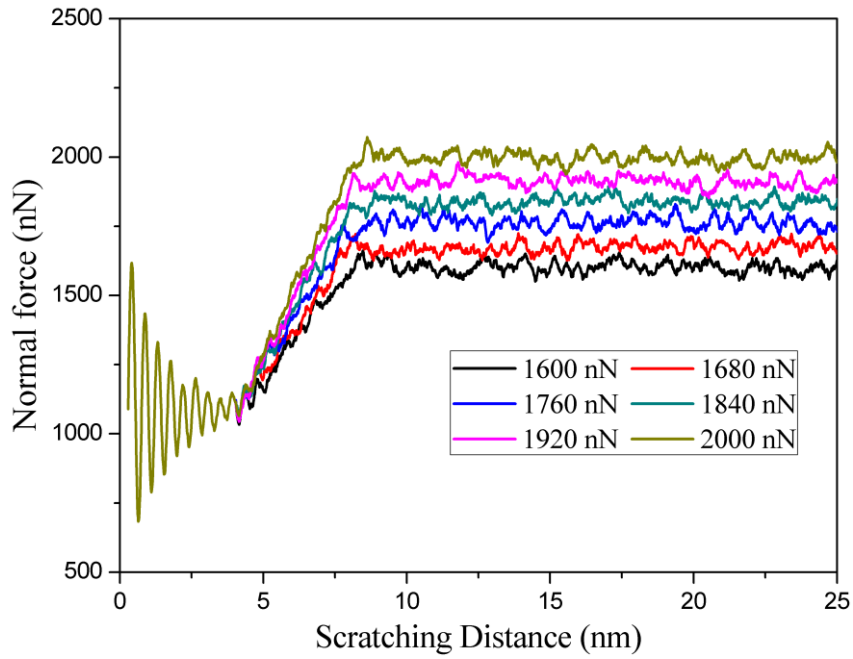


Figure 9-9. Normal forces of Si face with the oxide layer during constant-load scratching.

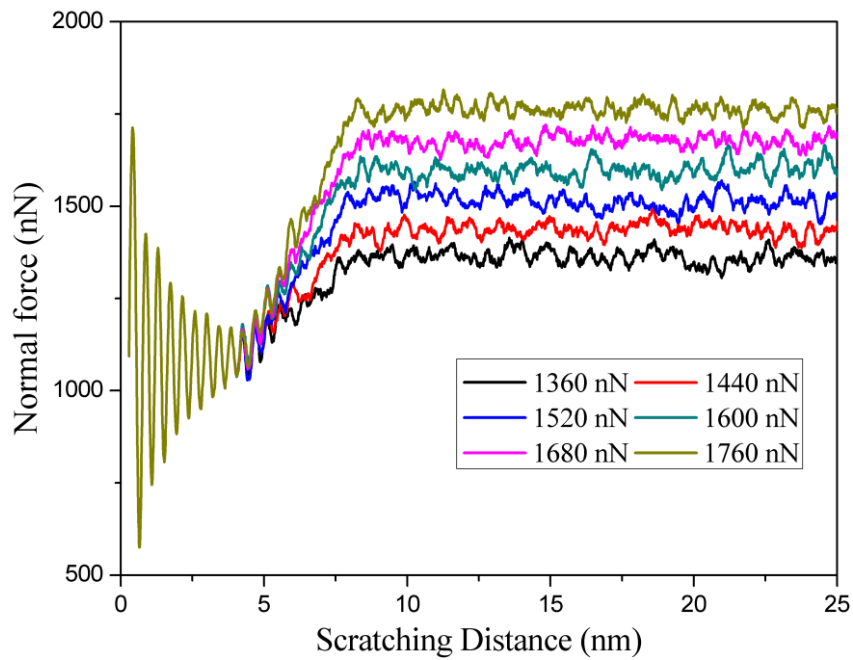


Figure 9-10. Normal forces of C face with the oxide layer during constant-load scratching.

Figure 9-11 shows the material removal of the Si face with the oxide layer under different normal loads. The atoms of the oxide layer are removed without damaging the perfect lattice of SiC under the loads less than 1760 nN. When the load gets larger, the lattice of SiC is damaged and amorphous structures appears on the surface. So, for the Si face, the critical load is 1760 nN.

Similarly, the same scratch simulations were conducted on the C face. Figure 9-12 shows the material removal of the C face with the oxide layer under different normal loads. The atoms of the oxide layer are removed without damaging the perfect lattice of SiC under the loads less than 1520 nN. When the load gets larger, the lattice of SiC is damaged and amorphous structures appear on the surface. For the C face, the critical load was significantly less than that of the Si face, only 1520 nN. This result is in great agreement with previous conclusion as well, because the Si face is harder than the C face and more difficult to remove both mechanically and chemically.

Moreover, it can be seen that the atoms of the oxide layer can be almost totally removed on the Si face under the loads less than the critical load, while for the C face, there remain many oxide-layer atoms on the scratched surface. This may be related to the chemical reactions on the C face. As discussed in Section 8.6, the occurrence and extent of the reactions were affected by whether the lattice structures of SiC were destroyed easily. In particular, for the C face, the lattice structures of SiC are easier to destroy and then form silicon oxide. The chemical reaction on the C face will occur during the scratching even under the load less than the critical load. This mode will influence the next SiC layer and then let it oxidize. So, the chemical reaction on the C face is harder to control than that on the Si face and it is difficult to totally remove the oxide layer on the C face.

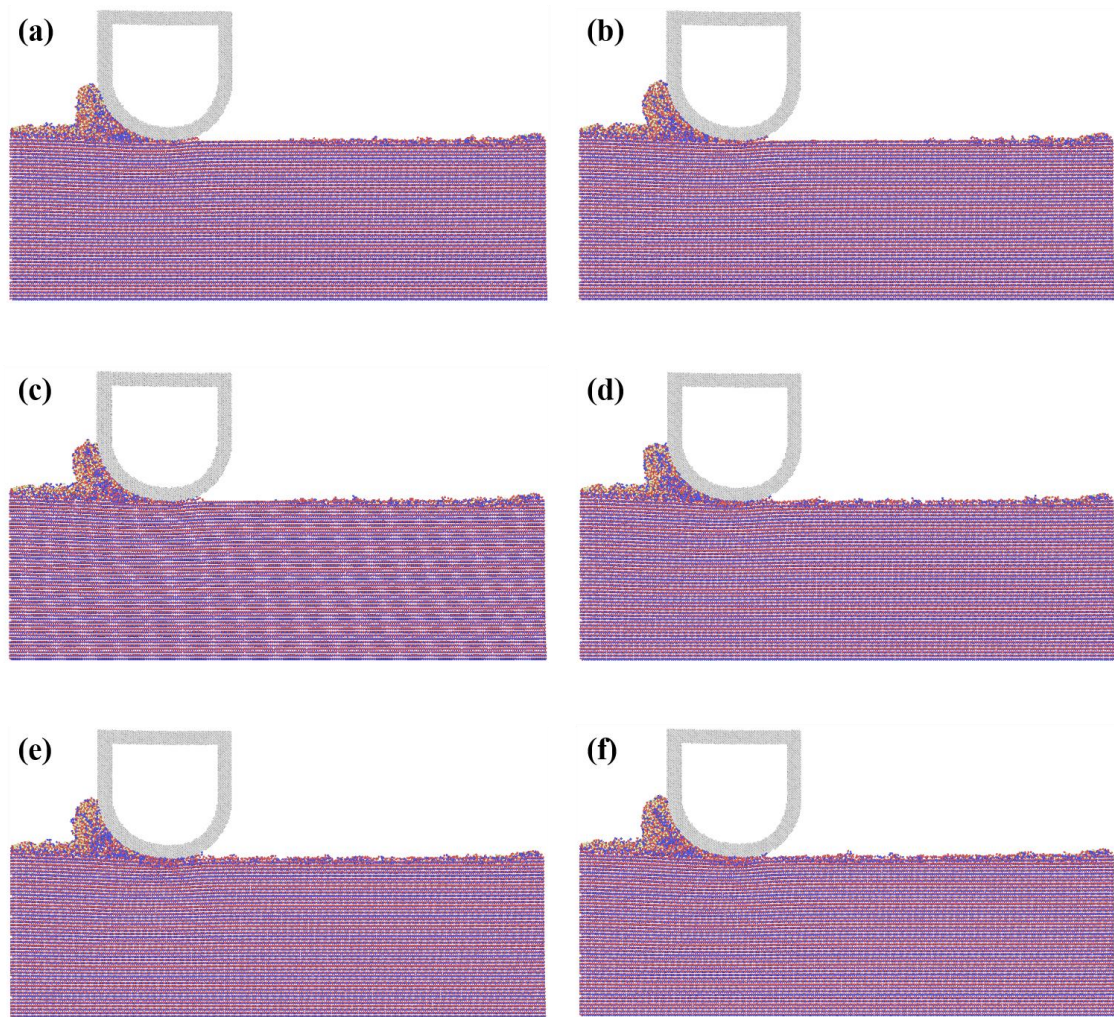


Figure 9-11. Material removal of Si face with oxide layer under different normal loads.
(a) 1600 nN, (b) 1680 nN, (c) 1760 nN, (d) 1840 nN, (e) 1920 nN, (f) 2000 nN.

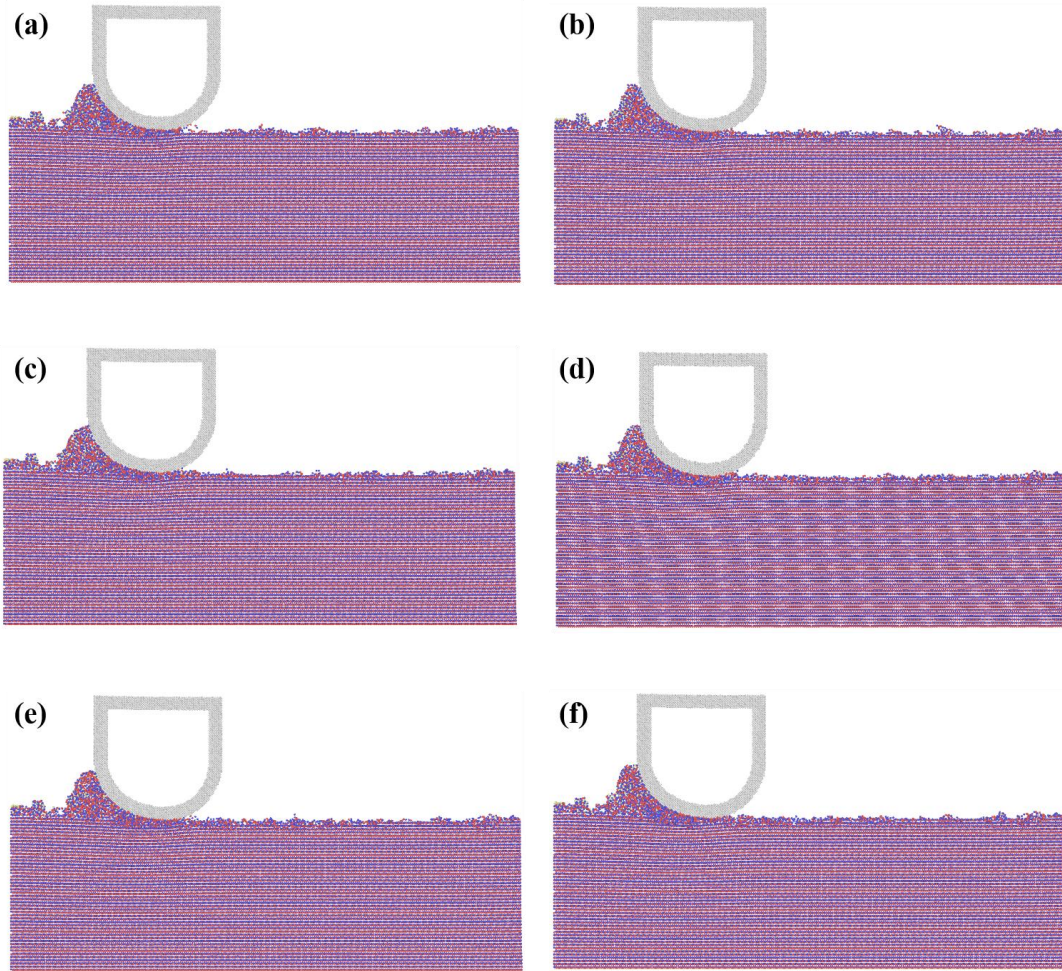


Figure 9-12. Material removal of C face with oxide layer under different normal loads.
(a) 1360 nN, (b) 1440 nN, (c) 1520 nN, (d) 1600 nN, (e) 1680 nN, (f) 1760 nN.

Chapter 10. Conclusion, recommendations and future work

10.1 Conclusion

The mechanisms of material removal, subsurface deformation and interface reactions were observed and analysed through a series of MD simulations and experiments on SiC. The following conclusions are drawn from the results and analyses:

- **The reliability of MD simulation**

The MD simulation results of nanomachining are treated with some scepticism sometimes, because it is difficult to be compared and verified by experiments. In this project, experimental and simulated results are compared and verified by similar trends and phenomena in terms of forces, material removal efficiency and subsurface morphology. Hence, the agreement between experimental and simulated results indicates that the MD simulation models and methods used in this research are reliable.

- **Nanoscale processing**

Here are some main conclusions in the MD simulations and experimental results of nanoindentation and nanoscratching.

- a. There is no obvious difference in the trends of indent forces in the indentation simulations and experiments, and they show similar characteristics at the subsurface. The hexagon pattern in the horizontal cross-sections views can be regarded as two mutually central symmetric triangles, and these amorphous patterns may be caused by the slip systems of 4H-SiC and 6H-SiC. Their slips mainly take place on the (0001) basal plane and along the $\langle 11\bar{2}0 \rangle$ directions, which depends on their special lattice structure.
- b. During scratching, dislocations and slips occur on both the C face and the Si face, mainly on the (0001) basal plane and the (10 $\bar{1}0$) plane. Dislocations and slips on the (0001) plane promote material removal. Due to the lower stress fluctuation peak, dislocations at the C face on the (0001) plane occur more easily.
- c. Material removal efficiency of the C face is higher than that of the Si face, and there is less subsurface amorphous deformation on the C face. Dislocations on the (0001) basal

plane are more likely to occur on the C face than on the Si face, which leads to lower scratching forces, fewer amorphous atoms, and higher MRR on the C face.

- d. In nanoscale processing, amorphous transformation and dislocations are the primary mechanisms of material deformation, which are evidenced in both MD simulation and experiments.

- **Effect of machining conditions**

In both experimental and simulation results, machining conditions, such as shape of abrasive particles, scratching speed and scratching direction, also have significant effects on nanometric material removal performance. Here are some main conclusions.

- a. Taking material removal efficiency, amorphous deformation and subsurface dislocations into consideration, spherical abrasive may be the best option in ultra-precision polishing.
- b. When the scratching speed increases, more and more workpiece materials are accumulated on both sides of the groove. This means that the increase in the scratching speed will result in the more obvious ductility of the material.
- c. In the [1-210] scratching direction, the wrinkle angles are 60 °, while in the [1-100] scratching direction, the wrinkle angles are 30 °. This phenomenon can be considered as the consequence of the dislocations and slips along <1-210> orientations {1-100} cylindrical planes.
- d. Moreover, MD simulation results show that setting the scratching cutting depth as an integer multiple of the height of a half lattice crystal may be more beneficial for removing materials and obtaining a substrate with better subsurface quality.

- **Effect of chemical reaction**

The chemical reactions between SiC atoms and water molecules during polishing and the effect of chemical products on material removal have been investigated. Here are some main conclusions.

- a. The occurrence of silicon dioxide in the conditions of pure water as the cooling liquid indicates that the 6H-SiC wafers can be oxidized by the water during polishing without

any acid or alkali conditions. Both the polishing experiments in previous literature and the RMD results show the same phenomena.

- b. The occurrence and extent of the reactions between SiC and H₂O are influenced by the destruction of 6H-SiC lattice structure. The lattice structures of both faces of 6H-SiC are much easier to be destroyed under the pressure from the diamond abrasive, so the reactions occurred more easily than without load.
- c. The material on the C face of 6H-SiC is oxidized faster than that on the Si face, directly resulting in the larger material removal efficiency of the C face than the Si face in the same conditions. As the result, the oxide layer on the C face is thicker than that on Si face.
- d. The atoms of oxide layer can be almost totally removed on the Si face under loads less than the critical load, while for the C face, there remain many oxide-layer atoms on the scratched surface. This indicates that the chemical reaction on the C face is harder to control than that on the Si face and it is difficult to totally remove the oxide layer on the C face.

10.2 Contribution to knowledge

The material deformation mechanism of 4H-SiC and 6H-SiC in nanomachining has been further revealed. The damage of a brittle material, such as SiC, could appear as plastic deformation and brittle fracture. Both amorphous transformation and dislocation can present plastic deformations. However, the dislocations in the scratched 4H-SiC and 6H-SiC are prone to crack growth when the fractured bonds do not recover. It is evidence that cracks generated on machined surface are initiated in the same direction as the dislocation occurrence that demonstrated in this research. The reason for the difference between the C face and Si face of SiC in nanomachining has been revealed in this study. Not only the mechanical actions but also the chemical reactions contribute the different efficiency in the material removal of the two faces. Moreover, the influence of chemical effect is more obvious in nanomachining. In addition, selecting the feed rate according to the layer structure of SiC may promote a better surface quality. This may be a useful guide for optimizing the actual machining process. Such a method for the selection of cutting feed may also be used to improve the machining performance of other brittle materials with layered structures.

10.3 Recommendations and future work

As concluded above, this research shows some new findings and phenomena in nanomachining using MD simulations and experiments, and provides reasonable explanations. However, there still are some problems needing to be further investigated and analysed in the future.

- a. In general, MD simulations are commonly used to analyse atomic interactions and provide qualitative guidance for people to understand the material removal mechanism at the nanometre level. It is still a challenge to provide precise potential functions and quantitative details because of the difficulties in acquiring a true molecular potential function that matches real application cases.
- b. Simulated and experimental results may conflict as a result of differences in scale. It is difficult to conduct material mechanical removal experimentally at the molecular level. Although the material removal performance in the simulation presents similar trends, they do not match well quantitatively. This could be due to limited computing capacity which limits the scale of the MD simulations making it difficult to simulate the scratching process at the actual experimental size level. Continuous improvements in computing facilities will enhance the ability of simulations to match experiments in the near future.
- c. This paper provides insights into material removal mechanisms, nanomechanical properties and deformation mechanism of 4H-SiC and 6H-SiC on the {0001} plane. The research methods introduced in this paper could also be applicable for the investigation of different SiC polytypes and other brittle materials. Understanding these problems could be beneficial to nanomachining of these hard and brittle materials.
- d. Chemical reactions in nanoscale processing are also critical to removal performance. This research only investigates and analyses its phenomena and mechanisms, but how to improve actual processing still needs further research in the future.

References

- [1] Goel, S., 2014. The current understanding on the diamond machining of silicon carbide. *Journal of Physics D: Applied Physics*, 47(24), p.243001.
- [2] Lee, H.S. and Jeong, H.D., 2009. Chemical and mechanical balance in polishing of electronic materials for defect-free surfaces. *CIRP annals*, 58(1), pp.485-490.
- [3] Lohrmann, A., Johnson, B.C., McCallum, J.C. and Castelletto, S., 2017. A review on single photon sources in silicon carbide. *Reports on Progress in Physics*, 80(3), p.034502.
- [4] Tan, T.H. and Yan, J., 2017. Atomic-scale characterization of subsurface damage and structural changes of single-crystal silicon carbide subjected to electrical discharge machining. *Acta Materialia*, 123, pp.362-372.
- [5] Perrone, D., 2007. Process and characterisation techniques on 4H-Silicon Carbide. *Micronanotechnology, Ph. D. thesis, Politecnico di Torino, Torino, Italy*.
- [6] Luo, X., Goel, S. and Reuben, R.L., 2012. A quantitative assessment of nanometric machinability of major polytypes of single crystal silicon carbide. *Journal of the European Ceramic Society*, 32(12), pp.3423-3434.
- [7] Lee, H., Kasuga, H., Ohmori, H., Lee, H. and Jeong, H., 2011. Application of electrolytic in-process dressing (ELID) grinding and chemical mechanical polishing (CMP) process for emerging hard–brittle materials used in light-emitting diodes. *Journal of crystal growth*, 326(1), pp.140-146.
- [8] Chen, X.F., Xu, X.G., Hu, X.B., Li, J., Jiang, S.Z., Ning, L.N., Wang, Y.M. and Jiang, M.H., 2007. Anisotropy of chemical mechanical polishing in silicon carbide substrates. *Materials Science and Engineering: B*, 142(1), pp.28-30.
- [9] Demenet, J.L., Amer, M., Tromas, C., Eyidi, D. and Rabier, J., 2013. Dislocations in 4H- and 3C- SiC single crystals in the brittle regime. *physica status solidi c*, 10(1), pp.64-67.

- [10] Ravindra, D., Patten, J.A. and Vanger, S.H., 2011. Ductile regime material removal of silicon carbide (SiC). *Silicon Carbide New Materials Production Methods and Application*, edited by SH Vanger, Nova Publishers, Trivandrum, India, pp.141-167.
- [11] Hu, X., Song, Z., Pan, Z., Liu, W. and Wu, L., 2009. Planarization machining of sapphire wafers with boron carbide and colloidal silica as abrasives. *Applied surface science*, 255(19), pp.8230-8234.
- [12] Lei, H. and Tong, K., 2016. Preparation of La-doped colloidal SiO₂ composite abrasives and their chemical mechanical polishing behavior on sapphire substrates. *Precision Engineering*, 44, pp.124-130.
- [13] Zhao, Y. and Chang, L., 2002. A micro-contact and wear model for chemical–mechanical polishing of silicon wafers. *Wear*, 252(3-4), pp.220-226.
- [14] Borucki, L., Witelski, T., Please, C., Kramer, P. and Schwendeman, D., 2004. A theory of pad conditioning for chemical-mechanical polishing. *Journal of Engineering Mathematics*, 50(1), pp.1-24.
- [15] Lee, H.S., Kim, D.I., An, J.H., Lee, H.J., Kim, K.H. and Jeong, H., 2010. Hybrid polishing mechanism of single crystal SiC using mixed abrasive slurry (MAS). *CIRP annals*, 59(1), pp.333-336.
- [16] Khanna, A.J., Gupta, S., Kumar, P., Chang, F.C. and Singh, R.K., 2019. Quantification of shear induced agglomeration in chemical mechanical polishing slurries under different chemical environments. *Microelectronic Engineering*, 210, pp.1-7.
- [17] Basim, G.B. and Moudgil, B.M., 2002. Effect of soft agglomerates on CMP slurry performance. *Journal of Colloid and Interface Science*, 256(1), pp.137-142.
- [18] Arima, K., Hara, H., Murata, J., Ishida, T., Okamoto, R., Yagi, K., Sano, Y., Mimura, H. and Yamauchi, K., 2007. Atomic-scale flattening of SiC surfaces by electroless chemical etching in HF solution with Pt catalyst. *Applied Physics Letters*, 90(20), p.202106.
- [19] Zhou, Y., Pan, G., Shi, X., Gong, H., Luo, G. and Gu, Z., 2014. Chemical mechanical planarization (CMP) of on-axis Si-face SiC wafer using catalyst nanoparticles in slurry. *Surface and Coatings Technology*, 251, pp.48-55.

- [20] Kubota, A., Yoshimura, M., Fukuyama, S., Iwamoto, C. and Touge, M., 2012. Planarization of C-face 4H-SiC substrate using Fe particles and hydrogen peroxide solution. *Precision Engineering*, 36(1), pp.137-140.
- [21] Deng, H. and Yamamura, K., 2013. Atomic-scale flattening mechanism of 4H-SiC (0 0 0 1) in plasma assisted polishing. *CIRP Annals*, 62(1), pp.575-578.
- [22] Deng, H., Monna, K., Tabata, T., Endo, K. and Yamamura, K., 2014. Optimization of the plasma oxidation and abrasive polishing processes in plasma-assisted polishing for highly effective planarization of 4H-SiC. *CIRP Annals*, 63(1), pp.529-532.
- [23] Yamamura, K., Takiguchi, T., Ueda, M., Deng, H., Hattori, A.N. and Zettsu, N., 2011. Plasma assisted polishing of single crystal SiC for obtaining atomically flat strain-free surface. *CIRP annals*, 60(1), pp.571-574.
- [24] Deng, H., Hosoya, K., Imanishi, Y., Endo, K. and Yamamura, K., 2015. Electrochemical mechanical polishing of single-crystal SiC using CeO₂ slurry. *Electrochemistry Communications*, 52, pp.5-8.
- [25] Murata, J., Yodogawa, K. and Ban, K., 2017. Polishing-pad-free electrochemical mechanical polishing of single-crystalline SiC surfaces using polyurethane–CeO₂ core–shell particles. *International Journal of Machine Tools and Manufacture*, 114, pp.1-7.
- [26] Park, K.W., Han, S.B. and Lee, J.M., 2007. Photo (UV)-enhanced performance of Pt–TiO₂ nanostructure electrode for methanol oxidation. *Electrochemistry communications*, 9(7), pp.1578-1581.
- [27] Lu, J., Luo, Q., Xu, X., Huang, H. and Jiang, F., 2019. Removal mechanism of 4H- and 6H-SiC substrates (0001 and 000 1) in mechanical planarization machining. *Proceedings of the Institution of Mechanical Engineers, Part B: Journal of Engineering Manufacture*, 233(1), pp.69-76.
- [28] Pan, Z.J., Feng, B., Wang, L. and Hao, J.M., 2013. Comparative chemical mechanical polishing studies of SiC (0001) and SiC (000-1) surface. *Equip. Electron. Prod. Manuf.*, 42, pp.19-23.

- [29] Luo, Q.F., Lu, J. and Xu, X.P., 2016. A comparative study on the material removal mechanisms of 6H-SiC polished by semi-fixed and fixed diamond abrasive tools. *Wear*, 350, pp.99-106.
- [30] Luo, Q.F., 2018. Research on Abrasive Polishing Removal Mechanisms of LED Substrates Materials. *Ph. D. thesis, Huaqiao University, Xiamen, China*.
- [31] Schuh, C.A. and Lund, A.C., 2004. Application of nucleation theory to the rate dependence of incipient plasticity during nanoindentation. *Journal of Materials research*, 19(7), pp.2152-2158.
- [32] Goel, S., Yan, J., Luo, X. and Agrawal, A., 2014. Incipient plasticity in 4H-SiC during quasistatic nanoindentation. *Journal of the mechanical behavior of biomedical materials*, 34, pp.330-337.
- [33] Li, Z., Zhang, F. and Luo, X., 2018. Subsurface damages beneath fracture pits of reaction-bonded silicon carbide after ultra-precision grinding. *Applied Surface Science*, 448, pp.341-350.
- [34] Grim, J.R., Benamara, M., Skowronski, M., Everson, W.J. and Heydemann, V.D., 2006. Transmission electron microscopy analysis of mechanical polishing-related damage in silicon carbide wafers. *Semiconductor science and technology*, 21(12), p.1709.
- [35] Li, C., Zhang, F., Meng, B. and Ma, Z., 2017. Simulation and experiment on surface morphology and mechanical properties response in nano-indentation of 6H-SiC. *Journal of Materials Engineering and Performance*, 26(3), pp.1000-1009.
- [36] Meng, B., Zhang, Y. and Zhang, F., 2016. Material removal mechanism of 6H-SiC studied by nano-scratching with Berkovich indenter. *Applied Physics A*, 122(3), p.247.
- [37] Wang, P., Ge, P., Ge, M., Bi, W. and Meng, J., 2019. Material removal mechanism and crack propagation in single scratch and double scratch tests of single-crystal silicon carbide by abrasives on wire saw. *Ceramics International*, 45(1), pp.384-393.
- [38] Duan, N., Yu, Y., Wang, W. and Xu, X., 2017. Analysis of grit interference mechanisms for the double scratching of monocrystalline silicon carbide by coupling the FEM and SPH. *International Journal of Machine Tools and Manufacture*, 120, pp.49-60.

- [39] Zhang, B. and Yin, J., 2019. The ‘skin effect’ of subsurface damage distribution in materials subjected to high-speed machining. *International Journal of Extreme Manufacturing*, 1(1), p.012007.
- [40] Bi, Z., Tokura, H. and Yoshikawa, M., 1988. Study on surface cracking of alumina scratched by single-point diamonds. *Journal of materials science*, 23(9), pp.3214-3224.
- [41] Duan, N., Wang, W., Yu, Y., Huang, H. and Xu, X., 2013. Dynamic simulation of single grain cutting of glass by coupling FEM and SPH. *China Mech. Eng*, 24, pp.2716-2721.
- [42] Duan, N., Yu, Y., Wang, W. and Xu, X., 2017. SPH and FE coupled 3D simulation of monocrystal SiC scratching by single diamond grit. *International Journal of Refractory Metals and Hard Materials*, 64, pp.279-293.
- [43] Goel, S., Luo, X. and Reuben, R.L., 2012. Molecular dynamics simulation model for the quantitative assessment of tool wear during single point diamond turning of cubic silicon carbide. *Computational Materials Science*, 51(1), pp.402-408.
- [44] Wang, J., Zhang, X. and Fang, F., 2016. Molecular dynamics study on nanometric cutting of ion implanted silicon. *Computational Materials Science*, 117, pp.240-250.
- [45] Maekawa, K. and Itoh, A., 1995. Friction and tool wear in nano-scale machining—a molecular dynamics approach. *Wear*, 188(1-2), pp.115-122.
- [46] Liu, Y., Li, B. and Kong, L., 2018. A molecular dynamics investigation into nanoscale scratching mechanism of polycrystalline silicon carbide. *Computational Materials Science*, 148, pp.76-86.
- [47] Kim, W.K. and Kim, B.H., 2017. A molecular dynamics study on atomistic mechanisms of nano-scale cutting process of sapphire. *Journal of Mechanical Science and Technology*, 31(9), pp.4353-4362.
- [48] Wang, Z., Chen, J., Wang, G., Bai, Q. and Liang, Y., 2017. Anisotropy of single-crystal silicon in nanometric cutting. *Nanoscale research letters*, 12(1), pp.1-11.

- [49] Verkhovtsev, A.V., Yakubovich, A.V., Sushko, G.B., Hanauske, M. and Solov'yov, A.V., 2013. Molecular dynamics simulations of the nanoindentation process of titanium crystal. *Computational materials science*, 76, pp.20-26.
- [50] Chamani, M., Farrahi, G.H. and Movahhedy, M.R., 2016. Molecular dynamics simulation of nanoindentation of nanocrystalline Al/Ni multilayers. *Computational Materials Science*, 112, pp.175-184.
- [51] Shi, J., Fang, L. and Sun, K., 2018. Friction and wear reduction via tuning nanoparticle shape under low humidity conditions: A nonequilibrium molecular dynamics simulation. *Computational Materials Science*, 154, pp.499-507.
- [52] Fang, T.H., Weng, C.I. and Chang, J.G., 2003. Molecular dynamics analysis of temperature effects on nanoindentation measurement. *Materials Science and Engineering: A*, 357(1-2), pp.7-12.
- [53] Chrobak, D., Tymiak, N., Beaver, A., Ugurlu, O., Gerberich, W.W. and Nowak, R., 2011. Deconfinement leads to changes in the nanoscale plasticity of silicon. *Nature nanotechnology*, 6(8), pp.480-484.
- [54] Mylvaganam, K. and Zhang, L.C., 2012. Effect of bct-5 Si on the indentation of monocrystalline silicon. In *Applied Mechanics and Materials* (Vol. 117, pp. 666-669). Trans Tech Publications Ltd.
- [55] Mylvaganam, K., Zhang, L.C., Eyben, P., Mody, J. and Vandervorst, W., 2009. Evolution of metastable phases in silicon during nanoindentation: mechanism analysis and experimental verification. *Nanotechnology*, 20(30), p.305705.
- [56] Cheong, W.C.D. and Zhang, L.C., 2000. Molecular dynamics simulation of phase transformations in silicon monocrystals due to nano-indentation. *Nanotechnology*, 11(3), p.173.
- [57] Sun, S., Peng, X., Xiang, H., Huang, C., Yang, B., Gao, F. and Fu, T., 2017. Molecular dynamics simulation in single crystal 3C-SiC under nanoindentation: Formation of prismatic loops. *Ceramics International*, 43(18), pp.16313-16318.

- [58] Zhu, B., Zhao, D. and Zhao, H., 2019. A study of deformation behavior and phase transformation in 4H-SiC during nanoindentation process via molecular dynamics simulation. *Ceramics International*, 45(4), pp.5150-5157.
- [59] Wu, Z., Liu, W., Zhang, L. and Lim, S., 2020. Amorphization and dislocation evolution mechanisms of single crystalline 6H-SiC. *Acta Materialia*, 182, pp.60-67.
- [60] Goel, S., Luo, X., Reuben, R.L. and Rashid, W.B., 2011. Atomistic aspects of ductile responses of cubic silicon carbide during nanometric cutting. *Nanoscale research letters*, 6(1), pp.1-9.
- [61] Meng, B., Yuan, D. and Xu, S., 2019. Coupling effect on the removal mechanism and surface/subsurface characteristics of SiC during grinding process at the nanoscale. *Ceramics International*, 45(2), pp.2483-2491.
- [62] Liu, Y., Li, B. and Kong, L., 2018. Molecular dynamics simulation of silicon carbide nanoscale material removal behavior. *Ceramics International*, 44(10), pp.11910-11913.
- [63] Wu, Z., Liu, W. and Zhang, L., 2017. Revealing the deformation mechanisms of 6H-silicon carbide under nano-cutting. *Computational Materials Science*, 137, pp.282-288.
- [64] Xiao, G., To, S. and Zhang, G., 2015. The mechanism of ductile deformation in ductile regime machining of 6H SiC. *Computational Materials Science*, 98, pp.178-188.
- [65] Meng, B., Yuan, D. and Xu, S., 2019. Atomic-Scale characterization of slip deformation and nanometric machinability of single-crystal 6H-SiC. *Nanoscale research letters*, 14(1), pp.1-9.
- [66] Meng, B., Yuan, D., Zheng, J. and Xu, S., 2019. Molecular dynamics study on femtosecond laser aided machining of monocrystalline silicon carbide. *Materials Science in Semiconductor Processing*, 101, pp.1-9.
- [67] Komanduri, R., Chandrasekaran, N. and Raff, L.M., 1998. Effect of tool geometry in nanometric cutting: a molecular dynamics simulation approach. *Wear*, 219(1), pp.84-97.

- [68] Zhu, P.Z., Hu, Y.Z., Wang, H. and Ma, T.B., 2011. Study of effect of indenter shape in nanometric scratching process using molecular dynamics. *Materials Science and Engineering: A*, 528(13-14), pp.4522-4527.
- [69] Dai, H., Du, H., Chen, J. and Chen, G., 2019. Investigation of tool geometry in nanoscale cutting single-crystal copper by molecular dynamics simulation. *Proceedings of the Institution of Mechanical Engineers, Part J: Journal of Engineering Tribology*, 233(8), pp.1208-1220.
- [70] Liu, B., Xu, Z., Chen, C., Li, R., Gao, X. and Liang, L., 2020. Numerical and experimental investigation on ductile deformation and subsurface defects of monocrystalline silicon during nano-scratching. *Applied Surface Science*, 528, p.147034.
- [71] Fung, K.Y., Tang, C.Y. and Cheung, C.F., 2017. Molecular dynamics analysis of the effect of surface flaws of diamond tools on tool wear in nanometric cutting. *Computational Materials Science*, 133, pp.60-70.
- [72] Meng, B., Qiu, P., Yuan, D. and Xu, S., 2019. Influence of microstructure on the diamond-machinability of hot-pressed silicon carbide: A molecular dynamics study. *Ceramics International*, 45(17), pp.22872-22879.
- [73] Goel, S., Luo, X., Comley, P., Reuben, R.L. and Cox, A., 2013. Brittle–ductile transition during diamond turning of single crystal silicon carbide. *International Journal of Machine Tools and Manufacture*, 65, pp.15-21.
- [74] Goel, S., 2013. *An atomistic investigation on the nanometric cutting mechanism of hard, brittle materials* (Doctoral dissertation, Heriot-Watt University).
- [75] Chen, L., He, H., Wang, X., Kim, S.H. and Qian, L., 2015. Tribology of Si/SiO₂ in humid air: transition from severe chemical wear to wearless behavior at nanoscale. *Langmuir*, 31(1), pp.149-156.
- [76] Yu, J., Kim, S.H., Yu, B., Qian, L. and Zhou, Z., 2012. Role of tribochemistry in nanowear of single-crystalline silicon. *ACS applied materials & interfaces*, 4(3), pp.1585-1593.

- [77] Van Duin, A.C., Dasgupta, S., Lorant, F. and Goddard, W.A., 2001. ReaxFF: a reactive force field for hydrocarbons. *The Journal of Physical Chemistry A*, 105(41), pp.9396-9409.
- [78] Newsome, D.A., Sengupta, D., Foroutan, H., Russo, M.F. and van Duin, A.C., 2012. Oxidation of silicon carbide by O₂ and H₂O: a ReaxFF reactive molecular dynamics study, Part I. *The Journal of Physical Chemistry C*, 116(30), pp.16111-16121.
- [79] Newsome, D.A., Sengupta, D. and van Duin, A.C., 2013. High-temperature oxidation of SiC-based composite: rate constant calculation from ReaxFF MD simulations, Part II. *The Journal of Physical Chemistry C*, 117(10), pp.5014-5027.
- [80] Šimonka, V., Hössinger, A., Weinbub, J. and Selberherr, S., 2017. ReaxFF reactive molecular dynamics study of orientation dependence of initial silicon carbide oxidation. *The Journal of Physical Chemistry A*, 121(46), pp.8791-8798.
- [81] Shi, J., Chen, J., Sun, K., Sun, J., Han, J. and Fang, L., 2017. Water film facilitating plastic deformation of Cu thin film under different nanoindentation modes: A molecular dynamics study. *Materials Chemistry and Physics*, 198, pp.177-185.
- [82] Shi, J., Zhang, Y., Sun, K. and Fang, L., 2016. Effect of water film on the plastic deformation of monocrystalline copper. *RSC advances*, 6(99), pp.96824-96831.
- [83] Ren, J., Zhao, J., Dong, Z. and Liu, P., 2015. Molecular dynamics study on the mechanism of AFM-based nanoscratching process with water-layer lubrication. *Applied Surface Science*, 346, pp.84-98.
- [84] Wen, J., Ma, T., Zhang, W., van Duin, A.C. and Lu, X., 2017. Atomistic mechanisms of Si chemical mechanical polishing in aqueous H₂O₂: ReaxFF reactive molecular dynamics simulations. *Computational Materials Science*, 131, pp.230-238.
- [85] Wen, J., Ma, T., Zhang, W., Psfogiannakis, G., van Duin, A.C., Chen, L., Qian, L., Hu, Y. and Lu, X., 2016. Atomic insight into tribochemical wear mechanism of silicon at the Si/SiO₂ interface in aqueous environment: Molecular dynamics simulations using ReaxFF reactive force field. *Applied Surface Science*, 390, pp.216-223.

- [86] Yeon, J., Van Duin, A.C. and Kim, S.H., 2016. Effects of water on tribochemical wear of silicon oxide interface: molecular dynamics (MD) study with reactive force field (ReaxFF). *Langmuir*, 32(4), pp.1018-1026.
- [87] Guo, X., Yuan, S., Wang, X., Jin, Z. and Kang, R., 2019. Atomistic mechanisms of chemical mechanical polishing of diamond (1 0 0) in aqueous H₂O₂/pure H₂O: molecular dynamics simulations using reactive force field (ReaxFF). *Computational Materials Science*, 157, pp.99-106.
- [88] Yuan, S., Guo, X., Lu, M., Jin, Z., Kang, R. and Guo, D., 2019. Diamond nanoscale surface processing and tribochemical wear mechanism. *Diamond and Related Materials*, 94, pp.8-13.
- [89] Goel, S., Luo, X., Agrawal, A. and Reuben, R.L., 2015. Diamond machining of silicon: a review of advances in molecular dynamics simulation. *International Journal of Machine Tools and Manufacture*, 88, pp.131-164.
- [90] Allen, M.P. and Tildesley, D.J., 2017. *Computer simulation of liquids*. Oxford university press.
- [91] Ercolessi, F., 1997. A molecular dynamics primer. *Spring college in computational physics, ICTP, Trieste*, 19.
- [92] Hernández, E.R., 2008, November. Molecular Dynamics: from basic techniques to applications (A Molecular Dynamics Primer). In *AIP Conference Proceedings* (Vol. 1077, No. 1, pp. 95-123). American Institute of Physics.
- [93] Zhang, L.C. and Tanaka, H., 1999. On the mechanics and physics in the nano-indentation of silicon monocrystals. *JSME International Journal Series A Solid Mechanics and Material Engineering*, 42(4), pp.546-559.
- [94] Landman, U., Luedtke, W.D., Burnham, N.A. and Colton, R.J., 1990. Atomistic mechanisms and dynamics of adhesion, nanoindentation, and fracture. *Science*, 248(4954), pp.454-461.
- [95] Rapaport, D.C., 2004. *The art of molecular dynamics simulation*. Cambridge university press.

- [96] Finnis, M., 2003. *Interatomic forces in condensed matter* (Vol. 1). OUP Oxford.
- [97] Yu, H., Adams, J.B. and Hector Jr, L.G., 2002. Molecular dynamics simulation of high-speed nanoindentation. *Modelling and Simulation in Materials Science and Engineering*, 10(3), p.319.
- [98] Fang, T.H., Weng, C.I. and Chang, J.G., 2002. Molecular dynamics simulation of nanolithography process using atomic force microscopy. *Surface Science*, 501(1-2), pp.138-147.
- [99] Ye, Y.Y., Biswas, R., Morris, J.R., Bastawros, A. and Chandra, A., 2003. Molecular dynamics simulation of nanoscale machining of copper. *Nanotechnology*, 14(3), p.390.
- [100] Cai, M.B., Li, X.P. and Rahman, M., 2007. Study of the mechanism of nanoscale ductile mode cutting of silicon using molecular dynamics simulation. *International Journal of Machine Tools and Manufacture*, 47(1), pp.75-80.
- [101] Tersoff, J., 1988. New empirical approach for the structure and energy of covalent systems. *Physical review B*, 37(12), p.6991.
- [102] Tersoff, J., 1988. Empirical interatomic potential for silicon with improved elastic properties. *Physical Review B*, 38(14), p.9902.
- [103] Rafii-Tabar, H. and Mansoori, G.A., 2018. Interatomic potential models for nanostructures. *arXiv preprint arXiv:1806.06291*.
- [104] Oluwajobi, A. and Chen, X., 2011. The effect of interatomic potentials on the molecular dynamics simulation of nanometric machining. *International Journal of Automation and Computing*, 8(3), pp.326-332.
- [105] Lennard-Jones, J.E., 1925. On the forces between atoms and ions. *Proceedings of the Royal Society of London. Series A, Containing Papers of a Mathematical and Physical Character*, 109(752), pp.584-597.
- [106] Brush, S.G., 1970. Interatomic forces and gas theory from Newton to Lennard-Jones. *Archive for Rational Mechanics and Analysis*, 39(1), pp.1-29.

- [107] Tersoff, J.J.P.R.B., 1989. Modeling solid-state chemistry: Interatomic potentials for multicomponent systems. *Physical review B*, 39(8), p.5566.
- [108] Foiles, S.M., 1985. Application of the embedded-atom method to liquid transition metals. *Physical Review B*, 32(6), p.3409.
- [109] Foiles, S.M., Baskes, M.I. and Daw, M.S., 1986. Embedded-atom-method functions for the fcc metals Cu, Ag, Au, Ni, Pd, Pt, and their alloys. *Physical review B*, 33(12), p.7983.
- [110] Baskes, M.I., 1992. Modified embedded-atom potentials for cubic materials and impurities. *Physical review B*, 46(5), p.2727.
- [111] Stillinger, F.H. and Weber, T.A., 1985. Computer simulation of local order in condensed phases of silicon. *Physical review B*, 31(8), p.5262.
- [112] Frenkel, D. and Smit, B., 2001. *Understanding molecular simulation: from algorithms to applications* (Vol. 1). Elsevier.
- [113] Zhang, J., 2011. Molecular dynamics study of generation mechanism of surface layer in nanomechanical machining of crystalline copper. *Harbin: Harbin Institute of Technology*, pp.117-118.
- [114] Oluwajobi, A.O. and Chen, X., 2010. The fundamentals of modelling abrasive machining using molecular dynamics. *International Journal of Abrasive Technology*, 3(4), pp.354-381.
- [115] Oluwajobi, A.O. and Chen, X., 2013. Effects of interatomic potentials on the determination of the minimum depth of cut in nanomachining. *International Journal of Abrasive Technology*, 6(1), pp.16-39.
- [116] Berendsen, H.J., Postma, J.V., van Gunsteren, W.F., DiNola, A.R.H.J. and Haak, J.R., 1984. Molecular dynamics with coupling to an external bath. *The Journal of chemical physics*, 81(8), pp.3684-3690.
- [117] Munetoh, S., Motooka, T., Moriguchi, K. and Shintani, A., 2007. Interatomic potential for Si–O systems using Tersoff parameterization. *Computational Materials Science*, 39(2), pp.334-339.

- [118] Liang, T., Zhou, M., Zhang, P., Yuan, P. and Yang, D., 2020. Multilayer in-plane graphene/hexagonal boron nitride heterostructures: Insights into the interfacial thermal transport properties. *International Journal of Heat and Mass Transfer*, 151, p.119395.
- [119] Liang, T., Zhang, P., Yuan, P. and Zhai, S., 2018. In-plane thermal transport in black phosphorene/graphene layered heterostructures: a molecular dynamics study. *Physical Chemistry Chemical Physics*, 20(32), pp.21151-21162.
- [120] Plimpton, S., 1995. Fast parallel algorithms for short-range molecular dynamics. *Journal of computational physics*, 117(1), pp.1-19.
- [121] Stukowski, A., 2009. Visualization and analysis of atomistic simulation data with OVITO—the Open Visualization Tool. *Modelling and Simulation in Materials Science and Engineering*, 18(1), p.015012.
- [122] Stukowski, A., Bulatov, V.V. and Arsenlis, A., 2012. Automated identification and indexing of dislocations in crystal interfaces. *Modelling and Simulation in Materials Science and Engineering*, 20(8), p.085007.
- [123] Honeycutt, J.D. and Andersen, H.C., 1987. Molecular dynamics study of melting and freezing of small Lennard-Jones clusters. *Journal of Physical Chemistry*, 91(19), pp.4950-4963.
- [124] Maras, E., Trushin, O., Stukowski, A., Ala-Nissila, T. and Jonsson, H., 2016. Global transition path search for dislocation formation in Ge on Si (001). *Computer Physics Communications*, 205, pp.13-21.
- [125] Faisal, N.H., Ahmed, R. and Reuben, R.L., 2011. Indentation testing and its acoustic emission response: applications and emerging trends. *International Materials Reviews*, 56(2), pp.98-142.
- [126] Gannepalli, A. and Mallapragada, S.K., 2001. Molecular dynamics studies of plastic deformation during silicon nanoindentation. *Nanotechnology*, 12(3), p.250.
- [127] Goel, S., Faisal, N.H., Luo, X., Yan, J. and Agrawal, A., 2014. Nanoindentation of polysilicon and single crystal silicon: Molecular dynamics simulation and experimental validation. *Journal of physics D: applied physics*, 47(27), p.275304.

- [128] Kiely, J.D. and Houston, J.E., 1998. Nanomechanical properties of Au (111),(001), and (110) surfaces. *Physical Review B*, 57(19), p.12588.
- [129] Hertzberg, R.W., Vinci, R.P. and Hertzberg, J.L., 2020. *Deformation and fracture mechanics of engineering materials*. John Wiley & Sons.
- [130] Tersoff, J., 1994. Chemical order in amorphous silicon carbide. *Physical Review B*, 49(23), p.16349.
- [131] Erhart, P. and Albe, K., 2005. Analytical potential for atomistic simulations of silicon, carbon, and silicon carbide. *Physical Review B*, 71(3), p.035211.
- [132] Devanathan, R., de la Rubia, T.D. and Weber, W.J., 1998. Displacement threshold energies in β -SiC. *Journal of nuclear materials*, 253(1-3), pp.47-52.
- [133] Rowe, W.B. and Chen, X., 1997. Characterization of the size effect in grinding and the sliced bread analogy. *International journal of production research*, 35(3), pp.887-899.
- [134] Heinzl, C. and Bleil, N., 2007. The use of the size effect in grinding for work-hardening. *CIRP annals*, 56(1), pp.327-330.
- [135] Yin, L., Vancoille, E.Y., Ramesh, K. and Huang, H., 2004. Surface characterization of 6H-SiC (0001) substrates in indentation and abrasive machining. *International Journal of Machine Tools and Manufacture*, 44(6), pp.607-615.
- [136] Huang, Y. and Zong, W., 2014. Molecular dynamic simulation for nanometric cutting of single-crystal face-centered cubic metals. *Nanoscale research letters*, 9(1), pp.1-9.
- [137] GUO, Y.B. and LIANG, Y.C., 2012. Atomistic simulation of thermal effects and defect structures during nanomachining of copper. *Transactions of Nonferrous Metals Society of China*, 22(11), pp.2762-2770.
- [138] Zhang, L., Huang, H., Zhao, H., Ma, Z., Yang, Y. and Hu, X., 2013. The evolution of machining-induced surface of single-crystal FCC copper via nanoindentation. *Nanoscale research letters*, 8(1), pp.1-13.

- [139] Tong, Z., Liang, Y., Jiang, X. and Luo, X., 2014. An atomistic investigation on the mechanism of machining nanostructures when using single tip and multi-tip diamond tools. *Applied Surface Science*, 290, pp.458-465.
- [140] Jiang-hua, G., Chun-tao, Z., Ya-ping, W., Xiu-lin, S. and Yong-bo, G., 2016. Simulation analysis of the effects of tool rake angle for workpiece temperature in single crystal copper nanometric cutting process. *International Jour. of Hybrid Inf. Tech*, 9(3), pp.407-414.
- [141] Shi, L.Q., Xie, J.X., Xi, M.D., Li, X.H. and Yu, F., 2014, June. Study on cutting mechanism of monocrystalline silicon using molecular dynamics on nanometric scale. In *2015 International Conference on Material Science and Applications (icmsa-15)* (pp. 117-120). Atlantis Press.
- [142] Rao, X., Zhang, F., Luo, X., Ding, F., Cai, Y., Sun, J. and Liu, H., 2019. Material removal mode and friction behaviour of RB-SiC ceramics during scratching at elevated temperatures. *Journal of the European Ceramic Society*, 39(13), pp.3534-3545.
- [143] Rao, X., Zhang, F., Luo, X. and Ding, F., 2019. Characterization of hardness, elastic modulus and fracture toughness of RB-SiC ceramics at elevated temperature by Vickers test. *Materials Science and Engineering: A*, 744, pp.426-435.
- [144] Levine, B.G., Stone, J.E. and Kohlmeyer, A., 2011. Fast analysis of molecular dynamics trajectories with graphics processing units—Radial distribution function histogramming. *Journal of computational physics*, 230(9), pp.3556-3569.

Appendixes

Appendix – A: List of papers published associated with this thesis

1. Tian Z, Xu X, Jiang F, et al. Study on nanomechanical properties of 4H-SiC and 6H-SiC by molecular dynamics simulations [J]. *Ceramics International*, 2019, 45(17): 21998-22006.
2. Tian Z, Chen X, Xu X. Molecular dynamics simulation of the material removal in the scratching of 4H-SiC and 6H-SiC substrates [J]. *International Journal of Extreme Manufacturing*, 2020, 2(4): 045104.

Appendix – B: Atom information

4H-SiC

C	0.000000	1.774197	2.513250
C	1.536500	0.887099	7.539750
C	0.000000	0.000000	0.000000
C	0.000000	0.000000	10.053000
C	-1.536500	2.661296	0.000000
C	-1.536500	2.661296	10.053000
C	3.073000	0.000000	0.000000
C	3.073000	0.000000	10.053000
C	1.536500	2.661296	0.000000
C	1.536500	2.661296	10.053000
C	0.000000	0.000000	5.026500
C	-1.536500	2.661296	5.026500
C	3.073000	0.000000	5.026500
C	1.536500	2.661296	5.026500
Si	0.000000	1.774197	4.403214
Si	1.536500	0.887099	9.429714
Si	0.000000	0.000000	1.889964
Si	-1.536500	2.661296	1.889964
Si	3.073000	0.000000	1.889964
Si	1.536500	2.661296	1.889964
Si	0.000000	0.000000	6.916464
Si	-1.536500	2.661296	6.916464
Si	3.073000	0.000000	6.916464
Si	1.536500	2.661296	6.916464
C	-1.536500	-0.887099	2.513250
C	1.536500	-0.887099	2.513250
C	-3.073000	1.774197	2.513250
C	-1.536500	4.435493	2.513250
C	4.609500	-0.887099	2.513250
C	3.073000	1.774197	2.513250
C	1.536500	4.435493	2.513250
C	0.000000	-1.774197	7.539750
C	-1.536500	0.887099	7.539750
C	-3.073000	3.548395	7.539750
C	0.000000	3.548395	7.539750
C	3.073000	-1.774197	7.539750
C	4.609500	0.887099	7.539750
C	3.073000	3.548395	7.539750

6H-SiC

C	0.000000	0.000000	0.000000
C	0.000000	0.000000	15.170000
C	-1.547500	2.680349	0.000000
C	-1.547500	2.680349	15.170000
C	3.095000	0.000000	0.000000
C	3.095000	0.000000	15.170000
C	1.547500	2.680349	0.000000

C	1.547500	2.680349	15.170000
C	0.000000	0.000000	7.585000
C	-1.547500	2.680349	7.585000
C	3.095000	0.000000	7.585000
C	1.547500	2.680349	7.585000
C	0.000000	1.786899	2.528333
C	1.547500	0.893449	10.113333
C	0.000000	1.786899	12.641666
C	1.547500	0.893449	5.056666
Si	0.000000	0.000000	1.896250
Si	-1.547500	2.680349	1.896250
Si	3.095000	0.000000	1.896250
Si	1.547500	2.680349	1.896250
Si	0.000000	0.000000	9.481250
Si	-1.547500	2.680349	9.481250
Si	3.095000	0.000000	9.481250
Si	1.547500	2.680349	9.481250
Si	0.000000	1.786899	4.425089
Si	1.547500	0.893449	12.010089
Si	0.000000	1.786899	14.537411
Si	1.547500	0.893449	6.952411
C	-1.547500	-0.893449	2.528333
C	1.547500	-0.893449	2.528333
C	-3.095000	1.786899	2.528333
C	-1.547500	4.467248	2.528333
C	4.642500	-0.893449	2.528333
C	3.095000	1.786899	2.528333
C	1.547500	4.467248	2.528333
C	0.000000	-1.786899	10.113333
C	-1.547500	0.893449	10.113333
C	-3.095000	3.573798	10.113333
C	0.000000	3.573798	10.113333
C	3.095000	-1.786899	10.113333
C	4.642500	0.893449	10.113333
C	3.095000	3.573798	10.113333
C	-1.547500	0.893449	5.056666
C	0.000000	3.573798	5.056666
C	1.547500	-0.893449	12.641666
C	3.095000	1.786899	12.641666

Diamond

C	0.000000	0.000000	0.000000
C	0.000000	0.000000	3.566790
C	0.000000	3.566790	0.000000
C	0.000000	3.566790	3.566790
C	3.566790	0.000000	0.000000
C	3.566790	0.000000	3.566790
C	3.566790	3.566790	0.000000
C	3.566790	3.566790	3.566790
C	0.000000	1.783395	1.783395
C	3.566790	1.783395	1.783395
C	1.783395	1.783395	0.000000

C	1.783395	1.783395	3.566790
C	1.783395	0.000000	1.783395
C	1.783395	3.566790	1.783395
C	2.675093	0.891698	2.675093
C	0.891698	0.891698	0.891698
C	0.891698	2.675093	2.675093
C	2.675093	2.675093	0.891698

H₂O

3 atoms

2 bonds

1 angles

Masses

1 1.007940

2 15.99940

Atoms

1	1	2	-1.0484	0.00	0.00	0.92
2	1	1	0.5242	0.91	-0.03	1.21
3	1	1	0.5242	0.05	0.25	0.00

Bonds

1 1 1 2

2 1 1 3

Angles

1 1 2 1 3